UNIVERSITEIT VAN PRETORIA
UNIVERSITY OF PRETORIA
YUNIBESITHI YA PRETORIA

MUTUAL ADMITTANCE BETWEEN CPW-FED SLOTS ON CONDUCTOR-BACKED TWO-LAYER SUBSTRATES

by

Jan Pieter Jacobs

Submitted in partial fulfillment of the requirements for the degree

Philosophiae Doctor

(Electronic Engineering)

in the

Department of Electrical, Electronic & Computer Engineering

School of Engineering

Faculty of Engineering, the Build Environment and Information Technology

UNIVERSITY OF PRETORIA

September 2007

SUMMARY

MUTUAL ADMITTANCE BETWEEN CPW-FED SLOTS ON CONDUCTOR-BACKED TWO-LAYER SUBSTRATES

Author: Jan Pieter Jacobs
Promotors: Prof. J. Joubert and Prof. J. W. Odendaal
Department: Electrical, Electronic & Computer Engineering
University: University of Pretoria
Degree: Philosophiae Doctor (Electronic Engineering)

Keywords: CPW-fed slots, mutual admittance, self-admittance, conductor-backed two-layer substrates, antenna arrays

Slot dipole antennas fed by coplanar waveguide (CPW) on substrates consisting of a single dielectric layer exhibit various attractive qualities, including significantly wider impedance bandwidth than comparable microstrip patch antennas. For applications that call for unidirectional radiation, such as antennas on airframes, a conducting back plane is needed. A CPW on a conductor-backed single-dielectric-layer substrate will always experience power leakage into the TEM parallel-plate mode. On the other hand, it is possible to design CPW lines on conductor-backed two-layer substrates that are free from leakage into the substrate. However, once the CPW is used as feed line to a slot dipole, power leakage into the TM_0 substrate mode caused by the transition between the CPW and the radiating slot, and by the radiating slot itself, may still severely compromise radiation efficiency.

This study has two main contributions to offer. First, a paucity of work on CPW-fed slot antennas on conductor-backed two-layer substrates is alleviated by providing a fuller characterization of single-slot behaviour on two-layer parallel-plate substrates than is currently available, and by systematically investigating a practically feasible minimum antenna configuration, namely broadside twin slots, that is not debilitated by the problem of substrate mode leakage. Results obtained with the moment-method-based electromagnetic simulator IE3D that emphasize the trade-off between radiation efficiency and impedance bandwidth are presented; they can be used for design purposes. For instance, with respect to single slots on a substrate with an electrically thin top dielectric layer and an air bottom layer, it is shown that radiation efficiency increases and bandwidth decreases

as height of the bottom substrate layer increases. For broadside twin slots, it is demonstrated that spacing close to half a wavelength of the two-layer parallel-plate TM_0 mode apart can yield a large improvement in radiation efficiency over that of a single slot (a reduction in bandwidth however occurs).

The second main contribution is the development of an approach for finding the mutual admittance Y_{12} between CPW-fed slots on conductor-backed two-layer substrates that can be more readily incorporated in an iterative array design procedure than a moment-method-based technique, yet is of comparable accuracy; it is built on a standard reciprocity-based expression. As an initial step, the mutual admittance between CPW-fed slots on a conductor-backed two-layer substrate with an air bottom layer is characterized using IE3D. This involves presenting curves for Y_{12} between twin slots against slot separation d along standard paths for slot half-lengths in the vicinities of the first and second resonant half-lengths of the corresponding isolated slots (such data might be used towards a first-order array design), and a study of the effect of back plane distance (*i.e.*, bottom layer height) on mutual coupling. The bulk of the thesis however is devoted to the above reciprocity-expression approach. Simplifying assumptions are outlined that make it possible to determine Y_{12} against d by performing a once-only moment-method analysis of each slot in isolation, and then calculating external and internal reaction integrals at each value of d. This is significantly more economical than carrying out a full moment-method analysis of the whole twin-slot structure at every instance of d. Evaluation of the internal reaction integral requires the appropriate component of the spatial-domain Green's function for the substrate, which is derived in a form containing Sommerfeld-type integrals; treatment of singularities is discussed. The reciprocity-expression approach is verified by comparing Y_{12} against d curves for twin slots and non-identical slot pairs on a variety of conductor-backed two-layer substrates to IE3D simulations. A procedure that involves judicious selection of reference planes is introduced by which agreement between the methods for the special case of twin slots with the same half-length as the corresponding isolated second-resonant slot can be even further improved. A measurement is provided that validate theoretical calculations.

OPSOMMING

WEDERSYDSE ADMITTANSIE TUSSEN KOPLANÊRE GOLFLEIER-GEVOERDE GLEUWE OP SUBSTRATE MET TWEE DIËLEKTRIESE LAE EN 'N AGTERSTE GRONDVLAK

Outeur: Jan Pieter Jacobs
Promotors: Prof. J. Joubert en prof. J. W. Odendaal
Departement: Elektriese, Elektroniese & Rekenaaringenieurswese
Universiteit: Universiteit van Pretoria
Graad: Philosophiae Doctor (Elektroniese Ingenieurswese)

Sleutelwoorde: koplanêre golfleier-gevoerde gleuwe, wedersydse admittansie, self-admittansie, parallel-plaat substrate met twee diëlektriese lae, antenne-samestellings

Gleuf-dipool antennes gevoer deur koplanêre golfleier (KPG) op substrate wat uit 'n enkele diëlektriese laag bestaan, het verskeie aantreklike eienskappe, onder meer beduidend beter impedansie-bandwydte as vergelykbare mikrostrook plakantennes. Vir toepassings wat unidireksionele straling benodig soos antennes wat op lugrame gemonteer is, word 'n geleidende agterste grondvlak benodig. 'n KPG op 'n substraat wat uit een diëlektriese laag bestaan met 'n grondvlak agter, sal altyd die TEM parallel-plaat-orde opwek en drywing afstaan aan hierdie orde. Aan die ander kant is dit moontlik om KPG-lyne te ontwerp op substrate met twee diëlektriese lae en 'n agterste grondvlak, wat nie drywing aan substraatordes sal verloor nie. Sodra hierdie KPG egter gebruik word om 'n gleuf-dipool te voer, kan drywingsverlies aan die TM_0 substraat-orde wat veroorsaak word deur die oorgang tussen die transmissielyn en die gleuf, asook deur die gleuf self, die stralingeffektiwiteit van die antenne ernstig benadeel.

Die twee hoofbydraes van hierdie studie is die volgende. Eerstens word die relatief min beskikbare navorsing oor KPG-gevoerde antennes op twee-diëlektriese-laag-substrate met 'n agterste grondvlak aangevul deur 'n vollediger karakterisering van die gedrag van enkele gleuwe op hierdie substrate. Ook word 'n realiseerbare gleufkonfigurasie, naamlik wye-sy tweeling-gleuwe wat die probleem van drywingsverlies aan substraatordes kan oorbrug, stelselmatig ondersoek. Resultate verkry met behulp van die momente-metode-gebaseerde simulator IE3D wat die gee-en-neem-verwantskap tussen stralingseffektiwiteit en impedansie-bandwydte illustreer, word getoon; hierdie resultate kan

gebruik word vir ontwerpsdoeleindes. Dit word byvoorbeeld getoon dat die stralingseffektiwiteit van enkelgleuwe op 'n substraat met 'n elektries-dun boonste diëlektriese laag en 'n onderste laag wat uit lug bestaan, toeneem en die bandwydte afneem as die hoogte van die onderste laag toeneem. Ook word gewys dat, wanneer wye-sy tweeling-gleuwe ongeveer helfte van die golflengte van die TM_0-orde in die substraat uitmekaar gespasieër is, 'n groot toename in stralingseffektiwiteit verkry kan word ten opsigte van dié van 'n enkele gleuf ('n afname in bandwydte vind egter plaas).

Die tweede hoofbydrae is die ontwikkeling van 'n metode om die wedersydse admittansie Y_{12} tussen KPG-gevoerde gleuwe op twee-diëlektriese-laag-substrate met 'n agterste grondvlak te bepaal wat meer geredelik in 'n iteratiewe samestelling-ontwerpsprosedure geïntegreer kan word as 'n momente-metode-gebaseerde tegniek, maar wat vergelykbare akkuraatheid het; die metode is gebaseer op 'n bekende wederkerigheidsformule. As 'n eerste stap word die wedersydse admittansie tussen KPG-gevoerde gleuwe op 'n twee-diëlektriese-laag-substraat met 'n agterste grondvlak waarvan die onderste laag lug is, gekarakteriseer met behulp van IE3D. Dit behels krommes vir Y_{12} teenoor d (die afstand tussen die gleuwe) vir standaard konfigurasies van tweeling-gleuwe met halflengtes in die omgewing van die eerste- en tweede-resonante halflengtes van die ooreenstemmende geïsoleerde gleuwe, asook 'n studie van die invloed van die afstand van die agterste grondvlak (*i.e.*, hoogte van die onderste diëlektriese laag) op die wedersydse koppeling (hierdie data kan aangewend word vir eerste-orde samestellings-ontwerpsdoeleindes). Die grootste deel van die tesis word gewy aan die wederkerigheidsformule-benadering hierbo genoem. Aannames word uiteengesit wat dit moontlik maak om Y_{12} teenoor d te bepaal deur elk van die geïsoleerde gleuwe slegs eenmalig te analiseer met behulp van die momente-metode, en dan eksterne en interne reaksie-integrale by elke waarde van d te bereken. Dit is aansienlik meer ekonomies as om 'n volle momente-metode-analise van die hele twee-gleuf-struktuur by elke waarde van d uit te voer. Vir berekening van die interne reaksie-integrale word die tersaaklike komponent van die ruimtelike-domein Green-funksie van die substraat vereis; daar word getoon hoe laasgenoemde afgelei kan word in 'n vorm wat Sommerfeld-tipe integrale bevat, en die numeriese hantering van singulariteite word bespreek. Die wederkerigheidsformule-benadering word geverifieër deur krommes vir Y_{12} teenoor d vir tweeling-gleuwe en nie-identiese gleufpare op 'n verskeidenheid van twee-diëlektriese-laag-substrate met 'n agterste grondvlak, te vergelyk met IE3D-simulasies. 'n Prosedure wat 'n toepaslike keuse van verwysingsvlakke behels, word aan die hand gedoen om die ooreenkoms tussen die metodes vir die spesiale geval van tweeling-gleuwe met dieselfde halflengte as die ooreenstemmende geïsoleerde tweede-resonante gleuf selfs verder te verbeter. 'n Meting word

getoon wat teoretiese berekeninge bevestig.

CONTENTS

CHAPTER 1 INTRODUCTION **1**

1.1 Background and objectives 1

1.2 Overview of thesis 7

CHAPTER 2 RADIATION EFFICIENCY AND IMPEDANCE BANDWIDTH OF SINGLE CPW-FED SLOT ANTENNA ON CONDUCTOR-BACKED TWO-LAYER SUBSTRATE **9**

2.1 Introduction 9

2.2 Numerical method and results 10

2.3 Conclusions 13

CHAPTER 3 RADIATION EFFICIENCY AND IMPEDANCE BANDWIDTH OF BROADSIDE CPW-FED TWIN SLOT ANTENNAS ON CONDUCTOR-BACKED TWO-LAYER SUBSTRATES **16**

3.1 Introduction 16

3.2 Numerical method 17

3.3 Influence of inter-slot distance 19

3.4 Influence of bottom substrate layer height 23

3.5 Conclusions 24

CHAPTER 4 GENERAL ASPECTS OF MUTUAL ADMITTANCE OF CPW-FED TWIN SLOTS ON CONDUCTOR-BACKED TWO-LAYER SUBSTRATES **28**

4.1 Introductory remarks 28

4.2 Mutual admittance of first- and second-resonance CPW-fed twin slots on conductor-backed two-layer substrate 29

4.2.1 Introduction 29

4.2.2 Method 30

4.2.3 Mutual admittance between broadside slots 31

4.2.4 Mutual admittance between collinear slots 39

4.2.5 Conclusions 40

4.3 Effect of back plane distance on mutual admittance between CPW-fed slots on conductor-backed two-layer substrates 41

4.3.1 Introduction . . . 41
4.3.2 Numerical method . . . 41
4.3.3 Results . . . 42
4.3.4 Conclusions . . . 44

CHAPTER 5 RECIPROCITY-EXPRESSION-BASED APPROACH FOR MUTUAL ADMITTANCE BETWEEN CPW-FED SLOTS ON CONDUCTOR-BACKED TWO-LAYER SUBSTRATES **45**

5.1 Introduction . . . 45
5.2 Formulation of reciprocity-expression approach for mutual admittance between CPW-fed slots on conductor-backed two-layer substrate . . . 48
5.2.1 Mutual admittance between centre-fed slots radiating into half-space . . . 48
5.2.2 Mutual admittance between CPW-fed slots on conductor-backed two-layer substrate . . . 50
5.2.2.1 External mutual admittance formulation . . . 52
5.2.2.2 Internal mutual admittance formulation . . . 55
5.3 Spatial-domain Green's function for conductor-backed two-layer substrate . . . 57
5.3.1 H_x^{TM} for $\hat{x}$-directed HMD against top conducting plate inside two-layer parallel-plate substrate . . . 60
5.3.2 H_x^{TE} for $\hat{x}$-directed HMD against top conducting plate inside two-layer parallel-plate substrate . . . 69
5.3.2.1 H_x^{TE} of $\hat{x}$-directed HMD in homogenous medium . . . 74
5.3.2.2 H_x^{TE} of $\hat{x}$-directed HMD inside two-layer parallel-plate substrate with top conducting plate removed . . . 79
5.3.2.3 Evaluation of singular integrals for H_x^{TE} of $\hat{x}$-directed HMD against top conducting plate inside two-layer parallel-plate substrate 81
5.4 Implementation and results . . . 87
5.4.1 Implementation strategy . . . 87
5.4.2 Results . . . 90
5.4.2.1 Substrate I: $h_1 = 0.05\lambda_d$, $h_2 = \lambda_0/6$, $\epsilon_{r1} = 3.38$, $\epsilon_{r2} = 1$ . . . 90
5.4.2.2 Substrate II: $h_1 = 0.1\lambda_d$, $h_2 = \lambda_0/6$, $\epsilon_{r1} = 6.15$, $\epsilon_{r2} = 1$ . . . 95
5.4.2.3 Substrate III: $h_1 = 0.013\lambda_d$, $h_2 = \lambda_0/6$, $\epsilon_{r1} = 2.2$, $\epsilon_{r2} = 1$ . . . 110
5.4.2.4 Effect of shift in two-port reference planes . . . 112
5.4.2.5 Experimental results . . . 115
5.5 Conclusions . . . 117

CHAPTER 6 CONCLUSIONS AND FUTURE WORK **121**

REFERENCES 125

CHAPTER 1
INTRODUCTION

1.1 BACKGROUND AND OBJECTIVES

Slot antennas fed by coplanar waveguide (CPW) exhibit various attractive qualities including significantly wider impedance bandwidth than microstrip patch antennas. Fig. 1.1 shows a CPW-fed rectangular slot dipole on a single-layer substrate, which is the simplest kind of practical CPW-fed slot with a standing-wave-type field distribution. The basic operation of such a slot is roughly as follows: the resonant frequency can be adjusted by adjusting the slot half-length L, while input impedance and bandwidth can be varied through adjustment of the slot width W (of course, fine-tuning could entail joint adjustments of these dimensions). Narrower slots yield wider E-plane radiation beamwidths [1]; the E-plane coincides with the plane $\phi = 90^\circ$ in Fig. 1.1. The fractional bandwidth (VSWR < 1.5) of such an antenna on an electrically thin substrate may exceed 10% [2], which is substantially greater than that of a rectangular microstrip patch on an electrically thin substrate. Recent years have seen a spate of articles introducing modified geometries aimed at enhancing the bandwidth even further, *e.g.*, [2–5], or achieve dual-band operation [6, 7]. A recently introduced broadband CPW-fed circular slot antenna was reported to have a fractional bandwidth of 143% [8]. In the sub-millimeter and millimeter-wave ranges, CPW-fed slots have been used as feeds in dielectric lens antennas for single-pixel atmospherical and astronomical applications [9]; arrays of CPW-fed slots are anticipated to be used in space missions [10].

There are also advantages implicit in the use of CPW as feed transmission line: CPW offers easy integration of lumped circuit elements which takes place entirely in the plane of the transmission line, and exhibits less dispersion than microstrip at millimeter-wave and submillimeter-wave frequencies.

For applications that call for unidirectional radiation such as antennas mounted on airframes, a conducting plane is needed to back the antenna structure. The transmission line is then referred to as

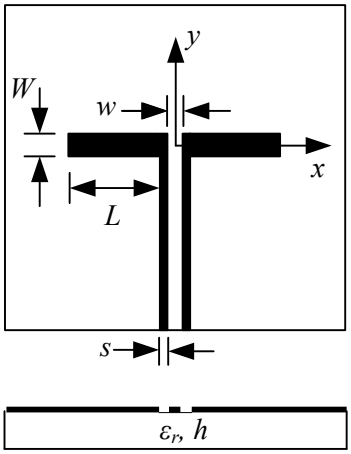

FIGURE 1.1: Top view, and side view looking into feed line of CPW-fed rectangular slot antenna on single-layer substrate. $L \equiv$ half-length and $W \equiv$ width of radiating slot dipole; $s \equiv$ slot width and $w \equiv$ centre strip width of feed line; $h \equiv$ height of dielectric layer; $\epsilon_r \equiv$ relative dielectric constant. The z axis points out of the page.

conductor-backed coplanar waveguide (CBCPW). A fundamental drawback of a simple single-layer CBCPW that is not laterally confined is power leakage into parallel-plate mode waves; a zero cutoff TEM mode is always present [11]. A CPW on a conductor-backed two-layer dielectric substrate may be designed to eliminate leakage into the substrate through appropriate choices of dielectric constants, layer heights and CPW dimensions [12, 13]. However, once the CPW is used as feed line to a radiating slot as shown in Fig. 1.2, power leakage into the TM_0 substrate mode (and potentially higher-order modes as well depending on the substrate height) caused by the discontinuity posed by the transition from the CPW into the radiating slot, and by the radiating slot itself, may still degrade radiation efficiency to such an extent that the antenna becomes unusable.

This thesis has two main objectives.

The *first* is to address a paucity of work on CPW-fed slot antennas on two-layer parallel-plate substrates[1]: while many studies have appeared on CPW-fed slots on single-layer substrates without conductor backing, only a handful are available addressing slots on the above two-layer substrate, *e.g.*, [14–16]. This objective is carried out in terms of both a fuller exploration of single-slot behaviour on two-layer parallel-plate substrates, and the investigation of a practically feasible minimum antenna configuration, namely a twin slot configuration, that is not debilitated by the problem of parallel-plate mode leakage. Emphasis is placed on the trade-off between radiation efficiency and impedance bandwidth as a function of substrate geometry, which has not been done

[1] The designations conductor-backed two-layer substrate and two-layer parallel-plate substrate will be used interchangeably in this thesis.

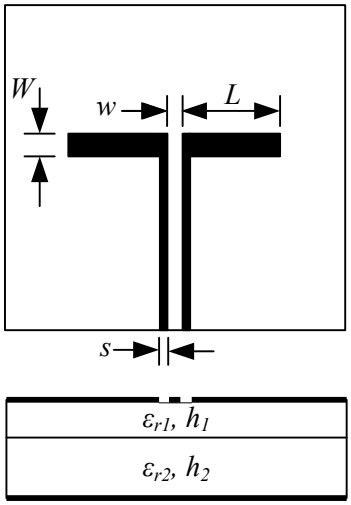

FIGURE 1.2: Top view, and side view looking into feed line of CPW-fed slot antenna on conductor-backed two-layer substrate. $s \equiv$ slot width and $w \equiv$ centre strip width of feed line; $L \equiv$ half-length and $W \equiv$ width of radiating slot dipole; h_1 and $h_2 \equiv$ heights of top and bottom dielectric layers; ϵ_{r1} and $\epsilon_{r2} \equiv$ relative dielectric constants of top and bottom layers.

previously.

The *second* main objective is to develop a technique, built on a standard reciprocity-based expression for centre-fed slots, to find the mutual admittance between two broadside CPW-fed slots on a two-layer parallel-plate substrate. It is instructive to formulate this objective in the context of antenna array design theory.

The design of high-performance arrays of longitudinal slots in rectangular waveguide has been well understood since the late 1970s/early 1980s, when a series of seminal papers by R. S. Elliott and co-workers, e.g., [17–20] made available a general iterative design procedure which notably accounted for mutual coupling in an accurate fashion. This made it possible to design non-uniform linear and planar arrays subject to stringent sidelobe level requirements. Other types of slot arrays that were reported in the wake of this work included arrays of transverse and longitudinal slots fed by boxed stripline [21–23], and slot arrays in the ground plane of microstrip line [24, 25].

In recent years, a variety of CPW-fed slot arrays on single-layer dielectric substrates have been reported. These include a wideband linear CPW-fed log-periodic dumb-bell slot array [26], amplifier arrays using CPW-fed folded slot antennas (*e.g.*, [27, 28]), a leaky-wave CPW-based slot antenna array for millimeter-wave applications [29], and CPW-fed two-dimensional slot arrays in multichip module-deposition (MCM-D) technology [30, 31] using metallic bridges realized on top of

a thin film deposited over the CPW feed lines to cancel excitation of the undesired slotline mode at discontinuities. None of these studies however addressed mutual coupling in a rigorous manner.

Of special interest to the present research are CPW-fed, *i.e.*, series-fed, linear slot arrays. Two kinds have been reported in the literature, namely *uniform* arrays, aimed at realizing an aperture distribution consisting of equal-amplitude and equal-phase element excitations [32–34], and *non-uniform* arrays, aimed at realizing an aperture distribution consisting of non-uniform amplitude, equal-phase excitations [35].[2]

More specifically, *uniform* CPW-fed arrays on single-layer dielectric substrates have been considered in [32–34]. In [32, 34], arrays on single-layer substrates that radiate in the presence of a back reflector positioned $\lambda_0/4$ away from the back (copper side) of the antenna are also described. Information given in [32, 33] regarding design procedures is very sparse; it was however possible in the course of the research undertaken for this thesis to successfully extend the iterative procedure of [34] to the design of an 8-element CPW-fed uniform array on a conductor-backed two-layer substrate as reported in [36]. The procedure relies on a full-wave electromagnetic simulator to compute the input impedance of individual slots as well as the input impedance of the array as a whole, and is notable for not requiring explicit mutual admittance or impedance calculations, yet indirectly does approximately account for the effects of mutual coupling via the above full-wave calculations.

As to *non-uniform* CPW-fed slot arrays, a design procedure is available for arrays on substrates consisting of a single thin dielectric layer [35]. The design of non-uniform arrays subject to rigorous sidelobe-level specifications generally requires explicit, accurate calculations of mutual coupling.[3] In [35], the problem of finding the mutual admittance between any two slots in the array is reduced, via a series of assumptions and approximations, to an equivalent problem that involves finding the mutual impedance between two wire dipoles in a homogeneous medium; a well-known reciprocity-based expression can be used for this purpose [18].[4] Since the authors apply their procedure to the design of a small uniform array only, the validity of the above approximations remains to be tested via the design of a non-uniform array subject to a low sidelobe level requirement.

Insight can be gained into how mutual coupling influences array functioning by briefly reviewing the network model underlying the design of linear broadside CPW-fed (*i.e.*, series-fed) slot arrays

[2] Both kinds have main beams at broadside.
[3] Trial-and-error approaches quickly become unfeasible as array size increases.
[4] This approach, which does not use the Green's function of the substrate, will be discussed in greater detail in Section 5.1.

[35]. Consider the generic array shown in Fig. 1.3. The substrate (not shown) could simply consist of a single dielectric layer as in [35], or be multi-layered, as in the case of the two-layer parallel-plate substrate implemented in [36]. There are N slots in the array that are spaced λ_{CPW} apart; this spacing ensures that slots are fed in phase. The half-length and width of each slot are denoted by L_m and W_m respectively, where $m = 1, 2, \ldots N$.

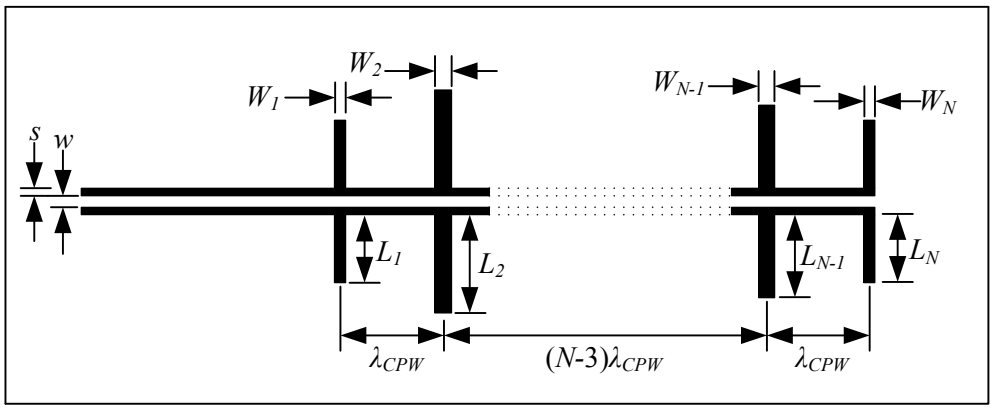

FIGURE 1.3: CPW-fed linear slot array ($N \geq 4$).

The above CPW-fed slot array can be represented as an equivalent transmission line circuit with the slots denoted by series impedances in the circuit [34, 35], as shown in Fig. 1.4. In terms of the usual multiport circuit formulation, with (V_m, I_m) the voltage and current pair at the terminals of slot m,

$$I_m = \sum_{n=1}^{N} Y_{mn} V_n \tag{1.1}$$

where $m = 1, 2, \ldots N$. In the above,

$$Y_{mn} = \frac{I_m}{V_n} \tag{1.2}$$

with $V_k = 0$ for $k \neq n$.

In the equivalent circuit of Fig. 1.4, each slot m is represented by its *active* (input) impedance Z_m^a, which includes the effects of mutual coupling with other slots in the array, or alternatively its active admittance $Y_m^a = 1/Z_m^a$. The active admittances Y_m^a can be obtained by dividing Eq. (1.1) by V_m:

$$Y_m^a = \frac{I_m}{V_m} = \sum_{n=1}^{N} Y_{mn} \frac{V_n}{V_m} \tag{1.3}$$

The input impedance of the array, Z_{in} can be expressed in terms of the active admittances Y_m^a as

$$Z_{in} = \sum_{m=1}^{N} \frac{1}{Y_m^a} \tag{1.4}$$

The above expression reflects the fact that the array of Fig. 1.4 is terminated in a short circuit; termination in other load impedances, *e.g.*, corresponding to tuning stubs, is also possible.

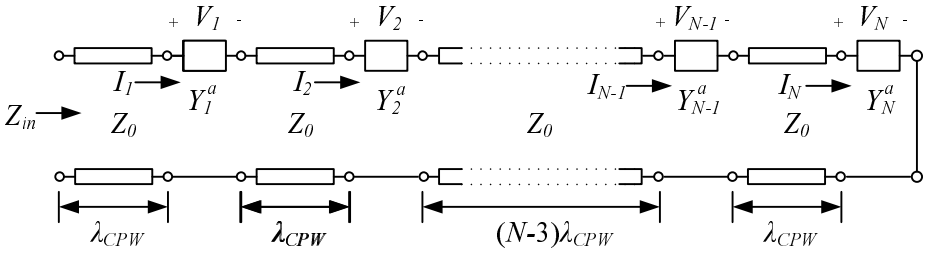

FIGURE 1.4: Transmission-line model for CPW-fed linear slot array.

In practice, it is normally assumed that the N-port self-admittances Y_{mm} are the same as the corresponding isolated slot self-admittances [35]. Also, it is strictly speaking necessary to calculate mutual admittances Y_{mn} in the context of the array, *i.e.*, with all the other slots present and short-circuited. However, the mutual admittance between a specific pair of slots is normally taken to be the mutual admittance between that pair of slots removed from the array in order to simplify calculations. Hence what may be termed a first-order interaction approach is adopted, neglecting the contribution of the rest of the short-circuited array [37].

In the open literature, mutual coupling between pairs of CPW-fed slots on multi-layered substrates has been calculated using a full method of moments (MoM) analysis approach [38] (the reciprocity-expression approach of [35] described earlier can only be applied to electrically thin, single-layer substrates and appears to require further investigation as noted). Hence, the second objective of the thesis, expressed more specifically, is to develop an alternative approach for finding (the first-order interaction approximation to) Y_{mn} of Eq. (1.2) using a simpler technique that would be more readily applicable in an array design procedure than a technique requiring a full MoM analysis, yet with comparable accuracy. An approach based on a standard reciprocity-based expression[5] will be formulated and implemented in conjunction with the appropriate substrate Green's function. In [10], it has been postulated (though not extensively motivated) that an accurate account of the CPW-to-radiating-slot transition in input impedance computations invariably requires a finely-discretized MoM analysis. Hence a question to be addressed is to what extent the accuracy of a simpler formulation would be affected by simplifying this particular aspect of a rigorous analysis, *i.e.*, circumventing a MoM analysis of the whole structure consisting of two radiating slots and their feed lines.

[5] It also has been the method of choice in earlier array designs such as the series-fed strip dipole array described in [18].

Both of the main objectives outlined above represent original contributions, some of which have been published [39–45]. An aspect of the second objective is the derivation of the required component of the spatial-domain Green's function for the magnetic field inside a conductor-backed two-layer substrate due to a horizontal magnetic dipole on the conducting plane adjacent to the higher-permittivity dielectric layer. The main objectives, subsidiary objectives, and their scope are specified in greater detail in the chapter-by-chapter overview of the thesis presented in Section 1.2.

1.2 OVERVIEW OF THESIS

The remaining chapters of the thesis are organized as follows.

In Chapter 2, radiation efficiency and impedance bandwidth of single matched CPW-fed slot dipoles on conductor-backed two-layer substrates are systematically investigated as a function of bottom substrate layer height.[6] Curves for radiating efficiency and return loss are provided that could be used to determine the bottom layer height that would yield the optimum efficiency/bandwidth combination for a particular application.

Chapter 3 investigates radiation efficiency and impedance bandwidth of matched broadside twin slot dipoles fed by CPW on a conductor-backed two-layer substrate as a function of distance between the slots, and height of the bottom substrate layer.[7] Previous reports dealing with slots on other layered media configurations indicated that radiation efficiency can be improved by using, instead of a single slot, two broadside slots spaced half a wavelength of the dominant surface-wave mode apart. The effect of bottom substrate height on gain and directivity is also investigated. The radiation efficiency of twin slots on a conductor-backed two-layer substrate is compared to that of previously reported twin slot antennas on a single dielectric substrate and a back plane placed $\lambda_0/4$ away from the etched side (λ_0 is the free-space wavelength). Measured scattering parameter results are presented to validate bandwidth computations.

In Chapter 4, general aspects of the mutual admittance between twin CPW-fed slots on a conductor-backed two-layer substrate with an air bottom layer are investigated using the full-wave moment-method-based simulator IE3D [46]. Two separate issues are addressed. First, a more comprehensive characterization of the mutual admittance between CPW-fed slots on a conductor-backed two-layer substrate than is currently available, is presented. Curves for the mutual admittance between first-resonance twin slots and second-resonance twin slots as a function of separation distance along standard paths are presented and compared to well-known curves for the

[6] Results presented in this chapter were published in [40].
[7] Results described in Chapter 3 were published in [42].

mutual admittance between two identical narrow center-fed slots on an infinite ground plane in free space. Second, the effect of an added conducting back plane on the mutual coupling between twin CPW-fed slots on a single-layer substrate is investigated as a function of back plane distance.[8]

Chapter 5 forms the bulk of the thesis. Here, a computational strategy, based on a well-known reciprocity-based expression, is developed for finding the mutual admittance between CPW-fed slots on a two-layer parallel-plate substrate (the context has been explained in Section 1.1). The mutual admittance Y_{12} between the slots can be viewed as the sum of external and internal mutual admittances: the external mutual admittance is due to coupling that takes place in the half-space adjacent to the slots, while the internal mutual admittance is due to coupling inside the substrate. In order to compute the internal mutual impedance, the appropriate component of the spatial-domain Green's function for the magnetic field inside a conductor-backed two-layer substrate due to a horizontal planar magnetic current density on the conducting plane adjacent to the higher-permittivity dielectric layer is required. A derivation is presented here which, to the knowledge of the author, has not been published elsewhere. Several results are presented for the mutual admittance between CPW-fed slots as a function of broadside inter-slot distance on a variety of two-layer parallel-plate substrates, and compared to results from the moment-method-based simulator IE3D. The effect of a shift in reference planes (situated along the CPW feed lines) on the two-port Y parameters is investigated and its implications for the reciprocity-expression approach considered. The relative contribution of external and internal mutual admittances to the total mutual admittance is discussed. Mutual admittance for twin slots with a fixed inter-slot distance is also computed as a function of frequency and compared to a measurement. Conclusions are drawn regarding the suitability of the reciprocity-based approach for accurate mutual admittance calculations as an alternative to moment-method-based calculations.

Finally, Chapter 6 presents general conclusions and suggestions for future work.

Throughout the thesis, all electromagnetic quantities are assumed to be sinusoidally time-varying according to an $e^{j\omega t}$ time dependence, which is suppressed. Vectors are denoted in boldface (*e.g.*, $\mathbf{E}$) and scalar quantities including vector components in italics (*e.g.*, E_x), while their spectral concomitants are indicated by means of adding a tilde to the original symbols (*e.g.*, $\tilde{\mathbf{E}}$ and $\tilde{E}_x$).

[8] This portion of the work served as basis for [43].

CHAPTER 2

RADIATION EFFICIENCY AND IMPEDANCE BANDWIDTH OF SINGLE CPW-FED SLOT ANTENNA ON CONDUCTOR-BACKED TWO-LAYER SUBSTRATE

2.1 INTRODUCTION

The objective of this chapter is to provide a systematic theoretical investigation of radiation efficiency and impedance bandwidth of a CPW-fed slot dipole on a conductor-backed two-layer substrate as a function of selected antenna dimensions, notably height of the bottom substrate layer.[1] Slot dipoles are attractive candidates for use in arrays due to their geometrical simplicity [34, 35]. Although a limited number of case studies of two-layer CBCPW-fed slot dipole antennas are available [14–16], systematic examinations of neither radiation efficiency, nor radiation efficiency in conjunction with impedance bandwidth, have been presented. For antennas on laterally infinite conductor-backed layered media, radiation efficiency can be defined as the ratio $\frac{P_{rad}}{P_{rad}+P_{sub}}$, where P_{rad} is radiated power, and P_{sub} is power associated with substrate modes [47, 48]; in the former definition, ohmic losses (conductor and dielectric) are considered negligible.

Previous studies of printed (non-CPW-fed) slot antennas have indicated a dependency between antenna height and radiation efficiency, for instance in the case of slots on thick substrates without conductor backing [49], and infinitesimal slots and rectangular slot dipoles on single-layer and two-layer parallel-plate substrates with conductor backing [47]. In [14, 16] a dependency between antenna height and radiation efficiency is suggested for CPW-fed slots on conductor-backed two-layer substrates but not fully investigated. This chapter examines radiation efficiency of matched (to 50 Ω) CPW-fed slots on a conductor-backed two-layer substrate as a function of height of the bottom

[1] Results presented in this chapter were published in [40].

substrate layer (the operating frequency is 2.4 GHz). The bottom substrate layer has the lower dielectric constant of the two layers. Increasing its height lowers the effective permittivity of the combined layers, improving radiation efficiency (a high effective permittivity would tend to confine electromagnetic fields to the inside of the antenna). As the interest lies in practically useful antennas, the concomitant impedance bandwidth is also considered. Furthermore, the influence of slot width on input impedance and radiation efficiency when substrate layer heights are fixed, is addressed.

2.2 NUMERICAL METHOD AND RESULTS

Numerical investigations were carried out using the moment method-based electromagnetic simulator IE3D [46], which uses a mixed-potential integral equation formulation [50] and assumes laterally infinite layered substrates.[2] In order to assess the program's performance with respect to planar slot antennas, the return loss, gain and directivity as a function of frequency, and principal radiation patterns were computed for two CPW-fed antennas reported in the literature: a CPW-fed slot dipole on a conductor-backed two-layer substrate [16] and a broadband slot antenna (consisting of a slot dipole capacitively coupled with another slot) on a single-layer substrate without conductor backing [51]. (Radiation efficiency can be calculated directly as gain divided by directivity [52].) In both cases good agreement with published results were obtained.[3]

The geometry of a CPW-fed slot dipole on a conductor-backed two-layer substrate is shown in Fig. 2.1.[4] In order to ensure a non-leaky transmission line, it is necessary (but not sufficient) for the top substrate layer to have a higher relative dielectric constant than the bottom substrate layer ($\epsilon_{r1} > \epsilon_{r2}$) [12, 13]. In simulations, dielectric constant values ϵ_{r1} and ϵ_{r2} were fixed throughout at respectively 2.2 and 1. For any slot dipole antenna used as a point of departure, the centre strip width w and slot widths s of the feed line were adjusted to yield a characteristic impedance of 50 Ω. These dimensions were kept constant when the effect of other dimensions of the structure, such as the height of the bottom substrate layer h_2, was investigated. Notably, feed line characteristic impedances deviated negligibly from 50 Ω when h_2 was varied as described below.

Fig. 2.2 graphs the input impedance against frequency of a slot dipole (referred to the edge of the slot) with half-length L = 53.8 mm, width W= 3 mm, top substrate layer height h_1 = 0.787 mm $\approx 0.01\lambda_d$, and bottom layer height $h_2 = 15$ mm $= 0.12\lambda_0$ (λ_d and λ_0 are the wavelengths in the dielectric and free space at 2.4 GHz). The curves corresponding to the real and imaginary

[2] A good overview of general characteristics of laterally open MoM formulations can be found in [50].
[3] In Sections 3.2, 4.3.3, and 5.4.2.5, measured results involving CPW-fed twin slots are presented and compared to IE3D calculations.
[4] For the purposes of this chapter and the next, the slot half-length L is defined to include the CPW slot width s. In Chapters 4 and 5, s is not considered part of L, which conforms to the definition of slot half-length in the CPW-fed array literature.

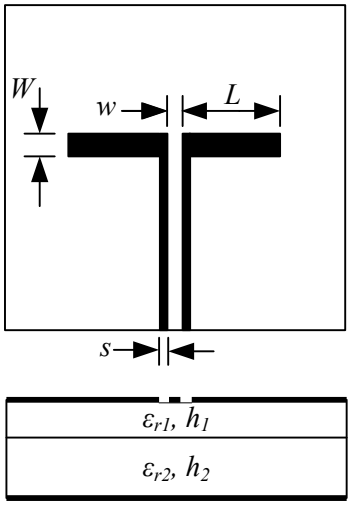

FIGURE 2.1: Top view, and side view looking into feed line of CPW-fed slot antenna on conductor-backed two-layer substrate. $L \equiv$ half-length and W= width of radiating slot dipole; $s \equiv$ slot width and $w \equiv$ centre strip width of feed line; h_1 and $h_2 \equiv$ heights of top and bottom dielectric layers; ϵ_{r1} and $\epsilon_{r2} \equiv$ relative dielectric constants of top and bottom layers.

components suggest the alternation of "steep" resonance regions with "flat" resonance regions; these curves are typical for the slots considered in this thesis (*cf.* [15]). Furthermore, antennas discussed in this chapter are designed to operate within the first "flat" resonance region because of the better matching possibilities compared to the "steep" regions (*cf.* [15]); the antenna of Fig. 2.2 thus would have an operating frequency corresponding to its second resonant frequency of 2.4 GHz. The form of the electric field in the radiating slot wil be considered at length in Chapter 4; it also has been treated elsewhere [14–16].

Since matched antennas are of interest and because it is known that input impedance can be adjusted by varying radiating slot width W [16], this dependency was investigated first for fixed half-length and substrate layer heights (L = 53.8 mm; h_1 = 0.787 mm; h_2 = 15 mm). The real and imaginary parts of the input impedance as a function of frequency are shown in Figs. 2.3 and 2.4 respectively for different slot widths. Inspection reveals a match to 50 Ω at 2.4 GHz for the case W/L = 0.056 (this antenna is the same as the $h_2 = 0.12\lambda_0$ case of Figs. 2.5 and 2.6 below). As W increased from L/40 to L/4, there was approximately a seven-fold increase in the value of the second-resonant input resistance (*i.e.*, the input impedance at the frequency where its imaginary component was zero). Radiation efficiency against frequency was also computed for each slot width. On the whole, and in particular in the vicinity of 2.4 GHz, radiation efficiency changed negligibly as W was varied in the manner described above. This appears to be consistent with the observation in [47] that, for rectangular slot dipoles on either single-layer or conductor-backed two-layer substrates, neither slot

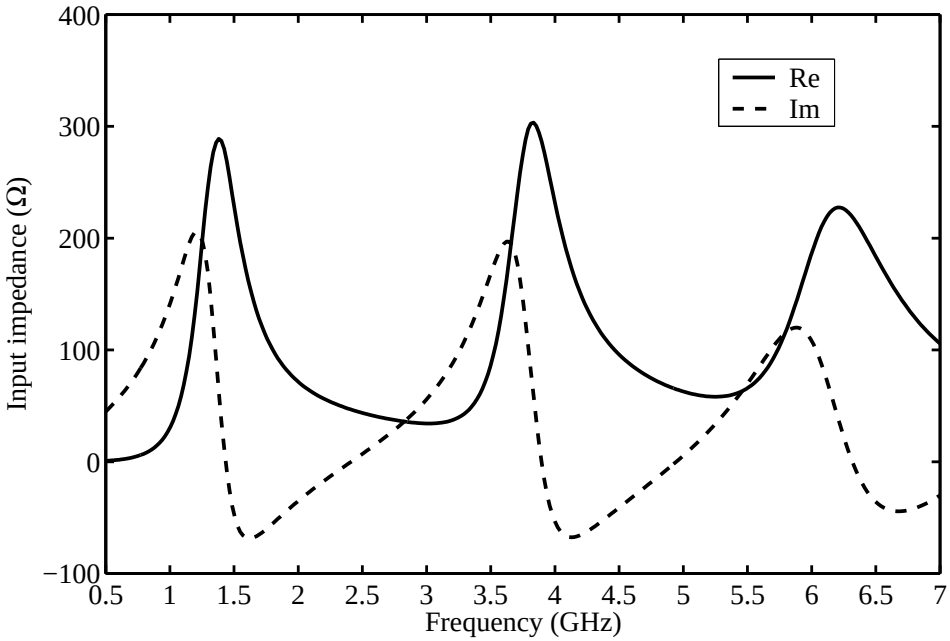

FIGURE 2.2: Input impedance of CPW-fed slot on two-layer parallel-plate substrate referred to edge of radiating slot. L = 53.8 mm; W= 3 mm; w = 10 mm; s = 0.25 mm; h_1 = 0.787 mm; h_2 = 15 mm; ϵ_{r1} = 2.2; ϵ_{r2} = 1.

length nor width has a significant effect on radiation efficiency.

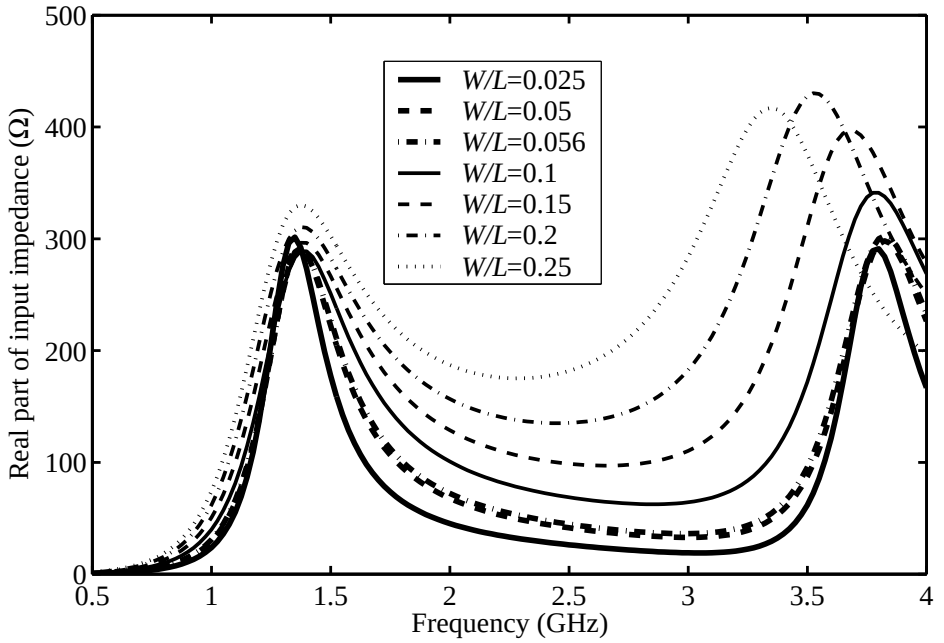

FIGURE 2.3: Influence of radiating slot width W on real part of input impedance. L = 53.8 mm; w = 10 mm; s = 0.25 mm; h_1 = 0.787 mm; h_2 = 15 mm; ϵ_{r1} = 2.2; ϵ_{r2} = 1.

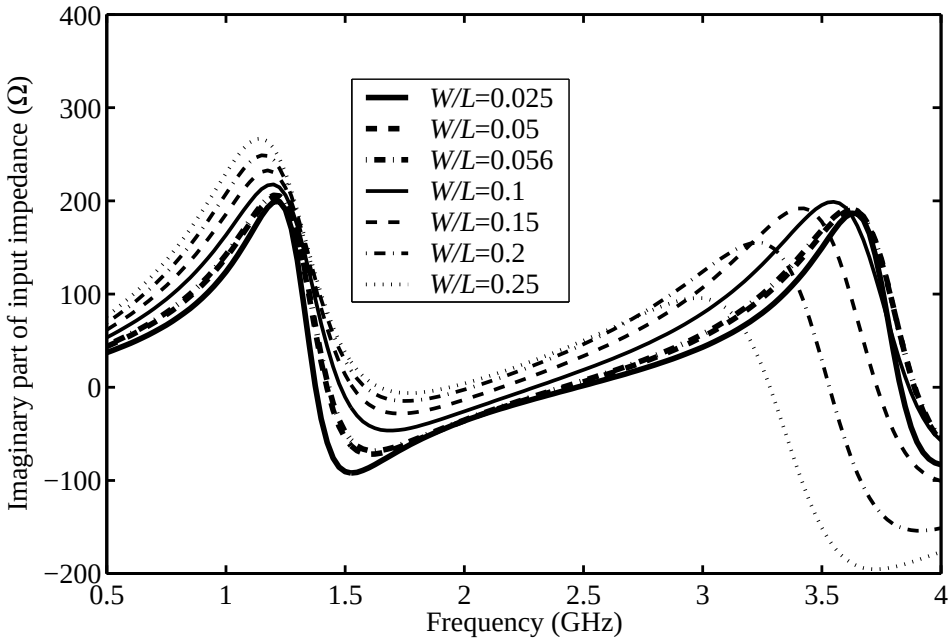

FIGURE 2.4: Influence of radiating slot width W on imaginary part of input impedance. L = 53.8 mm; w = 10 mm; s = 0.25 mm; h_1 = 0.787 mm; h_2 = 15 mm; ϵ_{r1} = 2.2; ϵ_{r2} = 1.

Next the effect was considered of bottom substrate layer height h_2 on radiation efficiency and impedance bandwidth of matched slot dipole antennas designed to operate at 2.4 GHz (in other words, slot dimensions were adjusted for each instance of h_2 to achieve an input match to 50 Ω at 2.4 GHz).

Fig. 2.5 shows return loss against frequency for different values of h_2. The interest was in slot dipoles that might potentially be used on airframes; hence the maximum value of h_2 was limited to less than 40 mm (40 mm = $0.32\lambda_0$ at 2.4 GHz; as before, λ_0 is the free-space wavelength at the operating frequency). Table 2.1 lists the impedance bandwidths at each value of h_2 corresponding to VSWR < 2 and VSWR < 1.5, as well as radiating slot dimensions. For both instances of VSWR, bandwidth decreased monotonically with increasing values of h_2. Fig. 2.6 shows the corresponding graph of radiation efficiency against frequency. Radiation efficiency increased markedly with increased height. However, as h_2 became larger, increases in radiation efficiency in response to the same incremental increases in height became less pronounced.

2.3 CONCLUSIONS

The behaviour of matched CPW-fed slots on conductor-backed two-layer substrates was systematically explored as a function of height of the bottom substrate layer. It was found for slots with a common operating frequency that radiation efficiency increased and bandwidth decreased as

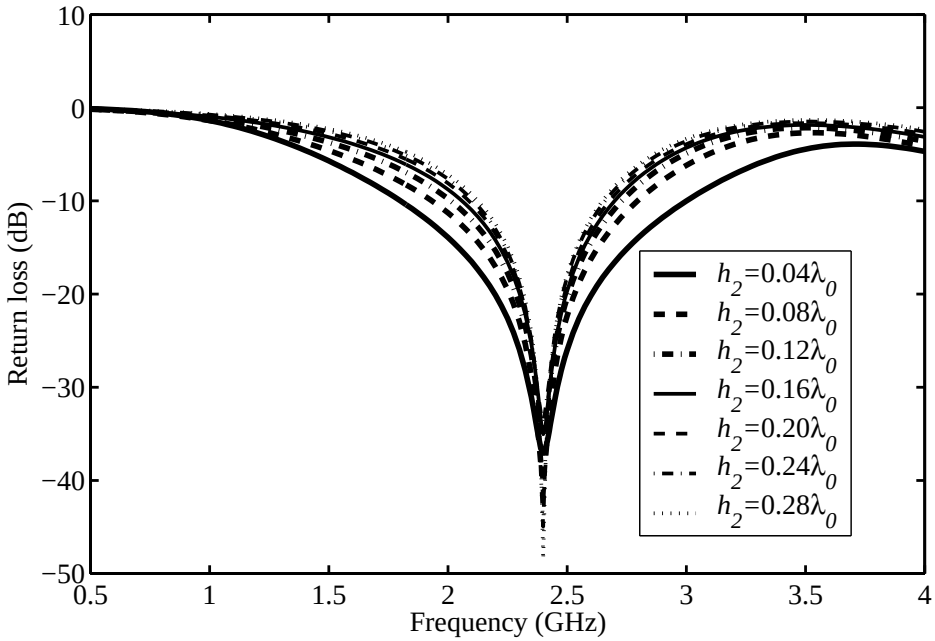

FIGURE 2.5: Influence of bottom substrate layer height h_2 on return loss for slots matched at 2.4 GHz. w = 10 mm; s = 0.25 mm; h_1 = 0.787 mm; ϵ_{r1} = 2.2; ϵ_{r2} = 1 (see Table 1 for radiating slot dimensions).

TABLE 2.1: Bandwidth against bottom substrate layer height h_2 for slots matched at 2.4 GHz. $w = 10$ mm; $s = 0.25$ mm; $h_1 = 0.787$ mm; $\epsilon_{r1} = 2.2$; $\epsilon_{r2} = 1$.

	Impedance bandwidth		Radiating slot dimensions (mm)	
h_2	VSWR < 2	VSWR < 1.5	L	W
0.04	52.3%	33%	49.9	1.1
0.08	38%	22.8%	53.3	2.2
0.12	31.6%	18.4%	53.8	3
0.16	28%	16.7%	53.6	3.8
0.2	26%	15.5%	53.3	4.6
0.24	24.3%	14.3%	52.9	5.4
0.28	23.1%	13.4%	52.3	6

height of the bottom substrate was increased. The most efficient antenna had a bottom dielectric layer height of $0.28\lambda_0$ (λ_0 is the free-space wavelength at the 2.4 GHz operating frequency) and a bandwidth of 13% (VSWR < 1.5); in this band, radiation efficiency varied between 56% and 59%. Curves for radiating efficiency and return loss for matched slots with different bottom substrate layer heights of the sort provided here could be used, in conjunction with expressed constraints

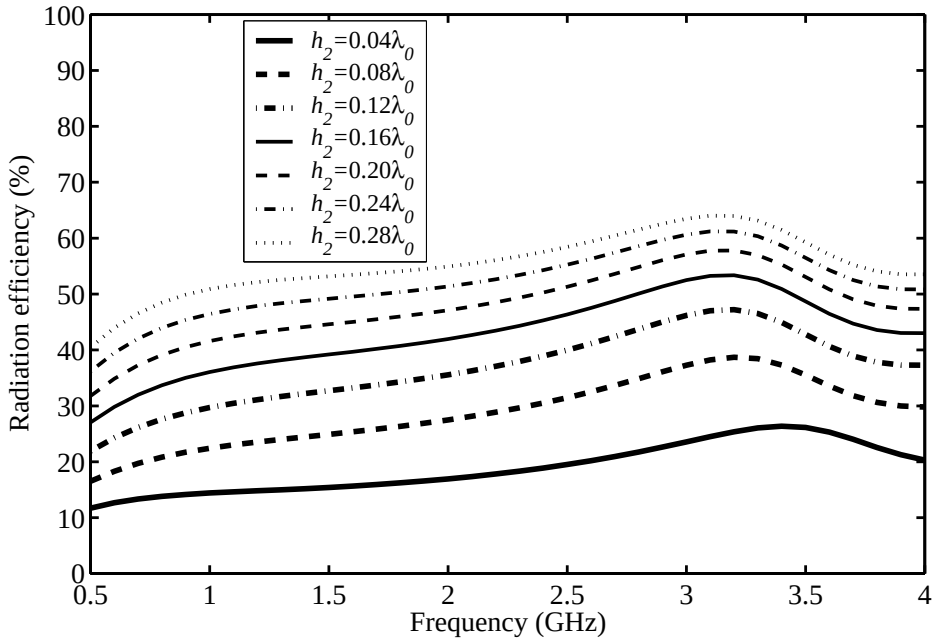

FIGURE 2.6: Influence of bottom substrate layer height h_2 on radiation efficiency for slots matched at 2.4 GHz. w = 10 mm; s = 0.25 mm; h_1 = 0.787 mm; ϵ_{r1} = 2.2; ϵ_{r2} = 1 (see Table 1 for radiating slot dimensions).

on antenna physical height, to determine the bottom layer height that would yield the optimum efficiency/bandwidth combination for a particular application.

CHAPTER 3

RADIATION EFFICIENCY AND IMPEDANCE BANDWIDTH OF BROADSIDE CPW-FED TWIN SLOT ANTENNAS ON CONDUCTOR-BACKED TWO-LAYER SUBSTRATES

3.1 INTRODUCTION

In the previous chapter, it was shown that low radiation efficiency due to parallel-plate mode leakage of matched CPW-fed single slots on conductor-backed two-layer high-low permittivity substrates may be notably improved by increasing the height of the bottom substrate layer at the cost of decreasing bandwidth. However, studies of other planar slot antennas have indicated that the radiation efficiency obtainable with a single slot can be greatly improved by placing two broadside slots half a wavelength of the dominant surface wave mode apart, resulting in substantial phase cancellation of that mode. This has for example been shown for elemental twin slots on a dielectric substrate with a thickness of $\lambda_d/4$ (λ_d is the wavelength in the dielectric) [49]; and for elemental twin slots on a 3-layer, high-low-high permittivity stack with each layer $\lambda_d/4$ thick, a configuration which manages to suppress strong coupling to all but the TM_0 mode [53]. With respect to slots on substrates consisting of one dielectric layer only, it was indicated in [49] that a limited improvement in radiation efficiency would result for a slot spacing aimed at canceling a particular surface wave mode when the substrate was high enough to allow propagation of several modes. In [54] it was demonstrated that the use of twin slots on $\lambda_d/4$ substrates, and twin slots on thin substrates, in both cases with a back reflector positioned $\lambda_0/4$ (a quarter free-space wavelength) away from the back (conductor) side of the antenna, also result in a vast improvement in radiation efficiency. In the case of $\lambda_d/4$ substrates, the use of twin slots achieves partial cancellation of both the parallel-plate TEM mode and the dielectric substrate TM_0 mode. In the thin substrate case, twin slots enhance efficiency predominantly through cancellation of the parallel-plate TEM mode. In [55] it was established that

using twin arc-slot radiators of appropriate radius of curvature and arc length could enhance guided leaky-wave cancellation even further. This slot shape ensures that surface wave cancellation is not limited to the slot broadside direction only. (Radiation efficiency of linear slot arrays of more than two elements was addressed in [34, 48].)

In this chapter, the focus is on radiation efficiency of CPW-fed twin (linear) slots on a conductor-backed two-layer substrate with high-low dielectric permittivities, the high permittivity layer being adjacent to the slots.[1] Fig. 3.1 shows the orientation of broadside twin slot dipoles, and explains notation with respect to geometrical parameters and material constants as applied in this chapter. Essentially two investigative goals were identified. The first was to explore the effect of inter-slot distance d on radiation efficiency while also establishing the concomitant effect on impedance bandwidth, relatively wide bandwidth being an appealing feature of CPW-fed slots. The second was to establish the effect of bottom substrate layer height h_2 on the radiation efficiency of optimally spaced twin slots, as it has been shown that radiation efficiency can be increased for single slots by increasing the bottom layer height (*cf.* Chapter 2); again, efficiency was to be considered in conjunction with bandwidth. Throughout, the interest lay in antennas that might be of practical use; hence each antenna configuration reported here involved matched single or twin slots.

It was noted earlier that high radiation efficiencies (*i.e.*, in the order of 90%) can be achieved by using appropriately spaced twin slots on either a $\lambda_d/4$ substrate with a back reflector positioned $\lambda_0/4$ away; or a thin ($\lambda_d/100$) substrate with a back reflector positioned $\lambda_0/4$ away [54]. The total height of these antennas may however become prohibitive for certain applications at microwave frequencies. It is shown below that comparable radiation efficiency may be attained using the structure of Fig. 3.1 – two dielectric layers sandwiched between two conducting plates – with a notably reduced profile compared to the structures of [54].

3.2 NUMERICAL METHOD

Numerical investigations were performed using the moment method-based electromagnetic simulator IE3D [46], assuming laterally infinite top and bottom conducting planes. Details regarding prior verification of the program's performance with respect to radiation efficiency and impedance bandwidth of CPW-fed single slot antennas were given in Chapter 1. In order to evaluate the program's performance with respect to structures containing more than one slot, and given the emphasis on impedance bandwidth in the present study, return loss as a function of frequency was computed for a test case involving matched CPW-fed twin slots on a conductor-backed two-layer

[1] Results described in this chapter were published in [42].

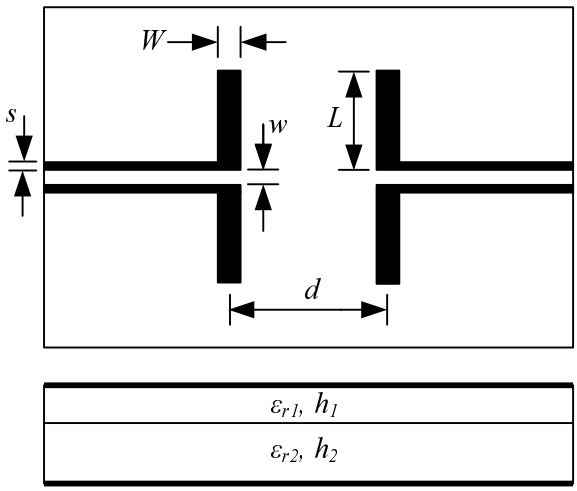

FIGURE 3.1: Top and side views of broadside CPW-fed twin slot antennas on conductor-backed two-layer substrate. $L \equiv$ half-length and $W \equiv$ width of radiating slots; $d \equiv$ distance between radiating slots; $s \equiv$ slot width and $w \equiv$ centre strip width of feed lines; h_1 and $h_2 \equiv$ dielectric layer heights; ϵ_{r1} and $\epsilon_{r2} \equiv$ relative dielectric constants.

substrate designed to operate at 8 GHz (*cf.* Fig. 3.1). The slots were spaced half a wavelength of the two-layer parallel-plate TM_0 mode apart [56]. Fig. 3.2 shows computed and measured results for return loss magnitude against frequency (the measurement was performed using a HP 8510C network analyzer). Good agreement between computation and measurement was obtained. The measured resonant frequency deviated by about 3% from the predicted value. Predicted and measured impedance bandwidth values also agreed well: 20.3% (VSWR < 2) and 11.5% (VSWR < 1.5) in the computed case, and 18.9% (VSWR < 2) and 10.9% (VSWR < 1.5) according to the measured return loss curve.

In simulations directed at investigating radiation efficiency and bandwidth in the manner described above, relative dielectric constant values ϵ_{r1} and ϵ_{r2} were fixed throughout at 2.2 and 1 respectively, while the top substrate layer was held constant at 0.787 mm (this is less than one hundredth of a dielectric wavelength at 2.4 GHz, the frequency at which simulations were carried out). A higher dielectric constant has to be chosen for the top substrate layer than for the bottom layer ($\epsilon_{r1} > \epsilon_{r2}$) in order to achieve a non-leaky transmission line [12]. The choice of a thin top layer in conjunction with a relatively low value of ϵ_{r1} was aimed at maximizing radiation efficiency as explained in Chapter 1. The centre strip width w and slot widths s of the feed lines were adjusted to yield a characteristic impedance of 50 Ω. These dimensions were kept constant when other dimensions of the antenna configuration were varied. Feed line characteristic impedances deviated negligibly from 50 Ω when the height of the bottom substrate layer h_2 was varied in the manner described below.

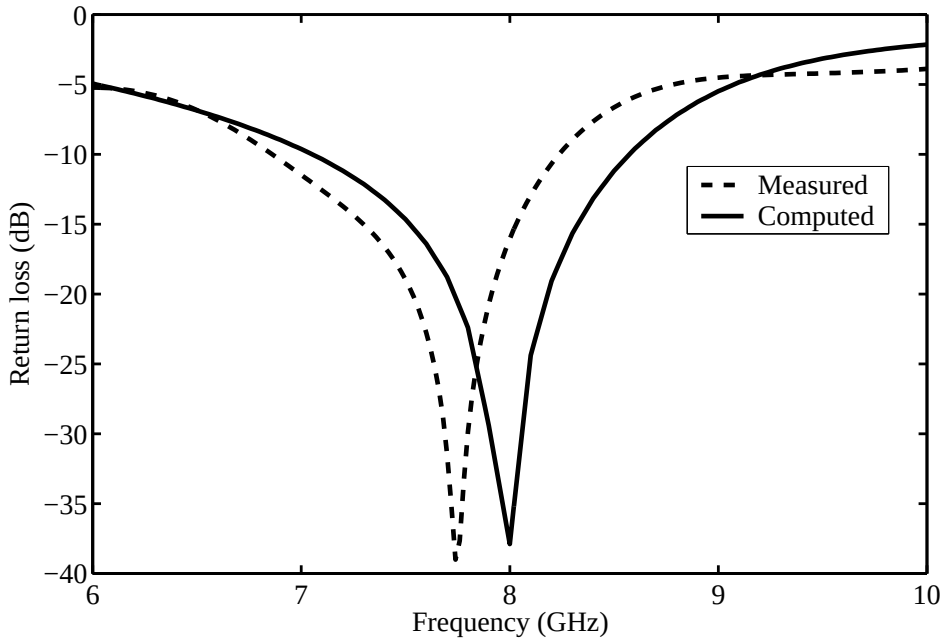

FIGURE 3.2: Return loss against frequency for broadside twin slots matched at 8 GHz. $L = 13.7$ mm; $W = 2.55$ mm; $d = 18.2$ mm; $w = 3.8$ mm; $s = 0.2$ mm; $h_1 = 0.813$ mm; $h_2 = 10$ mm; $\epsilon_{r1} = 3.38$; $\epsilon_{r2} = 1$.

3.3 INFLUENCE OF INTER-SLOT DISTANCE

The effect of inter-slot distance d on radiation efficiency was explored by varying d using increments of arbitrary value. Fig. 3.3 shows radiation efficiency at 2.4 GHz for twin slots as a function of normalized distance d/λ_0 (λ_0 is the free-space wavelength at 2.4 GHz). For each distance value corresponding to markers in the graph, the slots were matched at 2.4 GHz within the twin slot configuration using identical half-lengths L and widths W for each slot (feed lines were also identical). Slots were fed 180° out of phase at the feed line ports to achieve in-phase aperture field distributions. The bottom substrate layer height h_2 was fixed at $0.12\lambda_0$. This particular choice of h_2 (i.e., $h_2 = 15$ mm) was well below an upper limit of 40 mm motivated by an interest in antennas sufficiently thin to allow for use on airframes (*cf.* Chapter 2); it also precluded propagation of two-layer parallel-plate modes other than the TM_0 mode [56]. The radiation efficiency value at $d/\lambda_0 = 0$ shown in the graph of Fig. 3.3 pertains to a single slot matched at 2.4 GHz.

Fig. 3.3 reveals that radiation efficiency at 2.4 GHz for the matched twin slots increased monotonically as distance d was increased to $0.45\lambda_0$ and then decreased as d was further increased to $0.94\lambda_0$. Maximum radiation efficiency occurred for the case $d = 0.45\lambda_0$: 90% as opposed to 39% for the single slot. This value of d is close to half the wavelength of the two-layer parallel-plate TM_0 mode (λ_{TM_0}) at 2.4 GHz. Radiation efficiency at 2.4 GHz was the smallest for the case $d = 0.94\lambda_0$: 28% as opposed to 39% for the single slot case. This distance is close to λ_{TM_0},

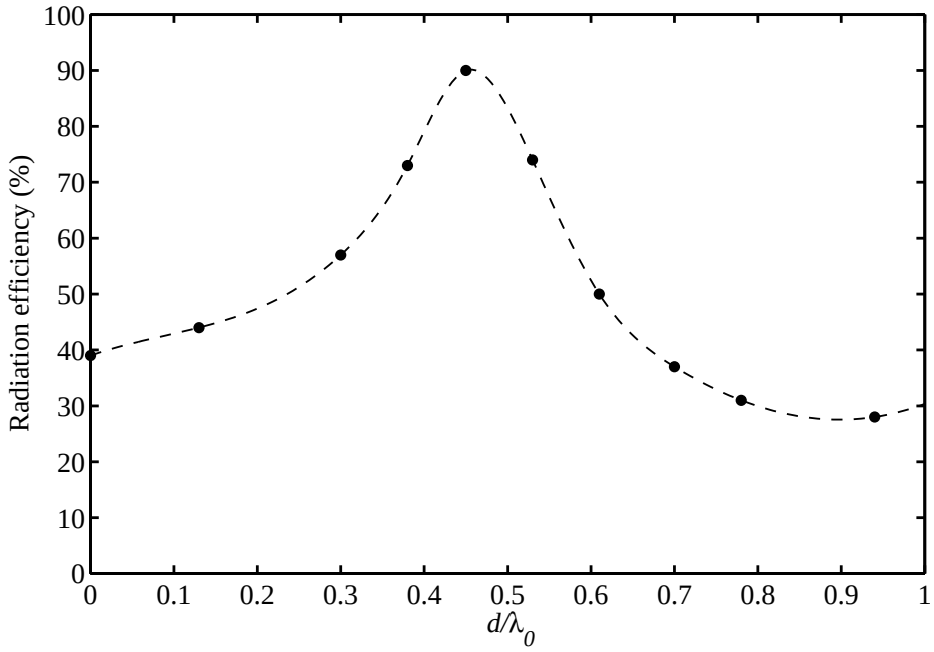

FIGURE 3.3: Radiation efficiency as a function of normalized distance d/λ_0 between slots matched at 2.4 GHz (λ_0 is the free-space wavelength at 2.4 GHz). $w = 10$ mm; $s = 0.25$ mm; $h_1 = 0.787$ mm; $h_2 = 0.12\lambda_0$ (15 mm); $\epsilon_{r1} = 2.2$; $\epsilon_{r2} = 1$. Radiation efficiency at $d/\lambda_0 = 0$ is that for a single slot matched at 2.4 GHz.

resulting in enhancement of the TM_0 fields in the slot broadside directions (an effect which is of course contrary to the desired phase cancellation).

Curves of return loss against frequency for the same twin slot configurations are presented in Fig. 3.4, while Table 3.1 lists twin slot impedance bandwidths at each value of d/λ_0 corresponding to the criteria VSWR < 2 and VSWR < 1.5 (radiating slot dimensions are also provided). The latter bandwidth values are graphed against normalized distance d/λ_0 in Fig. 3.5 (bandwidth values at $d/\lambda_0 = 0$ pertain to a single slot matched at 2.4 GHz). The impedance bandwidth for the highest radiation efficiency case ($d = 0.45\lambda_0$) was 13% (VSWR < 1.5), which is about two-thirds of the bandwidth of an matched single slot antenna on the same substrate. Notably, the case $d = 0.38\lambda_0$ had double the bandwidth (26.1%, VSWR < 1.5) of the best radiation efficiency case while its radiation efficiency at 73% was about four-fifths of the radiation efficiency in the best case, suggesting a reasonable compromise for situations where relatively large bandwidth is a priority.

Fig. 3.6 shows E-plane co-polarization patterns for a single slot matched at 2.4 GHz, and twin slots matched at the same frequency spaced $0.45\lambda_0$ apart (the optimum efficiency case of Fig. 3.3 and Table 3.1). In both cases cross-polarization levels were negligible. The twin slots' co-polarization pattern displays the narrower beamwidth and greater directivity expected for a small

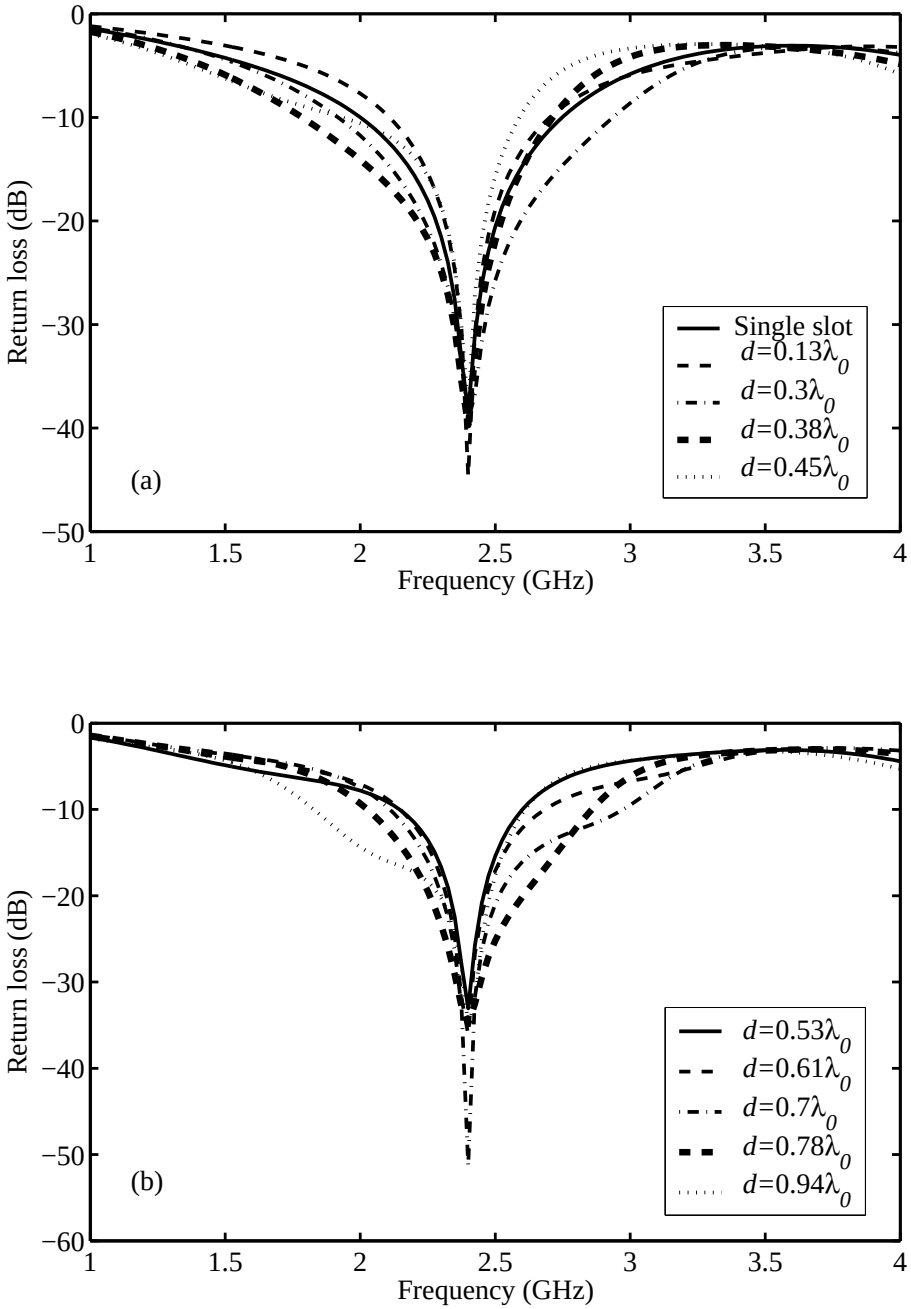

FIGURE 3.4: Return loss against frequency for (a) single slot matched at 2.4 GHz, and broadside twin slots matched at 2.4 GHz with spacings $d = 0.13\lambda_0$, $0.3\lambda_0$, $0.38\lambda_0$, $0.45\lambda_0$; and (b) matched twin slots with spacings $d = 0.53\lambda_0$, $0.61\lambda_0$, $0.7\lambda_0$, $0.78\lambda_0$, $0.94\lambda_0$ (λ_0 is the free-space wavelength at 2.4 GHz). $w = 10$ mm; $s = 0.25$ mm; $h_1 = 0.787$ mm; $h_2 = 0.12\lambda_0$ (15 mm); $\epsilon_{r1} = 2.2$; $\epsilon_{r2} = 1$.

(i.e., 2-element) array. In Fig. 3.7 the corresponding H-plane patterns are shown, in particular co- and cross-polarization patterns for the single slot, and the co-polarization pattern for the twin slots (cross-polarization is negligible in the latter case).

TABLE 3.1: Impedance bandwidth against normalized distance between slots d/λ_0, and corresponding radiating slot dimensions for twin slots matched at 2.4 GHz (λ_0 is the free-space wavelength at 2.4 GHz). $w = 10$ mm; $s = 0.25$ mm; $h_1 = 0.787$ mm; $h_2 = 0.12\lambda_0$ (15 mm); $\epsilon_{r1} = 2.2$; $\epsilon_{r2} = 1$. Bandwidth for matched single slot ($L = 53.8$ mm; $W = 3$ mm): 31.6% (VSWR < 2) and 18.4% (VSWR < 1.5).

	Impedance bandwidth		Radiating slot dimensions (mm)	
d/λ_0	VSWR < 2	VSWR < 1.5	L	W
0.13	26.3%	14.8%	49	3.8
0.3	44.3%	28.6%	51.7	2.0
0.38	40.3%	26.1%	55.5	2.3
0.45	30.3%	13.0%	57	3.5
0.53	20.5%	10.8%	54	4
0.61	24.1%	12.8%	51.7	3.7
0.7	37.8%	19.8%	50.7	3
0.78	36.1%	25.3%	51.7	2.3
0.94	33.8%	23.3%	55.5	3

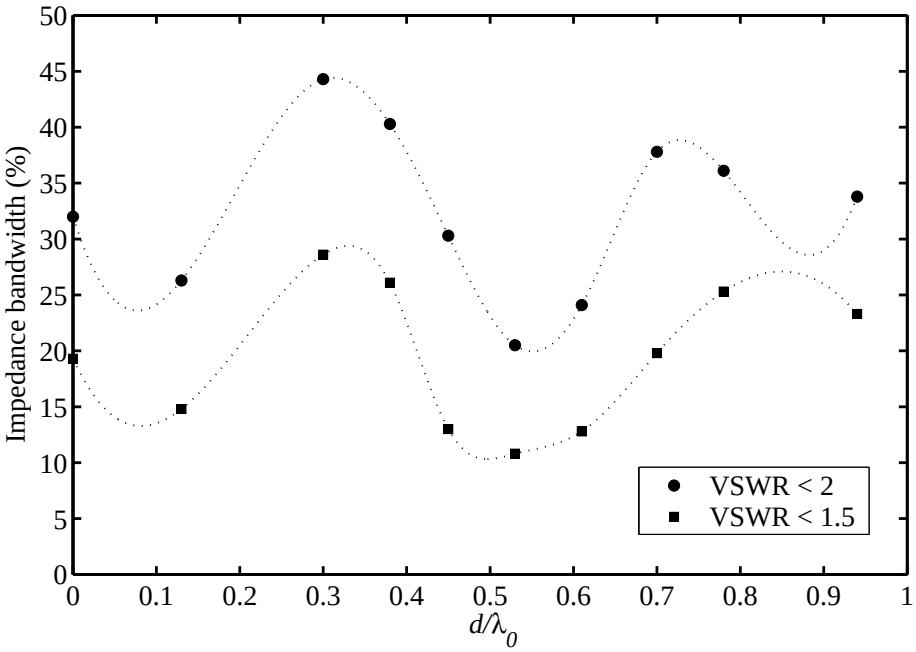

FIGURE 3.5: Impedance bandwidth as a function of normalized distance d/λ_0 between twin slots matched at 2.4 GHz (λ_0 is the free-space wavelength at 2.4 GHz). $w = 10$ mm; $s = 0.25$ mm; $h_1 = 0.787$ mm; $h_2 = 0.12\lambda_0$ (15 mm); $\epsilon_{r1} = 2.2$; $\epsilon_{r2} = 1$. Bandwidth values at $d/\lambda_0 = 0$ pertain to a single slot matched at 2.4 GHz.

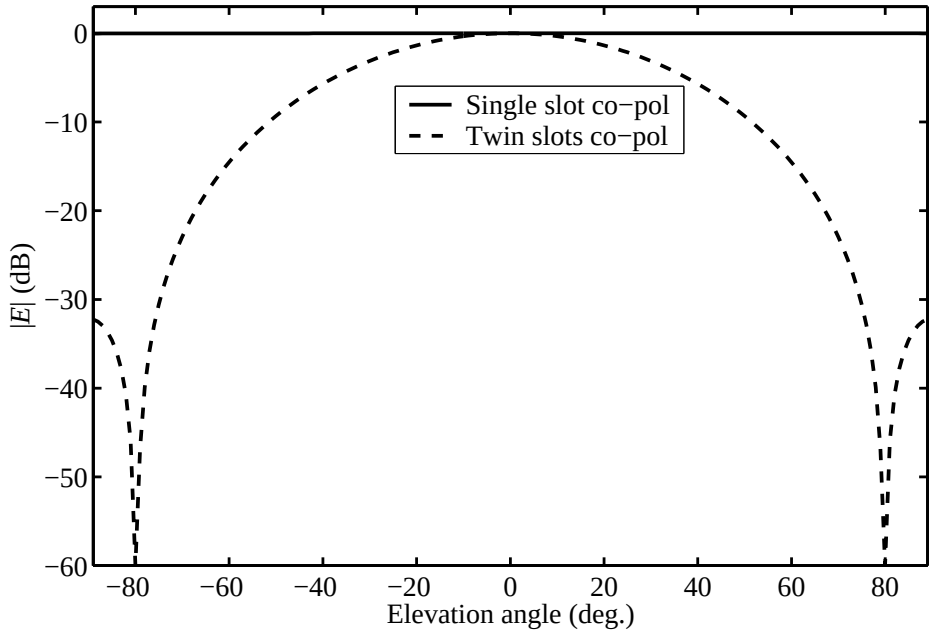

FIGURE 3.6: E-plane co-polarization patterns for a single slot matched at 2.4 GHz, and twin slots matched at 2.4 GHz spaced $0.45\lambda_0$ apart. $w = 10$ mm; $s = 0.25$ mm; $h_1 = 0.787$ mm; $h_2 = 15$ mm; $\epsilon_{r1} = 2.2$; $\epsilon_{r2} = 1$. Single slot: $L = 53.8$ mm; $W = 3$ mm. Twin slots: $L = 57$ mm; $W = 3.5$ mm.

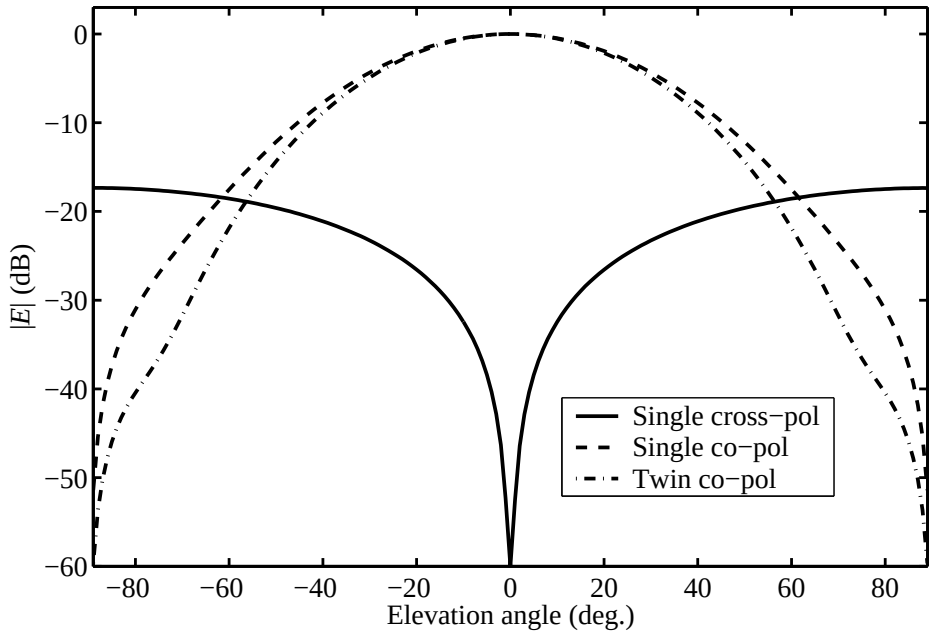

FIGURE 3.7: H-plane co-polarization and cross-polarization patterns for a single slot matched at 2.4 GHz, and H-plane co-polarization pattern for twin slots matched at 2.4 GHz spaced $0.45\lambda_0$ apart. $w = 10$ mm; $s = 0.25$ mm; $h_1 = 0.787$ mm; $h_2 = 15$ mm; $\epsilon_{r1} = 2.2$; $\epsilon_{r2} = 1$. Single slot: $L = 53.8$ mm; $W = 3$ mm. Twin slots: $L = 57$ mm; $W = 3.5$ mm.

3.4 INFLUENCE OF BOTTOM SUBSTRATE LAYER HEIGHT

Subsequently radiation efficiency and impedance bandwidth of $\lambda_{TM_0}/2$-spaced matched twin slots as a function of bottom substrate height h_2 was explored. This step was motivated by the finding in

Chapter 2 that radiation efficiency of CPW-fed single slots on conductor-backed two-layer high-low permittivity substrates may be notably improved by increasing the height of the bottom substrate layer, albeit at the cost of decreasing bandwidth. Also of interest was the effect of h_2 on directivity and gain.

The graph of Fig. 3.8 presents radiation efficiency against frequency for twin slots matched at 2.4 GHz spaced $\lambda_{TM_0}/2$ apart for different bottom layer heights h_2. Radiation efficiency at the operating frequency increased modestly with increasing h_2, which is not surprising given the already high efficiency associated with the lowest bottom substrate layer ($h_2 = 0.04\lambda_0 = 5$ mm). Thus a 3-fold increase in h_2 from $0.08\lambda_0$ to $0.24\lambda_0$ resulted in an increase in radiation efficiency of about 9%. Figs. 3.9 and 3.10 show the corresponding graphs of directivity and gain against frequency. It can be seen that neither gain nor directivity at 2.4 GHz is significantly affected as h_2 is varied. Fig. 3.11 shows return loss against frequency for different values of h_2, while Table 3.2 lists twin slot impedance bandwidths at each value of h_2 for VSWR < 2 and VSWR < 1.5, and the corresponding radiating slot dimensions. For both VSWR criteria, bandwidth decreased monotonically as h_2 was increased starting from $0.08\lambda_0$ (the lowest height case, $h_2 = 0.04\lambda_0$, did not conform to the decreasing trend and rather seemed to display a dual-band characteristic for VSWR < 2). The decrease was modest for the VSWR < 1.5 case: a 3-fold increase in h_2 from $0.08\lambda_0$ to $0.24\lambda_0$ resulted in a decrease in bandwidth of 5.5% from 21.5% to 16%. This decrease is less marked than that observed for a single slot subjected to similar increments in h_2 (*cf.* Chapter 2). In summary, given the already high radiation efficiency for the case $h_2 = 0.08\lambda_0$, a relatively large increase in height is necessary to effect a notable change in radiation efficiency; the same applies to bandwidth.

3.5 CONCLUSIONS

Radiation efficiency and impedance bandwidth of matched broadside CPW-fed twin slot dipoles on conductor-backed two-layer substrates were investigated as a function of distance between the slots, and height of the bottom substrate layer h_2. Radiation patterns were shown for optimally spaced twin slots, and the influence of h_2 on directivity and gain assessed. Twin slots on a relatively low substrate having $h_2 = 0.12\lambda_0$ were shown to yield more than double the radiation efficiency of a single slot on the same substrate (*i.e.*, 90% vs. 39%) when they were spaced close to half a wavelength of the two-layer parallel-plate TM_0 mode apart. The bandwidth of this configuration (13%, VSWR < 1.5) was about a third less than that of the matched single slot (*i.e.*, 18%). However, an inter-slot distance could be found that resulted in double the bandwidth of the maximally efficient case at the cost of a reasonable comprise with respect to radiation efficiency (73% vs. 90%). It was furthermore observed that the radiation efficiency of matched twin slots spaced $\lambda_{TM_0}/2$ apart could be further improved

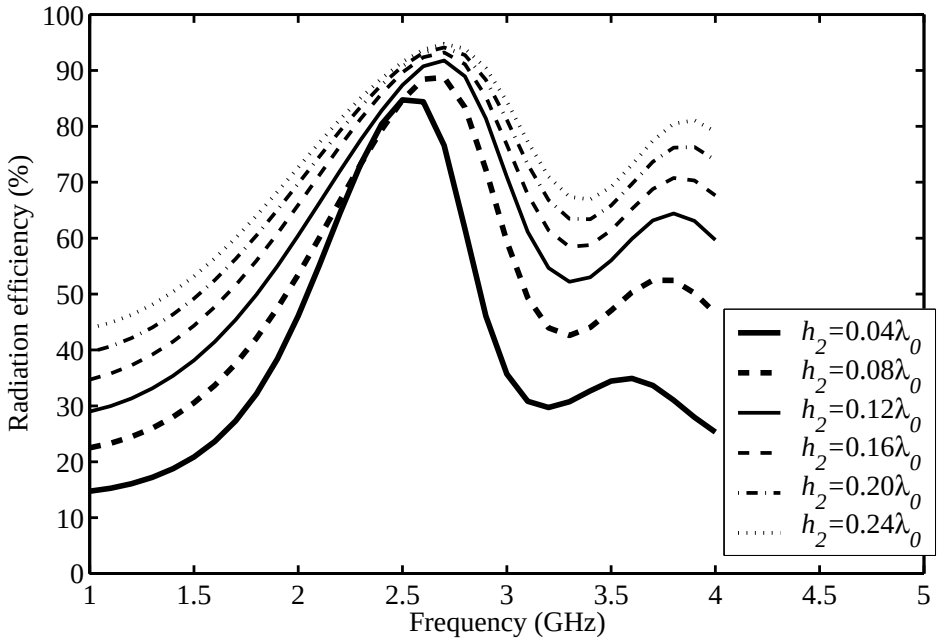

FIGURE 3.8: Influence of bottom substrate layer height h_2 on radiation efficiency for broadside twin slots spaced $\lambda_{TM_0}/2$ apart. The twin slots are matched at 2.4 GHz for each instance of h_2 (see Table 3.2 for slot dimensions). $w = 10$ mm; $s = 0.25$ mm; $h_1 = 0.787$ mm; $\epsilon_{r1} = 2.2$; $\epsilon_{r2} = 1$.

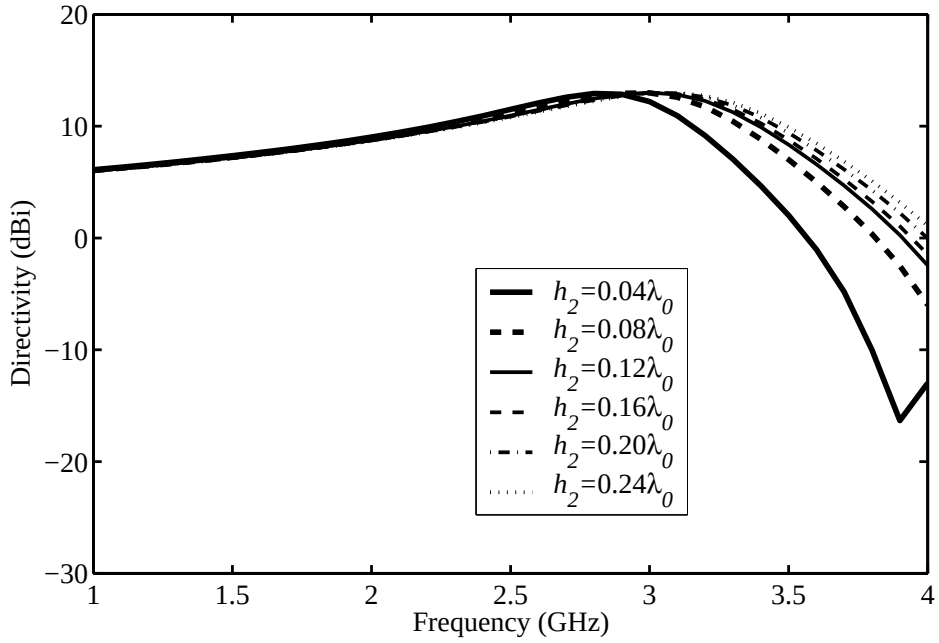

FIGURE 3.9: Influence of bottom substrate layer height h_2 on directivity for broadside twin slots spaced $\lambda_{TM_0}/2$ apart. The twin slots are matched at 2.4 GHz for each instance of h_2 (see Table 3.2 for slot dimensions). $w = 10$ mm; $s = 0.25$ mm; $h_1 = 0.787$ mm; $\epsilon_{r1} = 2.2$; $\epsilon_{r2} = 1$.

by increasing bottom substrate layer height h_2 (when h_2 = 0.08λ_0); bandwidth however decreased, albeit less markedly than in the case of a single slot. It was observed that radiation efficiency attainable with twin slots on two dielectric layers and a back conductor is comparable to that of twin

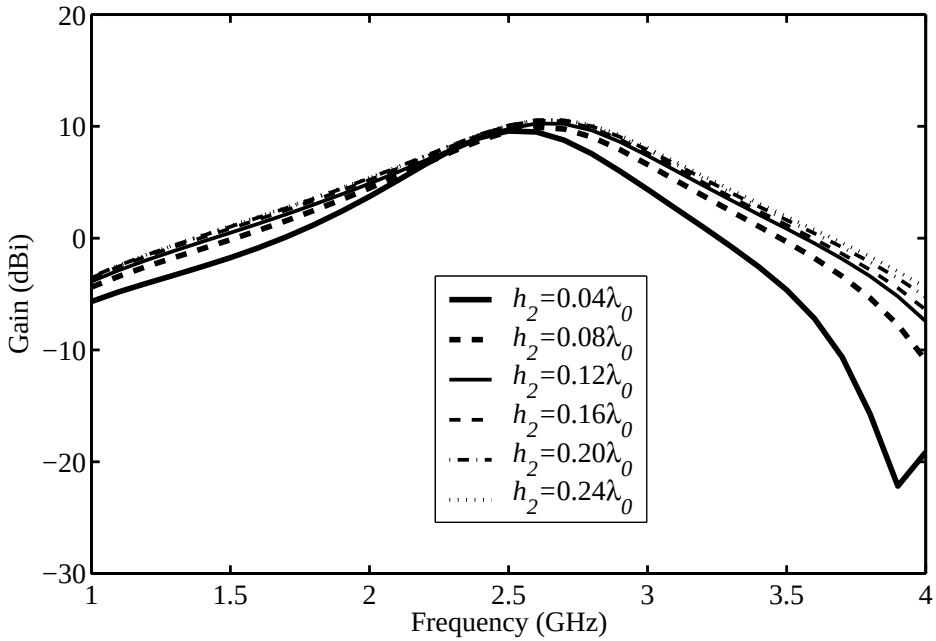

FIGURE 3.10: Influence of bottom substrate layer height h_2 on gain for broadside twin slots spaced $\lambda_{TM_0}/2$ apart. The twin slots are matched at 2.4 GHz for each instance of h_2 (see Table 3.2 for slot dimensions). $w = 10$ mm; $s = 0.25$ mm; $h_1 = 0.787$ mm; $\epsilon_{r1} = 2.2$; $\epsilon_{r2} = 1$.

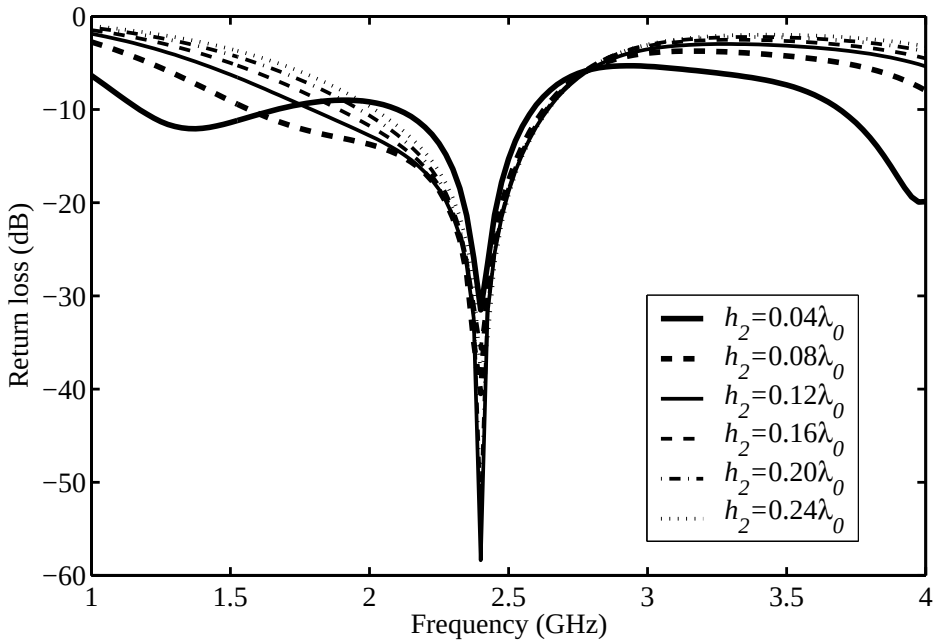

FIGURE 3.11: Influence of bottom substrate layer height h_2 on return loss for broadside twin slots spaced $\lambda_{TM_0}/2$ apart. The twin slots are matched at 2.4 GHz for each instance of h_2 (see Table 3.2 for slot dimensions). $w = 10$ mm; $s = 0.25$ mm; $h_1 = 0.787$ mm; $\epsilon_{r1} = 2.2$; $\epsilon_{r2} = 1$.

slots on $\lambda_d/4$ substrates (or thin substrates) with a back reflector positioned $\lambda_0/4$ away [54]. The lesser height of the two-layer parallel-plate structure would however be an advantage at microwave frequencies.

TABLE 3.2: Bandwidth against normalized bottom substrate layer height h_2/λ_0, and corresponding radiating slot dimensions for identical twin slots matched at 2.4 GHz. Slots were spaced $\lambda_{TM_0}/2$ apart; $h_1 = 0.787$ mm; $\epsilon_{r1} = 2.2$; $\epsilon_{r2} = 1$. In the case $h_2/\lambda_0 = 0.04$, the bandwidth given for VSWR < 2 corresponds to the second minimum (at 2.4 GHz) of the return loss curve in Fig. 3.11.

	Impedance bandwidth		Radiating slot dimensions (mm)	
d/λ_0	VSWR < 2	VSWR < 1.5	L	W
0.04	22.6%	10.8%	63	1.5
0.08	46.1%	21.5%	58	2
0.12	37.3%	20%	56.5	2.7
0.16	32.8%	18.3%	56	3.5
0.2	29.8%	17%	55	4
0.24	27.6%	16%	54	4.5

CHAPTER 4

GENERAL ASPECTS OF MUTUAL ADMITTANCE OF CPW-FED TWIN SLOTS ON CONDUCTOR-BACKED TWO-LAYER SUBSTRATES

4.1 INTRODUCTORY REMARKS

The present chapter is concerned with an exploratory investigation of the mutual admittance between identical (twin) CPW-fed slots on a single-layer substrate with a conducting back plane placed at a distance h_2 from the dielectric side of the substrate (the substrate can also be thought of as a conductor-backed two-layer substrate with an air bottom layer). While mutual coupling has been characterized to a greater or lesser extent for a number of kinds of slots on layered media including centre-fed rectangular slots on a dielectric half-space [57] and CPW-fed slots on two- and three-layer substrates without conductor backing [38], it has not yet, to the knowledge of the author, been done for CPW-fed slots on two-layer parallel-plate substrates. Fig. 4.1 shows a broadside twin slot configuration.[1]

Two separate issues are addressed, namely a characterization of the mutual admittance between twin slots with half-lengths in the vicinity of the first-resonance and second-resonance half-lengths of the corresponding isolated slots (Section 4.2), and an investigation of the effect of back plane distance on mutual coupling (Section 4.3).[2] Since each of Sections 4.2 and 4.3 are essentially self-contained, their respective conclusions sections (*i.e.*, Sections 4.2.5 and 4.3.4) replace the customary concluding section to the chapter.

[1] This configuration is similar to that of Fig. 3.1.
[2] A distinction is made between mutual admittance and mutual coupling that will be explained in the course of the chapter.

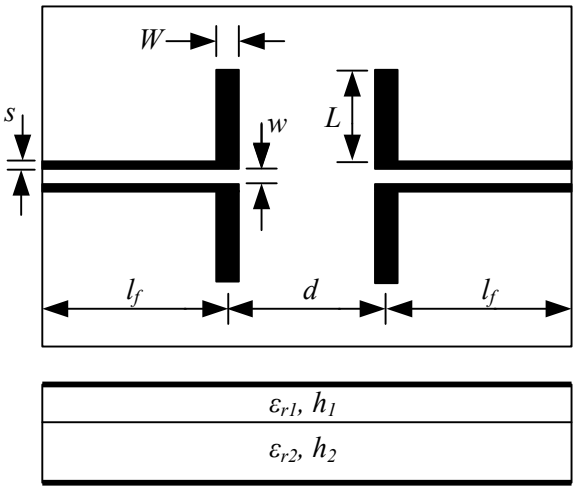

FIGURE 4.1: Top and side views of broadside CPW-fed twin slot antennas on conductor-backed two-layer substrate. $L \equiv$ half-length and $W \equiv$ width of radiating slots; $d \equiv$ distance between radiating slots; $s \equiv$ slot width and $w \equiv$ centre strip width of feed lines; $l_f \equiv$ length of feed lines; h_1 and $h_2 \equiv$ dielectric layer heights; ϵ_{r1} and $\epsilon_{r2} \equiv$ relative dielectric constants.

4.2 MUTUAL ADMITTANCE OF FIRST- AND SECOND-RESONANCE CPW-FED TWIN SLOTS ON CONDUCTOR-BACKED TWO-LAYER SUBSTRATE

4.2.1 Introduction

The aim of this section is to provide a more comprehensive characterization of the mutual admittance between CPW-fed slots on a conductor-backed two-layer substrate than is currently available. The characterization takes the form of curves for the mutual admittance between first-resonance twin slots and second-resonance twin slots as a function of separation distance along standard paths. Similar data is available for, *e.g.*, slots on semi-infinite substrates [57], first-resonance rectangular slots in the broad wall of rectangular waveguide [58], and first-resonance narrow center-fed slots on an infinite ground plane radiating in a homogeneous free space (graphs for the mutual impedance between the dual slender electric dipoles are well known and can be found in standard texts [18, Fig. 7.24], [59, Fig. 7.8]). In [57], the authors suggest that data of this nature can be used in the design of slot arrays using a first-order multi-port mutual admittance approach, where the array multi-port mutual admittance matrix is obtained by considering individual pairs of slots at a time (*cf.* Chapter 1). The mutual admittance curves for CPW-fed first- and second-resonance twin slots on a conductor-backed two-layer substrate presented in this chapter will be compared to findings relating to certain of the above types of slots. In the course of the investigation, the nature of first- and second-resonance slot electric field distributions will be addressed.

4.2.2 Method

Mutual admittance curves were computed using the moment-method-based electromagnetic simulator IE3D [60], which made it possible to explicitly account for feed line effects. Details of experimental results that verify the accuracy of IE3D with respect to mutual admittance computations involving CPW-fed slots on two-layer parallel-plate substrates are given in Sections 4.3 and 5.4.2.5.

The two-layer parallel-plate substrate and CPW feed lines were designed as follows. Relative dielectric constants ϵ_{r1} and ϵ_{r2} were 3.38 and 1 respectively, with substrate layer heights $h_1 = 0.813$ mm and $h_2 = 5$ mm; h_2 equals $\lambda_0/6$ at the 10 GHz simulation frequency, with λ_0 the free-space wavelength (the substrate was used in an earlier successful implementation of an 8-element uniform linear CPW-fed array [36]). A higher dielectric constant has to be chosen for the top substrate layer than for the bottom layer in order to help achieve a non-leaky CPW transmission line [12]. At 10 GHz, the only substrate mode that could propagate was the the TM_0 mode. A CPW centre strip width $w = 3.7$ mm and slot width $s = 0.2$ mm yielded a characteristic impedance of about 50 Ω.

Twin slot dimensions used in mutual admittance calculations were determined as follows.

First, an isolated CPW-fed radiating slot with a width $W = 0.4$ mm was designed to be resonant at 10 GHz by appropriately adjusting its half-length L. Half-lengths corresponding to the first and second resonances were $L_{res,1} = 0.27\lambda_s = 5.7$ mm and $L_{res,2} = 0.52\lambda_s = 10.87$ mm respectively (λ_s is the wavelength at 10 GHz of a 0.4 mm wide slotline on the two-layer parallel-plate substrate described above). $L_{res,1}$ and $L_{res,2}$ corresponded to resonant self-impedances of about 420 Ω and 14 Ω respectively.

Subsequently, mutual admittance Y_{12} against distance d was computed for two sets of twin slots based on the above isolated slots. Slot half-lengths for the first set were in the vicinity of $L_{res,1}$, while half-lengths for the second set were in the vicinity of $L_{res,2}$; in all cases W was 0.4 mm. Two slot configurations were investigated, namely broadside (*cf.* Fig. 4.1), and collinear. Throughout, lengths l_f of feed lines were $0.5\lambda_{CPW}$, where λ_{CPW} is the CPW wavelength at 10 GHz, in effect referring two-port network parameters to the centres of radiating slots.

For purposes of comparison, the mutual admittance between a set of identical broadside narrow rectangular slots in an infinite ground plane was computed against slot separation. Slot lengths $2l$ were in the vicinity of half a free-space wavelength corresponding to slots operating around their first resonances. Expressions for the mutual impedance Z_{12}^d between broadside slender electric dipoles

in free space, assuming sinusoidal current distributions, are available [18, Eqs. (7.155) and (7.156)]. The mutual admittance $Y_{12} = G_{12} + jB_{12}$ between the complementary centre-fed narrow slots in an infinite ground plane can be found from the former expressions using Booker's relation, $Y_{12} = (4/\eta_0^2)Z_{12}^d$, where η_0 is the intrinsic impedance of free space. The resulting graphs for identical broadside slots of length $2l$ are shown in Figs. 4.2 (G_{12}) and 4.3 (B_{12}); curves for $2l$ values of $0.375\lambda_0$, $0.5\lambda_0$ and $0.625\lambda_0$ are shown.

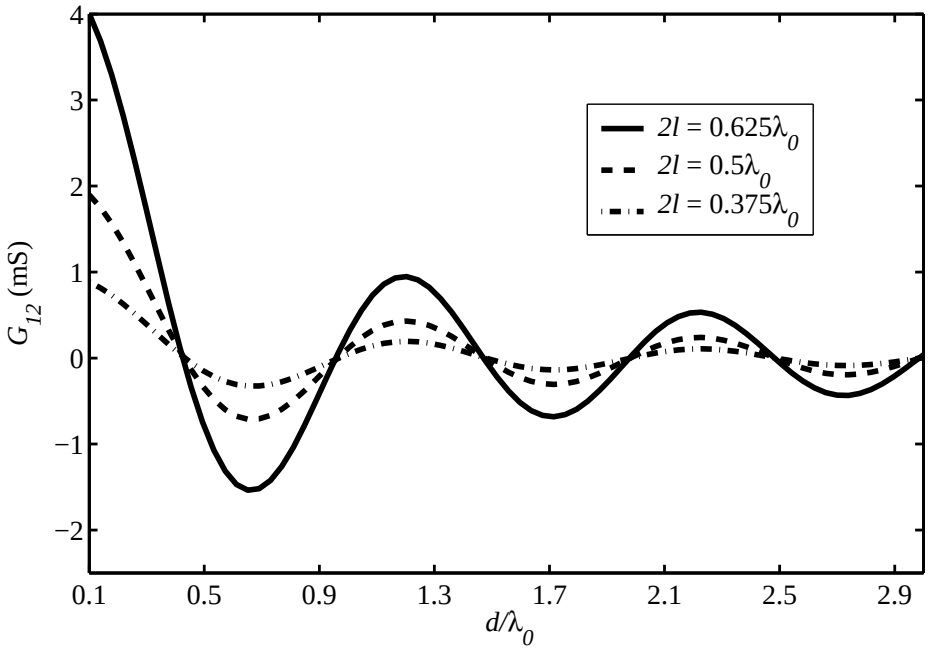

FIGURE 4.2: Mutual conductance G_{12} between identical centre-fed broadside narrow slots in an infinite ground plane against slot separation d/λ_0. The medium is homogeneous free space.

4.2.3 Mutual admittance between broadside slots

Figs. 4.4 and 4.5 show the magnitude and phase of the $\hat{y}$-directed aperture electric field along the centre of the isolated *first-resonance* slot which had $W = 0.4$ mm and $L = L_{res,1} = 0.27\lambda_s$ mm; the $\hat{x}$-directed field component can be considered negligible compared to the $\hat{y}$-component and is not shown (see Fig. 4.6 for coordinate axes). Fields for slots with half-lengths $0.9L_{res,1}$ and $1.1L_{res,1}$ are also shown. As expected, in all cases the field magnitude is approximately half-cosinusoidal while the phase is nearly constant. This is similar to electric currents on centre-fed cylindrical dipoles of comparable electrical lengths [18, Figs. 7.6 and 7.7]. Fig. 4.5 indicates that a change in slot half-length results in a phase that is offset with respect to the previous length's phase.

Plots of mutual admittance Y_{12} against broadside distance d/λ_{CPW} between twin slots with the above half-lengths are given in Fig. 4.7. The range of d was chosen as $0.9\lambda_{CPW} \leq d \leq 3\lambda_{CPW}$,

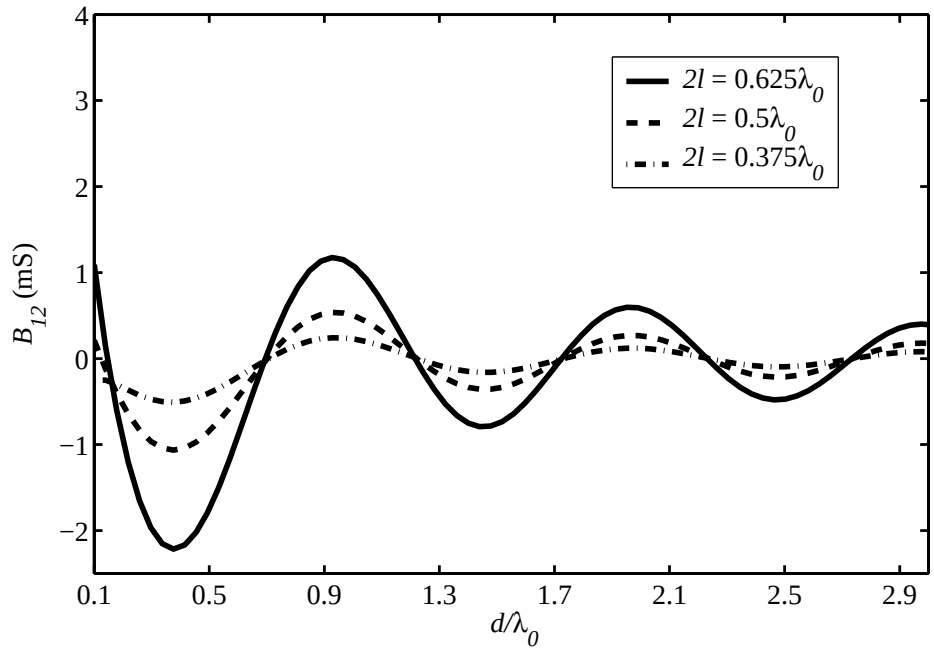

FIGURE 4.3: Mutual susceptance B_{12} between identical centre-fed broadside narrow slots in an infinite ground plane against slot separation d/λ_0. The medium is homogeneous free space.

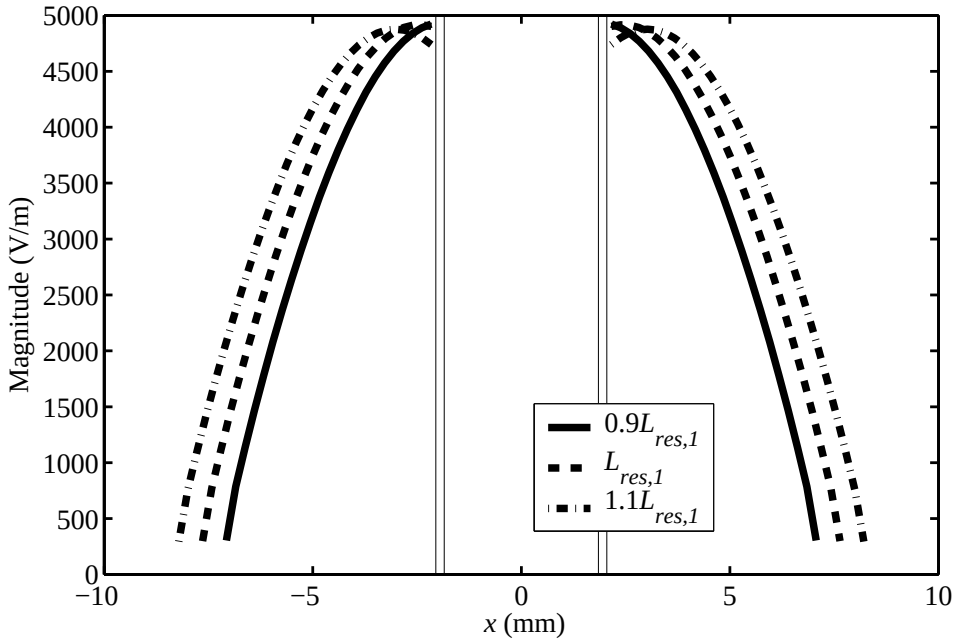

FIGURE 4.4: Magnitude of electric field of isolated slots with half-lengths in vicinity of first-resonance half-length $L_{res,1}$ on two-layer parallel-plate substrate. $L_{res,1} = 0.27\lambda_s = 5.7$ mm; $W = 0.4$ mm; $h_1 = 0.813$ mm; $h_2 = 5$ mm; $\epsilon_{r1} = 3.38$; $\epsilon_{r2} = 1$. Vertical lines correspond to positions of CPW slots.

given that mutual coupling in linear arrays with slots spaced λ_{CPW} apart has been taken into account for inter-slot spacings of up to $3\lambda_{CPW}$ [35]. The figure suggests that $|Y_{12}|$ increases as slot length increases, as in the case of centre-fed slots in an infinite ground plane (Figs. 4.2 and 4.3).

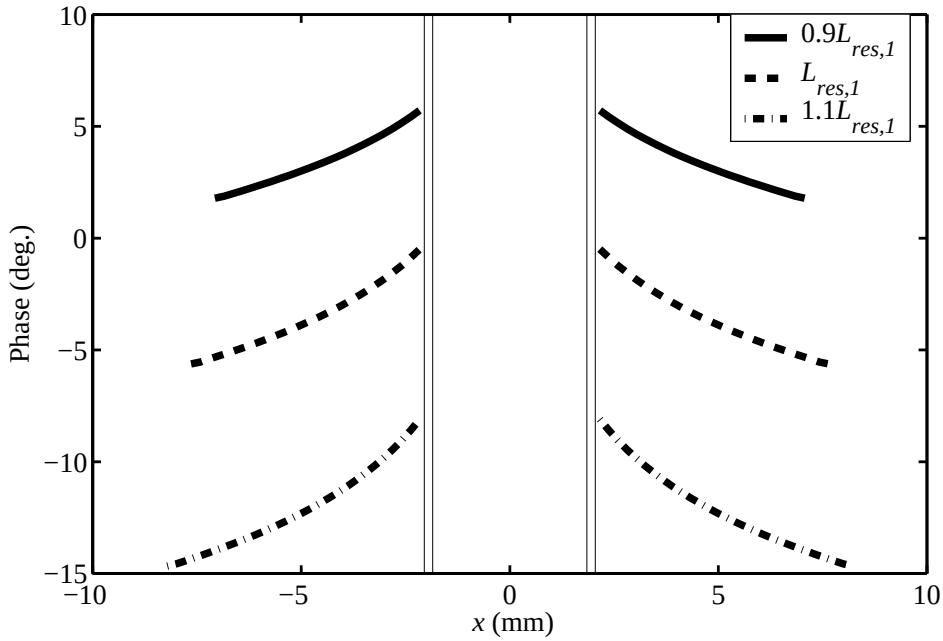

FIGURE 4.5: Phase of electric field of isolated slots with half-lengths in vicinity of first-resonance half-length $L_{res,1}$ on two-layer parallel-plate substrate. $L_{res,1} = 0.27\lambda_s = 5.7$ mm; $W = 0.4$ mm; $h_1 = 0.813$ mm; $h_2 = 5$ mm; $\epsilon_{r1} = 3.38$; $\epsilon_{r2} = 1$. Vertical lines correspond to positions of CPW slots.

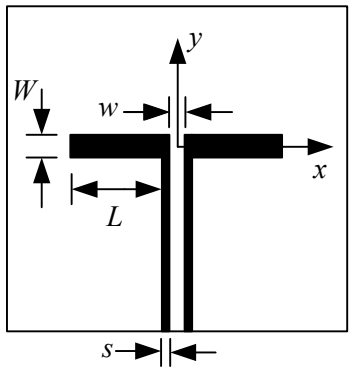

FIGURE 4.6: Orientation of coordinate system with respect to CPW-fed slot. The z-axis points out of the page.

Fig. 4.8 shows a plot of the magnitude of the normalized mutual admittance y_{12} against distance d/λ_{CPW}; y_{12} is the mutual admittance Y_{12} normalized to the magnitude of the relevant isolated slot self-admittance. The relative size of the mutual admittance magnitudes with respect to the slots' self-admittance magnitudes is an indicator of the extent of coupling between the slots. Fig. 4.8 indicates that mutual coupling is the greatest for the slots with $L = L_{res,1}$.

Since *second-resonance* slots have self-impedances that lie on relatively stationary (*i.e.*, "flat")

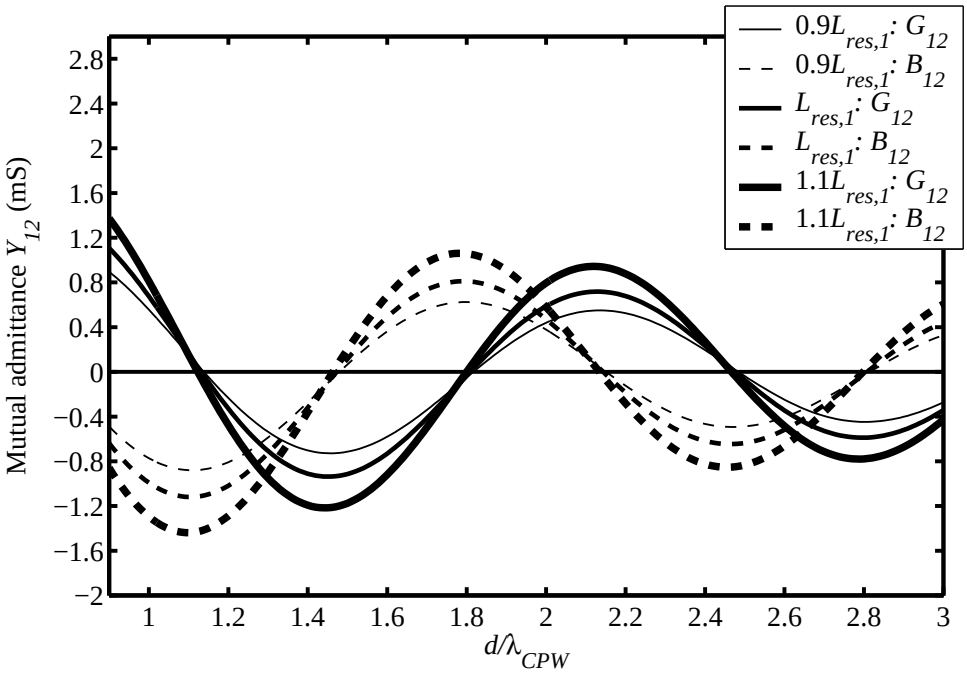

FIGURE 4.7: Mutual admittance between identical CPW-fed slots against broadside distance d/λ_{CPW} at 10 GHz on a two-layer parallel-plate substrate. Computations were performed for slot half-lengths in the vicinity of that of a first-resonant isolated slot. $W = 0.4$ mm; $h_1 = 0.813$ mm; $h_2 = 5$ mm; $\epsilon_{r1} = 3.38$; $\epsilon_{r2} = 1$.

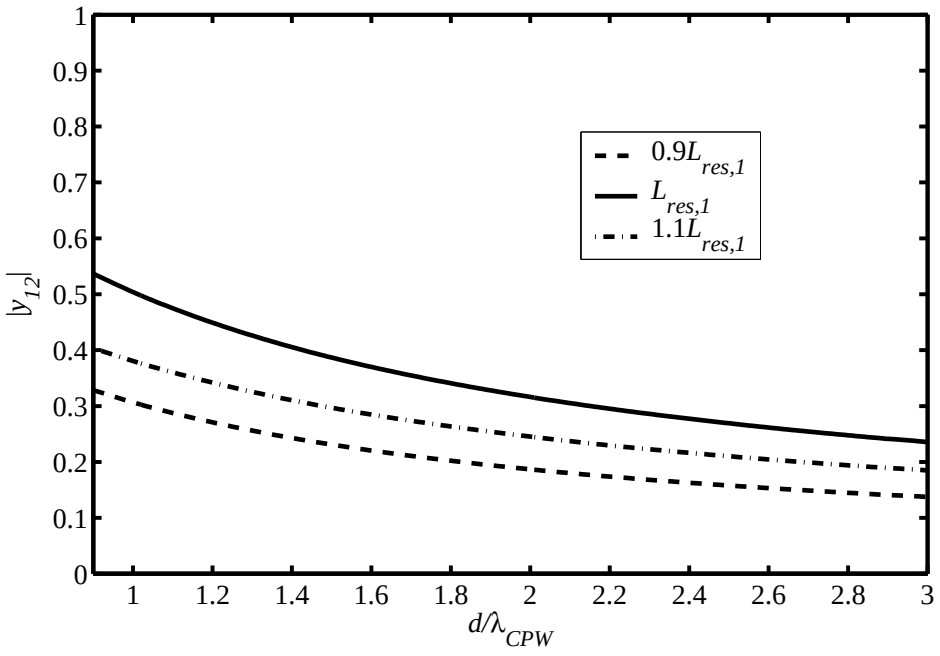

FIGURE 4.8: Magnitude of normalized mutual admittance between identical CPW-fed slots against broadside distance d/λ_{CPW} at 10 GHz on a two-layer parallel-plate substrate. Computations were performed for slot half-lengths in the vicinity of that of a first-resonant isolated slot. $W = 0.4$ mm; $h_1 = 0.813$ mm; $h_2 = 5$ mm; $\epsilon_{r1} = 3.38$; $\epsilon_{r2} = 1$.

portions of their self-impedance-against-frequency curves (*cf.* Fig. 2.2), these slots are preferable to first-resonance slots for use in arrays [34]. Figs. 4.9 and 4.10 show the aperture electric field along the slot centre for the isolated second-resonance slot described above ($W = 0.4$ mm, $L = L_{res,2} = 0.52\lambda_s = 5.7$ mm), as well as the fields for slots with half-lengths close to $L_{res,2}$, namely $0.85L_{res,2}$, $0.95L_{res,2}$, and $1.1L_{res,2}$. Field magnitudes resemble the magnitude of a full cycle of a sinusoid. Phases, while changing little in the outer reaches of the slots, exhibit a sharp rise closer to the CPW feed line which becomes more apparent as slot length increases, leading into a 180° phase reversal in the case of the $1.1L_{res,2}$ slot. Increases in slot length translate into phase offsets with respect to phases of preceding lengths. These results are similar to currents calculated for centre-fed cylindrical dipoles of comparable electrical lengths [18, Figs. 7.6 and 7.7].

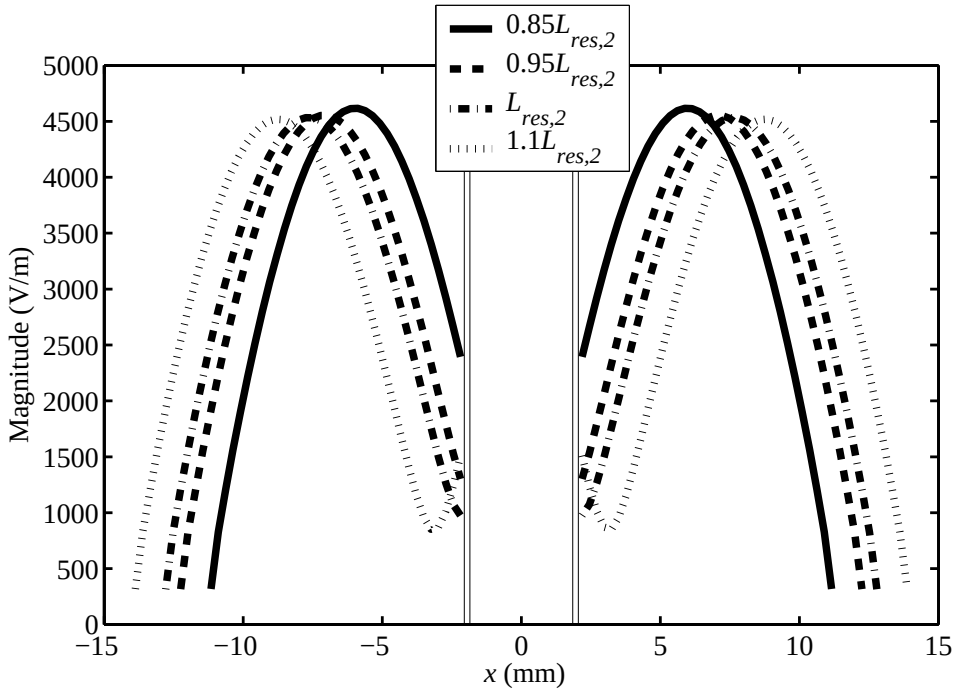

FIGURE 4.9: Magnitude of electric field of isolated slots with half-lengths in vicinity of second-resonance half-length on two-layer parallel-plate substrate. $L_{res,2} = 0.52\lambda_s = 10.87$ mm; $W = 0.4$ mm; $h_1 = 0.813$ mm; $h_2 = 5$ mm; $\epsilon_{r1} = 3.38$; $\epsilon_{r2} = 1$.

Figs. 4.11 and 4.12 show mutual conductance G_{12} and mutual susceptance B_{12} against broadside distance d for slot half-lengths $0.85L_{res,2}$, $0.95L_{res,2}$, $L_{res,2}$, and $1.1L_{res,2}$. A number of observations can be made with respect to Figs. 4.11 and 4.12 in conjunction with Fig. 4.13, which gives the magnitude of the mutual admittance. First, the set of second-resonance curves in these figures are not as regular in shape as the first-resonance curves of Fig. 4.7. The effect is most apparent for the $L_{res,2}$ twin slots, the second most apparent for the $1.1L_{res,2}$ twin slots, and the least apparent for twin slots with $L < L_{res,2}$ to the extent of being virtually unobservable for the case

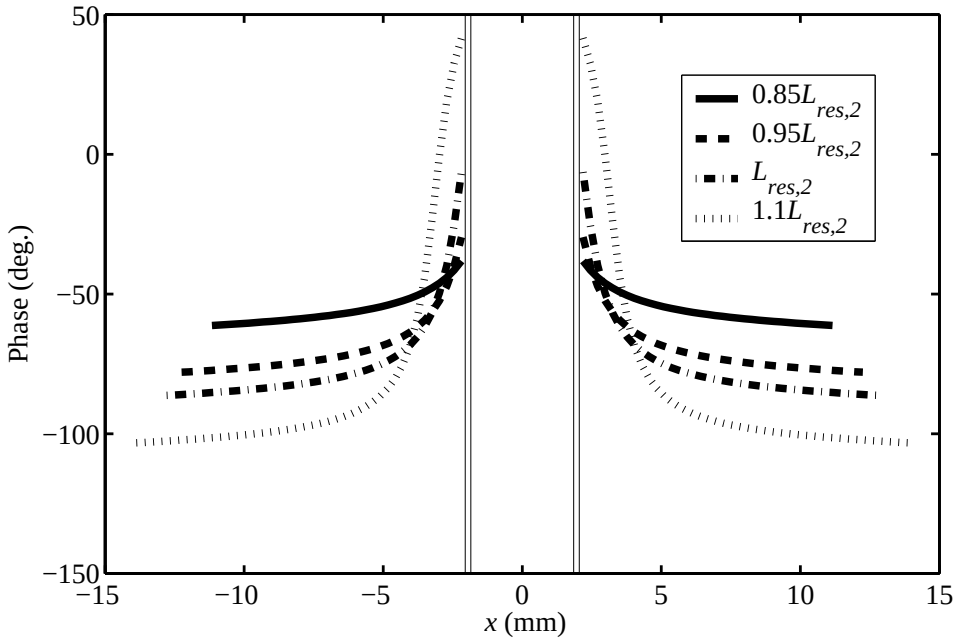

FIGURE 4.10: Phase of electric field of isolated slots with half-lengths in vicinity of second-resonance half-length on two-layer parallel-plate substrate. $L_{res,2} = 0.52\lambda_s = 10.87$ mm; W = 0.4 mm; h_1 = 0.813 mm; h_2 = 5 mm; ϵ_{r1} = 3.38; ϵ_{r2} = 1.

$L = 0.85L_{res,2}$. Second, the magnitude of the mutual admittance is highest for the resonant slot half-length (*i.e.*, $L = L_{res,2}$), and decreases as L increases or decreases as illustrated in Fig. 4.13. This is unlike the set of first-resonance curves, where the mutual admittance magnitude increases with increasing slot length. Third, the set of second-resonance mutual conductance curves are shifted with respect to each other; so are mutual susceptance curves. Thus a 5% decrease in $L_{res,2}$ results in a right shift of about $\lambda_{CPW}/5$ in the position of the first mutual conductance peak and a 10% increase in a left shift of about $\lambda_{CPW}/3$. This is unlike the curves in Fig. 4.7 for slots with half-lengths in the vicinity of $L_{res,1}$, and the curves for narrow centre-fed rectangular slots in an infinite ground plane. Here, changes in slot half-length have negligible influence on positions of maxima, minima and zero-crossings of conductance and susceptance curves that may be described as being "in phase". These shifts are probably linked to the fact that phases of second-resonance slot fields are not constant.

Fig. 4.14 shows a plot of the magnitude of the normalized mutual admittance y_{12} against distance d/λ_{CPW}; y_{12} is the mutual admittance Y_{12} of Fig. 4.13 normalized to the magnitude of the relevant isolated slot self-admittance. This measure confirms that, on the whole, mutual coupling is greatest for the slots with $L = L_{res,2}$.[3]

[3] It is also possible to normalize Y_{12} to the magnitude of the relevant two-port self-admittance Y_{11} (*cf.* Fig. 5.46). This yielded a similar hierarchy of mutual coupling sizes, *i.e.*, largest for the case $L = L_{res,2}$ and smallest for $L = 0.85L_{res,2}$.

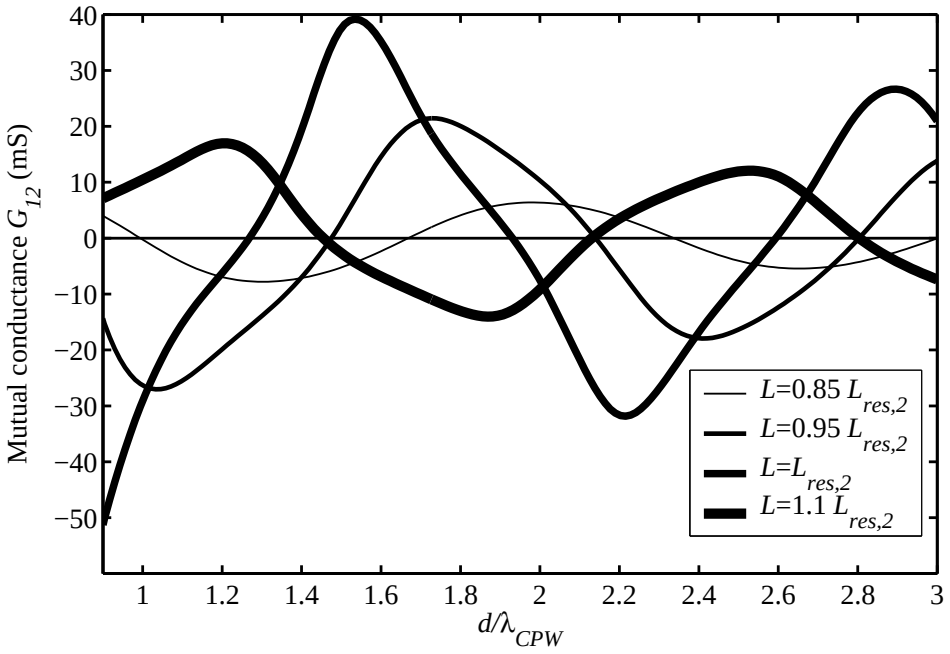

FIGURE 4.11: Mutual conductance between CPW-fed slots against broadside distance d/λ_{CPW} at 10 GHz for slot half-lengths in the vicinity of $L_{res,2}$. W = 0.4 mm; h_1 = 0.813 mm; h_2 = 5 mm; ϵ_{r1} = 3.38; ϵ_{r2} = 1.

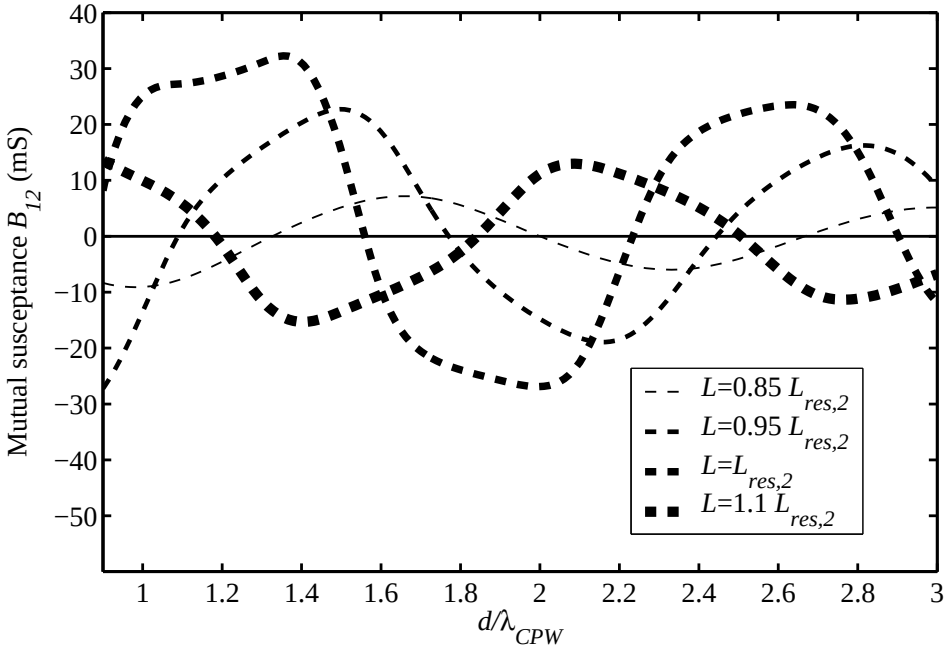

FIGURE 4.12: Mutual susceptance between CPW-fed slots against broadside distance d/λ_{CPW} at 10 GHz for slot half-lengths in the vicinity of $L_{res,2}$. W = 0.4 mm; h_1 = 0.813 mm; h_2 = 5 mm; ϵ_{r1} = 3.38; ϵ_{r2} = 1.

It is instructive to compare the relative magnitudes of the mutual admittance normalized to the magnitude of the relevant isolated slot self-admittance for slots at or close to resonance, namely $0.5\lambda_0$

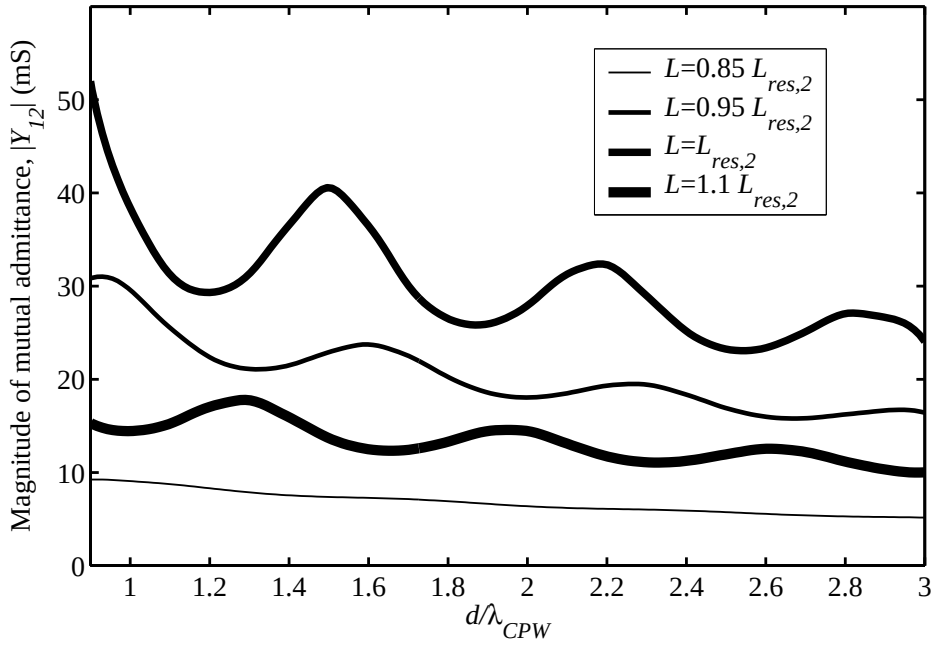

FIGURE 4.13: Magnitude of mutual admittance between CPW-fed twin slots against broadside distance d/λ_{CPW} at 10 GHz for slot half-lengths in the vicinity of $L_{res,2}$. W = 0.4 mm; h_1 = 0.813 mm; h_2 = 5 mm; ϵ_{r1} = 3.38; ϵ_{r2} = 1.

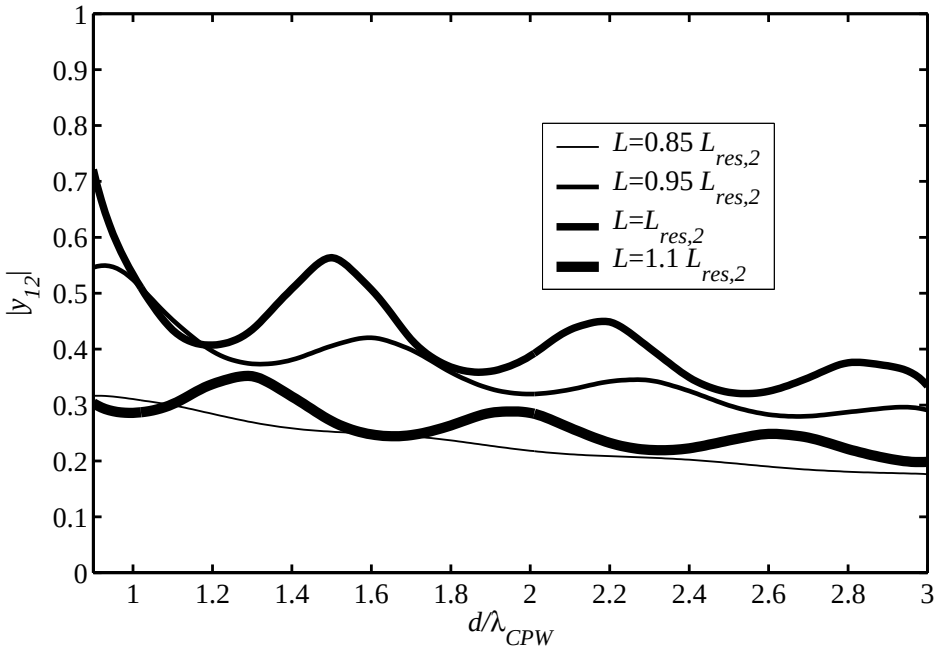

FIGURE 4.14: Magnitude of normalized mutual admittance between identical CPW-fed slots against broadside distance d/λ_{CPW} at 10 GHz for slot half-lengths in the vicinity of $L_{res,2}$. $W = 0.4$ mm; $h_1 = 0.813$ mm; $h_2 = 5$ mm; $\epsilon_{r1} = 3.38$; $\epsilon_{r2} = 1$.

centre-fed rectangular slots in an infinite ground plane in free space, CPW-fed slots on a two-layer parallel-plate substrate with $L = L_{res,1}$, and CPW-fed slots on a two-layer parallel-plate substrate with $L = L_{res,2}$ (the inter-slot spacing range is physically the same as that of Figs. 4.7 and 4.11–4.14).

On the whole, the normalized mutual admittance magnitude is smallest for the infinite ground plane slots, and largest in the case of the CPW-fed slots with $L = L_{res,2}$, suggesting that the effect of coupling is smallest for $0.5\lambda_0$ infinite ground plane slots, and largest for the CPW-fed slots with $L = L_{res,2}$.

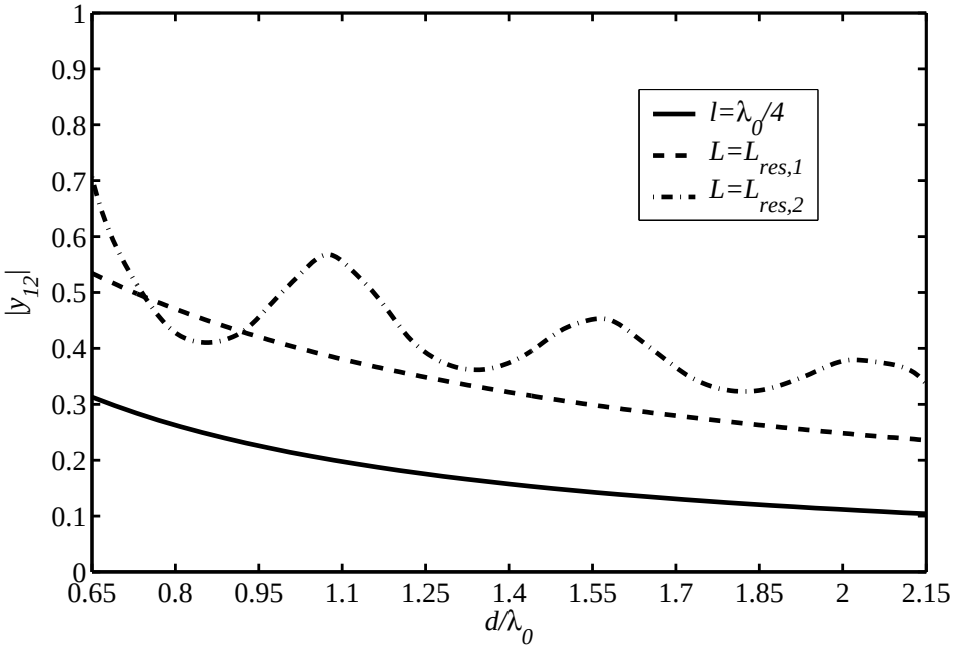

FIGURE 4.15: Magnitude of normalized mutual admittance, $|y_{12}|$, against slot separation d/λ_0 for identical centre-fed broadside narrow slots with length $2l = 0.5\lambda_0$ in infinite ground plane, and CPW-fed twin slots with $L = L_{res,1}$ and $L = L_{res,2}$ on conductor-backed two-layer substrate ($W = 0.4$ mm; $h_1 = 0.813$ mm; $h_2 = 5$ mm; $\epsilon_{r1} = 3.38$; $\epsilon_{r2} = 1$).

4.2.4 Mutual admittance between collinear slots

For the investigation of CPW-fed slots oriented in a collinear manner, two pairs of identical slots were considered. The first pair had $W = 0.4$ mm and $L = L_{res,2} = 0.52\lambda_s$, and the second pair $W = 0.4$ mm and $L = 1.1L_{res,2}$. The resulting mutual admittance curves are displayed in Fig. 4.16, with the largest mutual admittance values observed for the slots with $L = L_{res}$. As expected, mutual admittance on the whole was substantially less in the collinear direction; mutual coupling expressed as mutual admittance normalized to the magnitude of the relevant isolated slot self-admittance was in fact negligible compared to the broadside case. Positions of maxima and minima again showed relative shifts, contrary to the collinear curves for slender free-space dipoles in [18, Fig. 7.24], [59, Fig. 7.8]; curves however were regular in shape.

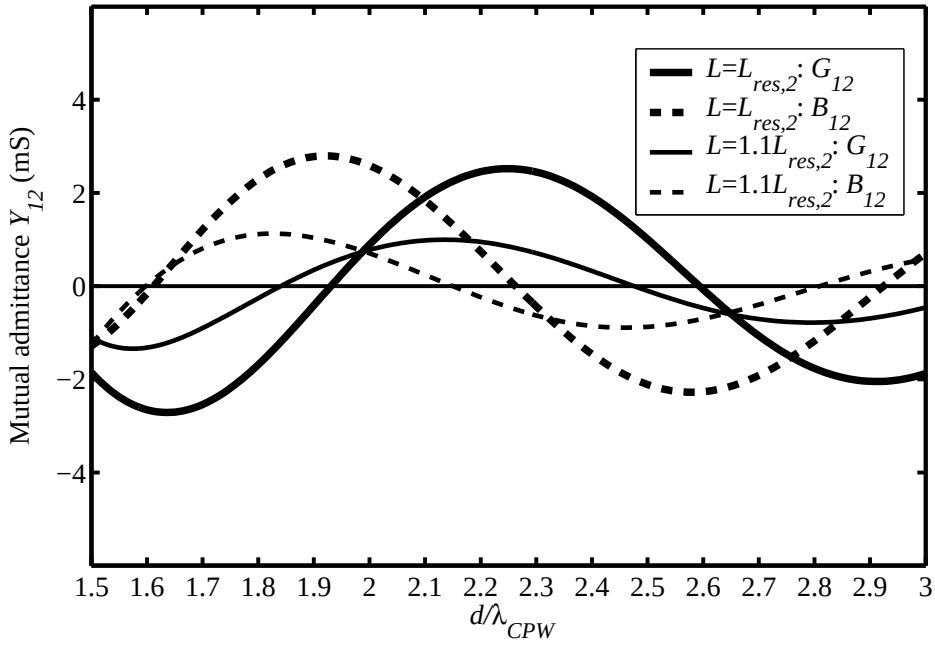

FIGURE 4.16: Mutual admittance between CPW-fed slots against collinear distance d/λ_{CPW} at 10 GHz for slot half-lengths in the vicinity of $L_{res,2}$. W = 0.4 mm; h_1 = 0.813 mm; h_2 = 5 mm; ϵ_{r1} = 3.38; ϵ_{r2} = 1.

4.2.5 Conclusions

A characterization of the mutual admittance between CPW-fed slots on a conductor-backed two-layer substrate, more comprehensive than had been available previously, was presented. The substrate allowed for propagation of the TM_0 surface-wave mode only. Mutual admittance between twin slots was computed using IE3D for a number of half-lengths in the vicinities of the first and second resonant half-lengths of the isolated slots as a function of slot separation along broadside and collinear paths; such data might be of use in the design of arrays in the manner suggested in [57]. Feed lines were $0.5\lambda_{CPW}$ long, in effect referring two-port network parameters to radiating slot centres. Mutual admittance curves for the set of broadside second-resonance twin slots were irregular in shape, and shifted with respect to each other, unlike the first-resonance curves that were similar in shape to mutual admittance curves for centre-fed narrow slots in an infinite ground plane. The irregularity was most marked for twin slots with $L = L_{res,2}$. Mutual coupling between broadside first-resonance CPW-fed twin slots and second-resonance CPW-fed twin slots on the two-layer parallel-plate substrate referred to the magnitude of the isolated slot self-admittance was greater than the mutual coupling between broadside $0.5\lambda_0$ centre-fed narrow rectangular slots in an infinite ground plane, with mutual coupling between the second-resonance CPW-fed slots greater than that between the first-resonance CPW-fed twin slots. Compared to the broadside case, mutual coupling between identical collinear slots with half-lengths in the vicinity of the second-resonance half-length was negligible.

4.3 EFFECT OF BACK PLANE DISTANCE ON MUTUAL ADMITTANCE BETWEEN CPW-FED SLOTS ON CONDUCTOR-BACKED TWO-LAYER SUBSTRATES

4.3.1 Introduction

In Chapter 3, the effect of back plane distance on radiation efficiency and impedance bandwidth of CPW-fed twin slots on a conductor-backed two-layer substrate with air bottom layer was explored (*cf.* Fig. 4.1). The present section investigates the effect of back plane distance on mutual coupling between CPW-fed twin slots on such a substrate.[4] For linear slot arrays on λ_d/4 substrates with a back reflector placed on the side of the CPW ground planes, it has been noted that a reflector distance of λ_0/4 has minimal effect on the antenna input impedance [34]. A question is whether for arrays on two-layer parallel-plate substrates, a bottom layer height h_2 of λ_0/4 would also result in a minimal effect on the array's input impedance; the question can be related to the extent of the influence of a back plane on internal coupling (*i.e.*, coupling on the dielectric side).

4.3.2 Numerical method

Numerical investigations were performed using IE3D [60]. Dielectric constants ϵ_{r1} and ϵ_{r2} were fixed at 3.38 and 1 respectively, while the top substrate layer height h_1 was set to 0.813 mm.[5] Simulations were carried out at 10 GHz. Three values of bottom layer height, or back plane distance, were considered, namely $h_2 = \infty$, λ_0/4, and λ_0/6 (at 10 GHz, $\lambda_0/4 = 7.5$ mm and $\lambda_0/6 = 5$ mm). The case $h_2 = \infty$ is equivalent to the absence of a back plane, while an h_2 value of λ_0/6 was used in an earlier successful implementation on the present substrate of an 8-element uniform linear CPW-fed array [36]. A CPW feed line was designed for the case $h_2 = \infty$ by adjusting the centre strip width w and slot width s to yield a characteristic impedance of about 50 Ω (end values of w and s were 3.7 mm and 0.2 mm respectively). Adding a back plane at λ_0/4 and λ_0/6 had negligible effect on the characteristic impedance; hence the same w and s values were used throughout.

For each of the cases $h_2 = \infty$, λ_0/4, and λ_0/6, an isolated (radiating) slot with a width W of 0.4 mm was designed to be resonant at 10 GHz by appropriately adjusting its half-length L. The resulting resonant slot half-lengths were 10.56 mm, 10.80 mm and 10.87 mm respectively, with corresponding self-impedances of 12.5 Ω, 11.2 Ω, and 13.9 Ω.

Subsequently, the mutual admittance Y_{21} between broadside twin slots as in Fig. 4.1 was

[4] Results presented in Section 4.3 were published in [43].
[5] As noted previously, a higher dielectric constant has to be chosen for the top substrate layer than for the bottom layer in order to help achieve a non-leaky transmission line.

computed as a function of inter-slot distance d for each instance of h_2. Slot dimensions were the same as those of the isolated resonant slot corresponding to the same h_2 (described above). The range of d was $0.9\lambda_{CPW} \leq d \leq 3\lambda_{CPW}$ (λ_{CPW} is the CPW wavelength at 10 GHz). Lengths l_f of feed lines were $0.5\lambda_{CPW}$, equivalent to referring two-port network parameters to the centres of radiating slots (λ_{CPW} is the CPW wavelength at 10 GHz).

4.3.3 Results

Fig. 4.17 shows the real and imaginary parts g_{21} and b_{21} of the normalized mutual admittance y_{21} as a function of normalized distance d/λ_{CPW} for each of the three cases $h_2 = \infty$, $\lambda_0/4$, and $\lambda_0/6$. y_{21} is the mutual admittance Y_{21} normalized with respect to the relevant isolated resonant slot self-admittance. Similar to Section 4.2, the reason for normalizing Y_{21} is that, in a linear (uniform) array context, the relative size of mutual admittance magnitudes with respect to the slots' self-admittance magnitudes can be viewed as an indicator of the extent of the effect of mutual coupling on the array input impedance (*cf.* Section 1.1).

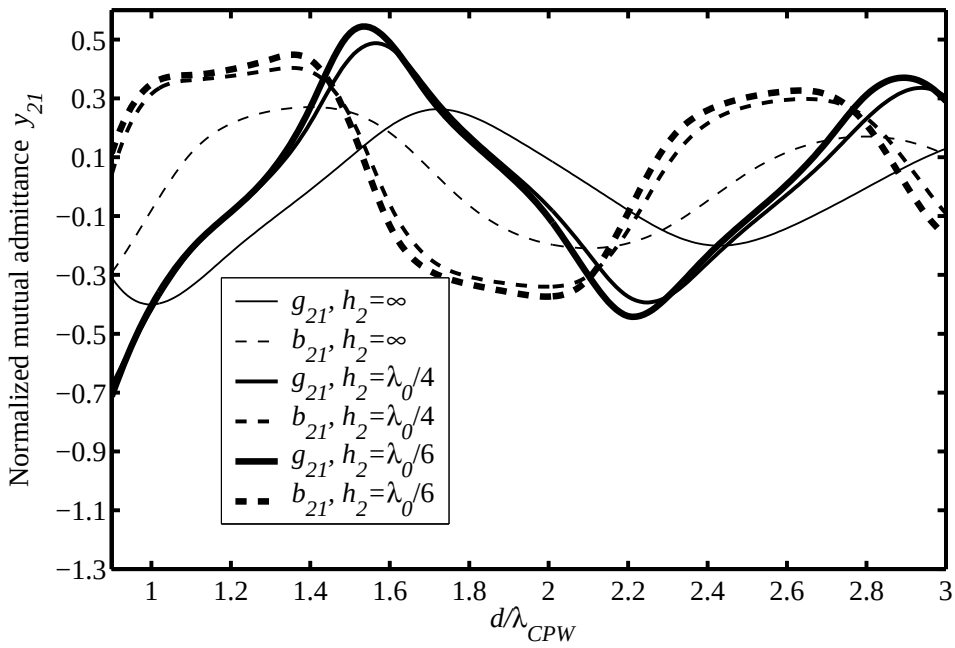

FIGURE 4.17: Real and imaginary parts g_{21} and b_{21} of normalized mutual admittance y_{21} against interslot distance d/λ_{CPW} at 10 GHz. W = 0.4 mm; h_1 = 0.813 mm; ϵ_{r1} = 3.38; ϵ_{r2} = 1.

The normalized curves indicate that, in the absence of a back plane, the maximum values of the magnitudes of the real part (G_{21}) and imaginary part (B_{21}) of the mutual admittance Y_{21} are about 40% and 27% respectively of the resonant slot self-admittance; the maximum of $|g_{21}|$ occurs at $d = \lambda_{CPW}$ and the maximum of $|b_{21}|$ at $d = 1.4\lambda_{CPW}$. Adding a back plane at $h_2 = \lambda_0/4$ results in significantly higher relative maximum values of about 68% and 40% for $|G_{21}|$ and $|B_{21}|$ respectively;

other extrema also show notable increases compared to the $h_2 = \infty$ case. The back plane has the effect of shifting the curves for g_{21} and b_{21} so that their extrema in general are not aligned with those of the curves for $h_2 = \infty$. These effects can be ascribed to internal mutual coupling (the external equivalent problem, concerned with fields in the half-space adjacent to the CPW ground planes, is unchanged by the addition of a back plane), indicating that the input impedance of an array on the single-layer substrate potentially could be significantly affected when a back plane is placed $\lambda_0/4$ away.[6] Decreasing the back plane distance to $h_2 = \lambda_0/6$ results in curves quite similar to, and more or less "in phase" with, the curves for the case $h_2 = \lambda_0/4$ with somewhat higher maximum values for g_{21} and b_{21} (0.71 and 0.45 respectively against 0.68 and 0.4). At $d = \lambda_{CPW}$ the magnitude of the real part of the mutual admittance was about 40% of the relevant resonant slot self-admittance for all cases of h_2.

In order to evaluate IE3D's performance with respect to computation of the mutual admittance curves of Fig. 4.17, S_{21} as a function of frequency was computed for a specific instance of each of the cases $h_2 = \infty$ and $h_2 = 5$ mm ($\lambda_0/6$ at 10 GHz) which corresponded to an inter-slot distance of 20.35 mm ($0.95\lambda_{CPW}$ at 10 GHz; the relevant values of y_{21} can be read from Fig. 4.17). S_{21} against frequency was also measured for manufactured versions of these two test cases. Fig. 4.18 shows good agreement between computed and measured results for $|S_{21}|$, both with and without the back plane.

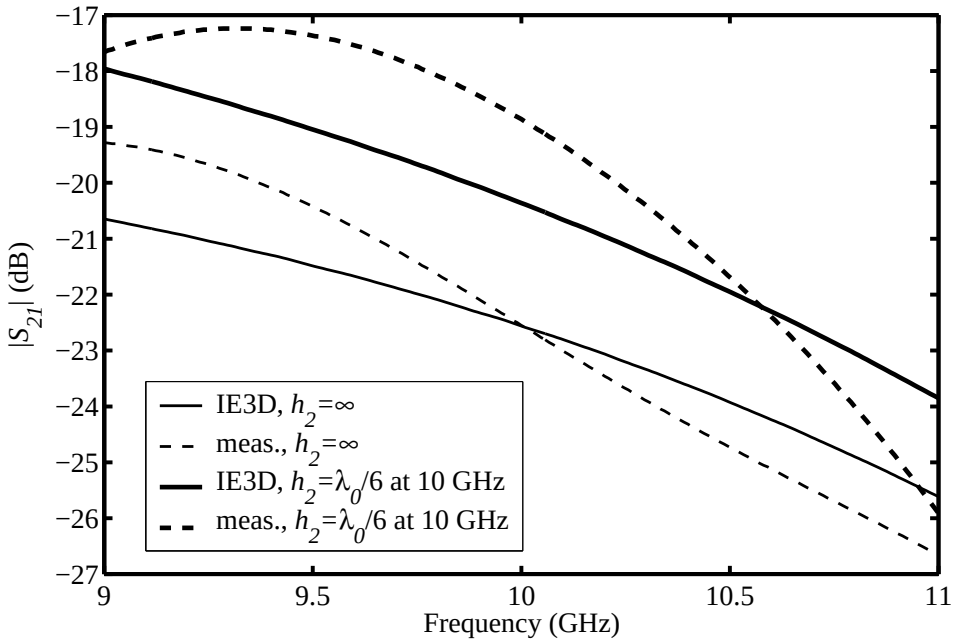

FIGURE 4.18: Computed and measured $|S_{21}|$ against frequency for twin slots spaced $d = 20.35$ mm apart (0.95 λ_{CPW} at 10 GHz) on conductor-backed two-layer substrate for back plane distances $h_2 = \infty$ and $h_2 = 5$ mm (λ_0/6 at 10 GHz). W = 0.4 mm; h_1 = 0.813 mm; ϵ_{r1} = 3.38; ϵ_{r2} = 1.

[6] The array's input impedance would of course ultimately be determined by the effect of the back plane on slot self-admittance values as well (*cf.* Eqs. (1.3) and (1.4)).

4.3.4 Conclusions

The effect of back plane distance on the normalized mutual admittance between CPW-fed slots on conductor-backed two-layered substrates was investigated. For the substrate under consideration, a back plane at a distance of $\lambda_0/4$ yielded curves of normalized mutual admittance against separation distance with substantially higher maxima and minima compared to the case where no back plane was present. A back plane distance of $\lambda_0/6$ produced normalized mutual admittance curves that were very similar in shape to those for the case $h_2 = \lambda_0/4$, but with somewhat larger maxima and minima, suggesting that the effect of mutual coupling increases as back plane distance decreases.

CHAPTER 5

RECIPROCITY-EXPRESSION-BASED APPROACH FOR MUTUAL ADMITTANCE BETWEEN CPW-FED SLOTS ON CONDUCTOR-BACKED TWO-LAYER SUBSTRATES

5.1 INTRODUCTION

In this chapter, a computational strategy, based on a well-known reciprocity-based expression, is developed for finding the mutual admittance between CPW-fed slots on a two-layer parallel-plate substrate. The geometry is shown in Fig. 5.1.[1] The mutual admittance between the slots can be viewed as the sum of external and internal mutual admittances: the external mutual admittance is due to coupling that takes place in the half-space adjacent to the slots, while the internal mutual admittance is due to coupling inside the substrate.

The method for calculating mutual admittance that is developed here is intended to serve as a simpler alternative to a moment-method-based approach, yet of comparable accuracy. Moment-method-based techniques have been used for finding mutual coupling between various kinds of planar radiating elements, including CPW-fed slots on multi-layer dielectric substrates without a back conductor [38], rectangular centre-fed slots on planar substrates [57, 61], and microstrip-fed printed antennas [62–64]. Mutual coupling in planar multi-port circuits have similarly been accounted for [65].

Of particular interest amongst the above is the rigorous moment-method analysis of CPW-fed twin slot antennas on multi-layer dielectric substrates without a back plane in [38]. In order to obtain the two-port impedance-matrix (Z) parameters for a particular twin slot configuration, the

[1] It differs from the twin slots of Fig. 4.1 only in allowing for different radiating slot dimensions.

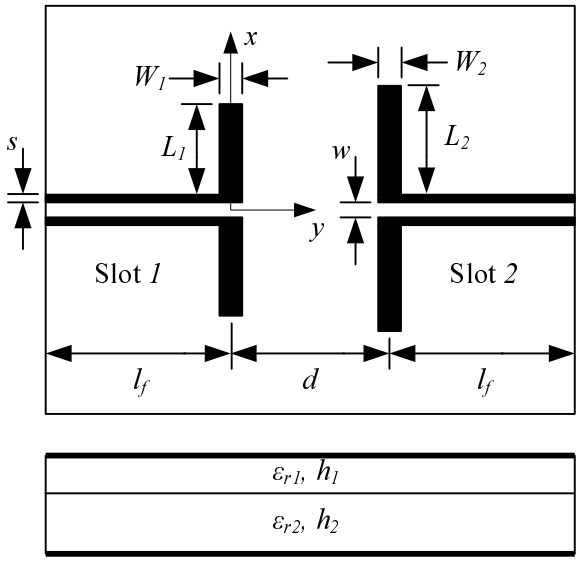

FIGURE 5.1: Top and side views of broadside (non-identical) CPW-fed twin slot antennas on conductor-backed two-layer substrate. L_1, L_2 $\equiv$ half-lengths and W_1, W_2 $\equiv$ widths of radiating slots; $d \equiv$ distance between radiating slots; $s \equiv$ slot width and $w \equiv$ centre strip width of feed lines; h_1, $h_2 \equiv$ dielectric layer heights; ϵ_{r1}, $\epsilon_{r2} \equiv$ relative dielectric constants; $l_f \equiv$ feed line lengths. The ground plane containing the slots coincides with the plane $z = 0$. A coordinate system is defined with its origin at the centre of slot *1*; the z axis points into the page.

moment method matrix equation is solved twice, once for an even excitation and once for an odd excitation (these labels refer to the phase relationship between the current sources placed at the terminals of each CPW-fed slot). Input impedances are calculated for each case, and used in simple algebraic equations to obtain the two-port Z parameters. Because of the symmetry of the twin slots, only two independent excitations are required (a more general procedure applied to non-symmetrical microstrip-fed planar dipoles can be found in [64]). A notable finding in [38] pertains to a simplification that involves removing the CPW feed lines and exciting the radiating slots by delta-gap current sources at their centres (this presumably involves forming single rectangular radiating slots from the two half-lengths of each of the former CPW-fed slots). The finding was that the phases of S parameters, and hence resonant frequencies, could only be predicted with sufficient accuracy for oscillator applications if the condition $\frac{w+2s}{\lambda_{eff}} < \frac{1}{50}$ held, where λ_{eff} presumably is the wavelength of the slotline corresponding to the radiating slot – in other words if very narrow CPW feeds were used. This appears to be interpreted in [10] as support for the notion that network-based simplifications do not apply as well to CPW-fed slots as to slots fed by other means, and that a complete full-wave, finely-meshed analysis of both the radiating slots and their CPW feeds is necessary when characterizing CPW-fed twin slot and double-slot (*i.e.*, H-configured)

antennas.[2]

Iterative array design algorithms require that the mutual admittance between all possible slot pairs in the array be calculated during every iteration, *e.g.*, [35]. For example, a linear array of N slots requires $N(N-1)/2$ mutual admittance calculations per iteration.[3] (In certain cases, the mutual coupling between slots that are far enough apart may be neglected.) Slot dimensions evolve over iterations until the algorithm converges to a solution that is satisfactory with respect to both the input impedance and aperture distribution requirements of the array. Carrying out a full moment-method analysis for each of these mutual admittance calculations would be very cumbersome.

In Chapter 1, it was noted that [35] reduces the problem of finding the mutual admittance between slots in a linear CPW-fed array on an electrically thin single-layer substrate to an equivalent problem that involves finding the mutual impedance between two wire dipoles in a homogeneous medium using a well-known variational formula derived for the latter purpose [18]. The Green's function of the substrate is not used. It was also observed that the validity of the relevant approximations and assumptions remains to be tested via the design of a non-uniform array subject to a stringent sidelobe level requirement; the approximations include replacing the array by its complementary strip-dipole array, and assuming a homogeneous medium with effective permittivity ε_{eff}, where ε_{eff} is the geometrical mean of the various slot effective permittivities. In the present work, no approximations regarding the inhomogeneous nature of the medium will be made; instead, the conductor-backed two-layer substrate will be rigorously accounted for by use of the appropriate Green's function.

The organization of the chapter is as follows. In Section 5.2, an approach that relies on a standard reciprocity-based expression is developed for finding the mutual admittance between CPW-fed twin slots on an infinite conductor-backed two-layer substrate. Section 5.3 contains an original derivation of the spatial-domain Green's function for two-layer parallel-plate substrates that is required for implementing the internal mutual admittance formulation that forms part of Section 5.2. Section 5.4 presents and discusses results for broadside CPW-fed twin slots and non-identical slot pairs on a variety of two-layer parallel-plate substrates. These results are compared to moment-method-based simulations using IE3D [60] and a measurement. Conclusions are stated in Section 5.5.

[2] As an alternative to the above full-wave analysis, the authors [10] introduce a new analysis for CPW-fed slots on semi-infinite substrates that reduces the number of unknowns but has the same accuracy as a finely-meshed MoM; the analysis relies on the representation of equivalent magnetic currents in terms of entire-domain basis functions defined in terms of analytical Green's functions of canonical geometries such as an infinite slotline.

[3] This number takes into account that $Y_{mn} = Y_{nm}$ due to reciprocity.

5.2 FORMULATION OF RECIPROCITY-EXPRESSION APPROACH FOR MUTUAL ADMITTANCE BETWEEN CPW-FED SLOTS ON CONDUCTOR-BACKED TWO-LAYER SUBSTRATE

5.2.1 Mutual admittance between centre-fed slots radiating into half-space

Consider two narrow rectangular slots labeled *1* and *2* in an infinite, perfectly conducting ground plane at $z = 0$ that radiate into the half-space $z > 0$, as shown in Fig. 5.2(a). The slots are assumed to be center-fed via two-wire lines by lumped voltage sources. The slots are backed by an arbitrary substrate (for example, the substrate could be an air half-space, as in the case of center-fed narrow slots in an infinite ground plane which is the dual of slender electric dipoles in free space, or a layered substrate such as the conductor-backed two-layer substrate of Fig. 5.1). The tangential electric field components in the slots are denoted $\mathbf{E}_{1,slot}$ and $\mathbf{E}_{2,slot}$.

An equivalent problem that pertains to the region $z > 0$ may be set up as follows. Using the surface equivalence theorem [52], the slots may be replaced by two equivalent magnetic surface current densities $\mathbf{M}_{1,eq} = \mathbf{E}_{1,slot} \times \hat{z}$ and $\mathbf{M}_{2,eq} = \mathbf{E}_{2,slot} \times \hat{z}$ on an infinite ground plane radiating into the half-space $z > 0$, as shown in Fig. 5.2(b). These equivalent currents ensure that the electromagnetic fields in the half-space $z > 0$ remain unchanged from their values in the situation of Fig. 5.2(a). (Details of applying the surface equivalence theorem are presented in Section 5.2.2.1.)

Based on a standard formulation [66], the mutual admittance between slots *1* and *2* of Fig. 5.2 due to coupling in the half-space $z > 0$ can be expressed as

$$Y_{12} = -\frac{1}{V_1 V_2'} \int_{S_2} \mathbf{H}_{21} \cdot \mathbf{M}_2' dS_2 \tag{5.1}$$

with

$\mathbf{H}_{21}$ the magnetic field of magnetic current $\mathbf{M}_1$ at the position of slot *2* when slot *1* is excited and radiates in *isolation* ($\mathbf{M}_1$ is the equivalent magnetic current representing slot *1* when slot *1* is excited and radiates in *isolation*)

$\mathbf{M}_2'$ the equivalent magnetic current representing slot *2* when slot *2* is excited and radiates in the presence of a short-circuited slot *1*

V_1 the terminal voltage of slot *1*, or the total magnetic current through the terminals of slot *1*, when slot *1* is excited and radiates in *isolation*

V_2' the terminal voltage of slot *2*, or the total magnetic current through the terminals of slot *2*, when slot *2* is excited and radiates in the presence of a short-circuited slot *1*

S_2 the surface area of slot *2*

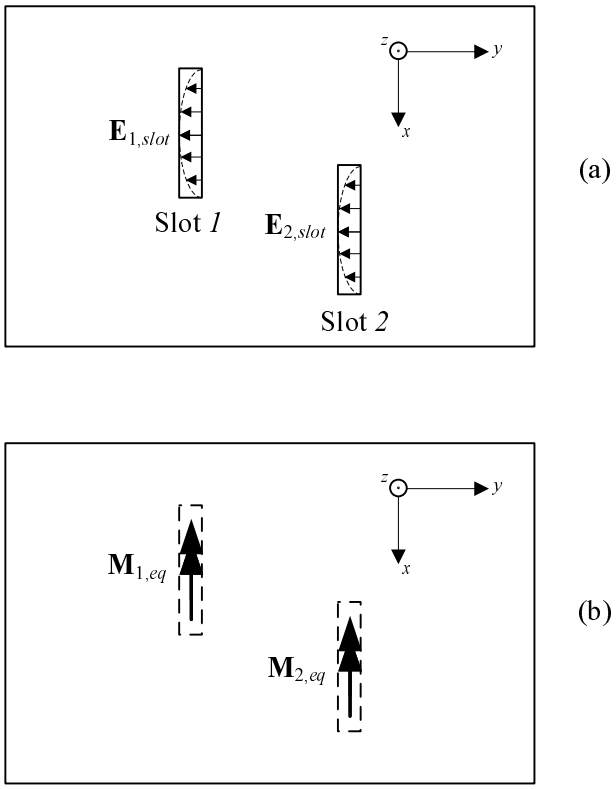

FIGURE 5.2: (a) Two narrow center-fed slots on a perfectly conducting ground plane radiating into the half-space $z > 0$. (b) The equivalent problem: two magnetic currents on a perfectly conducting ground plane. The dashed lines indicate the positions of the slots represented by the magnetic currents.

Crucial to the derivation of Eq. (5.1) is that the slots are center-fed by infinitesimal sources, which permits the introduction of terminal voltages and currents (hence the appearance of V_1 and V_2 in the equation). Noting that computation of $\mathbf{H}'_{21}$ requires use of the vector potential $\mathbf{F}$ for a magnetic current density radiating into a half-space on an infinite perfect electric conductor (PEC), Eq. (5.1) is consistent with [67, Eq. (14)].

If it can be assumed that the shape of the electric field in slot *2* when radiating in isolation is not significantly different when slot *2* radiates in the presence of a short-circuited slot *1*, Eq. (5.1) can be expressed in a form that is more readily implemented:

$$Y_{12} = -\frac{1}{V_1 V_2} \int_{S_2} \mathbf{H}_{21} \cdot \mathbf{M}_2 dS_2 \tag{5.2}$$

with

$\mathbf{H}_{21}$ the magnetic field of magnetic current $\mathbf{M}_1$ at the position of slot *2* when slot *1* is excited and radiates in *isolation* ($\mathbf{M}_1$ is the equivalent magnetic current representing slot

1 when slot *1* is excited and radiates in *isolation*)

$\mathbf{M}_2$ the equivalent magnetic current representing slot *2* when slot *2* is excited and radiates in *isolation*

V_1 the terminal voltage of slot *1*, or the total magnetic current through the terminals of slot *1*, when slot *1* is excited and radiates in *isolation*

V_2 the terminal voltage of slot *2*, or the total magnetic current through the terminals of slot *2*, when slot *2* is excited and radiates in *isolation*

S_2 the surface area of slot *2*

5.2.2 Mutual admittance between CPW-fed slots on conductor-backed two-layer substrate

Consider now two CPW-fed slots on a two-layer parallel-plate substrate that radiate into the half-space $z < 0$, as shown in Fig. 5.1.[4] Each slot can be conceived of as center-fed by a voltage (or current) source in the sense of Fig. 5.3. In other words, the CPW feed line can be thought of as originating from a short section of slotline which is excited at its centre by a lumped voltage source; the section of slotline is then extended via 90° angles to form the CPW. This excitation technique is consistent with the excitation of CPW and/or CPW-fed slots in moment-method-based analyses [68]. Since the overall composite slot is center-fed, the implication is that Eq. (5.1) can be used to find the mutual admittance between CPW-fed slots as well. The more complex shape of these slots (compared to center-fed rectangular slots) does not affect the form of that equation. For the relatively narrow CPW-fed slots on a two-layer parallel-plate substrate considered in this thesis, the shape of the electric field in slot *2* when radiating in isolation is not significantly different from the field when slot *2* radiates in the presence of a short-circuited slot *1*; this was confirmed using IE3D. Hence Eq. (5.2) can be used instead of Eq. (5.1).

In Sections 5.2.2.1 and 5.2.2.2 below, equivalent problems are formulated for the external and internal mutual admittance between CPW-fed slots on a two-layer parallel-plate substrate. For each equivalent problem, Eq. (5.2) can be used in conjunction with the appropriate Green's function to find the relevant contribution to the total mutual admittance, *i.e.*, external or internal. In both the external and internal cases, the following assumptions and conventions are adopted.

First, in order to simplify the integration in Eq. (5.2), the effects of mutual coupling between the respective CPW feed lines (including the originating slotline sections), and between CPW feed lines and radiating slots are assumed to be negligible. Mutual coupling between the originating slotline

[4] Denoting the air half-space by $z < 0$, as opposed to the above $z > 0$, is done for mathematical convenience and makes no difference to the argument that follows.

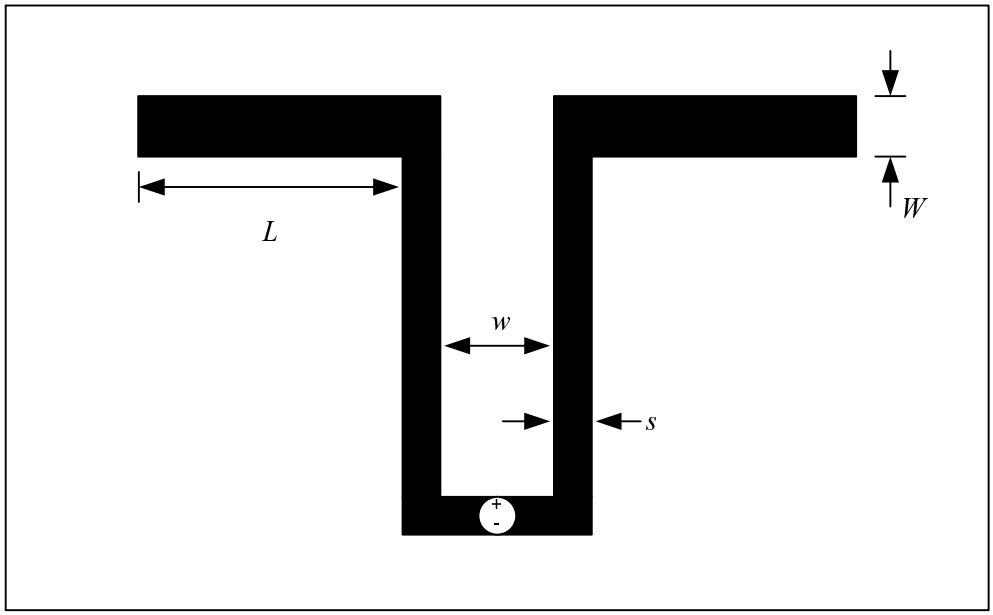

FIGURE 5.3: Top view of CPW-fed slot on conductor-backed two-layer substrate. The slot can be thought of as center-fed by a localized infinitesimal voltage source. $L \equiv$ half-length and $W \equiv$ width of radiating slot; $s \equiv$ slot width and $w \equiv$ centre strip width of CPW feed line.

sections (*cf.* Fig. 5.3) and radiating slots is also considered negligible (this assumption follows if the CPW feeds are sufficiently long). Hence for the purposes of evaluating the above reaction integral, only the radiating portions of CPW-fed slots *1* and *2* are taken into account, as illustrated in Fig. 5.4.

Second, the mutual admittance Y_{12} is referred to positions on the CPW feed lines that are some distance l_f away from radiating slot centres. Fig. 5.5 shows these reference planes, labelled $11'$ and $22'$; the terminal voltages V_1 and V_2 of Eq. (5.2) would need to be determined at these planes for each slot radiating in isolation. The tangential electric field in a CPW-fed slot (including the feed line) can be determined using the moment method [14, 15]; Figs. 4.9 and 4.10 show radiating slot fields obtained using IE3D. When for instance slot *1* is analyzed (in isolation) in IE3D, the excitation port can be user-defined to coincide with reference plane $11'$.[5] IE3D finds the port voltage – which is the same as the terminal voltage V_1 – in addition to the slot tangential electric field. It was verified that the port voltage is the integral of the electric field in one of the two CPW slots over the width of the slot. For example, if a moment-method discretization allowing for only one cell across the slot width is assumed, $V_1 = wE_{1x}^{CPW}$ at terminal plane $11'$, with w the slot width and $E_{1x}^{CPW}\hat{x}$ the electric field in the centre of the slot.[6] The implementation of terminal voltages will be discussed further in Section 5.4.1.

[5] It is assumed that the results of the manner in which IE3D excites the slot and the manner suggested in Fig. 5.3 will be the same at the reference planes and beyond (*i.e.*, towards the radiating slot).
[6] A discretization using edge cells in IE3D resulted in only a marginal difference in the port voltage.

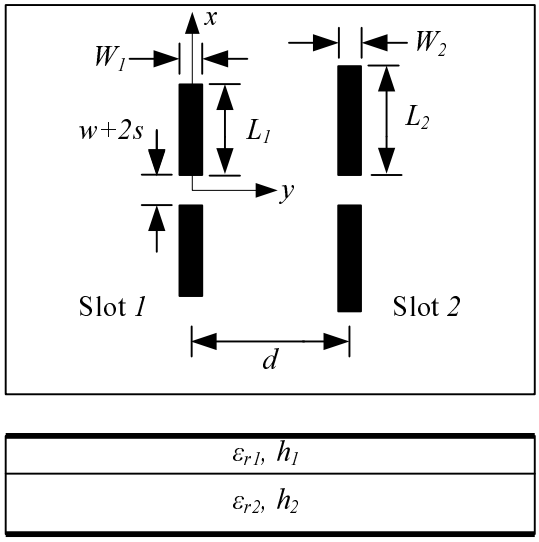

FIGURE 5.4: Top and side views of broadside slots on conductor-backed two-layer substrate. The CPW feed lines have been removed. L_1, $L_2 \equiv$ half-lengths and W_1, $W_2 \equiv$ widths of radiating slots; $d \equiv$ distance between radiating slots; h_1, $h_2 \equiv$ dielectric layer heights; ϵ_{r1}, $\epsilon_{r2} \equiv$ relative dielectric constants. The ground plane containing the slots coincides with the plane $z = 0$; the z axis points into the page.

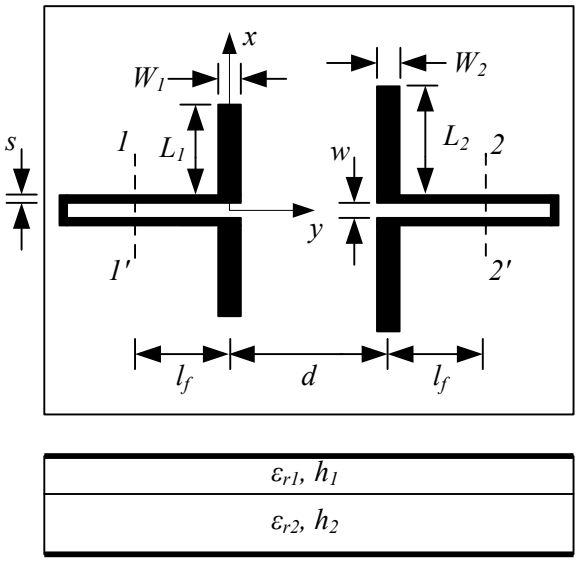

FIGURE 5.5: Broadside CPW-fed slot antennas on conductor-backed two-layer substrate with terminal reference planes $11'$ and $22'$. Each slot can be thought of as being excited in the manner shown in Fig. 5.3.

5.2.2.1 External mutual admittance formulation

In this section, it is showed how Eq. (5.2) may be applied to find the external mutual admittance between two CPW-fed slots on an infinite two-layer parallel-plate substrate. This involves setting

up equivalent problems for finding the quantities $\mathbf{H}_{21}$ and $\mathbf{M}_2$ that appear in the integral. Here, the quantities will be referred to as $\mathbf{H}_{21}^{ext}$ and $\mathbf{M}_2^{ext}$ in order to distinguish them from the internal problem. Hence,

$$Y_{12}^{ext} = -\frac{1}{V_1 V_2} \int_{S_2} \mathbf{H}_{21}^{ext} \cdot \mathbf{M}_2^{ext} dS_2 \tag{5.3}$$

With respect to the equivalent problem required to find $\mathbf{H}_{21}^{ext}$, consider Fig. 5.6(a), which is based on a side view of the two-layer parallel-plate substrate containing radiating slots only (*cf.* Fig. 5.4). Slot *2* has been removed, *i.e.*, replaced by conductor, in order to adhere to the definition of $\mathbf{H}_{21}^{ext}$ in Eq. (5.2) as the magnetic field due to slot *1* at the position of slot *2* when slot *1* radiates in isolation. The ground plane containing slot *1* is situated at $z = 0$. The half-space external to the slots is denoted by $z < 0$; hence the unit surface normal vector $\hat{n}$ points in the negative z direction. The tangential components of the electric field in the aperture of slot *1* are assumed to be known and given by $\mathbf{E}_{1,slot}$.

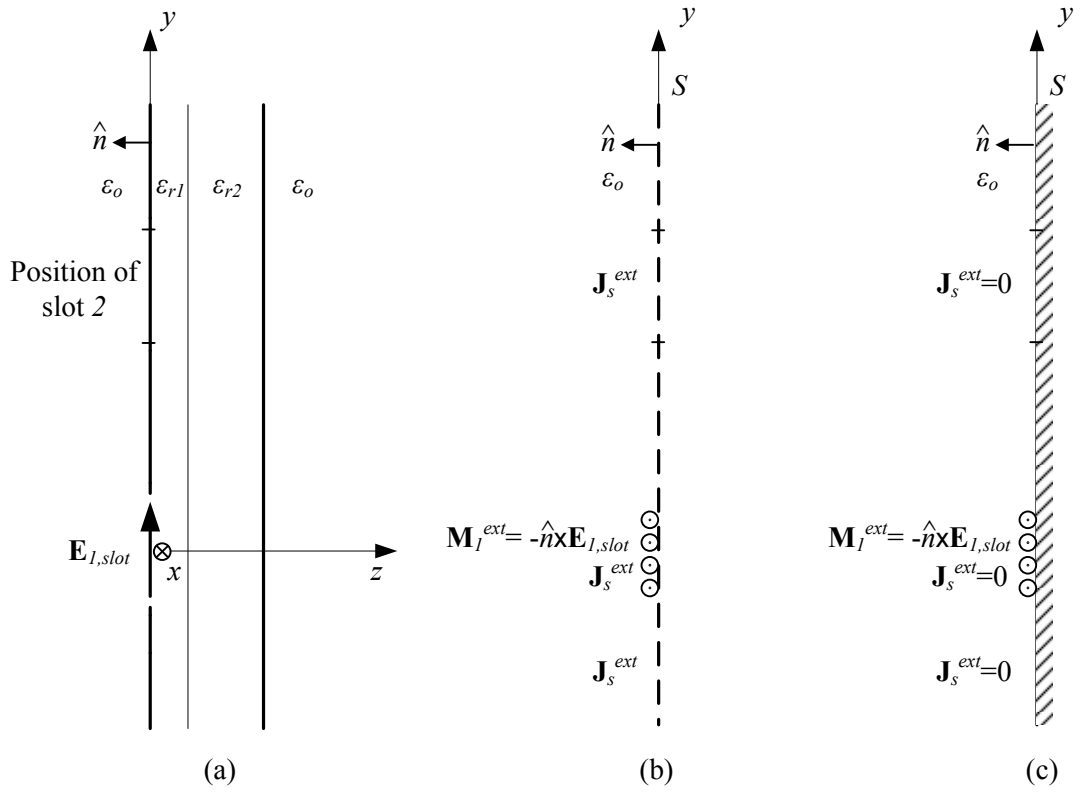

FIGURE 5.6: Steps in setting up an external equivalent model for one slot on a two-layer parallel-plate substrate. In (a)–(c), electromagnetic fields are the same in the region $z < 0$.

Fig. 5.6(b) and (c) demonstrate application of the surface equivalence theorem [69] to the slot of Fig. 5.6(a). In Fig. 5.6(b), an imaginary closed surface S, which is a plane of infinite extent, replaces the conducting plane containing the slot. Equivalent magnetic and electric surface current densities $\mathbf{M}_1^{ext}$ and $\mathbf{J}_s^{ext}$ are formed on this surface to ensure that the electromagnetic fields in the half-space

$z < 0$ remain unchanged from their values in the situation of Fig. 5.6(a). $\mathbf{M}_1^{ext}$ is non-zero only over the position of slot *1*, while $\mathbf{J}_s^{ext}$ is non-zero everywhere. If it is assumed that $\mathbf{E}_{1,slot} = E_{1y,slot}\hat{y}$, and since $\hat{n} = -\hat{z}$ for the external problem,

$$\mathbf{M}_1^{ext} = -\hat{n} \times E_{1y,slot}\hat{y} = -E_{1y,slot}\hat{x} = M_{1x}^{ext}\hat{x} \tag{5.4}$$

(The above assumption regarding aperture electric field components will be adhered to throughout. An investigation using IE3D of the centre fields along the lengths of representative CPW-fed slots revealed that the $\hat{x}$ component is in fact negligible.) In 5.6(c), a perfectly conducting plane approaches S from the right, shorting out $\mathbf{J}_s^{ext}$ everywhere but leaving $\mathbf{M}_1^{ext}$ intact.

In a half-space consisting of air over a PEC, the magnetic field $\mathbf{H}$ due to a general magnetic current density $\mathbf{M}$ can be calculated from

$$\mathbf{H} = -j\omega\mathbf{F} - j\frac{1}{\omega\mu_0\varepsilon_0}\nabla(\nabla \cdot \mathbf{F}) \tag{5.5a}$$

where the vector potential $\mathbf{F}$ is given as

$$\mathbf{F}(x, y, z) = \frac{\varepsilon_0}{2\pi}\int_V \mathbf{M}(x', y', z')\frac{e^{-jk_0R}}{R}dV' \tag{5.5b}$$

In the above, $R = \sqrt{(x-x')^2 + (y-y')^2 + (z-z')^2}$, and $k_0 = \omega\sqrt{\mu_0\varepsilon_0}$ is the free-space wave-number. Eqs. (5.5a) and (5.5b) correspond to [69, eqs. (6-109), (6-111)] except for the factor $\frac{1}{2\pi}$ in Eq. (5.5b) which reflects the fact that the magnetic current radiates in a half-space bordered by an infinite ground plane instead of free-space (*cf.* [70]).

The equivalent problem for $\mathbf{M}_2^{ext}$, which entails that slot *2* radiates in isolation, is derived in the same manner as that for slot *1*. The result is identical to that presented in Fig. 5.6(c) except that the equivalent magnetic surface current density is $\mathbf{M}_2^{ext}$ at the position of slot *2*. Assuming that $\mathbf{E}_{2,slot} = E_{2y,slot}\hat{y}$,

$$\mathbf{M}_2^{ext} = -E_{2y,slot}\hat{x} = M_{2x}^{ext}\hat{x} \tag{5.6}$$

Based on Eq. (5.6), Eq. (5.3) reduces to (*cf.* Fig. 5.4)

$$
\begin{aligned}
Y_{12}^{ext} &= -\frac{1}{V_1 V_2}\int_{S_2} H_{21x}^{ext} M_{2x}^{ext} dS_2 \\
&= -\frac{1}{V_1 V_2}\left\{ \int_{x=-(\frac{w}{2}+s+L_2)}^{-(\frac{w}{2}+s)} \int_{y=d-\frac{W_2}{2}}^{d+\frac{W_2}{2}} H_{21x}^{ext} M_{2x}^{ext} dxdy \right. \\
&+ \left. \int_{x=\frac{w}{2}+s}^{\frac{w}{2}+s+L_2} \int_{y=d-\frac{W_2}{2}}^{d+\frac{W_2}{2}} H_{21x}^{ext} M_{2x}^{ext} dxdy \right\}
\end{aligned} \tag{5.7}
$$

By combining Eqs. (5.4), (5.5b) and (5.5a) and considering rectangular vector components separately, H_{21x}^{ext} can be expressed as (*cf.* [69, Eqs. (6-111a), (6-108d), (6-108e)])

$$
H_{21x}^{ext}(x,y,z) = -\frac{j}{2\pi k_0 \eta_0}\int_{S_1} [G_1 M_{1x}^{ext}(x',y') + (x-x')^2 G_2 M_{1x}^{ext}(x',y')] e^{-jk_0 R} dx'dy' \tag{5.8a}
$$

with

$$
G_1 = \frac{-1 - jk_0 R + k_0^2 R^2}{R^3} \tag{5.8b}
$$

$$
G_2 = \frac{3 + j3k_0 R - k_0^2 R^2}{R^5} \tag{5.8c}
$$

In the above, $\eta_0 = \sqrt{\frac{\mu_0}{\varepsilon_0}}$ is the intrinsic impedance of free space, and $R = \sqrt{(x-x')^2 + (y-y')^2}$ (*i.e.*, in the plane of slot *2*).

5.2.2.2 Internal mutual admittance formulation

Eq. (5.2) may be used in a similar manner to find the internal mutual admittance Y_{12}^{int} between two CPW-fed slots on an infinite two-layer parallel-plate substrate. In particular,

$$
Y_{12}^{int} = -\frac{1}{V_1 V_2}\int_{S_2} \mathbf{H}_{21}^{int} \cdot \mathbf{M}_2^{int} dS_2 \tag{5.9}
$$

(Eq. (5.2) holds even though the slots are now considered to be radiating into the substrate, as the validity of the Lorentz reciprocity theorem, from which Eq. (5.2) is derived, extends to isotropic media that may be inhomogeneous [69].)

An equivalent problem for finding $\mathbf{H}_{21}^{int}$, which involves slot *1* radiating in isolation, is set up as follows. Fig. 5.7(a) shows a side view of the two-layer parallel-plate substrate containing radiating slots only with slot *2* removed. The unit surface normal vector $\hat{n}$ now points into the substrate. As before, the tangential electric field in slot *1* is $\mathbf{E}_{1,slot}$.

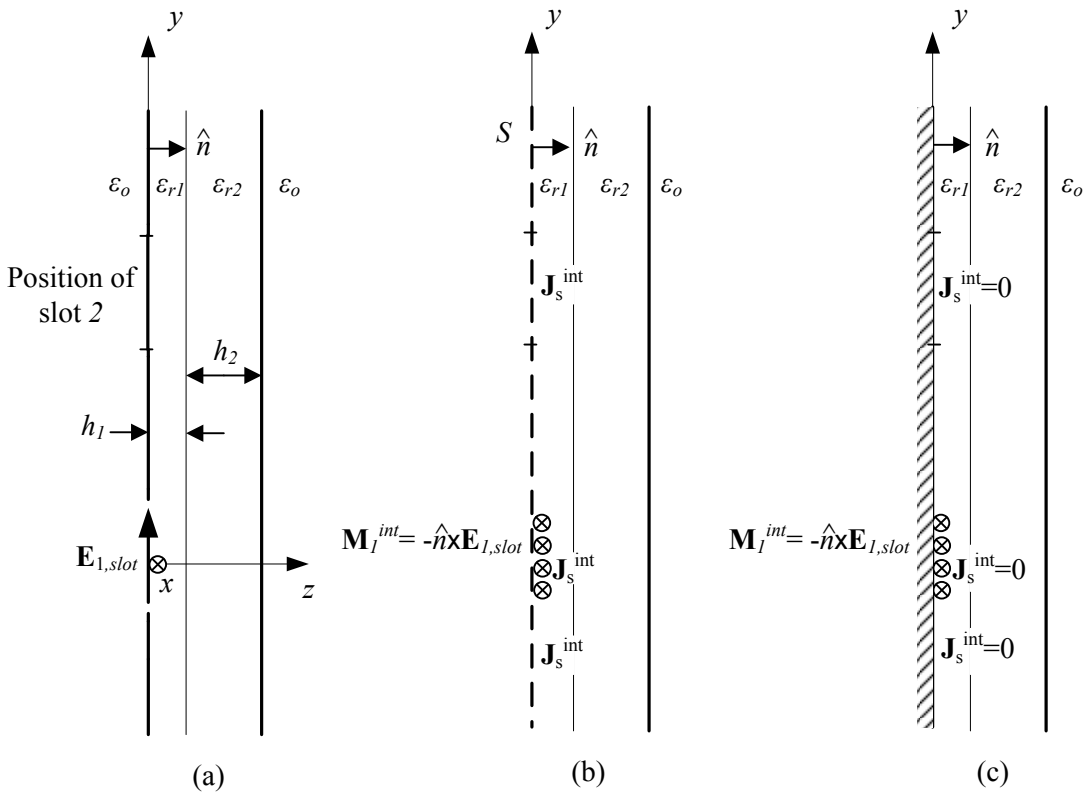

FIGURE 5.7: Steps in setting up an internal equivalent model for one slot on a two-layer parallel-plate substrate. In (a)–(c), electromagnetic fields are the same in the region $0 < z < h_1 + h_2$.

Application of the surface equivalence theorem yields equivalent currents in the place of slot *1* such that the fields inside the substrate, *i.e.*, for $0 < z < h_1 + h_2$, remain unchanged from their values in Fig. 5.7(a). Fig. 5.7(b) shows an imaginary closed surface S, which is an infinite plane, replacing the conducting plane containing the slot. Equivalent magnetic and electric current densities $\mathbf{M}_1^{int}$ and $\mathbf{J}_s^{int}$ are formed on this surface on the side facing the substrate. $\mathbf{M}_1^{int}$ is non-zero only over the positions of slot *1*, while $\mathbf{J}_s^{int}$ is non-zero everywhere. If $\mathbf{E}_{1,slot} = E_{1y,slot}\hat{y}$, and since $\hat{n} = \hat{z}$,

$$\mathbf{M}_1^{int} = -\hat{n} \times E_{1y,slot}\hat{y} = E_{1y,slot}\hat{x} = M_{1x}^{int}\hat{x} \tag{5.10}$$

It is then assumed that an imaginary conducting plane approaches S from the left, shorting out $\mathbf{J}_s^{int}$ everywhere but leaving $\mathbf{M}_1^{int}$ intact, as shown in Fig. 5.7(c).

The equivalent problem for $\mathbf{M}_2^{int}$ is derived in the same manner as for slot *1*. The result only differs from that presented in Fig. 5.7(c) in that the equivalent magnetic current density is $\mathbf{M}_2^{int}$ at the position of slot *2*. Assuming that $\mathbf{E}_{2,slot} = E_{2y,slot}\hat{y}$,

$$\mathbf{M}_2^{int} = E_{2y,slot}\hat{x} = M_{2x}^{int}\hat{x} \tag{5.11}$$

Substituting Eq. (5.11) into Eq. (5.9) yields

$$\begin{aligned} Y_{12}^{int} &= -\frac{1}{V_1 V_2}\int_{S_2} H_{21x}^{int} M_{2x}^{int} dS_2 \\ &= -\frac{1}{V_1 V_2}\left\{ \int_{x=-(\frac{w}{2}+s+L_2)}^{-(\frac{w}{2}+s)} \int_{y=d-\frac{W_2}{2}}^{d+\frac{W_2}{2}} H_{21x}^{int} M_{2x}^{int} dxdy \right. \\ &+ \left. \int_{x=\frac{w}{2}+s}^{\frac{w}{2}+s+L_2} \int_{y=d-\frac{W_2}{2}}^{d+\frac{W_2}{2}} H_{21x}^{int} M_{2x}^{int} dxdy \right\} \end{aligned} \tag{5.12}$$

H_{21x}^{int} can be found from

$$H_{21x}^{int}(\mathbf{r}) = \int_{S_1} G_{xx}^{HM}(\mathbf{r},\mathbf{r}') M_{1x}^{int}(\mathbf{r}') dS_1' \tag{5.13a}$$

which in the plane of the slots becomes

$$\begin{aligned} H_{21x}^{int}(x,y,0) &= \int_{S_1} G_{xx}^{HM}(x,y,0;x',y',0) M_{1x}^{int}(x',y') dx'dy' \\ &= \int_{x'=-(\frac{w}{2}+s+L_1)}^{-(\frac{w}{2}+s)} \int_{y'=-\frac{W_1}{2}}^{\frac{W_1}{2}} G_{xx}^{HM}(x,y,0;x',y',0) M_{1x}^{int}(x',y') dx'dy' \\ &+ \int_{x'=\frac{w}{2}+s}^{\frac{w}{2}+s+L_1} \int_{y'=-\frac{W_1}{2}}^{\frac{W_1}{2}} G_{xx}^{HM}(x,y,0;x',y',0) M_{1x}^{int}(x',y') dx'dy' \end{aligned} \tag{5.13b}$$

In the above, $G_{xx}^{HM}(x,y,0;x',y',0)$ is the $\hat{x}$ component of the spatial-domain magnetic field due to an $\hat{x}$-directed horizontal magnetic dipole (HMD) at $(x',y',0)$ on the ground plane adjacent to the higher-permittivity dielectric layer inside a two-layer parallel-plate substrate (primed and unprimed coordinates correspond to source and observation coordinates respectively). Section 5.3 is devoted to the derivation of G_{xx}^{HM}.

5.3 SPATIAL-DOMAIN GREEN'S FUNCTION FOR CONDUCTOR-BACKED TWO-LAYER SUBSTRATE

In this chapter, a spatial-domain expression is derived for the magnetic field H_x due to an $\hat{x}$-directed horizontal magnetic dipole (HMD) placed against the top plate inside a two-layer parallel-plate substrate (by "top plate" is meant the conducting plane that borders the higher-permittivity layer, *i.e.*, layer *1*). The position of the HMD coincides with the origin of the coordinate axes. Fig. 5.8 shows

the substrate and the placement of the HMD (*cf.* Fig. 5.1). It is only necessary to account for H_x at points in the plane of the magnetic dipole (*i.e.*, $z = 0$), since Eq. (5.12) requires the $\hat{x}$-component of the magnetic field due to slot *1* at the position of slot *2*, with both slots situated in the plane $z = 0$; hence the objective is to find $H_x(x, y, 0)$.

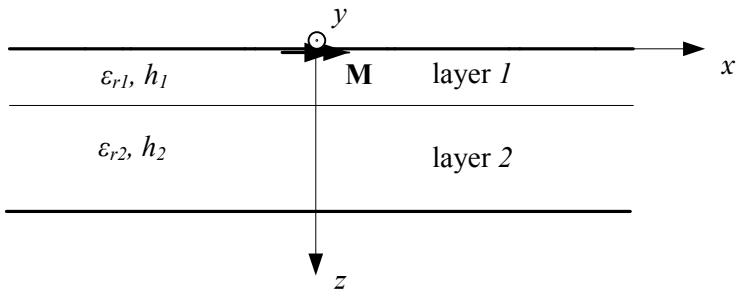

FIGURE 5.8: $\hat{x}$-directed horizontal magnetic dipole (HMD) inside a two-layer parallel-plate substrate. ε_{r1} and ε_{r2} are relative dielectric constants; $\mu = \mu_0$ in all layers.

The process of determining H_x is divided into two stages. First, the spectral-domain equivalent of H_x is found in closed form from general spectral-domain field expressions for multilayered media derived by Bhattacharrya [71].[7] Second, the spatial domain field H_x is obtained from its spectral domain equivalent by means of an inverse Fourier transform (*e.g.*, [71]), resulting in expressions containing Sommerfeld integrals that need to be evaluated numerically. To the author's knowledge, the spatial domain expressions for a two-layer parallel-plate substrate excited by a HMD that result from applying this procedure, and details of the treatment of the singularities in the integrals, are not currently available in the literature.[8,9]

For the sake of completeness, Bhattacharrya's method for finding the fields in a planar multilayered medium consisting of an arbitrary number of layers excited by planar electric and/or magnetic current distributions is now briefly outlined (full details can be found in [71, Chapters 1 and 2]). The geometry of such a medium is shown in Fig. 5.9. Its non-homogeneity pertains to its permittivity which can be expressed as $\varepsilon = \varepsilon(z)$, where z is the direction perpendicular to the interfaces between layers. The non-homogeneity is stepwise in nature, *i.e.*, within layer i of height h_i, $\varepsilon(z) = \varepsilon_0\varepsilon_{ri}$, which is a constant ($\varepsilon_{ri}$ is the relative permittivity in layer *i*, and ε_0 is the permittivity of free space). For the purposes of the present work, it can be assumed without a loss of generality

[7] A comprehensive review of techniques for finding Green's functions in planar layered media can be found in [72].
[8] The spectral-domain Green's function for the two-layer parallel-plate substrate presented in [73] appears to be incorrect.
[9] The spatial-domain Green's function for a single-layer parallel-plate substrate can be determined either in integral form or as a double infinite series [74]. Another instance of the latter form is the Green's function for an infinite periodic two-layer parallel-plate waveguide that can be determined in infinite-series form employing hybrid modes [75].

that the permeability $\mu = \mu_0$ everywhere.

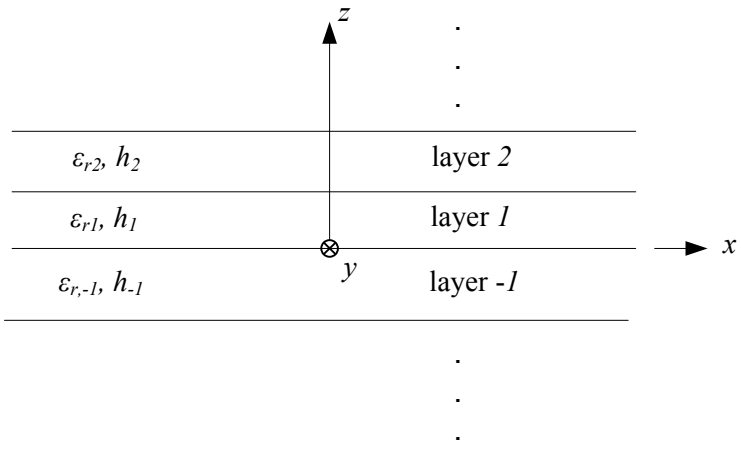

FIGURE 5.9: Geometry of a planar multilayered structure consisting of an arbitrary number of layers. $\mu = \mu_0$ in all layers.

In the above medium, the electromagnetic field outside of the source region can be decomposed into transverse magnetic (TM) and transverse electric (TE) components with respect to a reference direction perpendicular to the layer interfaces, *i.e.*, the $\hat{z}$-direction in Fig. 5.9. The total field can be expressed as the sum of TM_z and TE_z modes;[10] the subscript z will be suppressed in what follows. For TM mode fields, once the longitudinal component of the electric flux density vector, D_z^{TM} is known, the remaining field components D_x^{TM}, D_y^{TM}, B_x^{TM}, and B_y^{TM} can be found ($B_z^{TM} = 0$). Similarly for TE mode fields, if the longitudinal component of the magnetic flux density vector, B_z^{TE} is known, B_x^{TE}, B_y^{TE}, D_x^{TE}, and D_y^{TE} can be determined.

Bhattacharrya [71] derives spatial-domain non-linear, non-homogeneous differential equations for each of D_z^{TM} and B_z^{TE} that are valid everywhere in the substrate. Two-dimensional Fourier transforms of $D_z^{TM}(x, y, z)$ and $B_z^{TE}(x, y, z)$ with respect to their transverse coordinates x and y yield their spectral-domain equivalents, $\tilde{D}_z^{TM}(k_x, k_y, z)$ and $\tilde{B}_z^{TE}(k_x, k_y, z)$, with the two-dimensional Fourier transform of a function $f(x, y)$ defined as

$$\tilde{f}(k_x, k_y) = \mathcal{F}\{f(x, y)\} = \frac{1}{4\pi^2} \int_{-\infty}^{\infty} \int_{-\infty}^{\infty} f(x, y) e^{jk_x x} e^{jk_y y} dx dy \tag{5.14a}$$

and the inverse transform as

$$f(x, y) = \mathcal{F}^{-1}\{\tilde{f}(k_x, k_y)\} = \int_{-\infty}^{\infty} \int_{-\infty}^{\infty} \tilde{f}(k_x, k_y) e^{-jk_x x} e^{-jk_y y} dk_x dk_y \tag{5.14b}$$

[10] For some combinations of multilayered media and sources, the independent existence of either TM_z or TE_z waves is possible; this however does not apply to the present problem.

Replacing D_z^{TM} and B_z^{TE} with their inverse transforms in the above differential equations and taking the forward transforms yield differential equations for $\tilde{D}_z^{TM}(z)$ and $\tilde{B}_z^{TE}(z)$. Each differential equation can be combined with the Fourier transform of the appropriate Maxwell's divergence equation to yield a pair of transmission line equations in the spatial variable z, one pair containing $\tilde{D}_z^{TM}(z)$ and the other pair containing $\tilde{B}_z^{TE}(z)$. Within each pair, $\tilde{D}_z^{TM}(z)$ and $\tilde{B}_z^{TE}(z)$ are equivalent to the voltage $V(z)$ along the line, for which Bhattacharrya [71] presents closed-form solutions for planar electric and magnetic sources respectively.

These general solutions in the spectral domain, valid for an arbitrary number of dielectric layers excited by planar electric or magnetic sources, are used in the present work as a point of departure for deriving spatial-domain solutions H_x^{TM} and H_x^{TE} in the two-layer parallel-plate substrate of Fig. 5.8 due to a $\hat{x}$-directed HMD at the origin (see Sections 5.3.1 and 5.3.2), from which H_x can then be found in the plane of the slots (*i.e.*, $z = 0$) as

$$H_x(x, y, 0) = H_x^{TM}(x, y, 0) + H_x^{TE}(x, y, 0) \tag{5.15}$$

In what follows, the parallel plates of the two-layer parallel-plate substrate are assumed to be perfect electric conductors (PECs), and the dielectrics are assumed to be lossless.

5.3.1 H_x^{TM} for $\hat{x}$-directed HMD against top conducting plate inside two-layer parallel-plate substrate

Consider the two-layer parallel-plate structure of Fig. 5.8. The substrate is excited by a HMD at the origin which can be expressed as a volume current density,

$$\mathbf{M} = \delta(x)\delta(y)\delta(z)\hat{x} \tag{5.16a}$$

or equivalently a surface current density in the plane $z = 0$,

$$\mathbf{M}_s = M_{sx}\hat{x} = \delta(x)\delta(y)\hat{x} \tag{5.16b}$$

The preceding equations are related by $\mathbf{M} = \mathbf{M}_s\delta(z)$.

The objective is to find $\tilde{D}_z^{TM}$ from which all remaining TM field components, including H_x^{TM}, can be determined [71, p. 5] (for the sake of succinctness, the superscript TM is omitted for the remainder of the section). D_z and $\tilde{D}_z$ are a Fourier transform pair related according to Eq. (5.14),

$$\tilde{D}_z(k_x, k_y, z) = \frac{1}{4\pi^2} \int_{-\infty}^{\infty} \int_{-\infty}^{\infty} D_z(x, y, z) e^{jk_x x} e^{jk_y y} dx dy \tag{5.17a}$$

$$D_z(x,y,z) = \int_{-\infty}^{\infty}\int_{-\infty}^{\infty} \tilde{D}_z(k_x,k_y,z)e^{-jk_x x}e^{-jk_y y}dk_x dk_y \tag{5.17b}$$

In layer i, H_x can be expressed directly in terms of $\tilde{D}_z$ [71, p. 23] as follows:

$$H_x(x,y,z) = \omega \int_{-\infty}^{\infty}\int_{-\infty}^{\infty} \frac{k_y \tilde{D}_z(k_x,k_y,z)}{k_i^2 - k_{iz}^2} e^{-jk_x x}e^{-jk_y y}dk_x dk_y \tag{5.18}$$

In the above inverse Fourier transform, $k_{iz} = \sqrt{k_i^2 - k_x^2 - k_y^2}$ where $k_i = \omega\sqrt{\mu_i \varepsilon_i} = \omega\sqrt{\mu_0 \varepsilon_0 \varepsilon_{ri}}$ is the wave number for dielectric layer i, and $i = 1$ or 2.

For a two-layer parallel-plate substrate, the general multilayer TM mode spectral domain equivalent transmission line circuit ([71], Fig. 2.3) reduces to the circuit shown in Fig. 5.10, where the transmission line voltage $V(z)$ equals $\tilde{D}_z(k_x,k_y,z)$ of Eq. (5.18). The sections of transmission line with characteristic admittances y_{01}^m and y_{02}^m correspond to substrate layers *1* and *2* respectively. The parallel plates of the substrate (*cf.* Fig. 5.8), which are PECs, are represented by open circuits in the equivalent circuit. This is required since the component of an electric field perpendicular to a PEC (D_z in this case) is a maximum on the PEC.

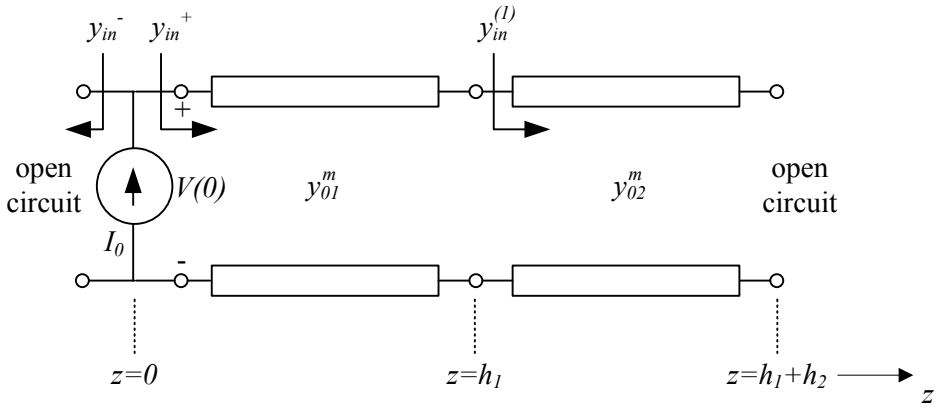

FIGURE 5.10: TM mode spectral domain equivalent circuit for two-layer parallel-plate substrate with planar magnetic current excitation at z = 0.

As only points in the plane $z = 0$ plane need to be considered, Eq. (5.18) reduces to

$$\begin{aligned} H_x(x,y,0) &= \omega \int_{-\infty}^{\infty}\int_{-\infty}^{\infty} \frac{k_y \tilde{D}_z(k_x,k_y,0)}{k_i^2 - k_{iz}^2} e^{-jk_x x}e^{-jk_y y}dk_x dk_y \\ &= \omega \int_{-\infty}^{\infty}\int_{-\infty}^{\infty} \frac{k_y V(0)}{k_i^2 - k_{iz}^2} e^{-jk_x x}e^{-jk_y y}dk_x dk_y \end{aligned} \tag{5.19}$$

In Eq. (5.19), $V(0)$ can be determined from [71, Eqs. (2.25) and (2.43)]; that is,

$$V(0) = \frac{I_0}{y_{in}^m} \tag{5.20}$$

In the preceding equation, I_0 is the value of the current source in the equivalent circuit, and $y_{in}^m = y_{in}^+ + y_{in}^-$ is the total input admittance at the source, with y_{in}^+ and y_{in}^- the input admittances seen when looking from the source into the transmission line in the $+z$ and $-z$ directions. I_0 in Eq. (5.20) can be found from [71, Table 2.1] as

$$I_0 = j(\mathbf{k}_\rho \times \tilde{\mathbf{M}}_\mathbf{s}) \cdot \hat{z} \tag{5.21a}$$

In Eq. (5.21a), $\mathbf{k}_\rho = k_\rho \hat{\rho} = k_x \hat{x} + k_y \hat{y}$, and the Fourier transform of Eq. (5.16b) yields

$$\tilde{M}_{sx} = \frac{1}{4\pi^2} \tag{5.21b}$$

Hence

$$I_0 = -j\frac{k_y}{4\pi^2} \tag{5.21c}$$

y_{in}^m in Eq. (5.20) can be found by noting that $y_{in}^- = 0$, and calculating y_{in}^+ using standard transmission line theory. In particular,

$$y_{in}^+ = y_{01}^m \frac{y_{in}^{(1)} + jy_{01}^m \tan k_{1z}h_1}{y_{01}^m + jy_{in}^{(1)} \tan k_{1z}h_1} \tag{5.22a}$$

with

$$y_{in}^{(1)} = jy_{02}^m \tan k_{2z}h_2 \tag{5.22b}$$

In the preceding two equations, $y_{0i}^m = jk_{iz}/\varepsilon_i$ is the (TM) characteristic admittance of transmission line i [71, Table 2.1] and $k_{iz} = \sqrt{k_i^2 - k_x^2 - k_y^2} = \sqrt{k_i^2 - k_\rho^2}$, where $i = 1$ or 2. From Eqs. (5.22a)–(5.22b) and $y_{in}^- = 0$ follows

$$y_{in}^m = \frac{k_{1z}}{\varepsilon_1} \frac{D_{TM}}{\varepsilon_2 k_{1z} - \varepsilon_1 k_{2z} \tan k_{1z}h_1 \tan k_{2z}h_2} \tag{5.22c}$$

In Eq. (5.22c), D_{TM} is the TM characteristic equation of the two-layer parallel-plate substrate [56], namely

$$D_{TM} = -\varepsilon_1 k_{2z} \tan k_{2z}h_2 - \varepsilon_2 k_{1z} \tan k_{1z}h_1 \tag{5.22d}$$

Combining Eqs. (5.21), (5.22), (5.20), and (5.19) yields

$$H_x(x, y, 0) = \frac{\omega}{j4\pi^2} \int_{-\infty}^{\infty} \int_{-\infty}^{\infty} \frac{k_y^2}{k_\rho^2} \frac{1}{y_{in}^m(k_x, k_y)} e^{-jk_x x} e^{-jk_y y} dk_x dk_y \tag{5.23}$$

Now make the change of variables

$$x = \rho\cos\phi \tag{5.24a}$$

$$y = \rho\sin\phi \tag{5.24b}$$

$$k_x = k_\rho\cos\alpha \tag{5.24c}$$

$$k_y = k_\rho\sin\alpha \tag{5.24d}$$

in Eq. (5.23) in order to effect a transformation in the spectral domain from rectangular coordinates (k_x, k_y) to cylindrical coordinates (k_ρ, α). This gives

$$\begin{aligned} H_x(\rho,\phi,0) &= C\int_{\alpha=0}^{2\pi}\int_{k_\rho=0}^{\infty}\frac{k_\rho^2\sin^2\alpha}{k_\rho^2}\frac{1}{y_{in}^m(k_\rho)}e^{-j(k_\rho\cos\alpha\cdot\rho\cos\phi+k_\rho\sin\alpha\cdot\rho\sin\phi)}k_\rho dk_\rho d\alpha \\ &= C\int_0^{\infty}\frac{1}{y_{in}^m(k_\rho)}\int_0^{2\pi}\sin^2\alpha e^{-jk_\rho\rho\cos(\alpha-\phi)}d\alpha k_\rho dk_\rho \\ &= C\int_0^{\infty}\frac{1}{y_{in}^m(k_\rho)}I_\alpha(k_\rho)k_\rho dk_\rho \end{aligned} \tag{5.25a}$$

with

$$I_\alpha(k_\rho) = \int_{-\phi}^{2\pi-\phi}\sin^2(\alpha+\phi)e^{-jk_\rho\rho\cos\alpha}d\alpha \tag{5.25b}$$

In the above, $C = \frac{\omega}{j4\pi^2}$, $\rho = \sqrt{x^2+y^2}$, and $k_\rho = \sqrt{k_x^2+k_y^2}$. Substituting the identity (*cf.* [56, Eq. (5-101)])

$$e^{-jk_\rho\rho\cos\alpha} = \sum_{n=-\infty}^{\infty} j^{-n}J_n(k_\rho\rho)e^{jn\alpha} \tag{5.26a}$$

into Eq. (5.25b) yields

$$I_\alpha(k_\rho) = \sum_{n=-\infty}^{\infty} j^{-n}J_n(k_\rho\rho)e^{-jn\phi}\int_0^{2\pi}e^{jn\alpha}\sin^2\alpha\, d\alpha \tag{5.26b}$$

The integral on the right hand side of Eq. (5.26b) can be solved using a standard identity [76, Eq. 14.523] in conjunction with l'Hospital's rule, giving

$$\int_0^{2\pi}e^{jn\alpha}\sin^2\alpha d\alpha = \begin{cases} \pi, & n=0 \\ -\frac{\pi}{2}, & n=-2,2 \\ 0, & \text{otherwise} \end{cases} \tag{5.26c}$$

Substitution of Eq. (5.26c) into Eq. (5.26b) yields

$$I_\alpha(k_\rho) = \frac{\pi}{2}J_{-2}(k_\rho\rho)e^{j2\phi} + \pi J_0(k_\rho\rho) + \frac{\pi}{2}J_2(k_\rho\rho)e^{-j2\phi} \tag{5.26d}$$

From the identity $J_{-n}(x) = (-1)^n J_n(x)$ [69, Eq. (IV-8)], it follows that $J_{-2}(x) = J_2(x)$. Substitution in Eq. (5.26d) gives

$$I_\alpha(k_\rho) = \pi J_0(k_\rho\rho) + \pi J_2(k_\rho\rho)\cos 2\phi \tag{5.26e}$$

Substitution of Eq. (5.26e) in Eq. (5.25a) gives

$$\begin{aligned} H_x(\rho,\phi,0) &= C\pi \int_0^\infty \frac{1}{y_{in}^m(k_\rho)} J_0(k_\rho\rho) k_\rho dk_\rho \\ &+ C\pi\cos 2\phi \int_0^\infty \frac{1}{y_{in}^m(k_\rho)} J_2(k_\rho\rho) k_\rho dk_\rho \\ &= \int_0^\infty F_0(k_\rho)dk_\rho + \cos 2\phi \int_0^\infty F_2(k_\rho)dk_\rho \\ &= I_0(\rho) + \cos 2\phi\, I_2(\rho) \end{aligned} \tag{5.27a}$$

Using Eq. (5.22c), the integrands $F_0(k_\rho)$ and $F_2(k_\rho)$ in Eq. (5.27a) may be expressed as

$$F_0(k_\rho) = C\pi \frac{k_\rho \varepsilon_1}{k_{1z}} \frac{\varepsilon_2 k_{1z} - \varepsilon_1 k_{2z} \tan k_{1z}h_1 \tan k_{2z}h_2}{D_{TM}} J_0(k_\rho\rho) \tag{5.27b}$$

$$F_2(k_\rho) = C\pi \frac{k_\rho \varepsilon_1}{k_{1z}} \frac{\varepsilon_2 k_{1z} - \varepsilon_1 k_{2z} \tan k_{1z}h_1 \tan k_{2z}h_2}{D_{TM}} J_2(k_\rho\rho) \tag{5.27c}$$

The integrals $I_0(\rho)$ and $I_2(\rho)$ in Eq. (5.27a) are Sommerfeld integrals that need to be evaluated numerically. While the integration path could be deformed (*e.g.*, [77]), the most straightforward approach is to integrate over the positive $\Re e(k_\rho)$ axis (*e.g.*, [78]).[11] Each integrand potentially is multi-valued (*i.e.*, four-valued) because of the two possible values each of $k_{1z} = \pm\sqrt{k_1^2 - k_\rho^2}$ and $k_{2z} = \pm\sqrt{k_2^2 - k_\rho^2}$. However, closer inspection of Eqs. (5.27b) and (5.27c) reveals that both integrands are even functions of k_{1z} and k_{2z}; hence there are no branch points associated with $k_\rho = k_1$ and $k_\rho = k_2$.[12] Plots of the (purely imaginary) integrands $F_0(k_\rho)$ and $F_2(k_\rho)$ are shown in Figs. 5.11–5.14 at f = 10 GHz for h_1 = 0.813 mm = 0.05λ_d, h_2 = 5 mm = λ_0/6, ϵ_{r1} = 3.38, and ϵ_{r2} = 1 (*i.e.*, Substrate I described in Section 5.4.2.1 below; λ_d is the wavelength in the dielectric at 10 GHz, and λ_0 the free-space wavelength). The plots in Figs. 5.11 and 5.12 correspond to $\rho = 20$ mm, while those in Figs. 5.13 and 5.14 are for $\rho = 64.5$ mm; the increased frequency of oscillation in the latter case is due to the larger arguments of the Bessel functions in Eqs. (5.27b) and (5.27c). (These ρ values approximately correspond to the beginning and final inter-slot distance value d in

[11] In general, $k_\rho = k'_\rho + jk''_\rho$; however, since the integration path does not involve imaginary values of k_ρ, the integration variable will be denoted as k_ρ throughout.

[12] This is consistent with the observation by Chew [79, p. 113] that branch points are physically associated with lateral waves that are only possible if the outer layers of the substrate are unbounded.

Figs. 5.24–5.40 of Chapter 5.)

Each of the integrations $I_0(\rho)$ and $I_2(\rho)$ can be divided into three regions that are evaluated separately [78]; the regions are $0 \leq k_\rho \leq k_2$ (Region *1*), $k_2 \leq k_\rho \leq k_1$ (Region *2*), and $k_1 \leq k_\rho$ (Region *3*). Total answers are obtained by adding the contributions from the three regions. Region boundaries are indicated in Figs. 5.11–5.14.[13]

The numerical integration in Region *1* is straightforward; while a change of integration variable $k_\rho = k_2 \cos t$ can be performed in order to render the integrand more smooth [78], it is not strictly necessary here.

In Region *2*, where $k_2 \leq k_\rho \leq k_1$, the singularities at the poles $k_\rho = k_{\rho o,0}$ (*cf.* Figs. 5.11 and 5.13) and $k_\rho = k_{\rho o,2}$ (*cf.* Figs. 5.12 and 5.14) require special attention. A familiar singularity extraction procedure [78, pp. 253-256] [80] is followed, which entails that a function containing the singularity is subtracted from the integrand (which may be F_0 or F_2), and then added to it. The integral of the function containing the singularity can be evaluated analytically, while the difference between the integrand and the function containing the singularity is an analytical function that can be integrated numerically. Thus,

$$\begin{aligned} F_i(k_\rho) &= [F_i(k_\rho) - F_{sing,i}(k_\rho)] + F_{sing,i}(k_\rho) \\ &= F_{d,i}(k_\rho) + F_{sing,i}(k_\rho) \end{aligned} \tag{5.28a}$$

where F_i is the integrand, $F_{d,i} = F_i(k_\rho) - F_{sing,i}(k_\rho)$ is the function from which the singularity has been extracted that can be integrated numerically, and $F_{sing,i}$ is the function containing the singularity given by

$$F_{sing,i} = \frac{R_i}{k_\rho - k_{\rho o,i}} \tag{5.28b}$$

In the above, R_i is the residue of the integrand F_i at the pole $k_{\rho o,i}$ where i = 0 or 2. Hence the integrals I_i in Eq. (5.27a) can be expressed in Region *2* as (*cf.* [78])

$$I_i = I_{d,i} + I_{sing,i} \tag{5.29a}$$

with

$$I_{d,i} = \int_{k_2}^{k_1} [F_i(k_\rho) - F_{sing,i}(k_\rho)] dk_\rho \tag{5.29b}$$

and

$$I_{sing,i} = \int_{k_2}^{k_1} F_{sing,i}(k_\rho) dk_\rho = R_i \ln\left(\frac{k_1 - k_{\rho o,i}}{k_{\rho o,i} - k_2}\right) \tag{5.29c}$$

[13] Since $k_1 = \sqrt{\varepsilon_{r1}} k_0$ and $k_2 = k_0$ for the present substrate, $k_1 > k_2$.

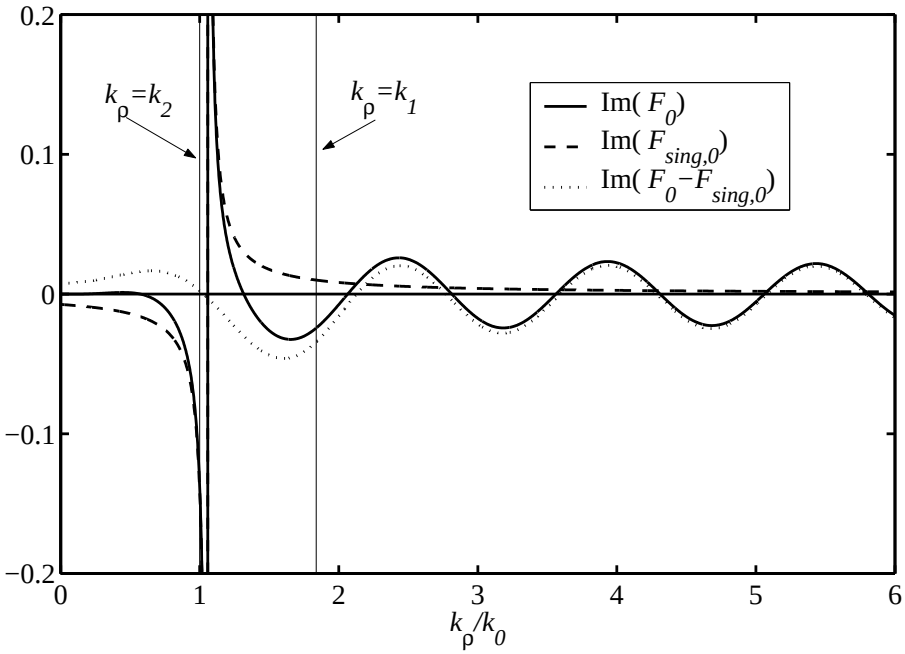

FIGURE 5.11: The integrand $F_0(k_\rho)$, the function containing the singularity $F_{sing,0}(k_\rho)$, and their difference. f = 10 GHz, ρ = 20 mm, h_1 = 0.813 mm = 0.05λ_d, h_2 = 5 mm = λ_0/6, ϵ_{r1} = 3.38, ϵ_{r2} = 1.

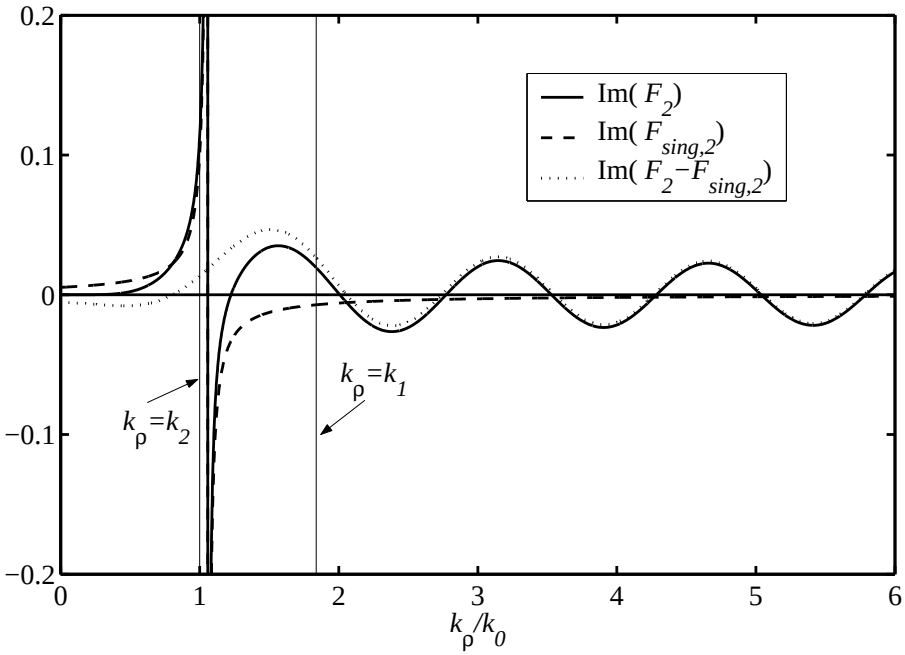

FIGURE 5.12: The integrand $F_2(k_\rho)$, the function containing the singularity $F_{sing,2}(k_\rho)$, and their difference. f = 10 GHz, ρ = 20 mm, h_1 = 0.813 mm = 0.05λ_d, h_2 = 5 mm = λ_0/6, ϵ_{r1} = 3.38, ϵ_{r2} = 1.

The smoothness of the difference function $F_{d,i}$ can be enhanced by the change of variables $k_\rho = k_0 \cosh t$ [78]. Eq. (5.29b) then becomes (similar to [78, Eq. (7.90)])[14]

[14] In Eq. (7.90) of [78], the radical sign in the upper boundary has erroneously been omitted.

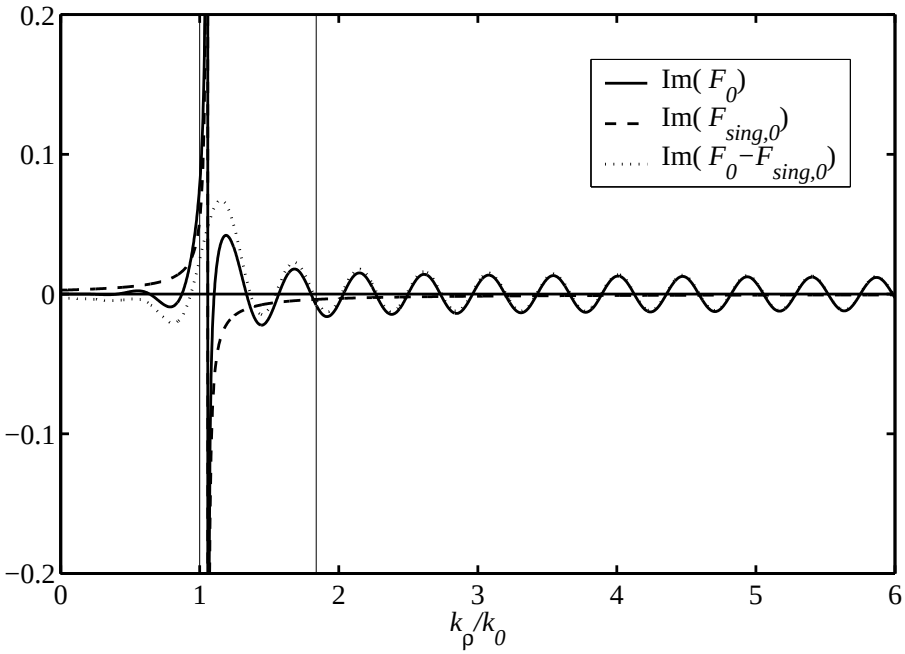

FIGURE 5.13: The integrand $F_0(k_\rho)$, the function containing the singularity $F_{sing,0}(k_\rho)$, and their difference. f = 10 GHz, ρ = 64.5 mm, h_1 = 0.813 mm = 0.05λ_d, h_2 = 5 mm = λ_0/6, ϵ_{r1} = 3.38, ϵ_{r2} = 1.

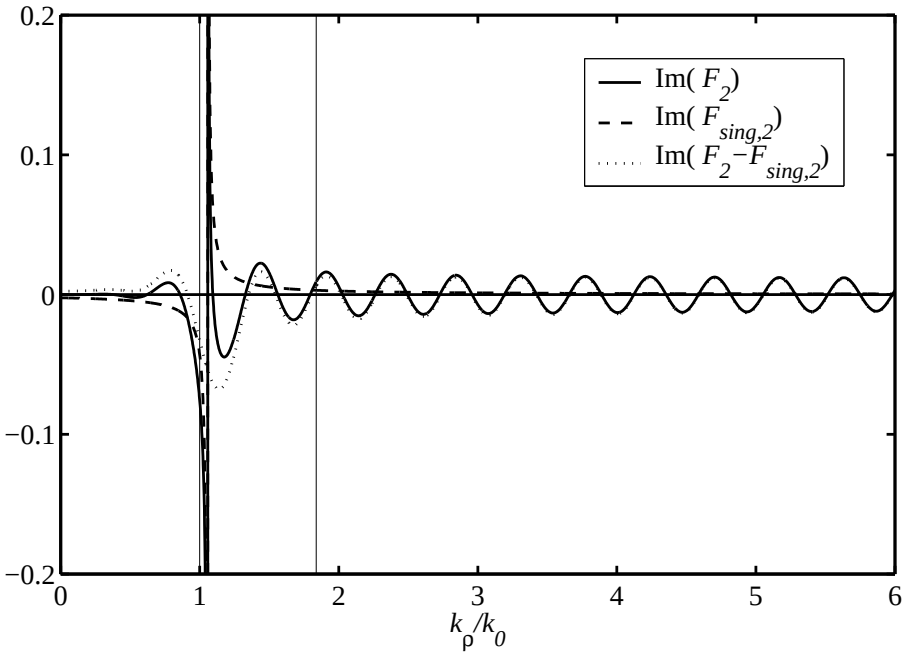

FIGURE 5.14: The integrand $F_2(k_\rho)$, the function containing the singularity $F_{sing,2}(k_\rho)$, and their difference. f = 10 GHz, ρ = 64.5 mm, h_1 = 0.813 mm = 0.05λ_d, h_2 = 5 mm = λ_0/6, ϵ_{r1} = 3.38, ϵ_{r2} = 1.

$$I_{d,i} = \int_0^{\cosh^{-1}\sqrt{\varepsilon_{r1}}} [F_i(k_0\cosh t) - F_{sing,i}(k_0\cosh t)]k_0\sinh t dt \tag{5.29d}$$

The residue R_i in Eq. (5.29c) may be evaluated by noting that if a complex function $f(k_\rho)$ can be written as a quotient $f(k_\rho) = \dfrac{g(k_\rho)}{h(k_\rho)}$ with $g(k_\rho)$ and $h(k_\rho)$ analytical at $k_\rho = k_{\rho o}$, and if h has a zero of order 1 at $k_\rho = k_{\rho o}$ such that f has a simple pole at $k_\rho = k_{\rho o}$, then

$$\mathrm{Res}(f(k_\rho), k_{\rho o}) = \frac{g(k_{\rho o})}{h'(k_{\rho o})} \tag{5.30}$$

where $\mathrm{Res}(f(k_\rho), k_{\rho o})$ is the residue of f at the pole $k_{\rho o}$ [81, p. 875]. From Eqs. (5.27b)–(5.27c), the integrand F_i, where i = 0 or 2, can be expressed as

$$F_i(k_\rho) = \frac{g_i(k_\rho)}{h(k_\rho)} \tag{5.31a}$$

with

$$g_i(k_\rho) = C\pi\varepsilon_1(j\varepsilon_2 k_{1z} - j\varepsilon_1 k_{2z}\tan k_{1z}h_1 \tan k_{2z}h_2)J_i(k_\rho\rho)k_\rho \tag{5.31b}$$

$$h(k_\rho) = jk_{1z}D_{TM} \tag{5.31c}$$

The residue R_i of F_i at the pole $k_{\rho o,i}$ is given by

$$\begin{aligned} R_i &= \mathrm{Res}(F_i, k_{\rho o,i}) \\ &= \frac{g_i(k_{\rho o,i})}{h'(k_{\rho o,i})} \end{aligned} \tag{5.32}$$

In the above, the numerator $g_i(k_{\rho o,i})$ can be found from Eq. (5.31b), while the denominator $h'(k_{\rho o,i})$ can be expressed as

$$h'(k_{\rho o,i}) = \left[D_{TM}\frac{d}{dk_\rho}\{jk_{1z}\} + jk_{1z}\frac{d}{dk_\rho}\{D_{TM}\}\right]_{k_\rho = k_{\rho o,i}} \tag{5.33a}$$

The derivatives in Eq. (5.33a) can be determined as follows. First,

$$\frac{d}{dk_\rho}\{jk_{1z}\} = -j\frac{k_\rho}{k_{1z}} \tag{5.33b}$$

Second,

$$\frac{d}{dk_\rho}\{D_{TM}\} = \frac{d}{dk_\rho}\{D_{TM1}\} + \frac{d}{dk_\rho}\{D_{TM2}\} \tag{5.33c}$$

In the preceding equation,

$$\begin{aligned} D_{TM1} &= -\varepsilon_1 k_{2z}\tan k_{2z}h_2 \\ D_{TM2} &= -\varepsilon_2 k_{1z}\tan k_{1z}h_1 \end{aligned} \tag{5.33d}$$

and

$$\begin{aligned} \frac{d}{dk_\rho}\{D_{TM1}\} &= -\varepsilon_2[-k_\rho h_1 \sec^2 k_{1z}h_1 - \frac{k_\rho}{k_{1z}}\tan k_{1z}h_1] \\ \frac{d}{dk_\rho}\{D_{TM2}\} &= -\varepsilon_1[-k_\rho h_2 \sec^2 k_{2z}h_2 - \frac{k_\rho}{k_{2z}}\tan k_{2z}h_2] \end{aligned} \tag{5.33e}$$

In Region *3*, the integrands F_0 and F_2 are slowly converging oscillating functions that can be difficult to integrate numerically.[15] The corresponding integrals I_i in Eq. (5.27a) can be expressed as

$$I_i = \int_{k_1}^{k_{\rho,upper}} F_i(k_\rho \rho) dk_\rho \tag{5.34}$$

where i = 0 or 2. In order to determine how large the upper integration boundary $k_{\rho,upper}$ had to be set, an iterative procedure suggested by Davidson [78, p. 257] was implemented. This involves repeatedly evaluating the integral with an increasing upper bound until a further increase in the upper bound makes no significant difference to the answer. In particular, the integral was initially evaluated for $k_{\rho,upper} = 10k_2 (= 10k_0)$ and $k_{\rho,upper} = 20k_2$. The difference between the results was computed and normalized by the magnitude of the integral in Region *2*, which typically contributes the most to the total integral due to the presence of the pole. If the normalized difference was above a threshold value (which always was the case), the upper integration limits were doubled, *i.e.*, to $k_{\rho,upper} = 20k_2$ and $k_{\rho,upper} = 40k_2$ for the second iteration, and a new normalized difference computed for comparison to the threshold. This procedure was repeated until the normalized difference was below the threshold value (typically 2% of the magnitude of the integral in Region *2*). Similar results were obtained by independently using a strategy based on the method of weighted averages for evaluating the tails of Sommerfeld integrals described in [80] and explained in greater detail in [83].

Since the integrals I_0 and I_2 in Eq. (5.27a) are functions of ρ only, it was only necessary to evaluate them once for a suitable range of ρ, and then store the resulting values in a lookup table from where they could be retrieved and/or interpolated in the course of evaluating Y_{12}^{int} (*cf.* Eqs. (5.12) and (5.13b)).

5.3.2 H_x^{TE} for $\hat{x}$-directed HMD against top conducting plate inside two-layer parallel-plate substrate

Consider the two-layer parallel-plate substrate of Fig. 5.8. As before, the substrate is excited by a HMD at the origin,

$$\mathbf{M}_s = M_{sx}\hat{x} = \delta(x)\delta(y)\hat{x} \tag{5.35}$$

The objective is to find $\tilde{B}_z^{TE}$ from which all remaining TE field components can be determined (the superscript TE will be omitted for the remainder of the section). B_z and $\tilde{B}_z$ are a Fourier transform pair (*cf.* Eq. (5.14)). In layer i, H_x can be expressed directly in terms of $\tilde{B}_z$ [71, p. 28] as follows:

$$H_x(x,y,z) = -\frac{j}{\mu_0} \int_{-\infty}^{\infty} \int_{-\infty}^{\infty} \frac{k_x}{k_i^2 - k_{iz}^2} \frac{\partial \tilde{B}_z(k_x,k_y,z)}{\partial z} e^{-jk_x x} e^{-jk_y y} dk_x dk_y \tag{5.36}$$

[15] Integration of the oscillating tails of Sommerfeld integrals is discussed at length in [82].

In the above, $k_{iz} = \sqrt{k_i^2 - k_x^2 - k_y^2}$ where $k_i = \omega\sqrt{\mu_i\varepsilon_i} = \omega\sqrt{\mu_0\varepsilon_0\varepsilon_{ri}}$ is the wavenumber of dielectric layer i, and i = 1 or 2.

For a two-layer parallel-plate substrate, the general multilayer TE mode spectral domain equivalent transmission line circuit ([71], Fig. 2.2) reduces to the circuit shown in Fig. 5.15, where the transmission line voltage $V(z)$ equals $\tilde{B}_z(k_x, k_y, z)$ of Eq. (5.36). The parallel-plates of the substrate are represented by short circuits in the equivalent circuit. This is required since B_z, the component of the magnetic field normal to the plates, is zero on them. The voltage at the input to the transmission line is denoted $V(0^+)$ (as opposed to $V(0)$ in the TM equivalent circuit of Fig. 5.10), as a discontinuity in voltage is presented by the series voltage source V_0.

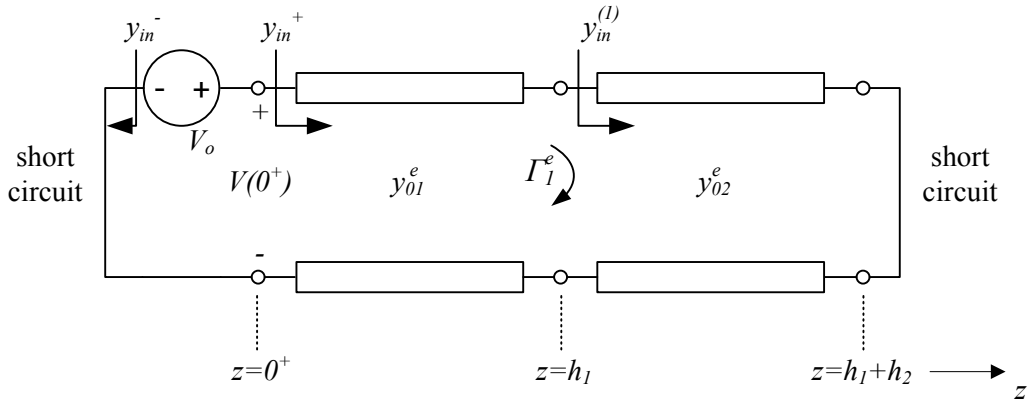

FIGURE 5.15: TE mode spectral domain equivalent circuit for two-layer parallel-plate substrate with planar magnetic current excitation at z = 0.

If only points in the plane $z = 0$ are considered, Eq. (5.36) reduces to[16]

$$\begin{aligned} H_x(x,y,0^+) &= -\frac{j}{\mu_0}\int_{-\infty}^{\infty}\int_{-\infty}^{\infty}\frac{k_x}{k_1^2-k_{1z}^2}\left[\frac{\partial\tilde{B}_z(k_x,k_y,z)}{\partial z}\right]_{z=0^+} e^{-jk_x x}e^{-jk_y y}dk_x dk_y \\ &= -\frac{j}{\mu_0}\int_{-\infty}^{\infty}\int_{-\infty}^{\infty}\frac{k_x}{k_1^2-k_{1z}^2}\left[\frac{\partial V_1(z)}{\partial z}\right]_{z=0^+} e^{-jk_x x}e^{-jk_y y}dk_x dk_y \end{aligned} \tag{5.37a}$$

In Eq. (5.37a), $V_1(z)$ is the transmission line voltage corresponding to layer *1*. $V_1(z)$ can be found from [71, Eq. (2.25)] as

$$V_1(z) = V(0^+)\frac{e^{-jk_{1z}(z-h_1)} + \Gamma_1^e e^{jk_{1z}(z-h_1)}}{e^{jk_{1z}h_1} + \Gamma_1^e e^{-jk_{1z}h_1}} \tag{5.37b}$$

[16] For practical purposes there is negligible difference between H_x evaluated at $z = 0^+$ and $z = 0$ due to continuity of the tangential magnetic field. The former form is however preferred for mathematical convenience as it lends itself to ready application of certain mathematical identities.

In Eq. (5.37b), Γ_1^e is given by

$$\Gamma_1^e = \frac{y_{01}^e - y_{in}^{(1)}}{y_{01}^e + y_{in}^{(1)}} \tag{5.37c}$$

where $y_{in}^{(1)} = -jy_{02}^e \cot k_{2z}h_2$, $y_{0i}^e = jk_{iz}/\mu_0$ is the (TE) characteristic admittance of transmission line i, and $i = 1$ or 2. Differentiating Eq. (5.37a) once with respect to z yields

$$\begin{aligned}\left[\frac{dV_1(z)}{dz}\right]_{z=0^+} &= jk_{1z}V(0^+)\frac{-1+\Gamma_1^e e^{-2jk_{1z}h_1}}{1+\Gamma_1^e e^{-2jk_{1z}h_1}} \\ &= jk_{1z}V_0\frac{-1+\Gamma_1^e e^{-2jk_{1z}h_1}}{1+\Gamma_1^e e^{-2jk_{1z}h_1}}\end{aligned} \tag{5.37d}$$

In the above, V_0 is the value of the voltage source in the equivalent circuit, given by [71, Table 2.1] as

$$V_0 = \tilde{\rho}_{ms} \tag{5.38a}$$

In the above, $\tilde{\rho}_{ms}$ is the Fourier transform of ρ_{ms}, the magnetic surface charge density of the source. ρ_{ms} can be related to the magnetic surface current density $\mathbf{M}_s$ by means of the continuity relation

$$\nabla \cdot \mathbf{M}_s = -j\omega\rho_{ms} \tag{5.38b}$$

Taking the two-dimensional Fourier transform of Eq. (5.38b) yields

$$-j\omega\tilde{\rho}_{ms} = -j\mathbf{k}_\rho \cdot \tilde{\mathbf{M}}_\mathbf{s} \tag{5.38c}$$

Combining Eqs. (5.21b), (5.38a) and (5.38c) gives

$$V_0 = \frac{k_x}{4\pi^2\omega} \tag{5.38d}$$

and combining Eqs. (5.38d), (5.37d), and (5.37a) yields

$$H_x(x,y,0^+) = -\frac{j}{4\pi^2\omega\mu_0}\int_{-\infty}^{\infty}\int_{-\infty}^{\infty}\frac{k_x^2}{k_1^2-k_{1z}^2}jk_{1z}V_0\frac{-1+\Gamma_1^e e^{-2jk_{1z}h_1}}{1+\Gamma_1^e e^{-2jk_{1z}h_1}}e^{-jk_x x}e^{-jk_y y}dk_x dk_y \tag{5.39}$$

Now substitute Eq. (5.24) in Eq. (5.39) in order to effect a transformation in the spectral domain from rectangular coordinates (k_x, k_y) into cylindrical coordinates (k_ρ, α). This gives

$$\begin{aligned}H_x(x,y,0^+) &= C\int_{\alpha=0}^{2\pi}\int_{k_\rho=0}^{\infty}\frac{k_\rho^2\cos^2\alpha}{k_\rho^2}G(k_\rho)e^{-j(k_\rho\cos\alpha\cdot\rho\cos\phi+k_\rho\sin\alpha\cdot\rho\sin\phi)}k_\rho dk_\rho d\alpha \\ &= C\int_0^\infty G(k_\rho)\int_0^{2\pi}\cos^2\alpha\, e^{-jk_\rho\rho\cos(\alpha-\phi)}d\alpha\, k_\rho dk_\rho \\ &= C\int_0^\infty G(k_\rho)I_\alpha(k_\rho)k_\rho dk_\rho\end{aligned} \tag{5.40a}$$

In Eq. (5.40a), $C = \frac{1}{4\pi^2\omega}$,[17] while $G(k_\rho)$ and $I_\alpha(k_\rho)$ are given by

$$G(k_\rho) = k_{1z}\frac{-1+\Gamma_1^e e^{-2jk_{1z}h_1}}{1+\Gamma_1^e e^{-2jk_{1z}h_1}} \tag{5.40b}$$

$$I_\alpha(k_\rho) = \int_{-\phi}^{2\pi-\phi} \cos^2(\alpha+\phi)e^{-jk_\rho\rho\cos\alpha}d\alpha \tag{5.40c}$$

Substituting the identity Eq. (5.26a) into Eq. (5.40c) yields

$$I_\alpha(k_\rho) = \sum_{n=-\infty}^{\infty} j^{-n}J_n(k_\rho\rho)e^{-jn\phi}\int_0^{2\pi} e^{jn\alpha}\cos^2\alpha\, d\alpha \tag{5.41a}$$

The integral on the right-hand side of Eq. (5.41a) can be solved using a standard identity [76, Eq. 14.524] in conjunction with l'Hospital's rule:

$$\int_0^{2\pi} e^{jn\alpha}\cos^2\alpha d\alpha = \begin{cases} \pi, & n=0 \\ \frac{\pi}{2}, & n=-2,2 \\ 0, & \text{otherwise} \end{cases} \tag{5.41b}$$

Substituting Eq. (5.41b) into Eq. (5.41a) yields

$$I_\alpha(k_\rho) = -\frac{\pi}{2}J_{-2}(k_\rho\rho)e^{j2\phi} + \pi J_0(k_\rho\rho) - \frac{\pi}{2}J_2(k_\rho\rho)e^{-j2\phi} \tag{5.41c}$$

Since $J_{-2}(x) = J_2(x)$, Eq. (5.41c) becomes

$$I_\alpha(k_\rho) = \pi J_0(k_\rho\rho) - \pi J_2(k_\rho\rho)\cos 2\phi \tag{5.41d}$$

Substitution of Eq. (5.41d) in Eq. (5.40a) gives

$$\begin{aligned} H_x(x,y,0^+) &= C\pi\int_0^\infty G(k_\rho)J_0(k_\rho\rho)k_\rho dk_\rho \\ &- C\pi\cos 2\phi\int_0^\infty G(k_\rho)J_2(k_\rho\rho)k_\rho dk_\rho \\ &= \int_0^\infty F_0(k_\rho)dk_\rho - \cos 2\phi\int_0^\infty F_2(k_\rho)dk_\rho \\ &= I_0(\rho) - \cos 2\phi I_2(\rho) \end{aligned} \tag{5.42a}$$

Using Eq. (5.40b), the integrands $F_0(k_\rho)$ and $F_2(k_\rho)$ in Eq. (5.42a) may be written as

$$F_0(k_\rho) = C\pi k_\rho k_{1z}\frac{-1+\Gamma_1^e e^{-2jk_{1z}h_1}}{1+\Gamma_1^e e^{-2jk_{1z}h_1}}J_0(k_\rho\rho) \tag{5.42b}$$

[17] Note that this value of C is different from the corresponding quantity in the derivation of H_x^{TM} in Section 5.3.1.

$$F_2(k_\rho) = C\pi k_\rho k_{1z} \frac{-1 + \Gamma_1^e e^{-2jk_{1z}h_1}}{1 + \Gamma_1^e e^{-2jk_{1z}h_1}} J_2(k_\rho \rho) \tag{5.42c}$$

The integrals $I_0(\rho)$ and $I_2(\rho)$ in Eq. (5.42a) are Sommerfeld integrals that need to be evaluated numerically, integrating over the positive $\Re e(k_\rho)$ axis. The possible multi-valued nature of the integrands was investigated given that k_{1z} and k_{2z} each have two possible values. However, inspection of Eqs. (5.42b) and (5.42c) revealed that both integrands are even functions of k_{1z} and k_{2z}; hence as in the TM case, there are no branch points associated with $k_\rho = k_1$ and $k_\rho = k_2$. Plots of the integrands $F_0(k_\rho)$ and $F_2(k_\rho)$ are shown in Fig. 5.16 at f = 10 GHz for ρ = 20 mm, h_1 = 0.813 mm = 0.05λ_d, h_2 = 5 mm = λ_0/6, ϵ_{r1} = 3.38, and ϵ_{r2} = 1 (*i.e.*, Substrate I of Section 5.4). The figure confirms that the integrands $F_0(k_\rho)$ and $F_2(k_\rho)$ are non-convergent, rendering the integrals $I_0(\rho)$ and $I_2(\rho)$ singular and therefore unsuitable for direct numerical integration (*cf.* [79, p. 118]).

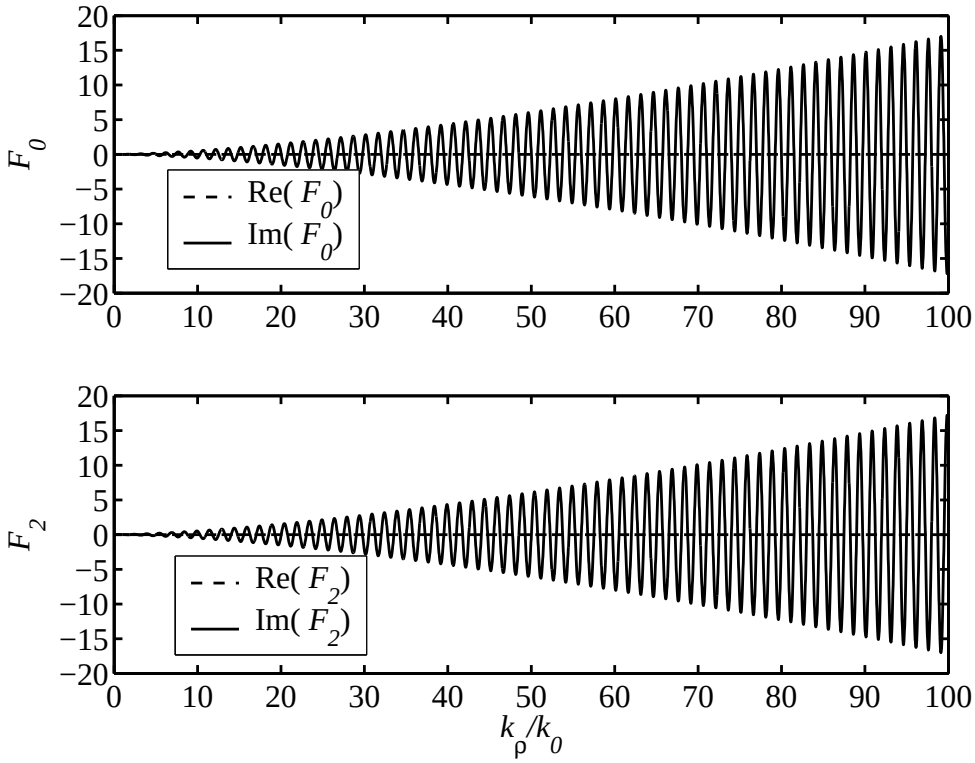

FIGURE 5.16: Plots of the TE integrands $F_0(k_\rho)$ and $F_2(k_\rho)$ for the two-layer parallel-plate substrate of Fig. 5.8. f = 10 GHz, ρ = 20 mm, h_1 = 0.813 mm = 0.05λ_d, h_2 = 5 mm = λ_0/6, ϵ_{r1} = 3.38, ϵ_{r2} = 1.

The evaluation of singular integrals of this nature, which typically arise when source and observation points lie in the same plane, is treated by Hansen [84] for substrates that have a conductor on one side only. The strategy implemented here to solve I_0 and I_2 in Eq. (5.42a) follows a broadly similar approach, requiring two further results. The first result entails expressions in integral form as

well as closed form for H_x^{TE} due to an $\hat{x}$-directed HMD placed at the origin of a homogenous medium with dielectric parameters ($\varepsilon_0\varepsilon_{r1}$, μ_0). The second is H_x^{TE} in integral form due to an $\hat{x}$-directed HMD inside the two-layer parallel-plate substrate of Fig. 5.8 with the conducting plane on the side of the source removed, and the adjacent half-space filled by a dielectric ($\varepsilon_0\varepsilon_{r1}$, μ_0) (the HMD is placed where it would have resided in the original two-layer parallel-plate substrate). These two results are derived in Sections 5.3.2.1 and 5.3.2.2 respectively. In Section 5.3.2.3, it is shown how they may be applied towards evaluating I_0 and I_2 in Eq. (5.42a).

5.3.2.1 H_x^{TE} of $\hat{x}$-directed HMD in homogenous medium

Consider a homogenous medium with permittivity $\varepsilon_1 = \varepsilon_0\varepsilon_{r1}$ and permeability μ_0 that is excited by a HMD at the origin, $\mathbf{M}_s = M_{sx}\hat{x} = \delta(x)\delta(y)\hat{x}$. As before, the objective is to find $\tilde{B}_z^{TE}$ from which all TE field components can be determined (the superscript TE will be omitted for the remainder of the section). In half-space *1* corresponding to $z > 0$, H_x can be expressed directly in terms of $\tilde{B}_z$ [71, p. 28]; that is,

$$H_x(x,y,z) = -\frac{j}{\mu_0}\int_{-\infty}^{\infty}\int_{-\infty}^{\infty}\frac{k_x}{k_1^2 - k_{1z}^2}\frac{\partial\tilde{B}_z(k_x,k_y,z)}{\partial z}e^{-jk_x x}e^{-jk_y y}dk_x dk_y \tag{5.43}$$

In the above, $k_{1z} = \sqrt{k_1^2 - k_x^2 - k_y^2}$ where $k_1 = \omega\sqrt{\mu_0\varepsilon_1}$ is the wave number.

For this medium, the general multilayer TE mode spectral domain equivalent transmission line circuit ([71], Fig. 2.2) reduces to the circuit shown in Fig. 5.17, which consists of two semi-infinite transmission lines fed by a series voltage source. The transmission line voltage $V(z)$ equals $\tilde{B}_z(k_x,k_y,z)$ of Eq. (5.43). Hence, for half-space *1* the latter equation becomes

$$H_x(x,y,z) = -\frac{j}{\mu_0}\int_{-\infty}^{\infty}\int_{-\infty}^{\infty}\frac{k_x}{k_1^2 - k_{1z}^2}\frac{\partial V_1(z)}{\partial z}e^{-jk_x x}e^{-jk_y y}dk_x dk_y \tag{5.44a}$$

$V_1(z)$ in Eq. (5.44a) can be determined from [71, Eq. (2.25)] as follows:

$$V_1(z) = V(0^+)e^{-jk_{1z}z} \tag{5.44b}$$

Since the characteristic admittances y_{01}^e and $y_{0,-1}^e$ are equal, voltage division yields

$$V(0^+) = \frac{V_0}{2} \tag{5.44c}$$

Combining the first derivative of Eq. (5.44b) with Eq. (5.44c) yields

$$\frac{dV_1(z)}{dz} = -jk_{1z}\frac{V_0}{2}e^{-jk_{1z}z} \tag{5.44d}$$

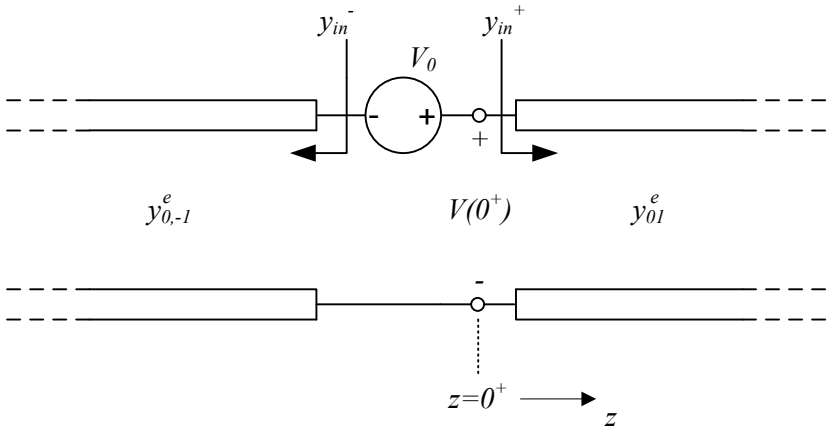

FIGURE 5.17: TE mode spectral domain equivalent circuit for homogeneous full-space with planar magnetic current excitation at $z = 0$.

Furthermore, combining Eqs. (5.38d), (5.44d) and (5.44a) gives

$$H_x(x,y,z) = \frac{1}{8\pi^2\omega\mu_0}\int_{-\infty}^{\infty}\int_{-\infty}^{\infty}\frac{k_x^2}{k_1^2-k_{1z}^2}(-k_{1z}e^{-jk_{1z}z})e^{-jk_xx}e^{-jk_yy}dk_xdk_y \tag{5.45}$$

Now substitute Eq. (5.24) in Eq. (5.45) in order to effect a transformation in the spectral domain from rectangular to cylindrical coordinates. A manipulation similar to that used to derive Eq. (5.42) from Eq. (5.40) gives

$$\begin{aligned} H_x(\rho,\phi,z) &= C^H\pi\int_0^{\infty}(-k_{1z}e^{-jk_{1z}z})J_0(k_\rho\rho)k_\rho dk_\rho \\ &- C^H\pi\cos 2\phi\int_0^{\infty}(-k_{1z}e^{-jk_{1z}z})J_2(k_\rho\rho)k_\rho dk_\rho \\ &= C^H\pi[i_0^H(\rho,z)-\cos 2\phi\, i_2^H(\rho,z)] \end{aligned} \tag{5.46a}$$

In the preceding equation, $C^H = \frac{1}{8\pi^2\omega\mu_0}$ and

$$i_0^H(\rho,z) = \int_0^{\infty}(-k_{1z}e^{-jk_{1z}z})J_0(k_\rho\rho)k_\rho dk_\rho \tag{5.46b}$$

$$i_2^H(\rho,z) = \int_0^{\infty}(-k_{1z}e^{-jk_{1z}z})J_2(k_\rho\rho)k_\rho dk_\rho \tag{5.46c}$$

Restricting Eq. (5.46a) to points in the plane $z = 0^+$ results in

$$\begin{aligned} H_x(\rho,\phi,z=0^+) &= \lim_{z\to 0^+}\left[C^H\pi\int_0^\infty(-k_{1z}e^{-jk_{1z}z})J_0(k_\rho\rho)k_\rho dk_\rho\right] \\ &- \lim_{z\to 0^+}\left[C^H\pi\cos 2\phi\int_0^\infty(-k_{1z}e^{-jk_{1z}z})J_2(k_\rho\rho)k_\rho dk_\rho\right] \\ &= \lim_{z\to 0^+} C^H\pi[i_0^H(\rho,z)-\cos 2\phi\, i_2^H(\rho,z)] \\ &= I_0^H(\rho)-\cos 2\phi\, I_2^H(\rho) \end{aligned} \tag{5.47a}$$

The objective is to find $I_0^H(\rho)$ and $I_2^H(\rho)$ in closed form; this entails determining closed-form expressions for

$$\begin{aligned} \lim_{z\to 0^+} i_0^H(\rho,z) &= \lim_{z\to 0^+}\left[\int_0^\infty(-k_{1z}e^{-jk_{1z}z})J_0(k_\rho\rho)k_\rho dk_\rho\right] \\ &= \frac{I_0^H(\rho)}{C^H\pi} \\ &= \frac{1}{C^H\pi}\int_0^\infty F_0^H(k_\rho)dk_\rho \end{aligned} \tag{5.47b}$$

and

$$\begin{aligned} \lim_{z\to 0^+} i_2^H(\rho,z) &= \lim_{z\to 0^+}\left[\int_0^\infty(-k_{1z}e^{-jk_{1z}z})J_2(k_\rho\rho)k_\rho dk_\rho\right] \\ &= \frac{I_2^H(\rho)}{C^H\pi} \\ &= \frac{1}{C^H\pi}\int_0^\infty F_2^H(k_\rho)dk_\rho \end{aligned} \tag{5.47c}$$

In Eqs. (5.47b) and (5.47c), the integrands F_0^H and F_2^H can be expressed as

$$F_0^H(k_\rho) = \lim_{z\to 0^+}(-k_\rho k_{1z}e^{-jk_{1z}z})J_0(k_\rho\rho) \tag{5.47d}$$

$$F_2^H(k_\rho) = \lim_{z\to 0^+}(-k_\rho k_{1z}e^{-jk_{1z}z})J_2(k_\rho\rho) \tag{5.47e}$$

$\lim_{z\to 0^+} i_0^H(\rho,z)$ in Eq. (5.47b) can be found by utilizing the identity [85, Eq. (A3)]

$$-\lim_{z\to 0^+}\int_0^\infty dk_\rho k_\rho k_z J_0(k_\rho\rho)e^{-jk_z z} = (\frac{k}{\rho^2}-\frac{j}{\rho^3})e^{-jk\rho} \tag{5.48a}$$

which in turn is derived from the Sommerfeld identity [86, Eq. (A1)]

$$\int_0^\infty dk_\rho\frac{k_\rho}{k_z}e^{-jk_z z}J_0(k_\rho\rho) = \frac{je^{-jkr}}{r} \tag{5.48b}$$

where $r = \sqrt{\rho^2 + z^2}$, by differentiating twice with respect to z and then taking the limit $z \to 0^+$. In particular,

$$\begin{aligned} \lim_{z\to 0^+} i_0^H(\rho, z) &= (\frac{k_1}{\rho^2} - \frac{j}{\rho^3})e^{-jk_1\rho} \\ &= \frac{I_0^H(\rho)}{C^H\pi} \end{aligned} \tag{5.48c}$$

The derivation of $\lim_{z\to 0^+} i_2^H(\rho, z)$ in Eq. (5.47c), on the other hand, requires more effort due to the presence of $J_2(k_\rho\rho)$ in the integrand. Subtracting the identities [87, Eq. 9.1.27]

$$J_1'(z) = J_0(z) - \frac{1}{z}J_1(z) \tag{5.49a}$$

$$J_1'(z) = -J_2(z) + \frac{1}{z}J_1(z) \tag{5.49b}$$

yields

$$J_2(z) = -J_0(z) + \frac{2}{z}J_1(z) \tag{5.49c}$$

Substituting Eqs. (5.49c) into (5.46c) gives

$$i_2^H = i_{21}^H - \frac{2}{\rho}i_{22}^H \tag{5.50a}$$

with

$$i_{21}^H = \int_0^\infty dk_\rho k_\rho k_{1z} e^{-jk_{1z}z} J_0(k_\rho\rho) \tag{5.50b}$$

$$i_{22}^H = \int_0^\infty dk_\rho k_{1z} e^{-jk_{1z}z} J_1(k_\rho\rho) \tag{5.50c}$$

Combining Eqs. (5.50b) and (5.48a) gives

$$\lim_{z\to 0^+} i_{21}^H(\rho, z) = (\frac{j}{\rho^3} - \frac{k_1}{\rho^2})e^{-jk_1\rho} \tag{5.51}$$

$\lim_{z\to 0^+} i_{22}^H(\rho, z)$ can be determined as follows. Noting from the identity [87, Eq. 9.1.28] that

$$J_0'(z) = \frac{dJ_0(z)}{dz} = -J_1(z) \tag{5.52}$$

it follows that Eq. (5.50c) can be expressed as

$$i_{22}^H = \int u(k_\rho)v'(k_\rho)dk_\rho \tag{5.53a}$$

with

$$u(k_\rho) = k_{1z}e^{-jk_{1z}z} \tag{5.53b}$$

$$v(k_\rho) = -\frac{1}{\rho}J_0(k_\rho\rho) \tag{5.53c}$$

(the chain rule of differentiation applied to Eq. (5.53c) gives $v'(k_\rho) = J_1(k_\rho\rho)$). Applying the integration-by-parts formula [88]

$$\int u(k_\rho)v'(k_\rho)dk_\rho = u(k_\rho)v(k_\rho) - \int u'(k_\rho)v(k_\rho)dk_\rho \tag{5.54}$$

to the right-hand side Eq. (5.50c) expressed in the form of Eq. (5.53) gives

$$i_{22}^H = f_{22}^H - i_{221}^H \tag{5.55a}$$

with

$$f_{22}^H = -\frac{1}{\rho}\left[k_{1z}e^{-jk_{1z}z}J_0(k_\rho\rho)\right]_{k_\rho=0}^{k_\rho=\infty} \tag{5.55b}$$

$$i_{221}^H = \int_0^\infty u'(k_\rho)v(k_\rho)dk_\rho \tag{5.55c}$$

Combining Eq. (5.53b), (5.53c) and (5.55c) yields

$$\begin{aligned} i_{221}^H &= \frac{1}{\rho}\int_0^\infty dk_\rho \frac{k_\rho}{k_{1z}}e^{-jk_{1z}z}J_0(k_\rho\rho) - \frac{jz}{\rho}\int_0^\infty dk_\rho k_\rho e^{-jk_{1z}z}J_0(k_\rho\rho) \\ &= \frac{j}{\rho}\frac{e^{-jk_1r}}{r} - \frac{jz^2}{\rho}(\frac{1}{r^3} + \frac{jk_1}{r^2})e^{-jk_1r} \end{aligned} \tag{5.56}$$

To arrive at the above result, use was made of the Sommerfeld identity Eq. (5.48b) as well as the identity

$$\int_0^\infty dk_\rho k_\rho e^{-jk_zz}J_0(k_\rho\rho) = z(\frac{1}{r^3} + \frac{jk}{r^2})e^{-jkr} \tag{5.57}$$

which can be obtained by differentiating the Sommerfeld identity once with respect to z. From Eq. (5.56) it follows that

$$\lim_{z\to 0^+} i_{221}^H(\rho, z) = \frac{je^{-jk_1\rho}}{\rho^2} \tag{5.58}$$

Taking the limit $z \to 0^+$ with respect to Eq. (5.55b) yields

$$\begin{aligned} \lim_{z\to 0^+} f_{22}^H(\rho, z) &= -\lim_{z\to 0^+, k_\rho\to\infty}\frac{1}{\rho}\left[k_{1z}e^{-jk_{1z}z}J_0(k_\rho\rho)\right] \\ &+ \lim_{z\to 0^+, k_\rho\to 0}\frac{1}{\rho}\left[k_{1z}e^{-jk_{1z}z}J_0(k_\rho\rho)\right] \end{aligned} \tag{5.59}$$

The negative root $k_{1z} = -\sqrt{k_1^2 - k_\rho^2}$ is now chosen. If $k_\rho \to \infty$, then

$$k_{1z} \approx -\sqrt{-k_\rho^2} = -jk_\rho \tag{5.60a}$$

Furthermore,

$$\lim_{k_\rho\to 0} k_{1z} = -\sqrt{k_1^2} = -k_1 \tag{5.60b}$$

Combining Eqs. (5.60) and (5.59) gives

$$\begin{aligned}\lim_{z\to 0^+,} f_{22}^H &= \lim_{z\to 0^+, k_\rho\to\infty} \frac{j}{\rho}\left[\sqrt{k_\rho}e^{-k_\rho z}\sqrt{\frac{2}{\pi\rho}}\cos(k_\rho\rho-\pi/4)\right] \\ &+ \lim_{z\to 0^+}\frac{1}{\rho}\left[-k_1 e^{jk_1 z}\cdot 1\right] \\ &= 0-\frac{k_1}{\rho} \\ &= -\frac{k_1}{\rho} \end{aligned} \tag{5.61}$$

In finding the preceding result, the small and large-argument forms of the zero-order Bessel function J_0 was used [56].

In summary, the integrals $I_0^H(\rho)$ and $I_2^H(\rho)$ in Eq. (5.47a) can be expressed in closed form as follows. From Eq. (5.48c),

$$I_0^H(\rho) = C^H\pi \lim_{z\to 0^+} i_0^H(\rho,z) = (\frac{k_1}{\rho^2}-\frac{j}{\rho^3})e^{-jk_1\rho} \tag{5.62a}$$

while combining Eqs. (5.50a), (5.51), (5.55a), (5.58), and (5.61) gives

$$I_2^H(\rho) = C^H\pi \lim_{z\to 0^+} i_2^H(\rho,z) = \frac{2k_1}{\rho^2}+(\frac{3j}{\rho^3}-\frac{k_1}{\rho^2})e^{-jk_1\rho} \tag{5.62b}$$

5.3.2.2 H_x^{TE} of $\hat{x}$-directed HMD inside two-layer parallel-plate substrate with top conducting plate removed

Consider a substrate that is identical in every respect to the two-layer parallel-plate substrate of Fig. 5.8 except for the conducting plane adjacent to the ε_{r1} dielectric layer having been removed, and the half-space $z<0$ being filled by the same dielectric material as layer *1*. As before, the substrate is excited by a HMD at the origin, $\mathbf{M}_s = M_{sx}\hat{x} = \delta(x)\delta(y)\hat{x}$. For this substrate, the general multilayer TE mode spectral domain equivalent transmission line circuit ([71], Fig. 2.2) reduces to the circuit shown in Fig. 5.18.

As in the case of the previous substrates, H_x in layer *1* can be expressed in terms of the equivalent transmission line voltage V_1 (*i.e.*, the voltage in the section of transmission line with characteristic admittance y_{01}^e) as follows:

$$H_x(x,y,z) = -\frac{j}{\mu_0}\int_{-\infty}^{\infty}\int_{-\infty}^{\infty}\frac{k_x}{k_1^2-k_{1z}^2}\frac{\partial V_1(z)}{\partial z}e^{-jk_x x}e^{-jk_y y}dk_x dk_y \tag{5.63}$$

If only points in the plane $z=0$ are considered, Eq. (5.63) reduces to

$$H_x(x,y,0^+) = -\frac{j}{\mu_0}\int_{-\infty}^{\infty}\int_{-\infty}^{\infty}\frac{k_x}{k_1^2-k_{1z}^2}\left[\frac{\partial V_1(z)}{\partial z}\right]_{z=0^+}e^{-jk_x x}e^{-jk_y y}dk_x dk_y \tag{5.64a}$$

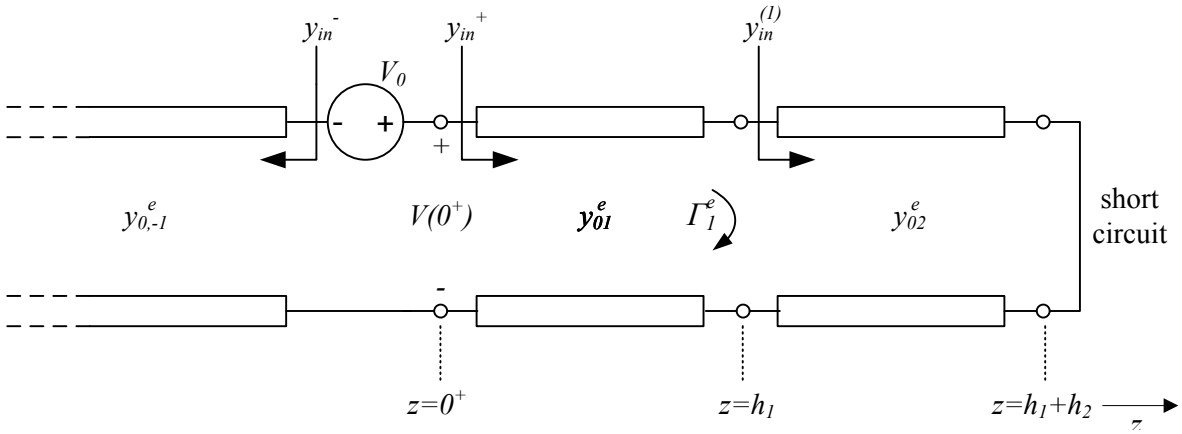

FIGURE 5.18: TE mode spectral domain equivalent circuit for two-layer parallel-plate substrate with top conducting plate removed.

In Eq. (5.64a), $V_1(z)$ can be found from [71, Eq. (2.25)] as

$$V_1(z) = V(0^+)\frac{e^{-jk_{1z}(z-h_1)} + \Gamma_1^e e^{jk_{1z}(z-h_1)}}{e^{jk_{1z}h_1} + \Gamma_1^e e^{-jk_{1z}h_1}} \tag{5.64b}$$

In Eq. (5.64b), which is the same as the corresponding equation for the two-layer-parallel-plate case, Γ_1^e is given by

$$\Gamma_1^e = \frac{y_{01}^e - y_{in}^{(1)}}{y_{01}^e + y_{in}^{(1)}} \tag{5.64c}$$

with $y_{in}^{(1)} = -jy_{02}^e \cot k_{2z}h_2$, and $y_{0i}^e = jk_{iz}/\mu_0$ the (TE) characteristic admittance of transmission line i, where $i = 1$ or 2. Differentiating Eq. (5.64b) once with respect to z yields

$$\left[\frac{dV_1(z)}{dz}\right]_{z=0^+} = jk_{1z}V(0^+)\frac{-1 + \Gamma_1^e e^{-2jk_{1z}h_1}}{1 + \Gamma_1^e e^{-2jk_{1z}h_1}} \tag{5.64d}$$

$V(0^+)$ in Eq. (5.64d) can be found from voltage division (see Fig. 5.18) as

$$\begin{aligned} V(0^+) &= V_0 \frac{\frac{1}{y_{in}^+}}{\frac{1}{y_{in}^+} + \frac{1}{y_{in}^-}} \\ &= V_0 \frac{y_{in}^-}{y_{in}^- + y_{in}^+} \end{aligned} \tag{5.65a}$$

In the preceding equation, V_0 is the value of the voltage source in the equivalent circuit, while y_{in}^- and y_{in}^+ are given by

$$y_{in}^- = y_{0,-1}^e = y_{01}^e \tag{5.65b}$$

$$\begin{aligned} y_{in}^+ &= y_{01}^e \frac{y_{in}^{(1)} + jy_{01}^e \tan k_{1z}h_1}{y_{01}^e + jy_{in}^{(1)} \tan k_{1z}h_1} \\ &= y_{01}^e \frac{-jy_{02}^e \cot k_{2z}h_2 + jy_{01}^e \tan k_{1z}h_1}{y_{01}^e + y_{02}^e \cot k_{2z}h_2 \tan k_{1z}h_1} \end{aligned} \tag{5.65c}$$

In Eq. (5.65b), $y^e_{0,-1}$ is the (TE) characteristic admittance of transmission line *-1* corresponding to the half-space $z < 0$.

Substituting Eqs. (5.65) and (5.64d) into Eq. (5.64a), and then implementing the change of variables Eq. (5.24) in order to effect a transformation in the spectral domain from rectangular to cylindrical coordinates ultimately gives

$$\begin{aligned} H_x(\rho,\phi,0^+) &= \int_0^\infty F_0^A(k_\rho)dk_\rho - \cos 2\phi \int_0^\infty F_2^A(k_\rho)dk_\rho \\ &= I_0^A(\rho) - \cos 2\phi I_2^A(\rho) \end{aligned} \tag{5.66a}$$

The integrands $F_0^A(k_\rho)$ and $F_2^A(k_\rho)$ in Eq. (5.66a) may be expressed as

$$F_0^A(k_\rho) = C^A \pi k_\rho k_{1z} \frac{y^e_{01}}{y^e_{01}+y^+_{in}} \frac{-1+\Gamma^e_1 e^{-2jk_{1z}h_1}}{1+\Gamma^e_1 e^{-2jk_{1z}h_1}} J_0(k_\rho\rho) \tag{5.66b}$$

$$F_2^A(k_\rho) = C^A \pi k_\rho k_{1z} \frac{y^e_{01}}{y^e_{01}+y^+_{in}} \frac{-1+\Gamma^e_1 e^{-2jk_{1z}h_1}}{1+\Gamma^e_1 e^{-2jk_{1z}h_1}} J_2(k_\rho\rho) \tag{5.66c}$$

In Eqs. (5.66b) and (5.66c), $C^A = \dfrac{1}{4\pi^2\omega\mu_0}$.

5.3.2.3 Evaluation of singular integrals for H_x^{TE} of $\hat{x}$-directed HMD against top conducting plate inside two-layer parallel-plate substrate

The integrands of the integrals required to find H_x for each of the three substrates discussed above (*i.e.*, the two-layer parallel-plate substrate, the homogeneous full-space and the two-layer parallel-plate substrate with top plate removed) are F_0, F_2, F_0^H, F_2^H, F_0^A, and F_2^A; they are given in Eqs. (5.42b), (5.42c), (5.47d), (5.47e), (5.66b), and (5.66c) respectively. By combining these equations with Eq. (5.42a), the TE magnetic field due to an $\hat{x}$-directed HMD at the origin of the two-layer parallel-plate substrate of Fig. 5.8 can be expressed as follows:

$$\begin{aligned} H_x(\rho,\phi,0) &= \int_0^\infty F_0(k_\rho)dk_\rho - \cos 2\phi \int_0^\infty F_2(k_\rho)dk_\rho \\ &= \int_0^\infty \left[(F_0 - F_0^A - F_0^H) + (F_0^A - F_0^H) + 2F_0^H\right] dk_\rho \\ &- \cos 2\phi \int_0^\infty \left[(F_2 - F_2^A - F_2^H) + (F_2^A - F_2^H) + 2F_2^H\right] dk_\rho \\ &= I_{0,1} + I_{0,2} + 2I_0^H - \cos 2\phi (I_{2,1} + I_{2,2} + 2I_2^H) \end{aligned} \tag{5.67a}$$

with

$$I_{0,1} = \int_0^\infty (F_0 - F_0^A - F_0^H)dk_\rho \tag{5.67b}$$

$$I_{0,2} = \int_0^\infty (F_0^A - F_0^H) dk_\rho \tag{5.67c}$$

$$I_{2,1} = \int_0^\infty (F_2 - F_2^A - F_2^H) dk_\rho \tag{5.67d}$$

$$I_{2,2} = \int_0^\infty (F_2^A - F_2^H) dk_\rho \tag{5.67e}$$

Figure 5.19 shows graphs of the various substrate integrands F_0, F_0^H and F_0^A as well as the difference functions $F_0 - F_0^A - F_0^H$ and $F_0^A - F_0^H$ that are the integrands in Eqs. (5.67b) and (5.67c) respectively. The graphs were calculated at f = 10 GHz for ρ = 20 mm, h_1 = 0.813 mm = 0.05λ_d, h_2 = 5 mm = λ_0/6, ϵ_{r1} = 3.38, and ϵ_{r2} = 1 (*i.e.*, Substrate I of Section 5.4.2.1 below; ρ is in the vicinity of λ_{CPW}, the wavelength at 10 GHz of a 50 Ω CPW on Substrate I). Figure 5.20 shows the corresponding graphs of F_2, F_2^H and F_2^A and the difference functions $F_2 - F_2^A - F_2^H$ and $F_2^A - F_2^H$ that are the integrands in Eqs. (5.67d) and (5.67e). Similar graphs for $\rho = 64.5$ mm $= 3\lambda_{CPW}$ are given in Figs. 5.21 and 5.22.

While the integrands F_i, F_i^H and F_i^A where $i = 0$ or 2 are singular in the sense that they increase indefinitely as $k_\rho \to \infty$, the difference functions $F_i - F_i^A - F_i^H$ and $F_i^A - F_i^H$ are decaying oscillating functions for $k_\rho > k_1$ that converge relatively quickly (*i.e.*, compared to the Sommerfeld integral tails in the TM case). Hence the integrals $I_{0,1}$, $I_{0,2}$, $I_{2,1}$, and $I_{2,2}$ were repeatedly evaluated with finite but increasing upper bounds $k_{\rho,upper}$ in the manner of the TM Region *3* integrals of Section 5.3.1, until increasing the upper bound further made no significant difference to the answer; a maximum upper bound of $k_{\rho,upper} = 200k_0$ was sufficient. It should be noted that Eq. (5.67a) can be implemented only because closed-form expressions for I_0^H and I_2^H in its third and sixth terms are available (*cf.* Eq. (5.62)).

Since the integrals $I_{0,1}$, $I_{0,2}$, $I_{2,1}$, and $I_{2,2}$ in Eq. (5.67) are functions of ρ only, it is sufficient to evaluate them once for a suitable range of ρ and then store the resulting values in a lookup table from where they can be retrieved and/or interpolated in the course of evaluating Y_{12}^{int}.

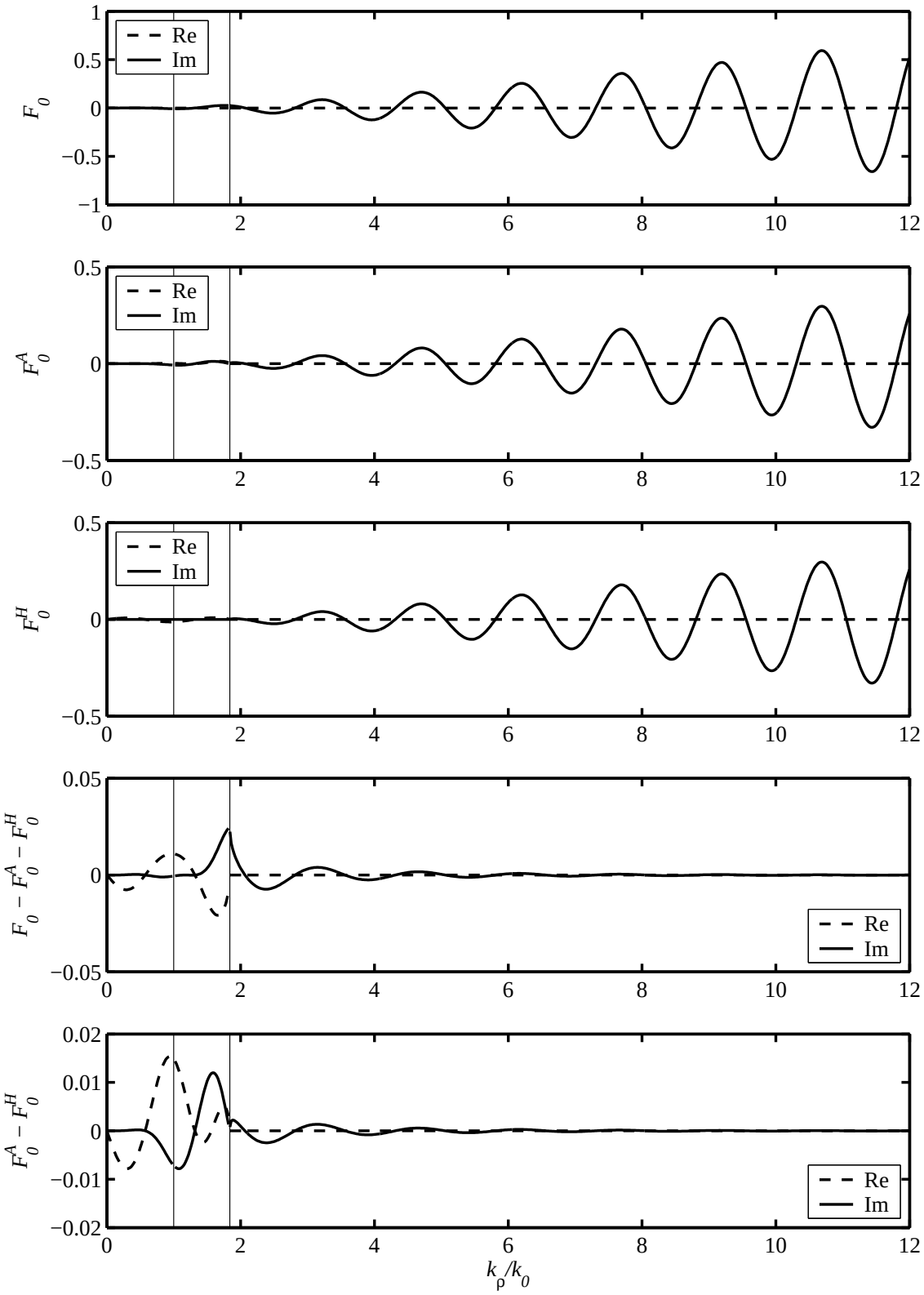

FIGURE 5.19: Plots of the TE integrands $F_0 - F_0^A - F_0^H$ and $F_0^A - F_0^H$, and their constituent functions F_0, F_0^A, and F_0^H. The vertical lines (from left to right) correspond to $k_\rho = k_2$ and $k_\rho = k_1$ respectively. f = 10 GHz, ρ = 20 mm, h_1 = 0.813 mm = 0.05λ_d, h_2 = 5 mm = λ_0/6, ϵ_{r1} = 3.38, ϵ_{r2} = 1.

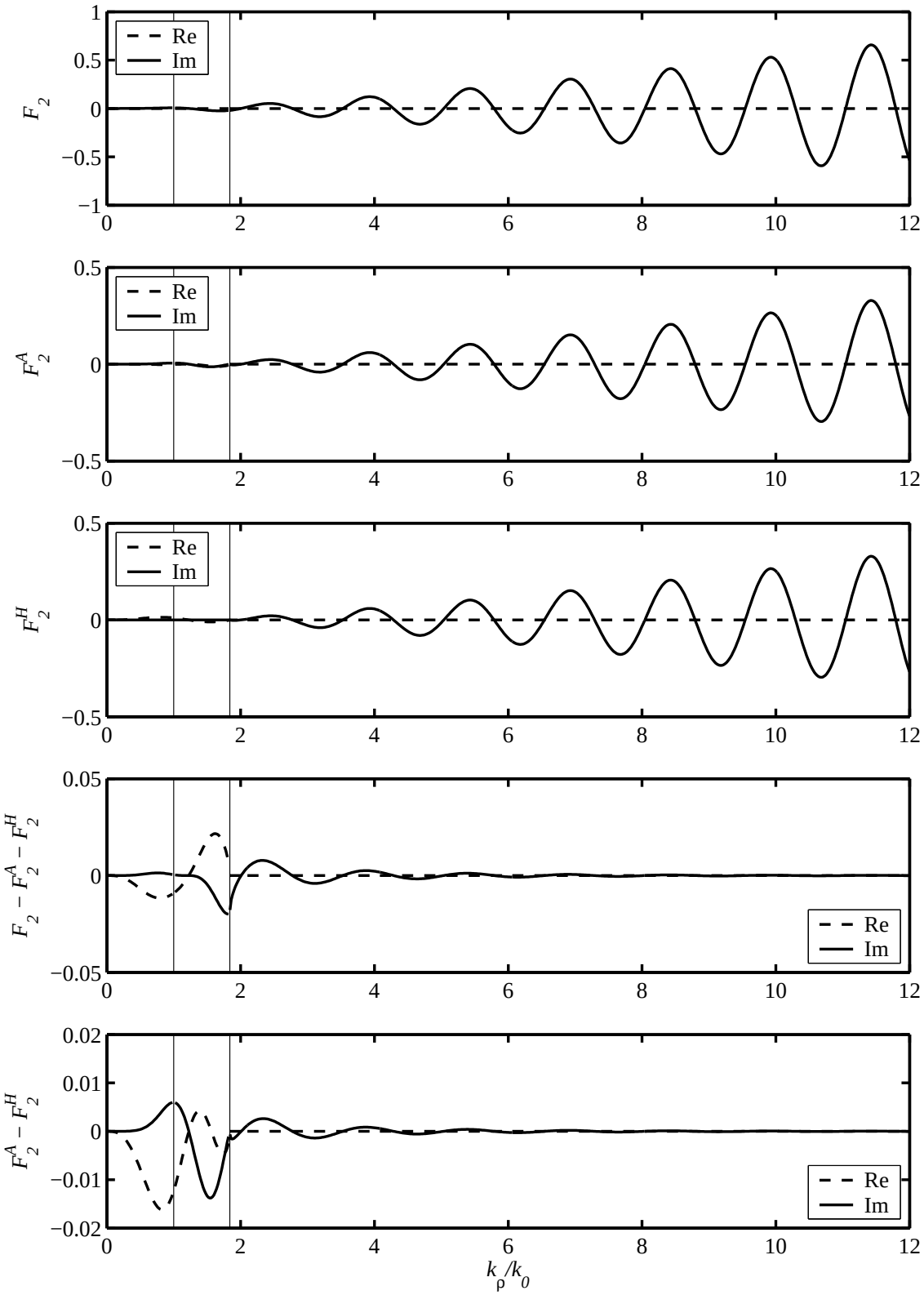

FIGURE 5.20: Plots of the TE integrands $F_2 - F_2^A - F_2^H$ and $F_2^A - F_2^H$, and their constituent functions F_2, F_2^A, and F_2^H. The vertical lines (from left to right) correspond to $k_\rho = k_2$ and $k_\rho = k_1$ respectively. f = 10 GHz, ρ = 20 mm, h_1 = 0.813 mm = 0.05λ_d, h_2 = 5 mm = λ_0/6, ϵ_{r1} = 3.38, ϵ_{r2} = 1.

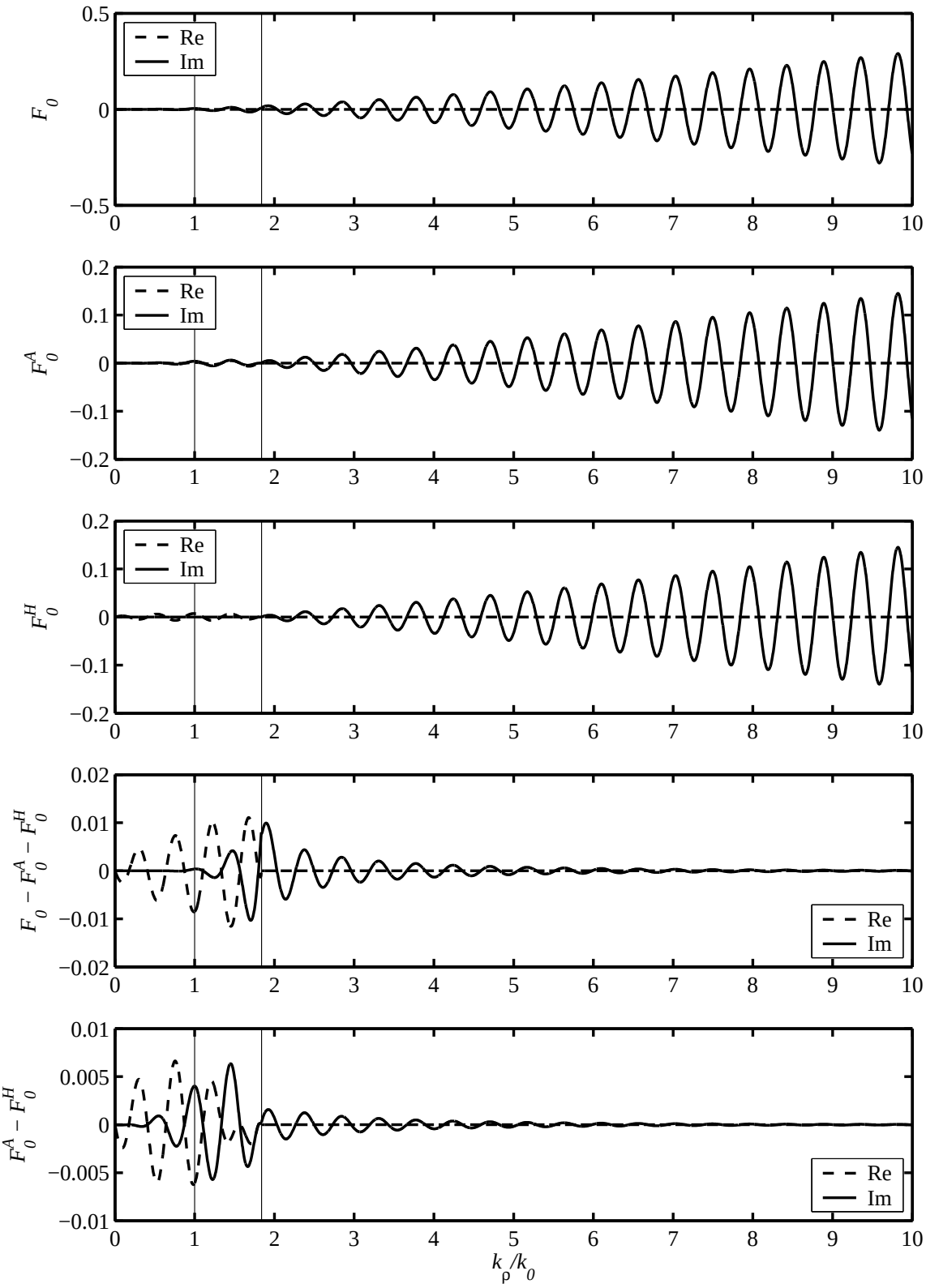

FIGURE 5.21: Plots of the TE integrands $F_0 - F_0^A - F_0^H$ and $F_0^A - F_0^H$, and their constituent functions F_0, F_0^A, and F_0^H. The vertical lines (from left to right) correspond to $k_\rho = k_2$ and $k_\rho = k_1$ respectively. f = 10 GHz, ρ = 64.5 mm, h_1 = 0.813 mm = 0.05λ_d, h_2 = 5 mm = λ_0/6, ϵ_{r1} = 3.38, ϵ_{r2} = 1.

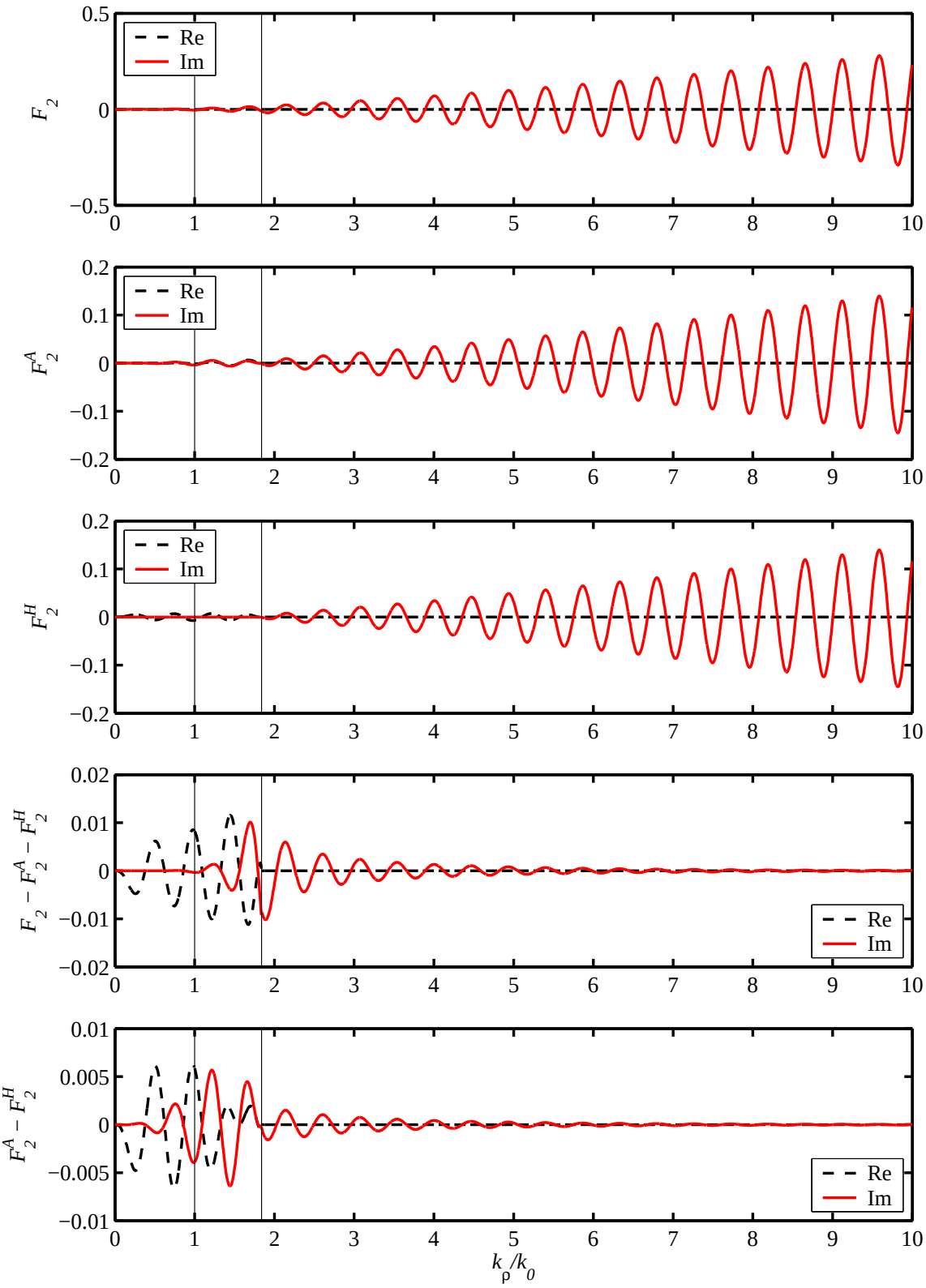

FIGURE 5.22: Plots of the TE integrands $F_2 - F_2^A - F_2^H$ and $F_2^A - F_2^H$, and their constituent functions F_2, F_2^A, and F_2^H. The vertical lines (from left to right) correspond to $k_\rho = k_2$ and $k_\rho = k_1$ respectively. f = 10 GHz, ρ = 64.5 mm, h_1 = 0.813 mm = 0.05λ_d, h_2 = 5 mm = λ_0/6, ϵ_{r1} = 3.38, ϵ_{r2} = 1.

5.4 IMPLEMENTATION AND RESULTS

5.4.1 Implementation strategy

The present section gives details of the implementation of the reciprocity-based formulation developed in Section 5.2 for finding the mutual admittance between broadside CPW-fed slots on a two-layer parallel-plate substrate. It is also described how the moment-method-based simulator IE3D was used to generate results against which the reciprocity-formulation results could be compared. The actual computed results are presented in Section 5.4.2.

Mutual admittance Y_{12} as a function of broadside inter-slot distance d was computed at 10 GHz for slots on three substrates, namely

- Substrate I: h_1 = 0.813 mm = 0.05λ_d; h_2 = 5 mm = λ_0/6; ϵ_{r1} = 3.38; ϵ_{r2} = 1
- Substrate II: h_1 = 1.21 mm = 0.1λ_d; h_2 = 5 mm = λ_0/6; ϵ_{r1} = 6.15; ϵ_{r2} = 1
- Substrate III: h_1 = 0.254 mm = 0.013λ_d; h_2 = 5 mm = λ_0/6; ϵ_{r1} = 2.2; ϵ_{r2} = 1

(in the above, λ_d is the wavelength in the top dielectric layer, and λ_0 the free-space wavelength at 10 GHz). Substrate I, the substrate chosen as reference, was used in an earlier successful implementation of an 8-element uniform linear CPW-fed array [36]. Substrates II and III had top dielectric layers that were electrically significantly thicker and thinner, respectively, than that of Substrate I, *i.e.*, 0.1λ_d and 0.013λ_d as opposed to 0.05λ_d. All substrates had an air bottom layer with an electric height of λ_0/6, and allowed for propagation of the TM_0 two-layer parallel-plate mode only.

Also computed was Y_{12} against frequency for a twin slot configuration on Substrate I where all dimensions including d were kept constant. This result was compared with a measurement to be discussed in Section 5.4.2.5.

Details of using IE3D to find Y_{12} against d for two CPW-fed slots on any of the above substrates at 10 GHz were as follows. Using a moment-method-based approach implies that the entire two-slot structure needs to be solved for each instance of d. Ports were defined at the ends of CPW feed lines that were $l_f = \lambda_{CPW}/2$ long; feed lines thus only extended as far as the terminal planes in Fig. 5.5 (λ_{CPW} is the CPW wavelength at 10 GHz). From the full-wave solution, IE3D calculates the two-port admittance matrix, or Y parameters of the structure referred to the above ports (choosing $l_f = \lambda_{CPW}/2$ ensured that Y parameters were referred to the centres of radiating slots). While $Y_{12} = Y_{21}$ was the parameter of interest, the two-port self-admittances $Y_{11} = Y_{22}$ were used in interpreting some of the results presented in Section 5.4.2. (A separation into external and internal

mutual admittances was of course not possible.)

When implementing the reciprocity-expression approach to find Y_{12} against d, each of the two CPW-fed slots were first simulated in isolation using IE3D.[18] The geometry of isolated CPW-fed slot m is shown in Fig. 5.23, where $m = 1$ or 2. The CPW feed line length was $l_f = \lambda_{CPW}/2$. In IE3D, a port was defined at the end of the feed line, which coincided with the terminal voltage reference plane mm', as noted in Section 5.2.2. Analyzing slot m in IE3D yielded the tangential electric field along the centre of the radiating slot, $\mathbf{E}_{m,slot} = E_{my,slot}\hat{y}$ (the longitudinal centre of the radiating slot coincides with the x axis in Fig. 5.23).[19] A discretization allowing for only one cell across the width of the radiating slot was adopted. This facilitated implementation of the simplifying assumption that the transverse component of the slot field was constant, having its longitudinal centre value across the width of the slot. The analysis also yielded the terminal voltage V_m at terminal plane mm'.

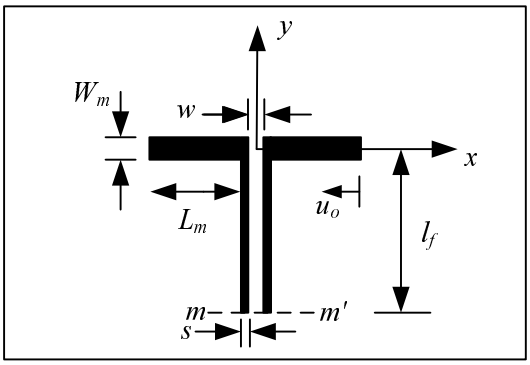

FIGURE 5.23: Top view of isolated CPW-fed slot m, where $m = 1$ or 2. $L_m \equiv$ half-length and $W_m \equiv$ width of radiating slot; $s \equiv$ slot width and $w \equiv$ centre strip width of feed line; $l_f \equiv$ length of feed line; $u_o \equiv$ distance from outer edge.

From the electric fields in the isolated slots, external and internal equivalent magnetic currents M_{1x}^{ext}, M_{2x}^{ext}, M_{1x}^{int}, and M_{2x}^{int} were obtained using Eqs. (5.4), (5.6), (5.10), and (5.11). M_{1x}^{ext} and M_{1x}^{int} are required to find H_{21x}^{ext} and H_{21x}^{int} using Eqs. (5.8a) and (5.13b) respectively. Subsequently, Y_{12}^{ext} and Y_{12}^{int} in Eqs. (5.7) and (5.12) were evaluated for each instance of slot separation d, and the total mutual admittance Y_{12} was found from $Y_{12} = Y_{12}^{ext} + Y_{12}^{int}$. In accordance with the definition of the quantities that constitute Eq. (5.2), M_{1x}^{ext}, M_{2x}^{ext}, M_{1x}^{int}, M_{2x}^{int}, V_1 and V_2 were kept the same for all values of d. The actual implementation of integrals in the preceding equations were done in Matlab using the NAG routine D01FCF [89].

[18] In the case of twin slots, only one slot needed to be simulated.
[19] As noted before, the $\hat{x}$-component of the field was considered negligible.

Further comment is in order regarding the terminal voltage V_m of an isolated slot m (*cf.* Fig. 5.23; $m = 1$ or 2). Consider first a narrow rectangular slot on an infinite ground plane in free space that is fed at its centre by means of two wires. The aperture tangential electric field can be be approximated in an accurate manner by a piecewise sinusoidal function. If the field is assumed constant across the width of the slot, the slot's terminal voltage is readily calculated as the product of the field at the centre of the slot, and the slot width. The calculation procedure does not depend on slot length;[20] the terminal voltage is always determined from the field value at the centre of the slot.

An exploratory numerical investigation was carried out to determine whether the terminal voltage of an isolated CPW-fed slot on a two-layer parallel-plate substrate (*i.e.*, the voltage seen at the reference plane mm' in Fig. 5.23) could be determined in a like manner from its radiating slot electric field. First, IE3D was used to design an isolated slot with a width $W = 0.4$ mm on Substrate I to be at its second resonance at 10 GHz; this resulted in a half-length of $L_{res} = 10.87$ mm and a resonant self-impedance of about 14 Ω (*cf.* Section 4.2.2). The CPW feed line was $l_f = \lambda_{CPW}/2$ long. Subsequently, IE3D was used to analyze eleven slots that were identical in all respects to the above resonant slot except for their half-lengths L that varied in the range $0.85L_{res} \leq L \leq 1.15L_{res}$ (as before, the moment-method discretization was done such that only one cell was allowed across the radiating slot width.) For each L, the longitudinal tangential electric field in the centre of the slot, as well as the port voltage V_t was recorded; the port was defined at the terminal plane mm' shown in Fig. 5.23 (the IE3D port voltage V_t is the same as the terminal voltage V_m, and includes the effect of the CPW-to-radiating-slot transition). The aim was to find out whether (and where) for a particular slot length a radiating slot voltage could be found that was equal to the (CPW slot) terminal voltage. Here, the radiating slot voltage V_{slot} at a position x in the slot is defined as $V_{slot}(x) = W \cdot E_{y,slot}(x)$, where $E_{y,slot}(x)\hat{y}$ is the slot tangential electric field (the field is assumed constant in the transverse direction). Hence, for each L, a $V^o_{slot} = V_{slot}(x_o)$ was determined, which was the value of $V_{slot}(x)$ closest to the terminal voltage V_t out of all possible $V_{slot}(x)$ (V^o_{slot} was located at $x = x_o$).

In Table 5.1, the position of V^o_{slot}, expressed as normalized distance from the radiating slot outer edge u_o/L (see Fig. 5.23), is listed against L/L_{res}. Two measures pertaining to the closeness between V^o_{slot} and V_t is also given. These reveal a generally close correspondence between V^o_{slot} and V_t; the biggest difference in magnitude occurred for $L = L_{res}$, where $|V^o_{slot}|$ was about 7% smaller than $|V_t|$. If the right half of the CPW-fed slot of Fig. 5.23 is considered, the position where V^o_{slot} must be "read off" coincides with the boundary between the CPW slot and radiating slot for all L. The implication is that, if the reciprocity-based expressions are intended to be used in an array design algorithm requiring multiple evaluations, it will be straightforward to establish terminal voltages once

[20] Center-fed slots in an infinite ground plane are normally assumed to operate around their first resonant lengths.

slot electric fields are known. Slot field information can be obtained at the same time lookup tables for the self-admittances of isolated slots are compiled via moment-method-based calculations (*e.g.*, [19, 35]). Alternatively, only the complex amplitude of the slot field (as opposed to the complete field distribution) can be obtained from the isolated slot analysis, and then used to scale generic functions that approximate the slot field; for example, it is relatively simple to relate piecewise sinusoidal functions to slot field magnitudes.

TABLE 5.1: Position in slot of radiating slot voltage closest to terminal voltage for various slot half-lengths, and difference between radiating slot voltage and terminal voltage. u_o is distance from the radiating slot outer edge. W = 0.4 mm; h_1 = 0.813 mm; h_2 = 5 mm; ϵ_{r1} = 3.38; ϵ_{r2} = 1.

$\frac{L}{L_{res}}$	$\frac{u_o}{L}$	$\frac{\lvert V_{slot}\rvert - \lvert V_t\rvert}{\lvert V_t\rvert}$ (%)	$\angle(V_{slot}) - \angle(V_t)$ (deg.)
0.85	1.00	3.7	-3.9
0.88	1.00	2.1	-4.2
0.91	1.00	-0.2	-4.3
0.94	1.00	-3.2	-3.7
0.97	1.00	-6.5	-1.8
1.00	1.00	-7.4	0.0
1.03	1.00	-5.9	1.7
1.06	0.99	-3.5	2.3
1.09	0.99	-1.6	2.1
1.12	0.99	-2.1	1.1
1.15	0.99	-1.2	0.8

5.4.2 Results

In this section, results are presented for the computation of Y_{12} against d for slots on Substrates I, II, and III (Sections 5.4.2.1, 5.4.2.2 and 5.4.2.3), and for Y_{12} against frequency for twin slots with a fixed spacing on Substrate I (Section 5.4.2.5). In all cases, results obtained using the reciprocity-expression approach are compared to moment-method-based results computed using IE3D.

5.4.2.1 Substrate I: $h_1 = 0.05\lambda_d$, $h_2 = \lambda_0/6$, ϵ_{r1} = 3.38, ϵ_{r2} = 1

A 50 Ω CPW feed line was designed on this substrate in IE3D with $w = 3.7$ mm and $s = 0.2$ mm (*cf.* Section 4.2.2). Subsequently, an isolated CPW-fed slot with a width W of 0.4 mm was designed to operate at its second resonance at 10 GHz, resulting in a half-length $L = L_{res} = 10.87$ mm and a

resonant self-impedance of about 14 Ω.

Mutual admittance Y_{12} against distance d with $0.9\lambda_{CPW} \leq d \leq 3\lambda_{CPW}$ was computed for four pairs of identical broadside slots, *i.e.*, twin slots, based on the above slot (λ_{CPW} is the CPW wavelength at 10 GHz). While all four pairs had $W_1 = W_2 = 0.4$ mm, their half-lengths $L_1 = L_2$ were $0.85L_{res}$, $0.95L_{res}$, L_{res}, and $1.1L_{res}$.[21] In all cases, feed line lengths were $l_f = 0.5\lambda_{CPW}$.

The real and imaginary parts of the mutual admittance Y_{12} against normalized broadside distance d/λ_{CPW} for twin slots with $L_1 = L_2 = 0.85L_{res}$ = 9.24 mm are shown in Fig. 5.24; results from both the reciprocity-expression approach and IE3D are represented. Likewise, Y_{12} for twin slots with $L_1 = L_2 = 0.95L_{res}$ = 10.33 mm, $L_1 = L_2 = L_{res}$ = 10.87 mm, and $L_1 = L_2 = 1.1L_{res}$ = 11.96 mm are shown in Figs. 5.25, 5.26, and 5.29 respectively. For the case $L_1 = L_2 = L_{res}$, Figs. 5.27 and 5.28 show the magnitude and phase of Y_{12} against d/λ_{CPW}.

Figs. 5.24–5.29 reveal close agreement between Y_{12} computed using the reciprocity-expression approach, and IE3D. Agreement is very good for twin slots with half-lengths $L = 0.85L_{res}$, and somewhat less so for the cases $L_1 = L_2 = 0.95L_{res}$, $1.1L_{res}$, and L_{res} in order of decreasing goodness of agreement. Especially in the case $L_1 = L_2 = L_{res}$, IE3D curves seem visually "irregular" in the sense that each appears like a version of the corresponding curve from the reciprocity-expression approach with some oscillation superimposed (*cf.* Figs. 5.26 and 5.27)[22] – this is true to a lesser extent of the cases $L = 1.1L_{res}$ and $L = 0.95L_{res}$.

In order to investigate the above differences further, two-port self-admittances $Y_{11} = Y_{22}$ calculated by IE3D were considered in conjunction with the Y_{12} curves of Figs. 5.24–5.29. Fig. 5.30 shows the real and imaginary parts of the two-port self-admittance Y_{11} against broadside distance d/λ_{CPW} for the case $L_1 = L_2 = L_{res}$ at 10 GHz. The (resonant) self-admittance of the corresponding isolated slot, $Y_{self} = 72$ mS computed using IE3D is also shown; it can be seen that Y_{11} takes the form of a decaying oscillation about Y_{self}. Fig. 5.31 displays the magnitude of Y_{11} against d/λ_{CPW}, as well as $|Y_{self}|$; Fig. 5.32 gives the corresponding phases. As d increases, Y_{11} approaches Y_{self}, as expected. Similarly, Fig. 5.33 shows $|Y_{11}|$ against d/λ_{CPW} for the case $L_1 = L_2 = 0.85L_{res}$, and $|Y_{self}|$ for an isolated $0.85L_{res}$ slot, which has $Y_{self} = 29.2\angle 52°$ mS (again computed using IE3D); corresponding phases are given in Fig. 5.34. Magnitude and phase curves for the case $L_1 = L_2 = 1.1L_{res}$ are presented in Figs. 5.35 and Fig. 5.36. For an isolated $1.1L_{res}$ slot, $Y_{self} = 50.5\angle -53.7°$ mS.

[21] Only broadside slots were investigated as this is the configuration relevant to series-fed linear array designs [35, 36].
[22] This was noted previously in Section 4.2.3.

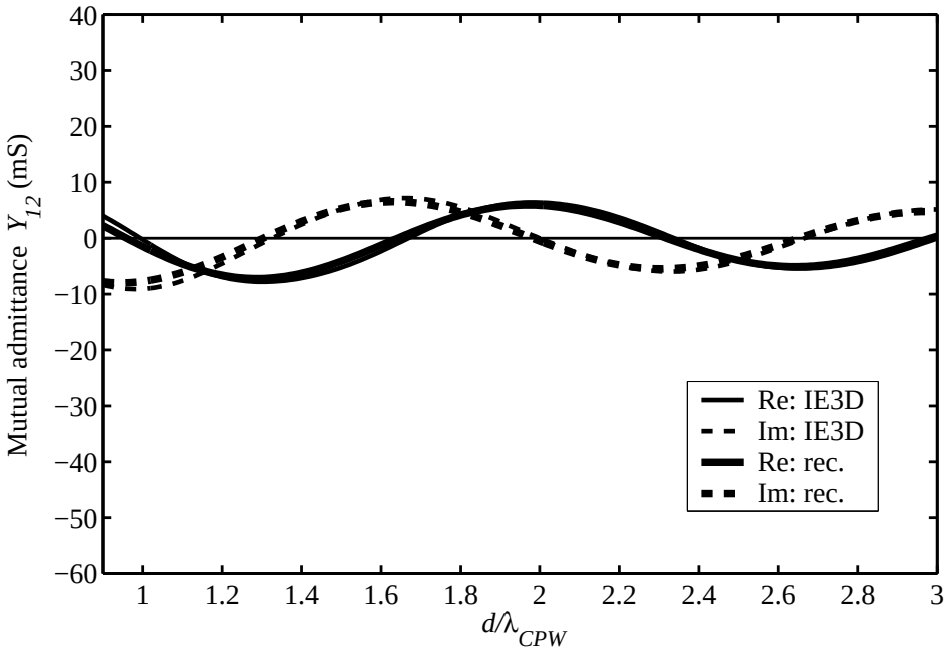

FIGURE 5.24: Mutual admittance Y_{12} against broadside distance d/λ_{CPW} at 10 GHz for CPW-fed twin slots with $L_1 = L_2 = 0.85L_{res}$ = 9.24 mm on Substrate I. $W_1 = W_2$ = 0.4 mm; h_1 = 0.813 mm; h_2 = 5 mm; ϵ_{r1} = 3.38; ϵ_{r2} = 1; $l_f = 0.5\lambda_{CPW}$. (rec.: computed using reciprocity-expression approach.)

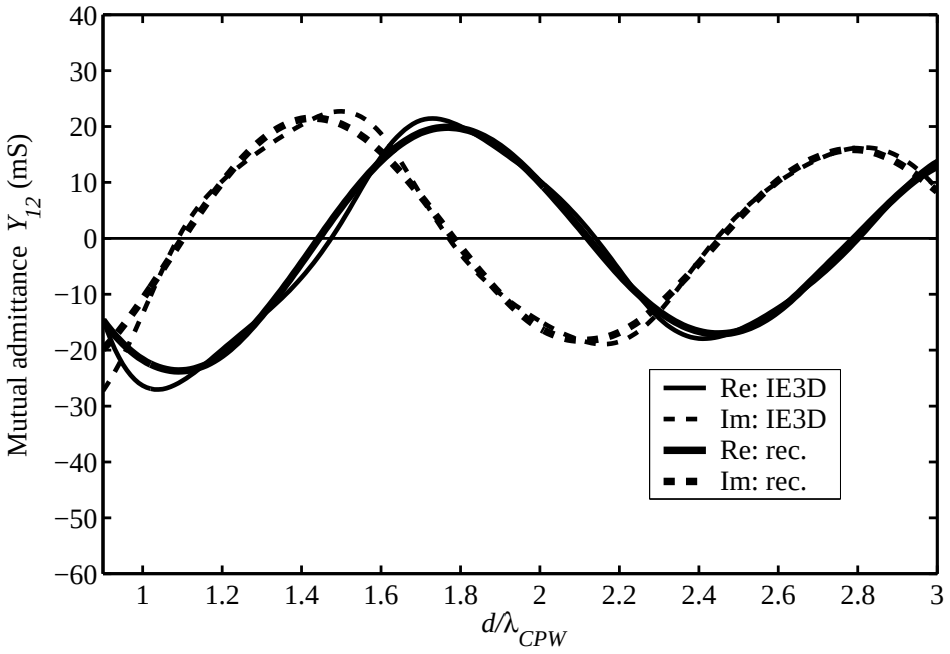

FIGURE 5.25: Mutual admittance Y_{12} against broadside distance d/λ_{CPW} at 10 GHz for CPW-fed twin slots with $L_1 = L_2 = 0.95L_{res}$ = 10.33 mm on Substrate I. $W_1 = W_2$ = 0.4 mm; h_1 = 0.813 mm; h_2 = 5 mm; ϵ_{r1} = 3.38; ϵ_{r2} = 1; $l_f = 0.5\lambda_{CPW}$.

In accordance with Eq. (5.2), the reciprocity-expression approach utilizes magnetic currents

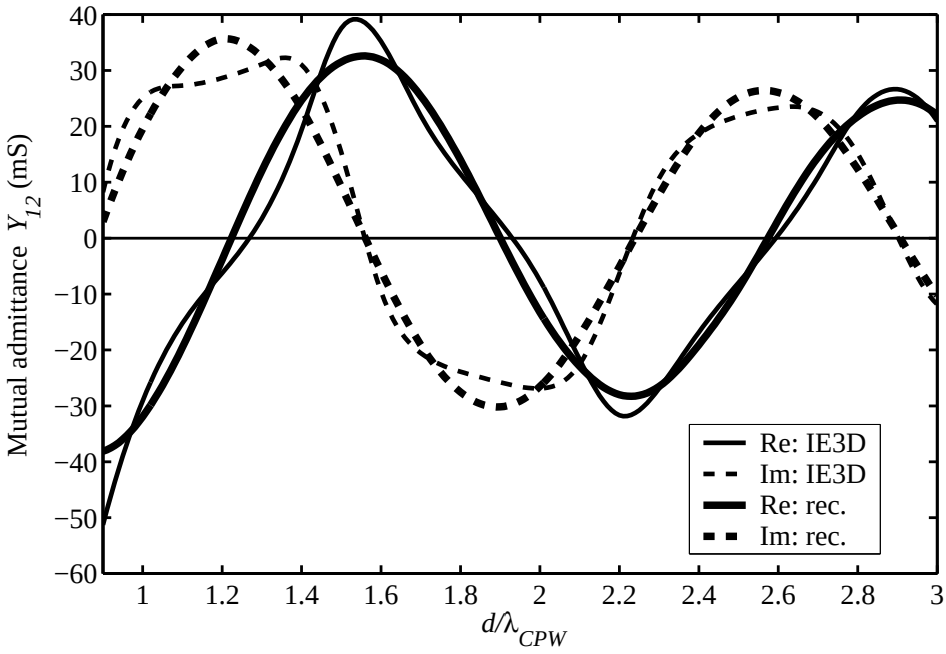

FIGURE 5.26: Mutual admittance Y_{12} against broadside distance d/λ_{CPW} at 10 GHz for CPW-fed twin slots with $L_1 = L_2 = L_{res}$ = 10.87 mm on Substrate I. $W_1 = W_2$ = 0.4 mm; h_1 = 0.813 mm; h_2 = 5 mm; ϵ_{r1} = 3.38; ϵ_{r2} = 1; $l_f = 0.5\lambda_{CPW}$.

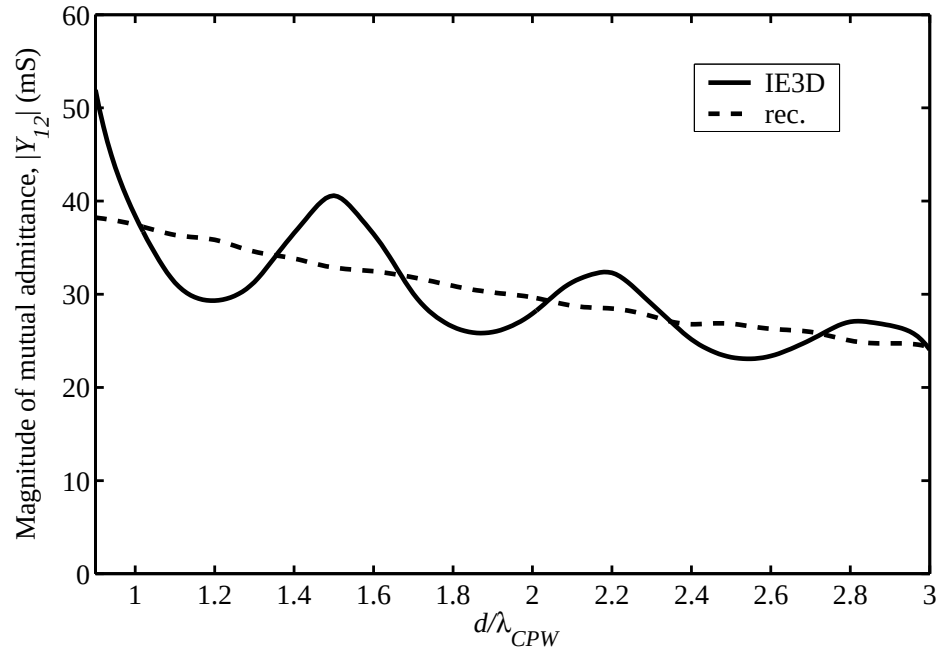

FIGURE 5.27: Magnitude of mutual admittance Y_{12} against broadside distance d/λ_{CPW} at 10 GHz for CPW-fed twin slots with $L_1 = L_2 = L_{res}$ = 10.87 mm on Substrate I. $W_1 = W_2$ = 0.4 mm; h_1 = 0.813 mm; h_2 = 5 mm; ϵ_{r1} = 3.38; ϵ_{r2} = 1; $l_f = 0.5\lambda_{CPW}$.

associated with slots radiating in isolation, *i.e.*, impressed currents; the underlying assumption is that slot self-admittances do not change with d. The two-port self-admittances computed by IE3D,

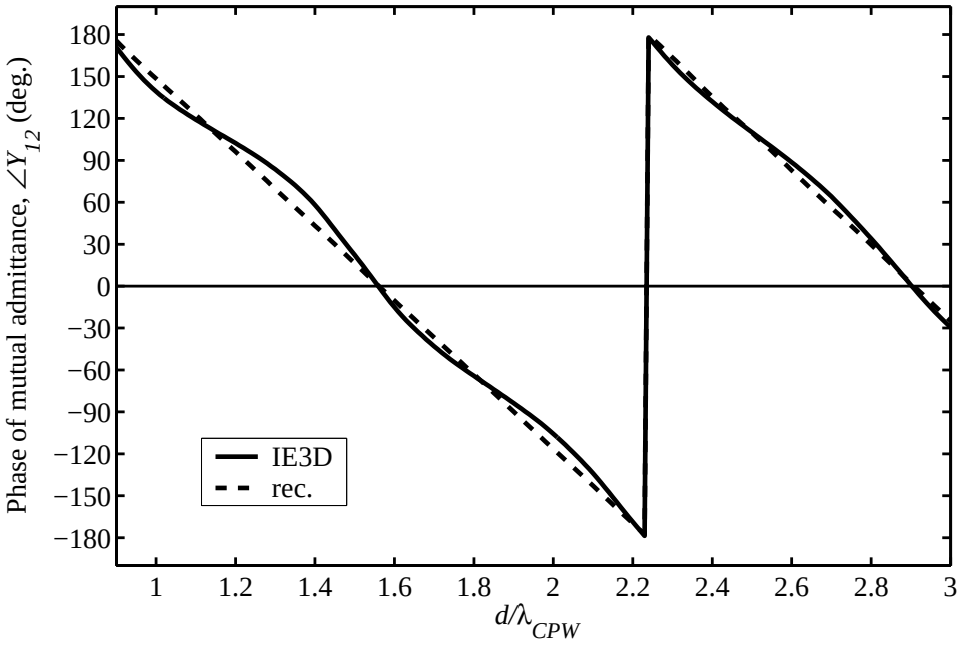

FIGURE 5.28: Phase of mutual admittance Y_{12} against broadside distance d/λ_{CPW} at 10 GHz for CPW-fed twin slots with $L_1 = L_2 = L_{res}$ = 10.87 mm on Substrate I. W_1 = W_2 = 0.4 mm; h_1 = 0.813 mm; h_2 = 5 mm; ϵ_{r1} = 3.38; ϵ_{r2} = 1; $l_f = 0.5\lambda_{CPW}$.

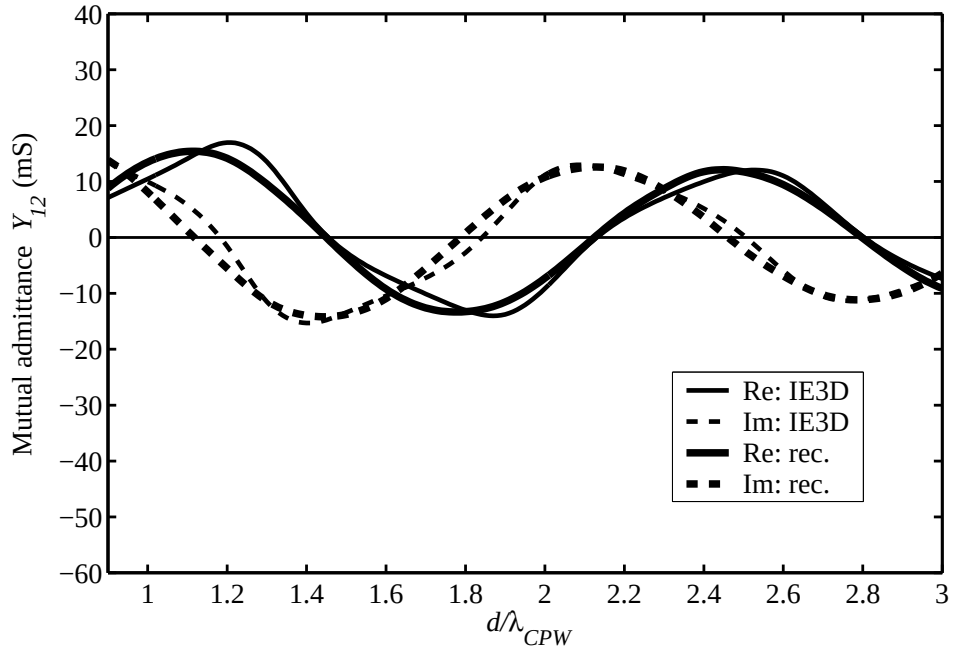

FIGURE 5.29: Mutual admittance Y_{12} against broadside distance d/λ_{CPW} at 10 GHz for CPW-fed twin slots with L_1 = L_2 = 1.1L_{res} = 11.96 mm on Substrate I. W_1 = W_2 = 0.4 mm; h_1 = 0.813 mm; h_2 = 5 mm; ϵ_{r1} = 3.38; ϵ_{r2} = 1; $l_f = 0.5\lambda_{CPW}$.

however, appear to oscillate about the self-admittances of the isolated slots. This is most marked for the case $L_1 = L_2 = L_{res}$ as seen in the magnitude plot of Fig. 5.31, and (considerably) less so

for the cases $L_1 = L_2 = 0.85L_{res}$ and $L_1 = L_2 = 1.1L_{res}$ in Figs. 5.33 and 5.35 respectively. The extent of the oscillations are mirrored by the extent of the apparent "superimposed oscillations" of the IE3D Y_{12} curves: it is the most marked for the case $L_1 = L_2 = L_{res}$, and least significant for $L_1 = L_2 = 0.85L_{res}$; furthermore, $|Y_{11}|$ and $|Y_{12}|$ oscillations appear to be synchronized (*e.g.*, Figs. 5.31 and 5.27). Hence discrepancies between IE3D and the reciprocity-expression approach for Y_{12} can be related to different accounts for slot self-admittances in the two models.

In order to subject the reciprocity-expression approach to further verification, the mutual admittance between two pairs of non-identical slots were computed. Fig. 5.37 shows the real and imaginary parts of Y_{12} for the first pair, which had $L_1 = 0.85L_{res}$, $L_2 = 1.1L_{res}$, and $W_1 = W_2$ = 0.4 mm. The second pair had $L_1 = 0.85L_{res}$, $L_2 = L_{res}$, and $W_1 = W_2$ = 0.4 mm; these results are displayed in Fig. 5.38. Good agreement is observed between results obtained using the reciprocity-expression approach and IE3D.

The reciprocity-expression approach can be used to form an estimate of the relative contributions of external and internal mutual admittances to the total mutual admittance; the external and internal admittances can be expressed as $Y_{12}^{ext} = G_{12}^{ext} + jB_{12}^{ext}$ and $Y_{12}^{int} = G_{12}^{int} + jB_{12}^{int}$. Fig. 5.39(a)–(d) show Y_{12}^{ext} and Y_{12}^{int} for each of the cases $L_1 = L_2 = 0.85L_{res}$, $0.95L_{res}$, L_{res}, and $1.1L_{res}$. It is clear that the internal mutual admittance predominates. Fig. 5.40 shows the magnitudes of Y_{12}^{ext} and Y_{12}^{int} for the above cases on one graph. For each of the four half-lengths, the magnitude of the internal mutual admittance starts out at about 2.6 times the magnitude of the external mutual admittance. At the end of the range of d/λ_{CPW}, $|Y_{12}^{int}|$ is about five times the value of $|Y_{12}^{ext}|$. This is not unexpected since $|Y_{12}^{int}|$ is determined by guided fields, unlike $|Y_{12}^{ext}|$.

5.4.2.2 Substrate II: $h_1 = 0.1\lambda_d$, $h_2 = \lambda_0/6$, ϵ_{r1} = 6.15, ϵ_{r2} = 1

The top layer of Substrate II has the greatest electrical thickness of the three substrates, namely $0.1\lambda_d$ compared to $0.05\lambda_d$ of Substrate I and $0.013\lambda_d$ of Substrate II. It is included here for purposes of verification of the reciprocity-expression approach, and would not be a substrate of choice for antenna applications over Substrates I and III that have lower effective dielectric permittivities and hence greater radiation efficiency (*cf.* Chapters 2 and 3). The procedure for presentation and organization of results essentially follows that of the previous section. A 50 Ω CPW feed line was designed on Substrate II with $w = 0.68$ mm and $s = 0.15$ mm. Next, an isolated CPW-fed radiating slot with a width W of 0.7 mm was designed to operate at its second resonance at 10 GHz by adjusting its half-length to $L = L_{res} = 7.77$ mm; its resonant self-impedance was about 10 Ω.

The real and imaginary parts of the mutual admittance Y_{12} against normalized broadside

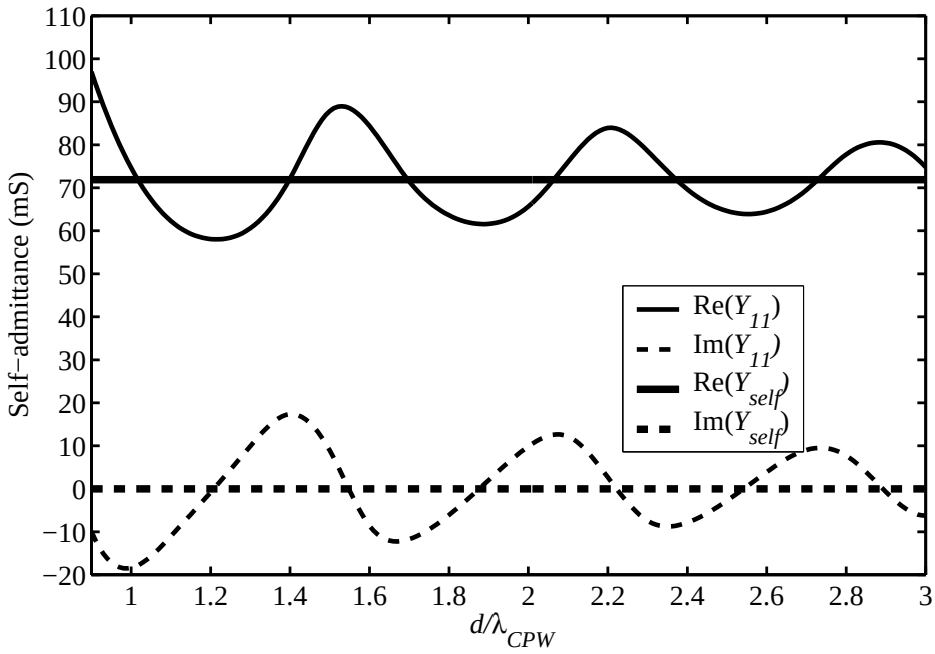

FIGURE 5.30: Two-port self-admittance Y_{11} against broadside distance d/λ_{CPW} for CPW-fed twin slots with $L_1 = L_2 = L_{res}$ = 10.87 mm on Substrate I, and resonant isolated self-admittance Y_{self} (both computed at 10 GHz with IE3D). $W_1 = W_2$ = 0.4 mm; h_1 = 0.813 mm; h_2 = 5 mm; ϵ_{r1} = 3.38; ϵ_{r2} = 1; $l_f = 0.5\lambda_{CPW}$.

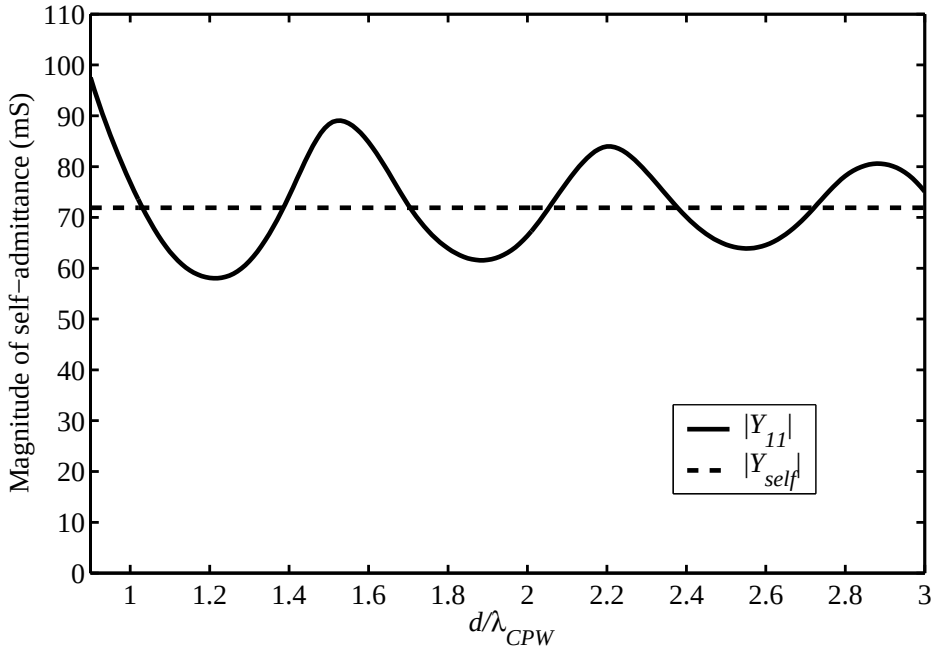

FIGURE 5.31: Magnitude of two-port self-admittance Y_{11} against broadside distance d/λ_{CPW} for CPW-fed twin slots with $L_1 = L_2 = L_{res}$ = 10.87 mm on Substrate I, and magnitude of resonant isolated self-admittance Y_{self} (both computed at 10 GHz with IE3D). $W_1 = W_2$ = 0.4 mm; h_1 = 0.813 mm; h_2 = 5 mm; ϵ_{r1} = 3.38; ϵ_{r2} = 1; $l_f = 0.5\lambda_{CPW}$.

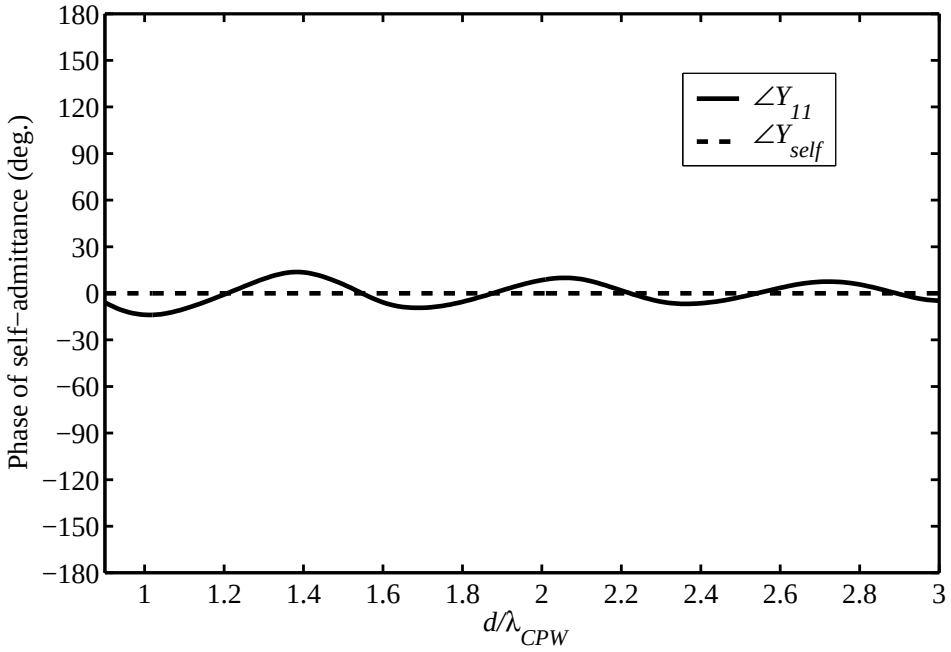

FIGURE 5.32: Phase of two-port self-admittance Y_{11} against broadside distance d/λ_{CPW} for CPW-fed twin slots with $L_1 = L_2 = L_{res}$ = 10.87 mm on Substrate I, and phase of resonant isolated self-admittance Y_{self} (both computed at 10 GHz with IE3D). $W_1 = W_2$ = 0.4 mm; h_1 = 0.813 mm; h_2 = 5 mm; ϵ_{r1} = 3.38; ϵ_{r2} = 1; $l_f = 0.5\lambda_{CPW}$.

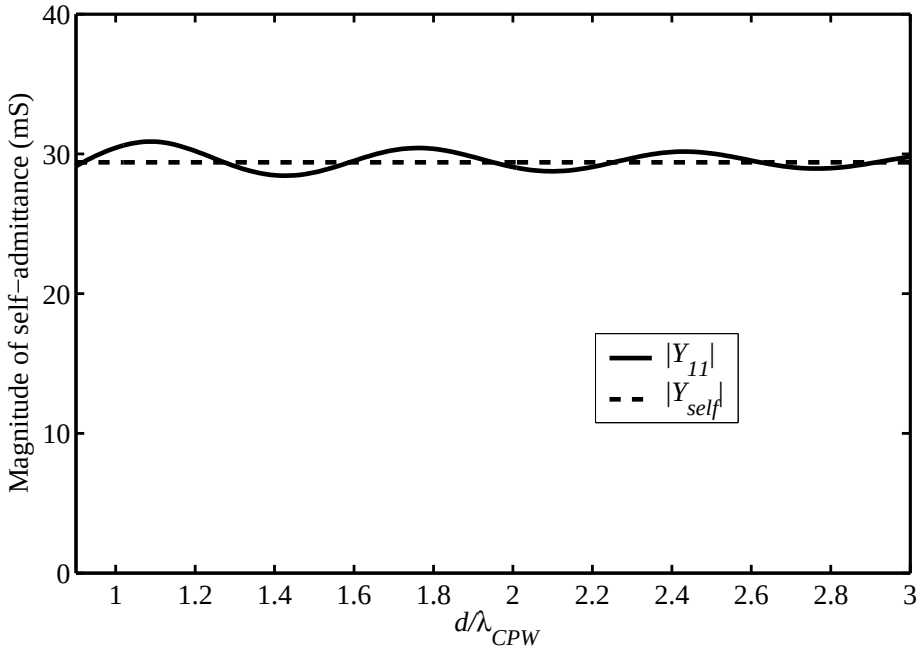

FIGURE 5.33: Magnitude of two-port self-admittance Y_{11} against broadside distance d/λ_{CPW} for CPW-fed twin slots with $L_1 = L_2 = 0.85L_{res}$ = 9.24 mm on Substrate I, and magnitude of resonant isolated self-admittance Y_{self} (both computed at 10 GHz with IE3D). $W_1 = W_2$ = 0.4 mm; h_1 = 0.813 mm; h_2 = 5 mm; ϵ_{r1} = 3.38; ϵ_{r2} = 1; $l_f = 0.5\lambda_{CPW}$.

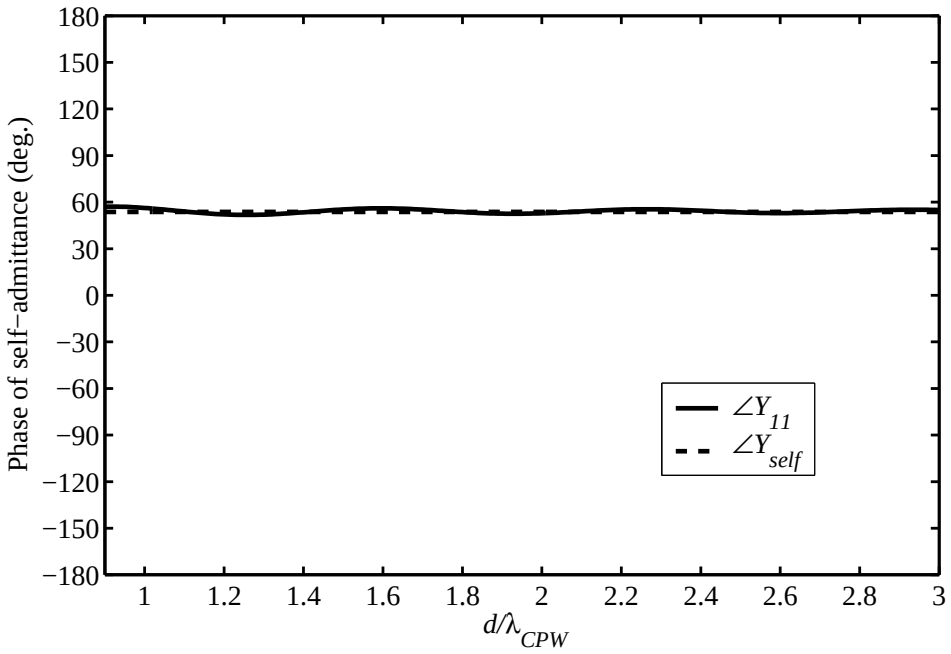

FIGURE 5.34: Phase of two-port self-admittance Y_{11} against broadside distance d/λ_{CPW} for CPW-fed twin slots with $L_1 = L_2 = 0.85L_{res} = 9.24$ mm on Substrate I, and phase of resonant isolated self-admittance Y_{self} (both computed at 10 GHz with IE3D). $W_1 = W_2 = 0.4$ mm; $h_1 = 0.813$ mm; $h_2 = 5$ mm; $\epsilon_{r1} = 3.38$; $\epsilon_{r2} = 1$; $l_f = 0.5\lambda_{CPW}$.

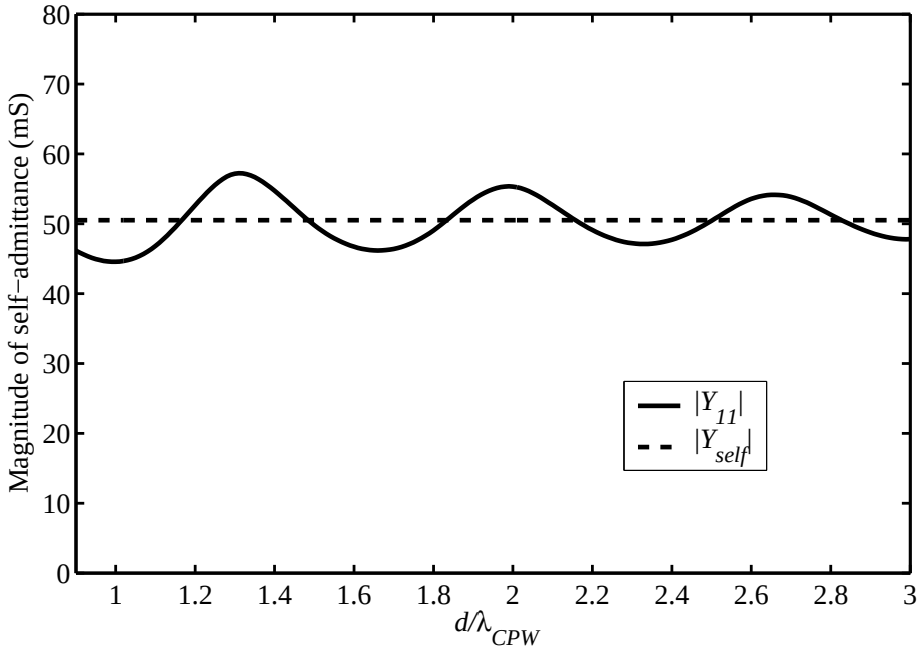

FIGURE 5.35: Magnitude of two-port self-admittance Y_{11} against broadside distance d/λ_{CPW} for CPW-fed twin slots with $L_1 = L_2 = 1.1L_{res} = 11.96$ mm on Substrate I, and magnitude of resonant isolated self-admittance Y_{self} (both computed at 10 GHz with IE3D). $W_1 = W_2 = 0.4$ mm; $h_1 = 0.813$ mm; $h_2 = 5$ mm; $\epsilon_{r1} = 3.38$; $\epsilon_{r2} = 1$; $l_f = 0.5\lambda_{CPW}$.

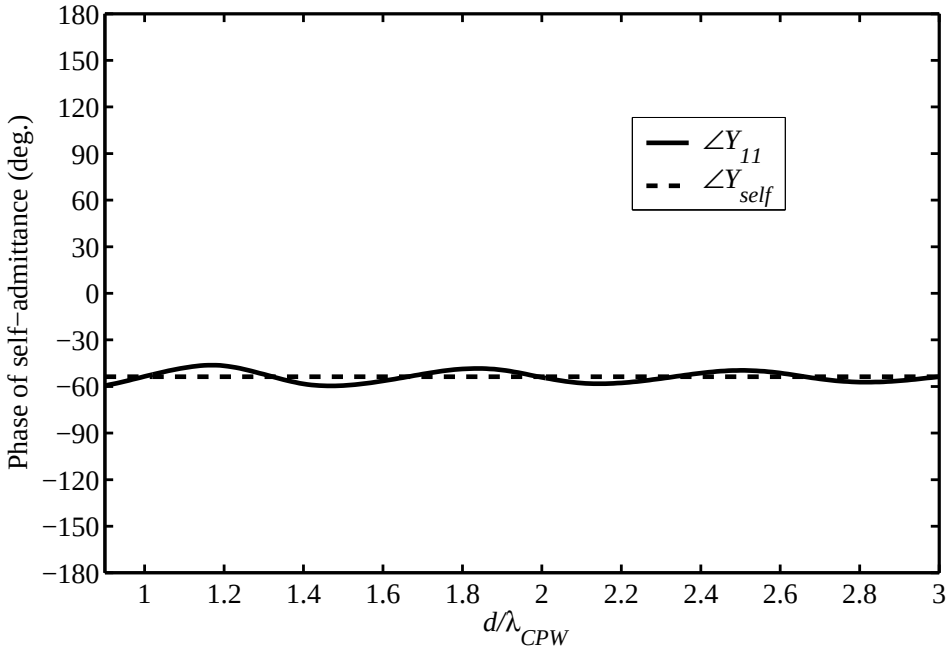

FIGURE 5.36: Phase of two-port self-admittance Y_{11} against broadside distance d/λ_{CPW} for CPW-fed twin slots with $L_1 = L_2 = 1.1L_{res}$ = 11.96 mm on Substrate I, and phase of resonant isolated self-admittance Y_{self} (both computed at 10 GHz with IE3D). $W_1 = W_2 = 0.4$ mm; $h_1 = 0.813$ mm; $h_2 = 5$ mm; $\epsilon_{r1} = 3.38$; $\epsilon_{r2} = 1$; $l_f = 0.5\lambda_{CPW}$.

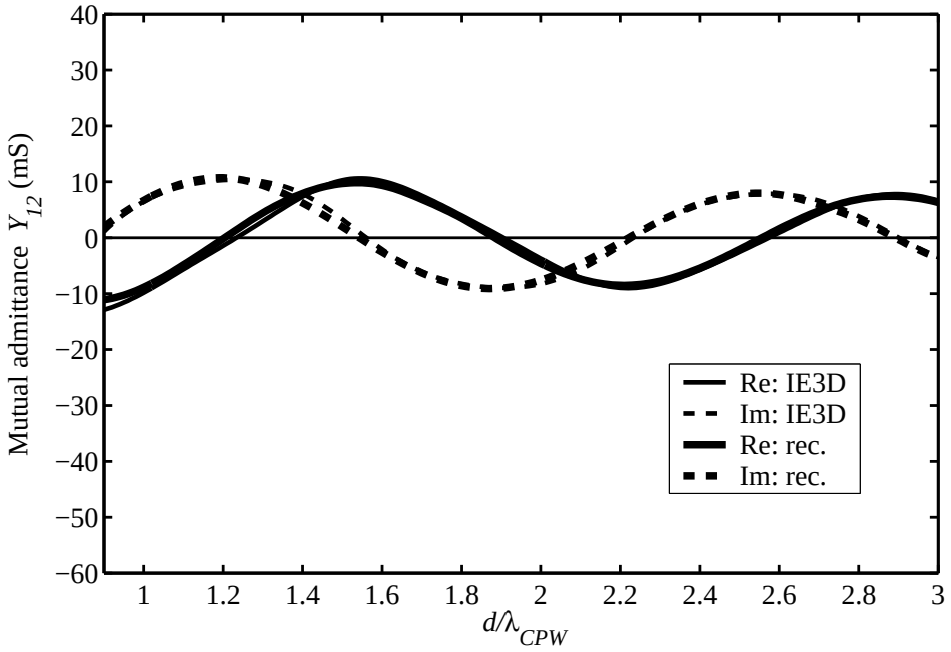

FIGURE 5.37: Mutual admittance Y_{12} against broadside distance d/λ_{CPW} at 10 GHz for *non-identical* CPW-fed broadside slots with $L_1 = 0.85L_{res} = 9.24$ mm and $L_2 = 1.1L_{res} = 11.96$ mm on Substrate I. $W_1 = W_2 = 0.4$ mm; $h_1 = 0.813$ mm; $h_2 = 5$ mm; $\epsilon_{r1} = 3.38$; $\epsilon_{r2} = 1$; $l_f = 0.5\lambda_{CPW}$.

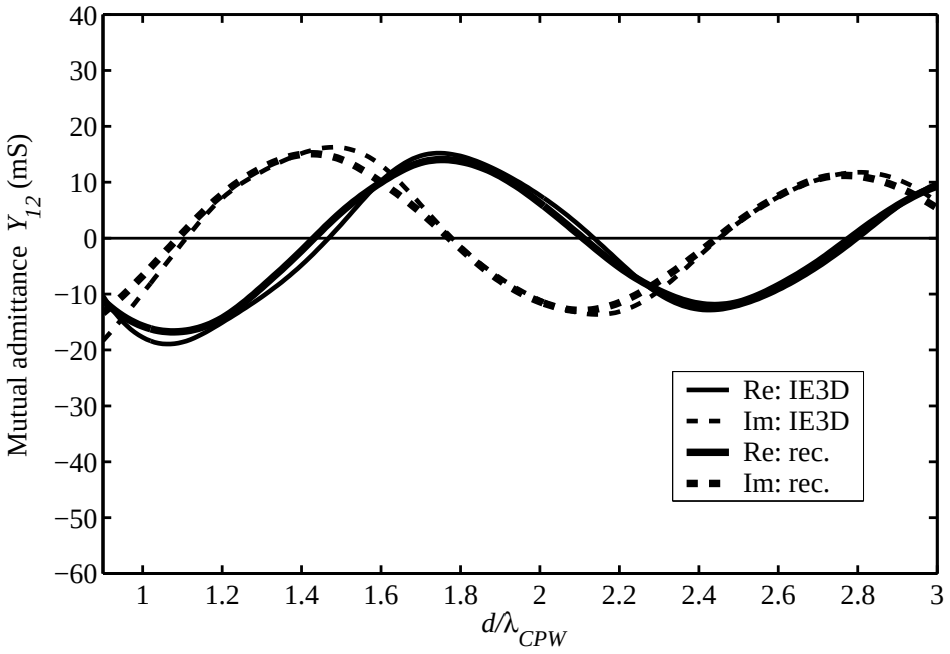

FIGURE 5.38: Mutual admittance Y_{12} against broadside distance d/λ_{CPW} at 10 GHz for *non-identical* CPW-fed broadside slots with $L_1 = 0.85L_{res} = 9.24$ mm and $L_2 = L_{res} = 10.87$ mm on Substrate I. W_1 = W_2 = 0.4 mm; h_1 = 0.813 mm; h_2 = 5 mm; ϵ_{r1} = 3.38; ϵ_{r2} = 1; $l_f = 0.5\lambda_{CPW}$.

distance d/λ_{CPW} for twin slots with $L_1 = L_2 = 0.9L_{res}$ = 6.99 mm computed using the reciprocity-expression approach and IE3D are shown in Fig. 5.41. Likewise, Y_{12} against d/λ_{CPW} for twin slots with $L_1 = L_2 = L_{res}$ = 7.77 mm, and $L_1 = L_2 = 1.1L_{res}$ = 8.55 mm are shown in Figs. 5.42 and 5.45 respectively. For the case $L_1 = L_2 = L_{res}$, Fig. 5.43 shows the magnitude of Y_{12} against d/λ_{CPW}, and Fig. 5.44 the phase. Feed line lengths were $l_f = 0.5\lambda_{CPW}$ throughout.

Figs. 5.41–5.45 shows a similar pattern of agreement between Y_{12} computed using the reciprocity expression and IE3D as in the case of Substrate I: agreement is best for the shortest twin slots, while for the L_{res} twin slots IE3D curves seem irregular when compared to the reciprocity-expression curves in a manner similar to that observed for L_{res} twin slots on Substrate I. However, in the case of Substrate II the irregularity seems more marked. In order to investigate this further, two-port self-admittances $Y_{11}(= Y_{22})$ calculated using IE3D were considered in conjunction with the Y_{12} curves of Figs. 5.41–5.45. Fig. 5.46 shows the real and imaginary parts of the two-port self-admittance Y_{11} against broadside distance d/λ_{CPW} for the case $L_1 = L_2 = L_{res}$ at 10 GHz. Fig. 5.47 shows the magnitude of Y_{11} against d/λ_{CPW}, as well as the magnitude of the resonant isolated self-admittance, $Y_{self} = 100$ mS, computed using IE3D as described earlier; Fig. 5.48 gives the corresponding phases. Similarly, Fig. 5.49 shows $|Y_{11}|$ against d/λ_{CPW} for the case $L_1 = L_2 = 0.9L_{res}$, and $|Y_{self}|$ for an isolated $0.9L_{res}$ slot, which has $Y_{self} = 45.4\angle 53°$ mS; corresponding phases are given in Fig. 5.50. Magnitude and phase curves for the case $L_1 = L_2 = 1.1L_{res}$ are presented in Figs. 5.51

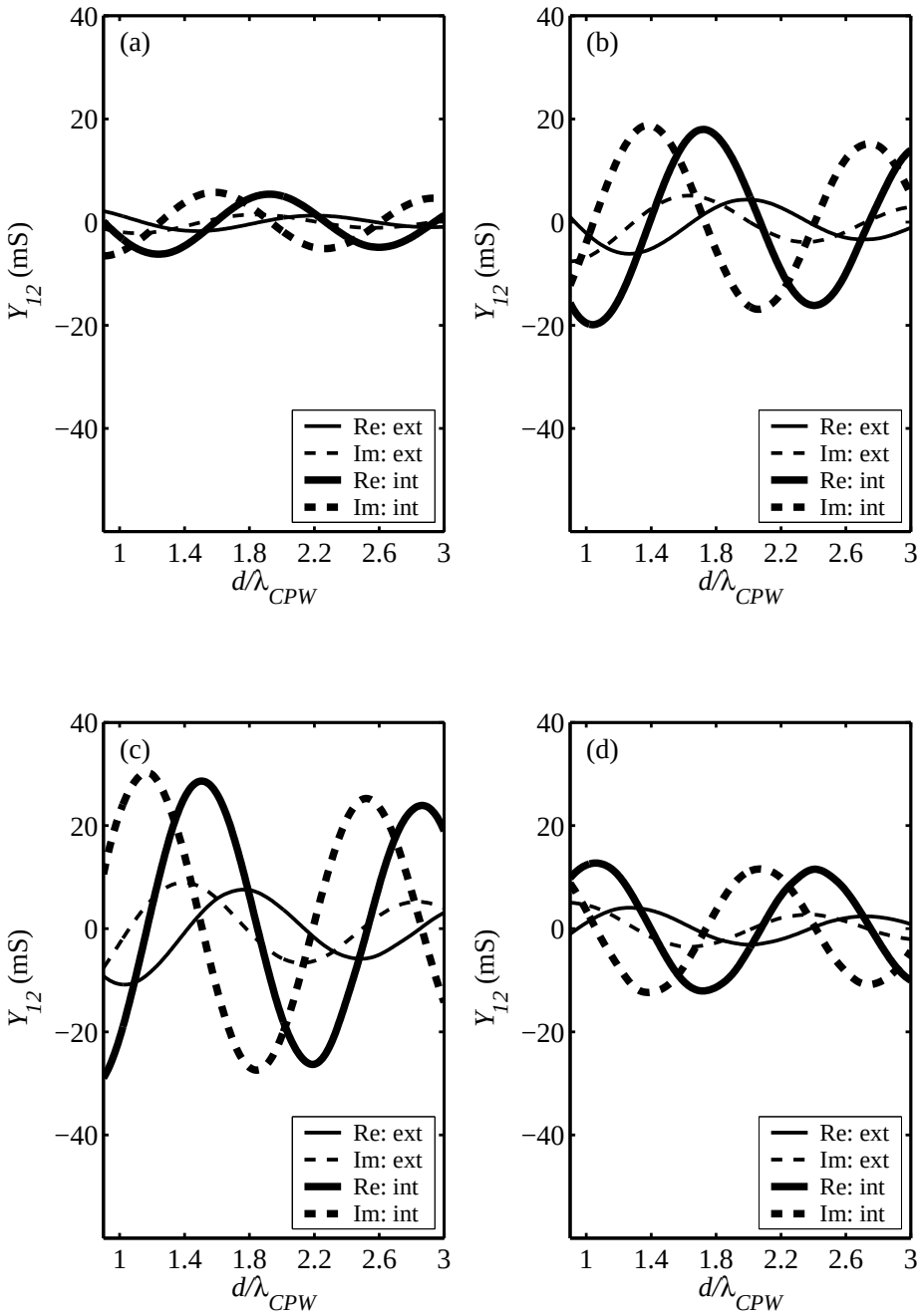

FIGURE 5.39: Y_{12}^{ext} and Y_{12}^{int} against d/λ_{CPW} computed using the reciprocity-expression approach for slots on Substrate I with (a) $L_1 = L_2 = 0.85L_{res}$, (b) $L_1 = L_2 = 0.95L_{res}$, (c) $L_1 = L_2 = L_{res}$, and (d) $L_1 = L_2 = 1.1L_{res}$. W_1 = W_2 = 0.4 mm; h_1 = 0.813 mm; h_2 = 5 mm; ϵ_{r1} = 3.38; ϵ_{r2} = 1; $l_f = 0.5\lambda_{CPW}$.

and Fig. 5.52. For an isolated $1.1L_{res}$ slot, $Y_{self} = 59.6\angle -60.9°$ mS.

As for slots on Substrate I, the two-port self-admittances computed by IE3D appear to oscillate with a decaying envelope about the self-admittances of the isolated slots that are assumed constant regardless of d in the reciprocity-expression approach. This is most apparent for the case

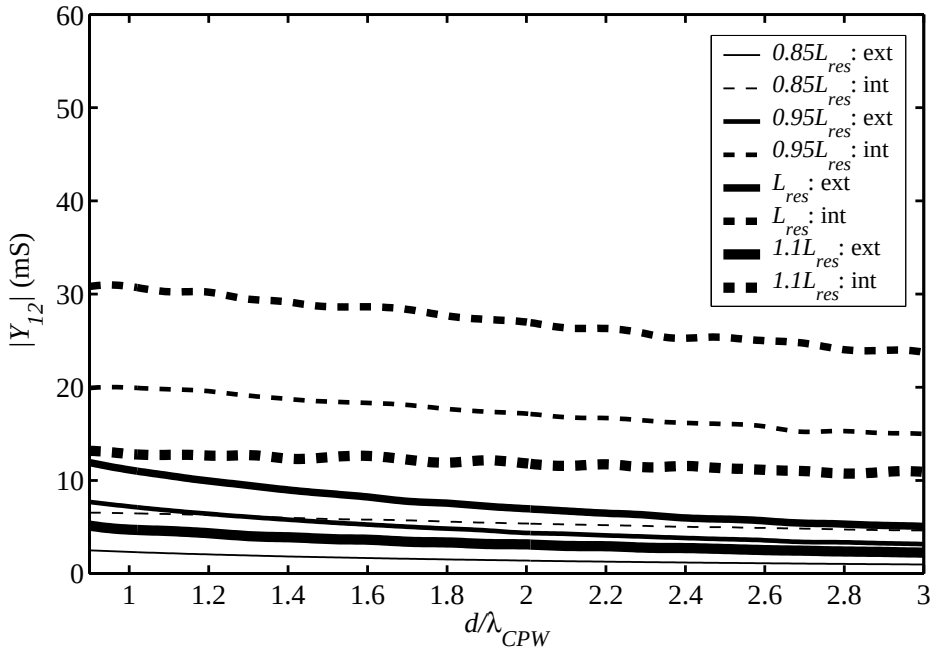

FIGURE 5.40: $|Y_{12}^{ext}|$ and $|Y_{12}^{int}|$ against d/λ_{CPW} for twin slots on Substrate I with $L_1 = L_2 = 0.85L_{res}$, $L_1 = L_2 = 0.95L_{res}$, $L_1 = L_2 = L_{res}$, and $L_1 = L_2 = 1.1L_{res}$. $W_1 = W_2 = 0.4$ mm; $h_1 = 0.813$ mm; $h_2 = 5$ mm; $\epsilon_{r1} = 3.38$; $\epsilon_{r2} = 1$; $l_f = 0.5\lambda_{CPW}$.

$L_1 = L_2 = L_{res}$ as seen in Fig. 5.47, and less so for the cases $L_1 = L_2 = 0.9L_{res}$ and $1.1L_{res}$ (Figs. 5.49 and 5.51). The extent of these oscillations are reflected in the "irregularities" of the IE3D curves for Y_{12} that are the most marked for the case $L_1 = L_2 = L_{res}$, and least significant for $L_1 = L_2 = 0.9L_{res}$; also, $|Y_{11}|$ and $|Y_{12}|$ oscillations appear to be synchronized. As before, discrepancies between IE3D and the reciprocity-expression approach for Y_{12} are consistent with differing accounts for self-admittances in the two models.

As noted previously, the reciprocity-expression approach allows for an estimation of the relative contributions of external and internal mutual admittances to the total mutual admittance,[23] and Fig. 5.53(a)–(c) show Y_{12}^{ext} and Y_{12}^{int} for each of the cases $L_1 = L_2 = 0.9L_{res}$, L_{res}, and $1.1L_{res}$. It is clear that the internal mutual admittance is the dominant contributor. Fig. 5.54 shows the magnitudes of Y_{12}^{ext} and Y_{12}^{int} for the above cases on one plot. It is seen that for each of the three slot half-lengths, the magnitude of the internal mutual admittance is about three times greater than that of the external mutual admittance when $d = 0.9\lambda_{CPW}$, and between five and six times greater when $d = 3\lambda_{CPW}$. Compared to the corresponding curves for Substrate I (*i.e.*, Fig. 5.39 and Fig. 5.40), the electrically thicker top layer of Substrate II appears to concentrate the fields more within it, resulting in greater coupling within the substrate (*cf.* [12]).

[23] The term "estimation" is particularly apt for the $L_1 = L_2 = L_{res}$ case; here the biggest difference is observed between the total mutual admittance obtained using IE3D and the reciprocity-expression approach.

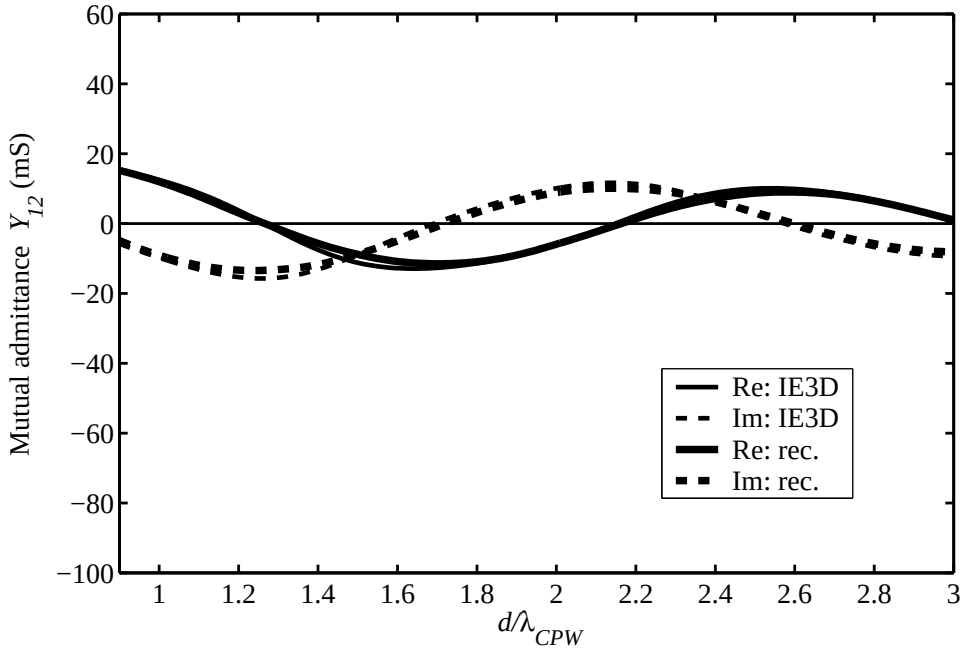

FIGURE 5.41: Mutual admittance Y_{12} against broadside distance d/λ_{CPW} at 10 GHz for CPW-fed twin slots with $L_1 = L_2 = 0.9L_{res} = 6.99$ mm on Substrate II. $W_1 = W_2 = 0.7$ mm; $h_1 = 1.21$ mm; $h_2 = 5$ mm; $\epsilon_{r1} = 6.15$; $\epsilon_{r2} = 1$; $l_f = 0.5\lambda_{CPW}$.

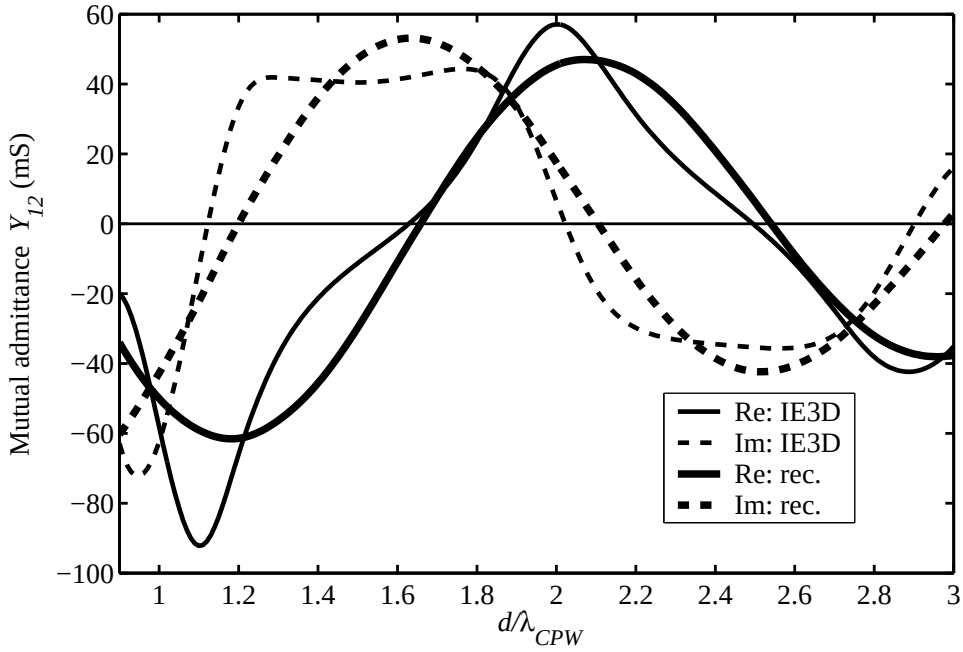

FIGURE 5.42: Mutual admittance Y_{12} against broadside distance d/λ_{CPW} at 10 GHz for CPW-fed twin slots with $L_1 = L_2 = L_{res} = 7.77$ mm on Substrate II. $W_1 = W_2 = 0.7$ mm; $h_1 = 1.21$ mm; $h_2 = 5$ mm; $\epsilon_{r1} = 6.15$; $\epsilon_{r2} = 1$; $l_f = 0.5\lambda_{CPW}$.

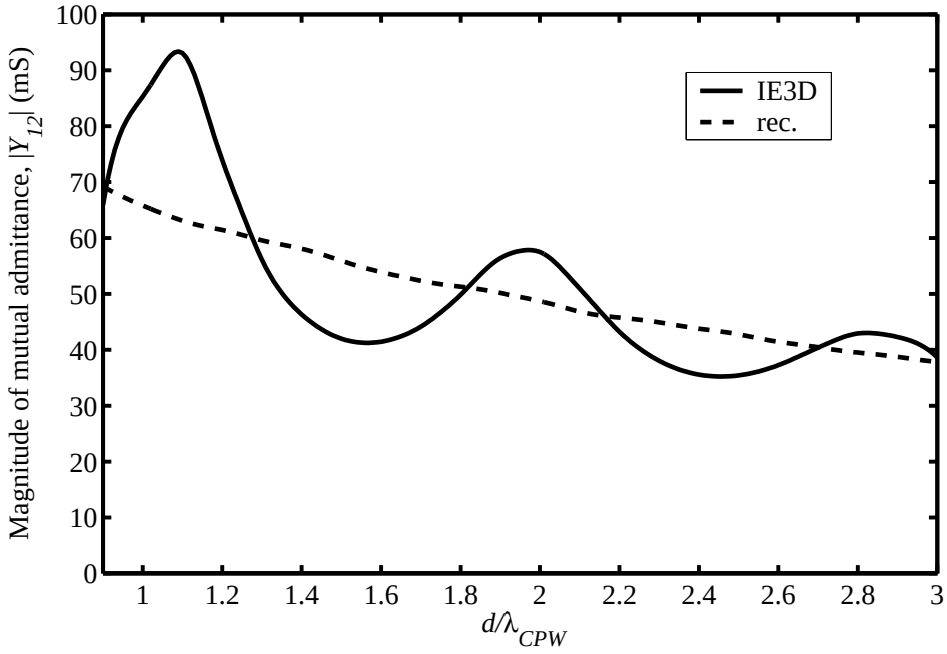

FIGURE 5.43: Magnitude of mutual admittance Y_{12} against broadside distance d/λ_{CPW} at 10 GHz for CPW-fed twin slots with $L_1 = L_2 = L_{res}$ = 7.77 mm on Substrate II. $W_1 = W_2$ = 0.7 mm; h_1 = 1.21 mm; h_2 = 5 mm; ϵ_{r1} = 6.15; ϵ_{r2} = 1; $l_f = 0.5\lambda_{CPW}$.

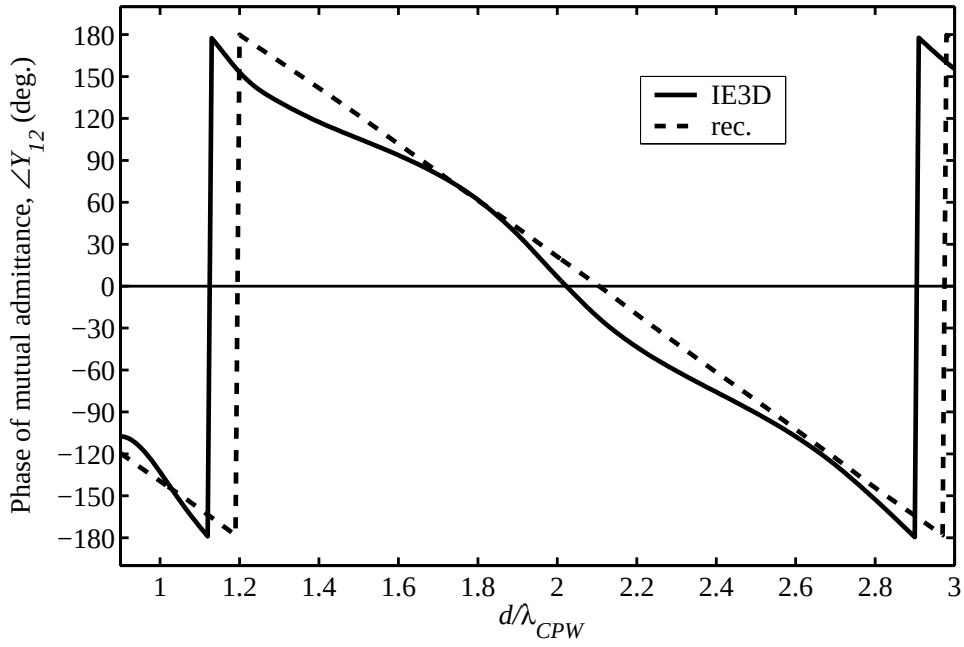

FIGURE 5.44: Phase of mutual admittance Y_{12} against broadside distance d/λ_{CPW} at 10 GHz for CPW-fed twin slots with $L_1 = L_2 = L_{res}$ = 7.77 mm on Substrate II. $W_1 = W_2$ = 0.7 mm; h_1 = 1.21 mm; h_2 = 5 mm; ϵ_{r1} = 6.15; ϵ_{r2} = 1; $l_f = 0.5\lambda_{CPW}$.

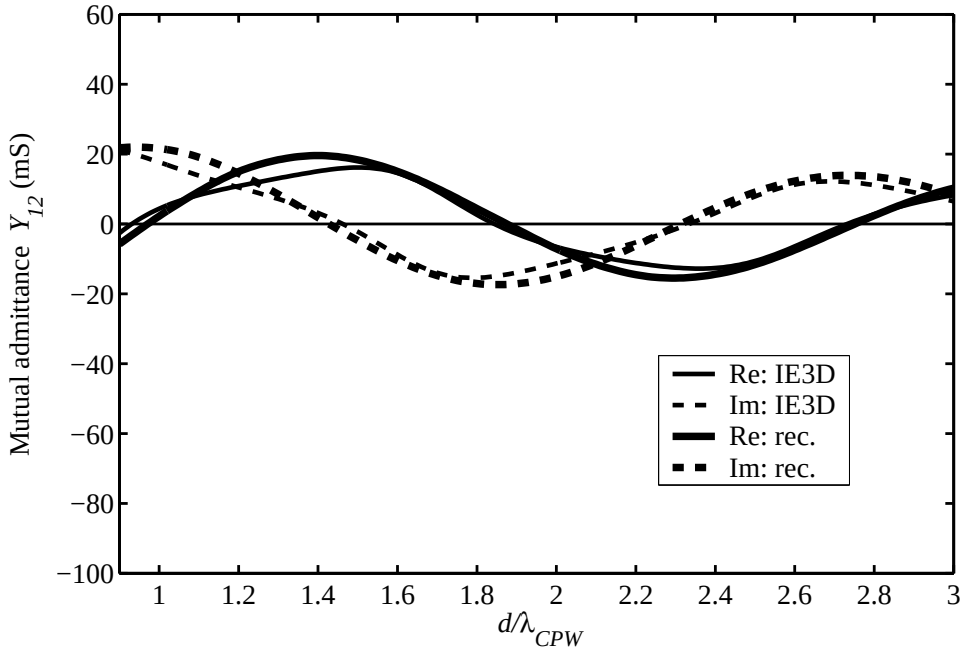

FIGURE 5.45: Mutual admittance Y_{12} against broadside distance d/λ_{CPW} at 10 GHz for CPW-fed twin slots with $L_1 = L_2 = 1.1L_{res}$ = 8.55 mm on Substrate II. $W_1 = W_2$ = 0.7 mm; h_1 = 1.21 mm; h_2 = 5 mm; ϵ_{r1} = 6.15; ϵ_{r2} = 1; $l_f = 0.5\lambda_{CPW}$.

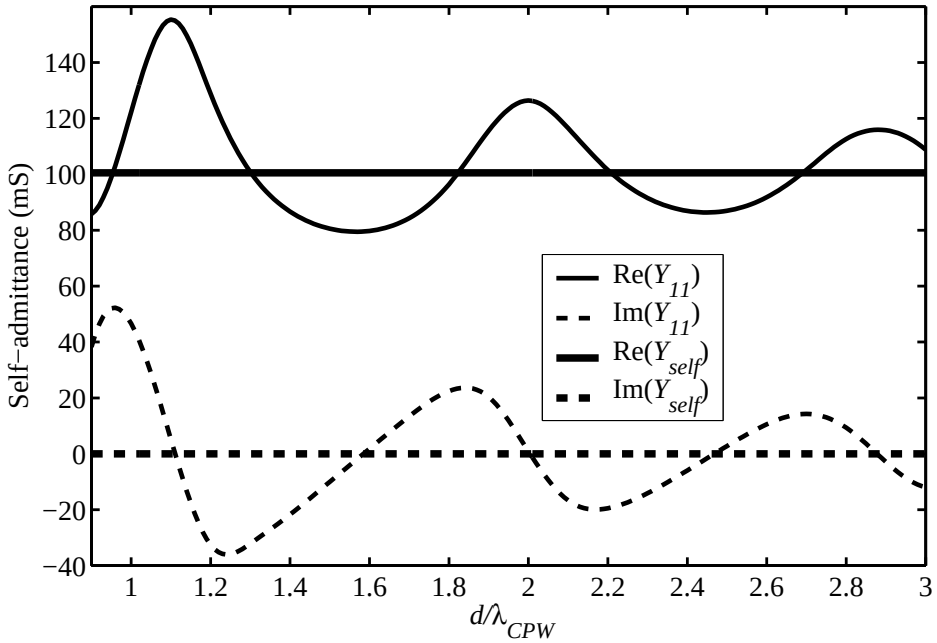

FIGURE 5.46: Two-port self-admittance Y_{11} against broadside distance d/λ_{CPW} for CPW-fed twin slots with $L_1 = L_2 = L_{res}$ = 7.77 mm on Substrate II, and resonant isolated self-admittance Y_{self} (both computed at 10 GHz with IE3D). $W_1 = W_2$ = 0.7 mm; h_1 = 1.21 mm; h_2 = 5 mm; ϵ_{r1} = 6.15; ϵ_{r2} = 1; $l_f = 0.5\lambda_{CPW}$.

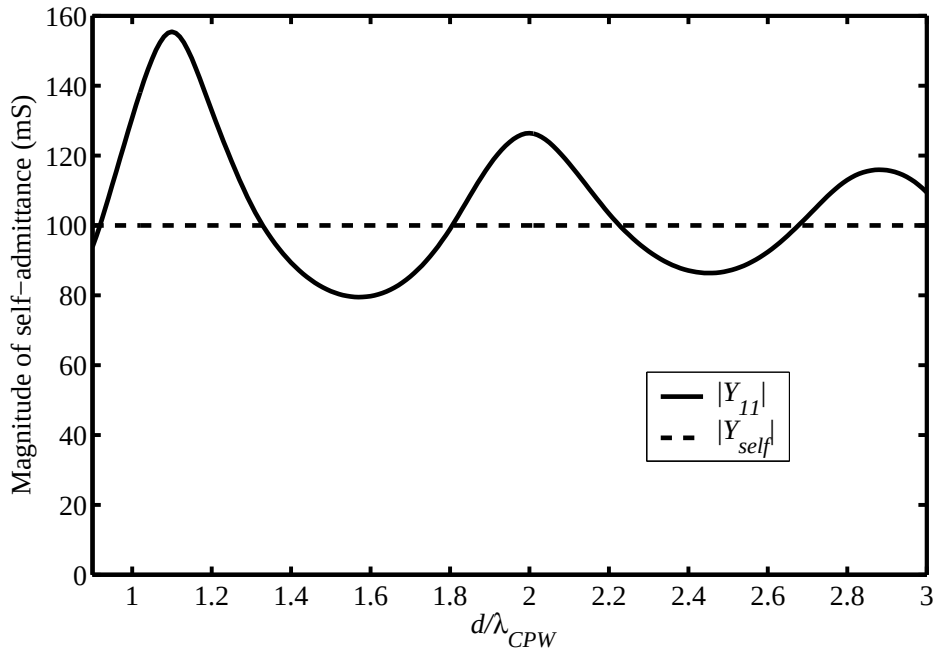

FIGURE 5.47: Magnitude of two-port self-admittance Y_{11} against broadside distance d/λ_{CPW} for CPW-fed twin slots with L_1 = L_2 = L_{res} = 7.77 mm on Substrate II, and magnitude of resonant isolated self-admittance Y_{self} (both computed at 10 GHz with IE3D). W_1 = W_2 = 0.7 mm; h_1 = 1.21 mm; h_2 = 5 mm; ϵ_{r1} = 6.15; ϵ_{r2} = 1; $l_f = 0.5\lambda_{CPW}$.

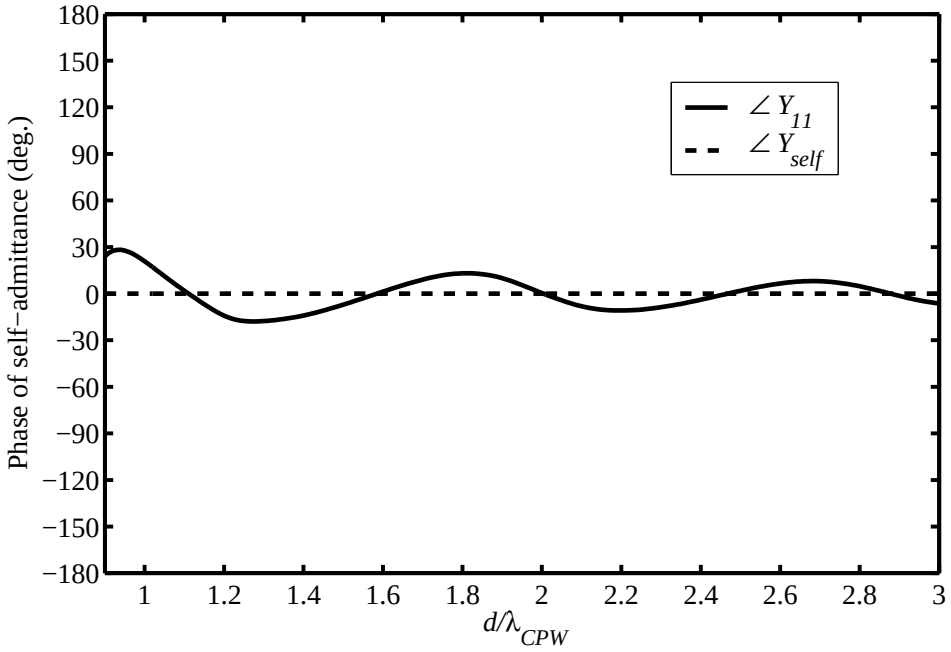

FIGURE 5.48: Phase of two-port self-admittance Y_{11} against broadside distance d/λ_{CPW} for CPW-fed twin slots with L_1 = L_2 = L_{res} = 7.77 mm on Substrate II, and phase of resonant isolated self-admittance Y_{self} (both computed at 10 GHz with IE3D). W_1 = W_2 = 0.7 mm; h_1 = 1.21 mm; h_2 = 5 mm; ϵ_{r1} = 6.15; ϵ_{r2} = 1; $l_f = 0.5\lambda_{CPW}$.

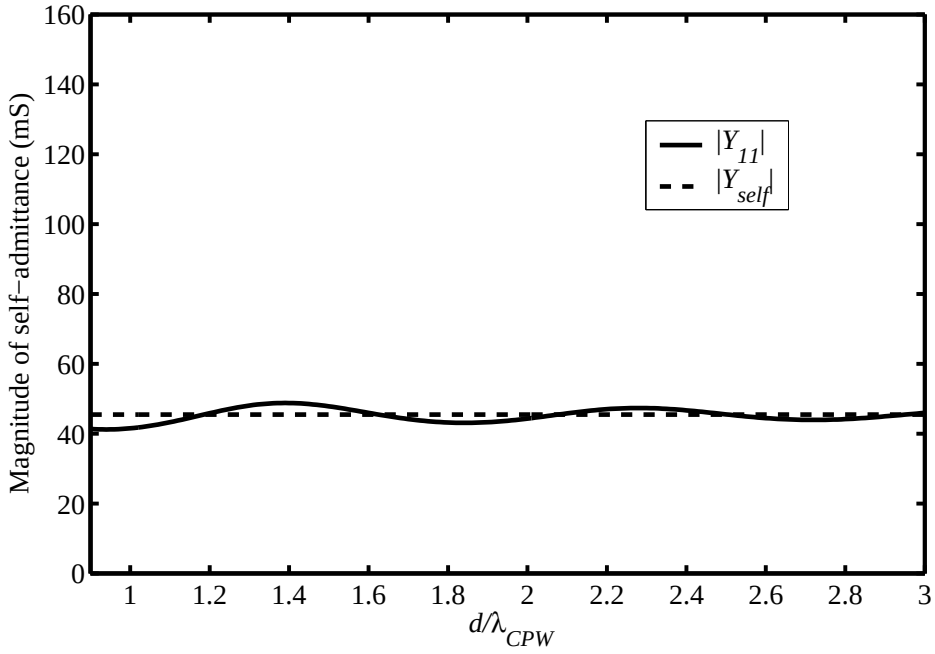

FIGURE 5.49: Magnitude of two-port self-admittance Y_{11} against broadside distance d/λ_{CPW} for CPW-fed twin slots with $L_1 = L_2 = 0.9L_{res}$ = 6.99 mm on Substrate II, and magnitude of resonant isolated self-admittance Y_{self} (both computed at 10 GHz with IE3D). $W_1 = W_2$ = 0.7 mm; h_1 = 1.21 mm; h_2 = 5 mm; ϵ_{r1} = 6.15; ϵ_{r2} = 1; $l_f = 0.5\lambda_{CPW}$.

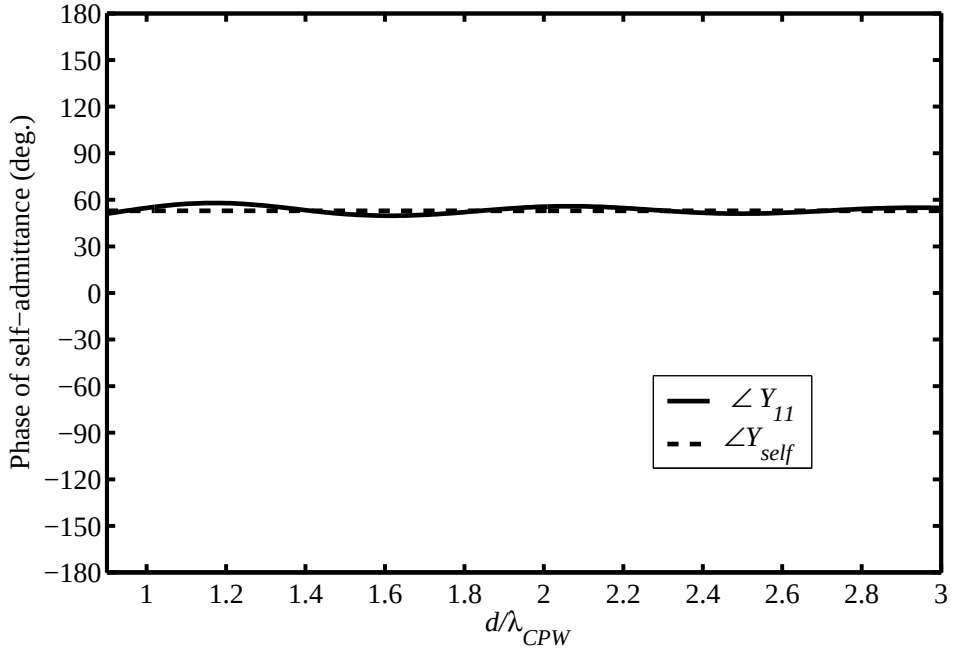

FIGURE 5.50: Phase of two-port self-admittance Y_{11} against broadside distance d/λ_{CPW} for CPW-fed twin slots with $L_1 = L_2 = 0.9L_{res}$ = 6.99 mm on Substrate II, and phase of resonant isolated self-admittance Y_{self} (both computed at 10 GHz with IE3D). $W_1 = W_2$ = 0.7 mm; h_1 = 1.21 mm; h_2 = 5 mm; ϵ_{r1} = 6.15; ϵ_{r2} = 1; $l_f = 0.5\lambda_{CPW}$.

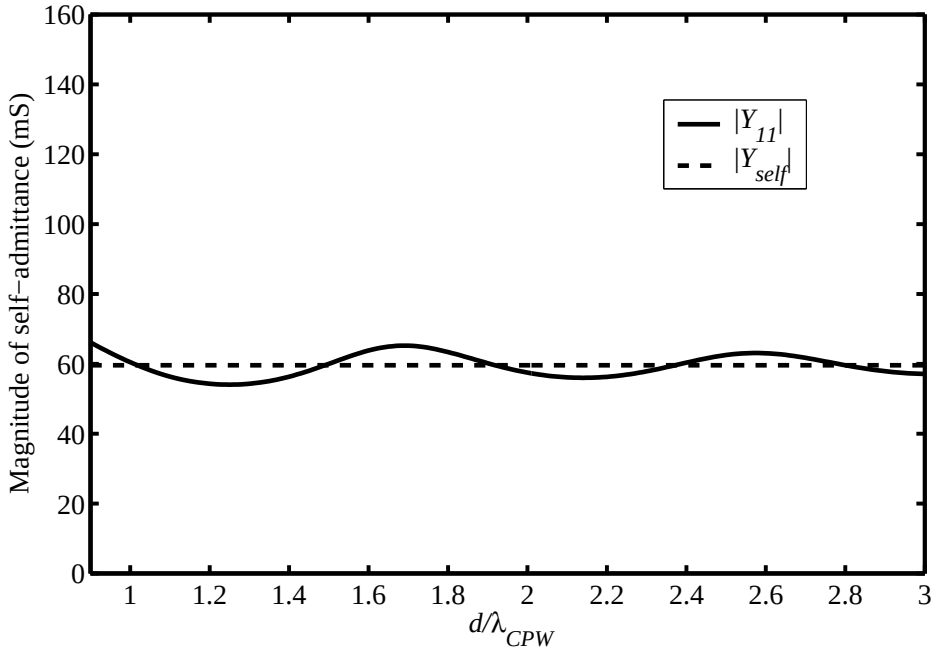

FIGURE 5.51: Magnitude of two-port self-admittance Y_{11} against broadside distance d/λ_{CPW} for CPW-fed twin slots with $L_1 = L_2 = 1.1L_{res}$ = 8.55 mm on Substrate II, and magnitude of resonant isolated self-admittance Y_{self} (both computed at 10 GHz with IE3D). $W_1 = W_2$ = 0.7 mm; h_1 = 1.21 mm; h_2 = 5 mm; ϵ_{r1} = 6.15; ϵ_{r2} = 1; $l_f = 0.5\lambda_{CPW}$.

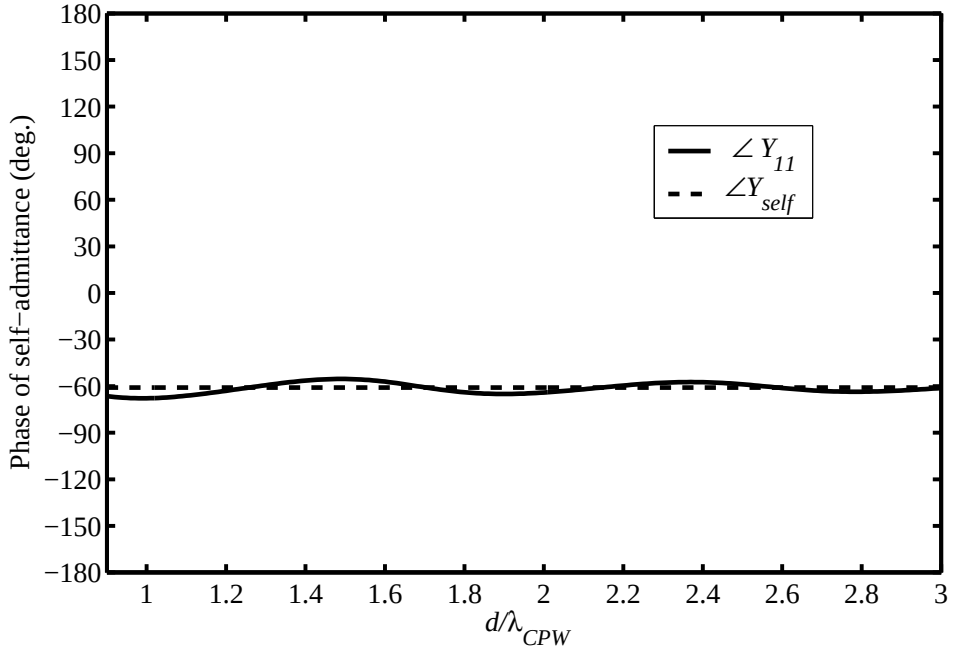

FIGURE 5.52: Phase of two-port self-admittance Y_{11} against broadside distance d/λ_{CPW} for CPW-fed twin slots with $L_1 = L_2 = 1.1L_{res}$ = 8.55 mm on Substrate II, and phase of resonant isolated self-admittance Y_{self} (both computed at 10 GHz with IE3D). $W_1 = W_2$ = 0.7 mm; h_1 = 1.21 mm; h_2 = 5 mm; ϵ_{r1} = 6.15; ϵ_{r2} = 1; $l_f = 0.5\lambda_{CPW}$.

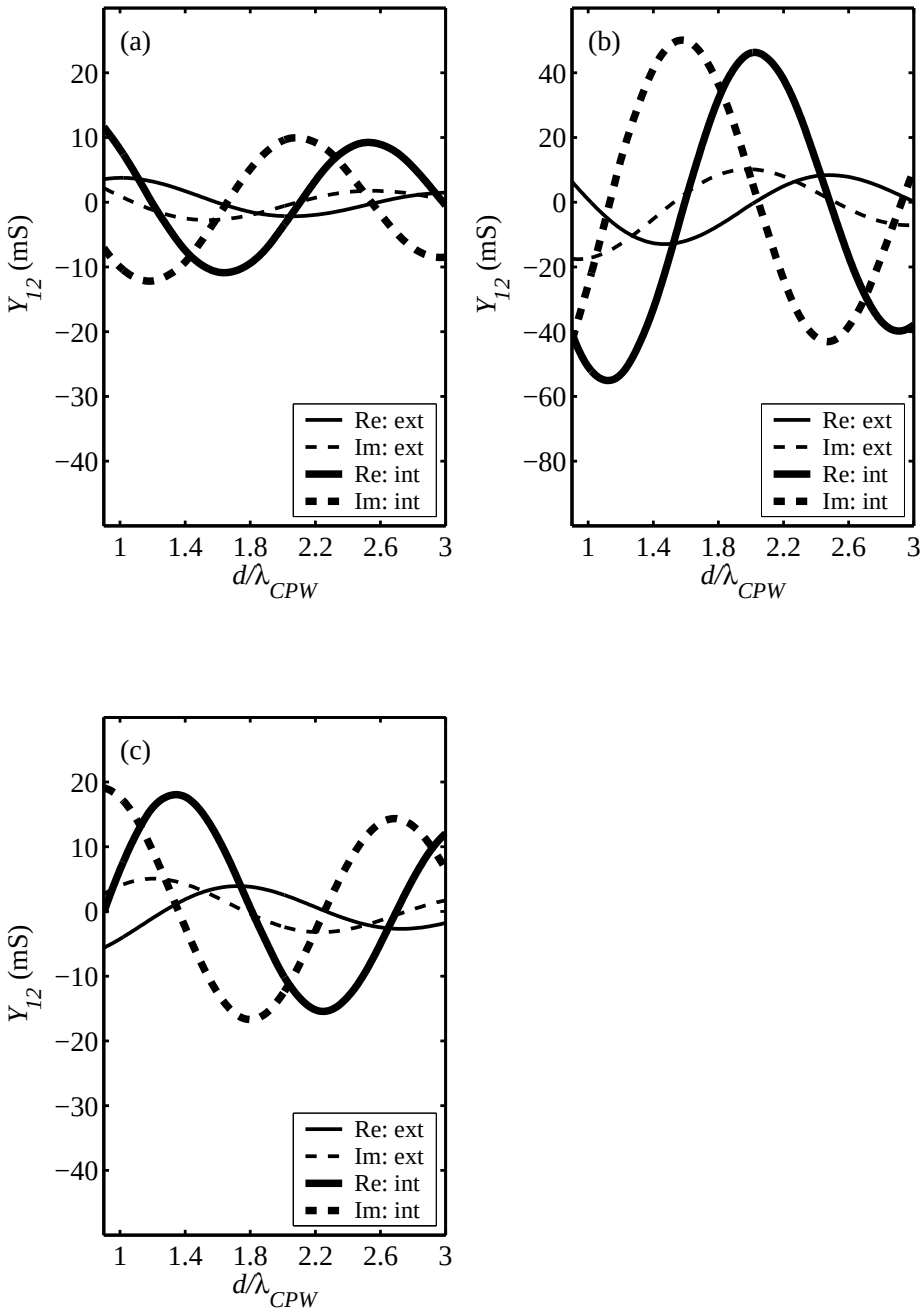

FIGURE 5.53: Y_{12}^{ext} and Y_{12}^{int} against d/λ_{CPW} computed using the reciprocity-expression approach for slots on Substrate II with (a) $L_1 = L_2 = 0.9L_{res}$, (b) $L_1 = L_2 = L_{res}$, and (c) $L_1 = L_2 = 1.1L_{res}$. $W_1 = W_2 = 0.7$ mm; $h_1 = 1.21$ mm; $h_2 = 5$ mm; $\epsilon_{r1} = 6.15$; $\epsilon_{r2} = 1$; $l_f = 0.5\lambda_{CPW}$.

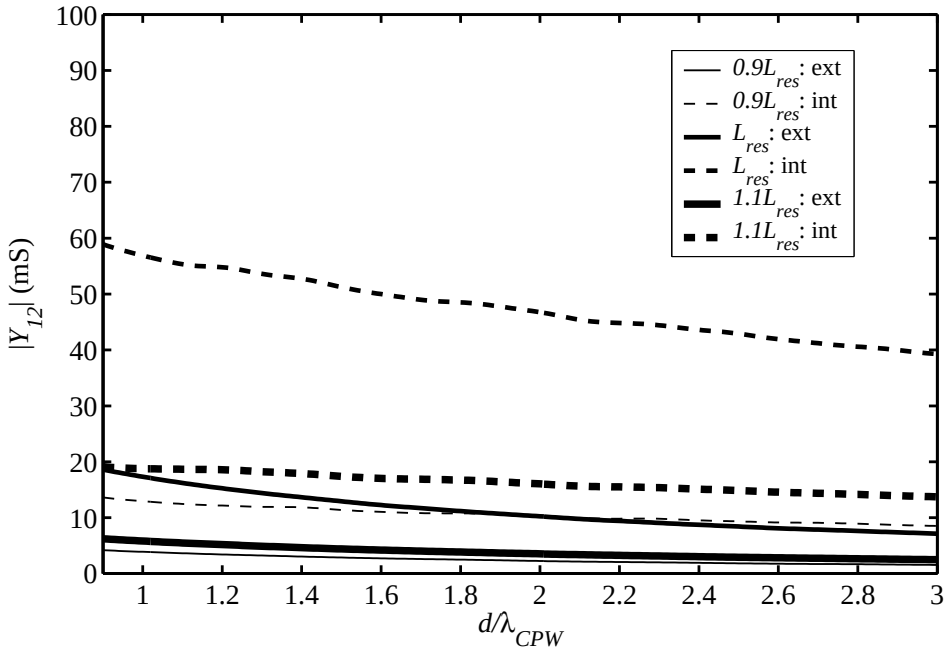

FIGURE 5.54: $|Y_{12}^{ext}|$ and $|Y_{12}^{int}|$ against d/λ_{CPW} for twin slots on Substrate II with $L_1 = L_2 = 0.9L_{res}$, $L_1 = L_2 = L_{res}$, and $L_1 = L_2 = 1.1L_{res}$. $W_1 = W_2 = 0.7$ mm; $h_1 = 1.21$ mm; $h_2 = 5$ mm; $\epsilon_{r1} = 6.15$; $\epsilon_{r2} = 1$; $l_f = 0.5\lambda_{CPW}$.

5.4.2.3 Substrate III: $h_1 = 0.013\lambda_d$, $h_2 = \lambda_0/6$, $\epsilon_{r1} = 2.2$, $\epsilon_{r2} = 1$

The top layer of Substrate III is substantially thinner electrically than that of Substrate I, *i.e.*, $0.013\lambda_d$ as opposed to $0.05\lambda_d$. An 86 Ω CPW feed line was designed on this substrate in IE3D that had $w = 1.2$ mm and $s = 0.3$ mm. Next, an isolated CPW-fed radiating slot with a width W of 0.18 mm was designed to operate at its second resonance at 10 GHz resulting in $L = L_{res} = 12.75$ mm and a resonant self-impedance of about 16 Ω. Mutual admittance Y_{12} against distance d with $0.9\lambda_{CPW} \leq d \leq 3\lambda_{CPW}$ was computed for three instances of twin slots with $W_1 = W_2 = 0.18$ mm throughout, and slot half-lengths of $L_1 = L_2 = 0.9L_{res}$, L_{res}, and $1.1L_{res}$.

The real and imaginary parts of the mutual admittance Y_{12} against normalized broadside distance d/λ_{CPW} for twin slots with $L_1 = L_2 = 0.9L_{res} = 11.48$ mm computed using the reciprocity-expression approach and IE3D are shown in Fig. 5.55. Y_{12} curves for twin slots with half-lengths $L_{res} = 12.75$ mm and $1.1L_{res} = 14.03$ mm are shown in Figs. 5.56 and 5.57 respectively; feed line lengths were $l_f = 0.5\lambda_{CPW}$ throughout. Figs. 5.55–5.57 confirm the main trends exhibited by slots on Substrates I and II; given this similarity and the detailed investigations already presented in Sections 5.4.2.1 and 5.4.2.2, the present substrate will not be treated further here.

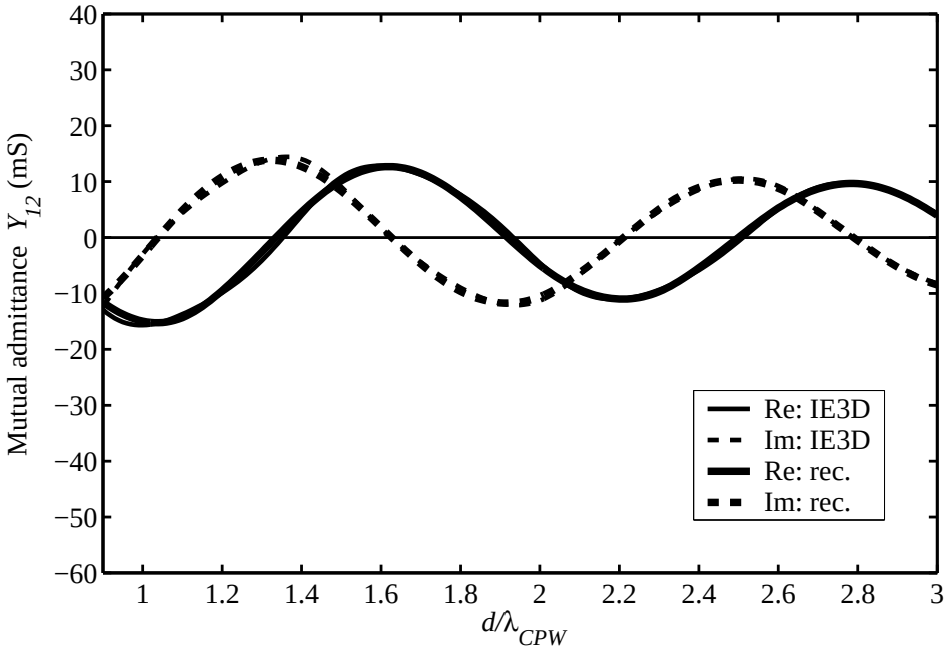

FIGURE 5.55: Mutual admittance Y_{12} against broadside distance d/λ_{CPW} at 10 GHz for CPW-fed twin slots with $L_1 = L_2 = 0.9L_{res}$ = 11.48 mm on Substrate III. $W_1 = W_2$ = 0.18 mm; h_1 = 0.254 mm; h_2 = 5 mm; ϵ_{r1} = 2.2; ϵ_{r2} = 1; $l_f = 0.5\lambda_{CPW}$.

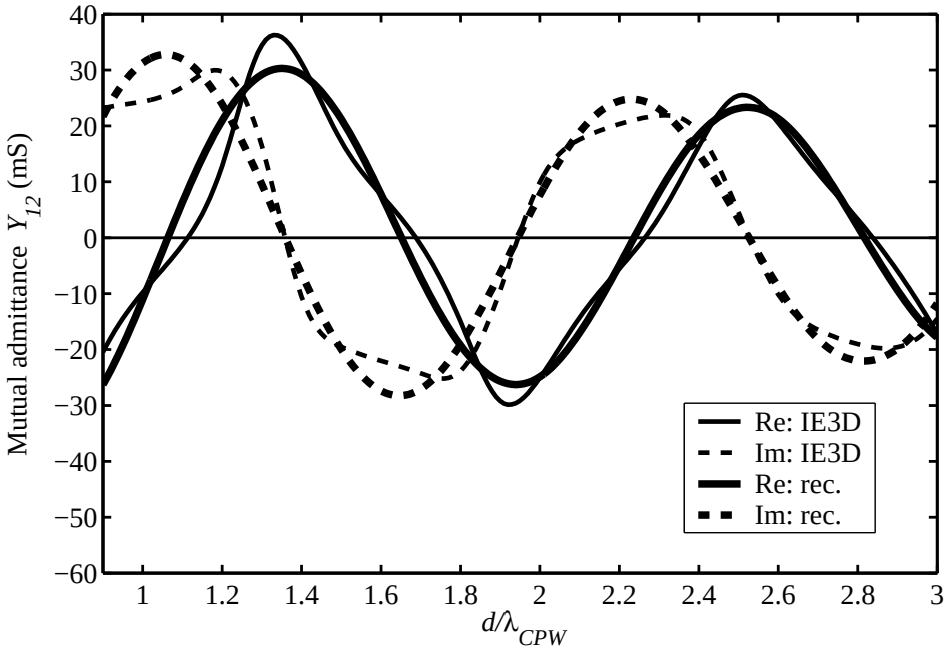

FIGURE 5.56: Mutual admittance Y_{12} against broadside distance d/λ_{CPW} at 10 GHz for CPW-fed twin slots with $L_1 = L_2 = L_{res}$ = 12.75 mm on Substrate III. $W_1 = W_2$ = 0.18 mm; h_1 = 0.254 mm; h_2 = 5 mm; ϵ_{r1} = 2.2; ϵ_{r2} = 1; $l_f = 0.5\lambda_{CPW}$.

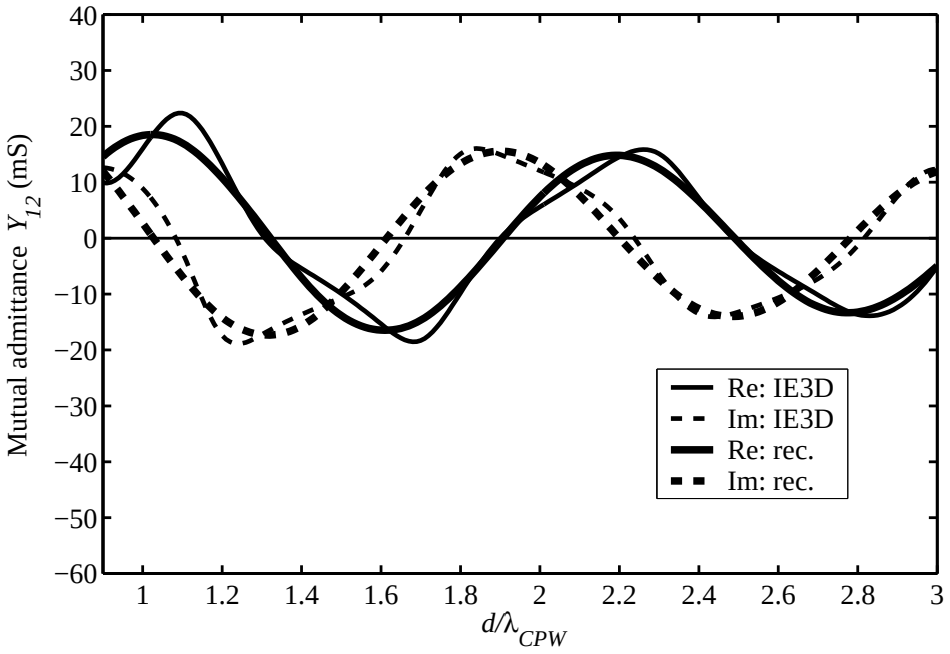

FIGURE 5.57: Mutual admittance Y_{12} against broadside distance d/λ_{CPW} at 10 GHz for CPW-fed twin slots with $L_1 = L_2 = 1.1L_{res}$ = 14.03 mm on Substrate III. $W_1 = W_2$ = 0.18 mm; h_1 = 0.254 mm; h_2 = 5 mm; ϵ_{r1} = 2.2; ϵ_{r2} = 1; $l_f = 0.5\lambda_{CPW}$.

5.4.2.4 Effect of shift in two-port reference planes

Noting that a shift in reference planes has impedance transformation implications, Y_{12} against d was computed for broadside twin slots on Substrate I with $L_1 = L_2 = L_{res}$, and CPW feed lines of length $l_f = 0.4\lambda_{CPW}$ (instead of $0.5\lambda_{CPW}$ as before). Results obtained using the reciprocity-expression approach and IE3D are shown in Fig. 5.58. The IE3D result is now free from the "irregular" behaviour displayed in Fig. 5.26 for feed line lengths of $0.5\lambda_{CPW}$, and the agreement between the two methods is quite good. Fig. 5.59 shows the real and imaginary parts of the two-port self-admittance Y_{11} against d/λ_{CPW}, as well as the isolated self-admittance Y_{self} computed using a $0.4\lambda_{CPW}$ feed line; the quantities are in close agreement. The moment-method (IE3D) Y_{11} is essentially free from the oscillatory behaviour about the isolated slot self-admittance seen in the $l_f = 0.5\lambda_{CPW}$ case (*cf.* Fig. 5.30). Hence, when reference planes are defined at the ends of feed lines of length $l_f = 0.4\lambda_{CPW}$, the assumption in the reciprocity-expression method of slot self-admittances that do not change from the isolated slot self-admittance value as d varies, is borne out by the IE3D two-port Y_{11}. This explains the good agreement between the two methods in regard to Y_{12} of Fig. 5.58.

In a further step, the IE3D Y parameters of Figs. 5.58 and 5.59 were transformed to the original reference planes at the ends of $l_f = 0.5\lambda_{CPW}$ feed lines by converting them to S parameters using

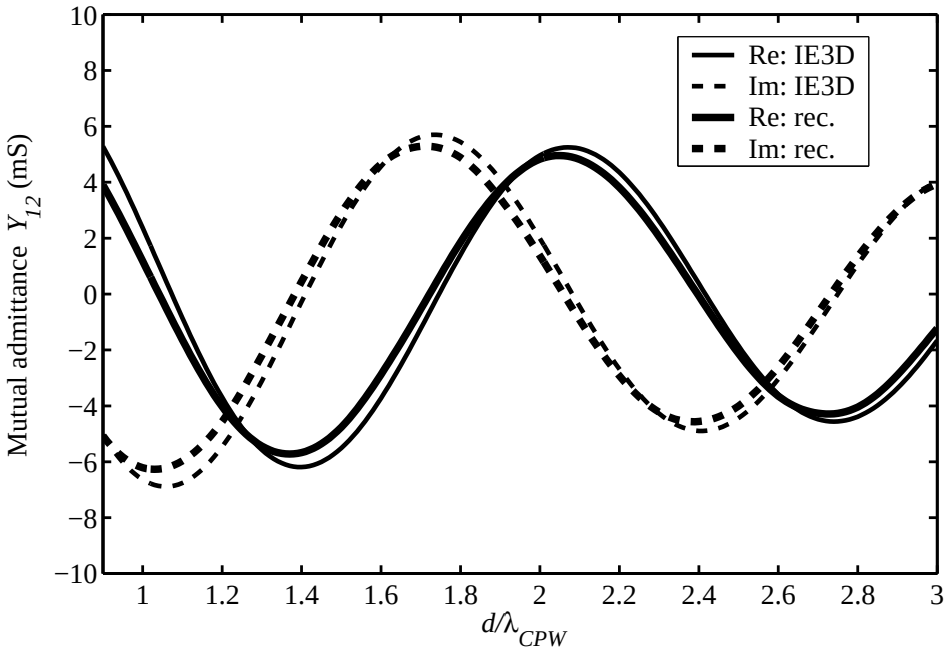

FIGURE 5.58: Mutual admittance Y_{12} against broadside distance d/λ_{CPW} at 10 GHz for CPW-fed twin slots with $L_1 = L_2 = L_{res}$ = 10.87 mm on Substrate I with $l_f = 0.4\lambda_{CPW}$. $W_1 = W_2$ = 0.4 mm; h_1 = 0.813 mm; h_2 = 5 mm; ϵ_{r1} = 3.38; ϵ_{r2} = 1.

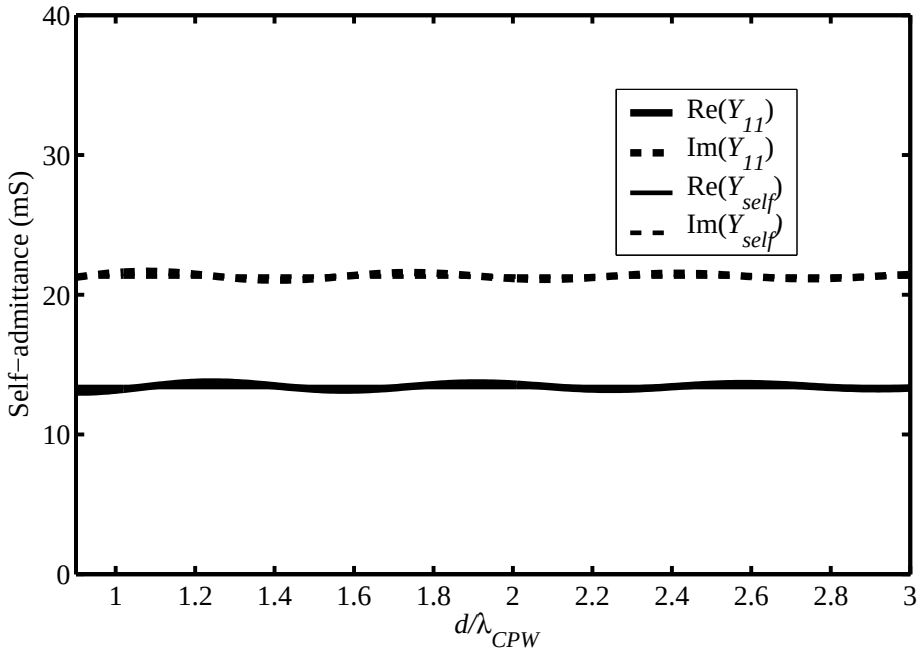

FIGURE 5.59: Two-port self-admittance Y_{11} against broadside distance d/λ_{CPW} for CPW-fed twin slots with $L_1 = L_2 = L_{res}$ = 10.87 mm on Substrate I with $l_f = 0.4\lambda_{CPW}$, and isolated slot self-admittance Y_{self} (both computed with IE3D at 10 GHz). $W_1 = W_2$ = 0.4 mm; h_1 = 0.813 mm; h_2 = 5 mm; ϵ_{r1} = 3.38; ϵ_{r2} = 1.

standard formulas [90, Table 4.2], multiplying these S parameters by a phase factor corresponding to an outward shift in reference planes of $0.1\lambda_{CPW}$, and converting the transformed S parameters

back to Y parameters. Results for Y_{11} and Y_{12} were very close to the original IE3D Y_{11} and Y_{12} of Figs. 5.30 and 5.26, suggesting that these $0.1\lambda_{CPW}$ sections of CPW for the original twin slot configuration ($l_f = 0.5\lambda_{CPW}$) fulfill a largely impedance-transforming role in the manner of sections of transmission line, with minimal coupling to other slots in the twin slot configuration.

Transforming the reciprocity-expression Y_{12} of Fig. 5.58 ($l_f = 0.4\lambda_{CPW}$) in conjunction with Y_{self} of Fig. 5.59 ($l_f = 0.4\lambda_{CPW}$) back to reference planes corresponding to $l_f = 0.5\lambda_{CPW}$, yielded a Y_{12} in close agreement with the original IE3D-computed Y_{12} of Fig. 5.26, as shown in Fig. 5.60 (in the 2×2 matrix of two-port Y parameters, the positions on the diagonal were filled by Y_{self} for all values of d). Notably, the reciprocity-expression Y_{12} curves now are "irregular" in a manner similar to the IE3D curves obtained for $l_f = 0.5\lambda_{CPW}$. This suggests that the reciprocity-expression approach can be used as follows to obtain Y_{12} curves for L_{res} twin slots – referred to the centres of radiating slots – that take on the "irregular" behaviour of the corresponding IE3D curves. First, identify a set of reference planes (and the corresponding feed line lengths) for which Y_{11} against d is relatively constant. Second, since the reciprocity-expression assumption of unchanging self-admittances would apply, determine Y_{12} using the reciprocity-expression method; this includes a once-off moment-method analysis of the corresponding isolated slot, which could yield the isolated self-admittance Y_{self} in addition to the required slot field and terminal voltage. Finally, construct an approximate Y parameter matrix from Y_{self} and Y_{12} for each value of d, and transform it to $l_f = 0.5\lambda_{CPW}$ reference planes as described above.

In order to confirm the above observations, Y_{12} against d was computed for CPW-fed twin slots with $L_1 = L_2 = L_{res}$ and $W_1 = W_2 = 0.7$ mm on Substrate II with feed lines of length $l_f = 0.4\lambda_{CPW}$. Results obtained using the reciprocity-expression approach and IE3D are shown in Fig. 5.61. The agreement between the two methods is very good. Fig. 5.62 shows the real and imaginary parts of the two-port self-admittance Y_{11} against d/λ_{CPW}, as well as the isolated self-admittance Y_{self} computed using a $0.4\lambda_{CPW}$ feed line; the quantities are in very close agreement. Hence the assumption in the reciprocity-expression method of slot self-admittances that do not change with d is validated by the IE3D two-port Y_{11}, explaining the good agreement between the two methods with respect to Y_{12} in Fig. 5.61.

As before, the IE3D Y parameters of Figs. 5.61 and 5.62 were transformed back to reference planes at the ends of the original $l_f = 0.5\lambda_{CPW}$ feed lines. Results for Y_{11} and Y_{12} were virtually identical to the original IE3D Y_{11} and Y_{12} of Figs. 5.46 and 5.42, suggesting in regard to the original twin slot configuration ($l_f = 0.5\lambda_{CPW}$) that there is negligible interaction between the outermost $0.1\lambda_{CPW}$ sections of CPW and the rest of the structure. Hence these $0.1\lambda_{CPW}$ sections of CPW

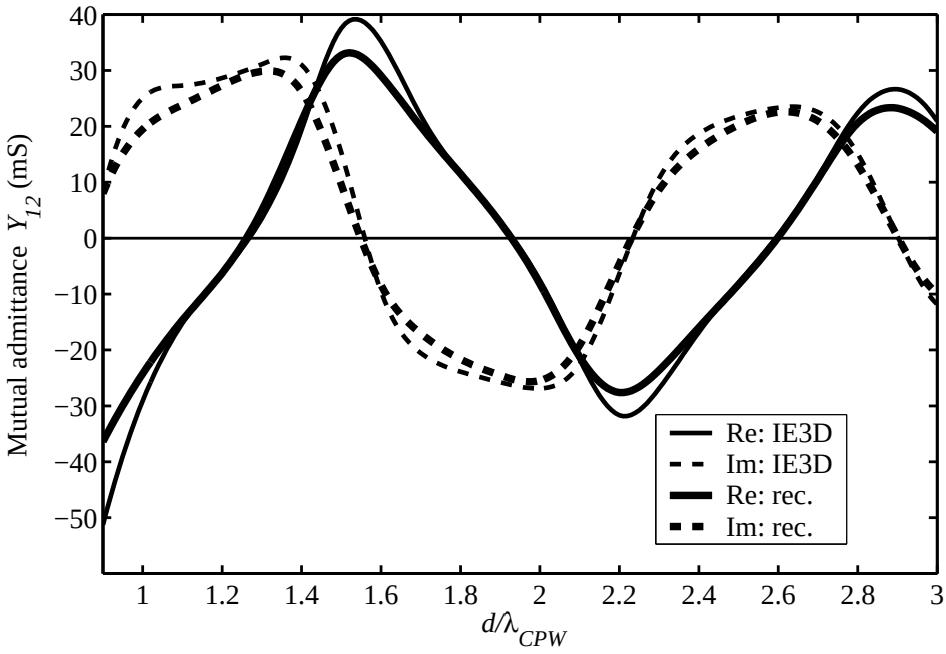

FIGURE 5.60: Mutual admittance Y_{12} against broadside distance d/λ_{CPW} at 10 GHz for CPW-fed twin slots with L_1 = L_2 = L_{res} = 10.87 mm on Substrate I. Reciprocity-expression results were transformed from reference planes $l_f = 0.4\lambda_{CPW}$ to $l_f = 0.5\lambda_{CPW}$ (IE3D results are the same as in Fig. 5.26). W_1 = W_2 = 0.4 mm; h_1 = 0.813 mm; h_2 = 5 mm; ϵ_{r1} = 3.38; ϵ_{r2} = 1.

appear to behave in a purely transmission-line-like manner.

Transforming the reciprocity-expression Y_{12} of Fig. 5.61 ($l_f = 0.4\lambda_{CPW}$) in conjunction with Y_{self} of Fig. 5.62 back to reference planes corresponding to $l_f = 0.5\lambda_{CPW}$ in the manner described above, yielded a Y_{12} in close agreement with the original IE3D-computed Y_{12} of Fig. 5.42, as shown in Fig. 5.63 (in the matrix of two-port Y parameters, the positions on the diagonal were filled by Y_{self} for all values of d). As in the Substrate I case, the reciprocity-expression Y_{12} curves were now "irregular" in a manner similar to that of the IE3D curves obtained for $l_f = 0.5\lambda_{CPW}$. This confirms that accurate Y_{12} curves referred to the centres of radiating slots can be obtained from the reciprocity-expression approach in the manner proposed above.

5.4.2.5 Experimental results

Y_{12} against frequency was computed using the reciprocity-expression approach and IE3D for a twin slot configuration with a layout such as that of Fig. 5.1 on Substrate I (see Section 5.4.2.1) using fixed radiating slot dimensions $L_1 = L_2 = L_{res,\,10\,GHz}$ = 10.87 mm and $W_1 = W_2 = 0.4$ mm, and a fixed inter-slot spacing $d = \lambda_{CPW,\,10\,GHz} = 21.5$ mm, where $L_{res,\,10\,GHz}$ and $\lambda_{CPW,\,10\,GHz}$ are the slot second-resonant half-length and CPW wavelength respectively at 10 GHz (CPW dimensions were those of Section 5.4.2.1).

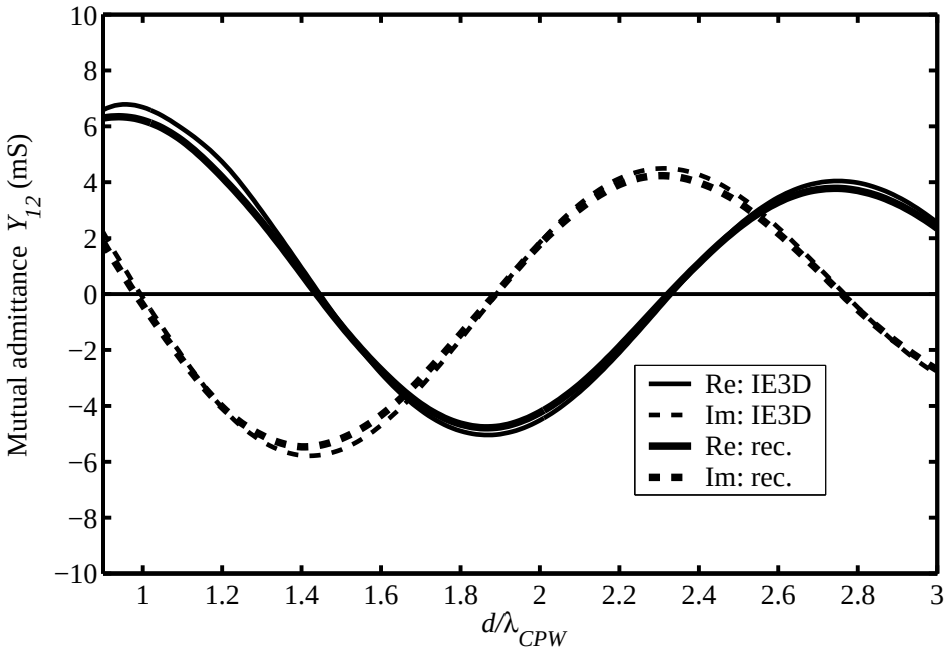

FIGURE 5.61: Mutual admittance Y_{12} against broadside distance d/λ_{CPW} at 10 GHz for CPW-fed twin slots with $L_1 = L_2 = L_{res}$ = 7.77 mm on Substrate II with $l_f = 0.4\lambda_{CPW}$. $W_1 = W_2$ = 0.7 mm; h_1 = 1.21 mm; h_2 = 5 mm; ϵ_{r1} = 6.15; ϵ_{r2} = 1.

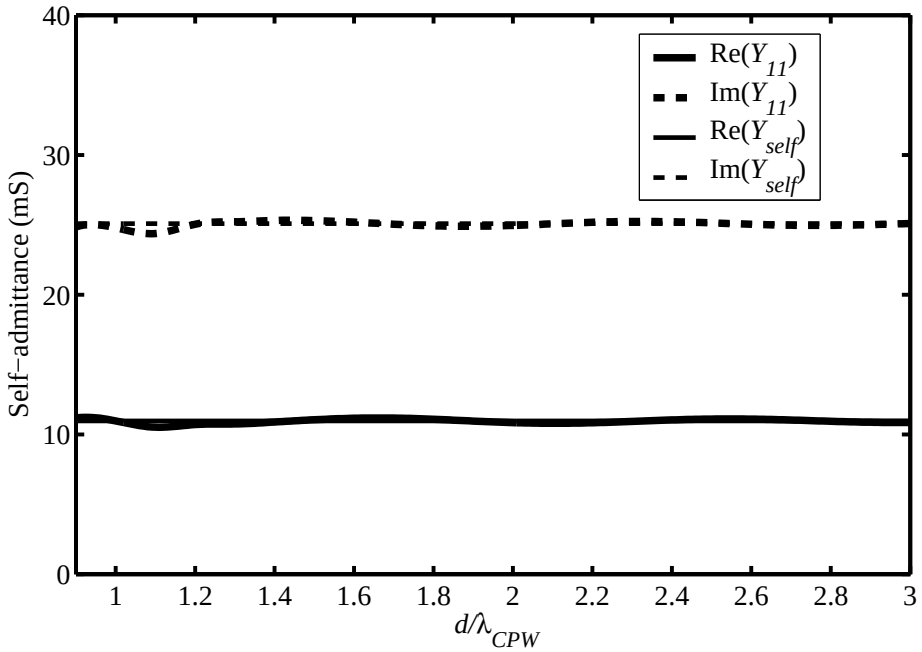

FIGURE 5.62: Two-port self-admittance Y_{11} against broadside distance d/λ_{CPW} at 10 GHz computed with IE3D for CPW-fed twin slots with $L_1 = L_2 = L_{res}$ = 7.77 mm on Substrate II with $l_f = 0.4\lambda_{CPW}$. $W_1 = W_2$ = 0.7 mm; h_1 = 1.21 mm; h_2 = 5 mm; ϵ_{r1} = 6.15; ϵ_{r2} = 1.

The twin slot configuration was subsequently etched on RO4003C laminate that served as top

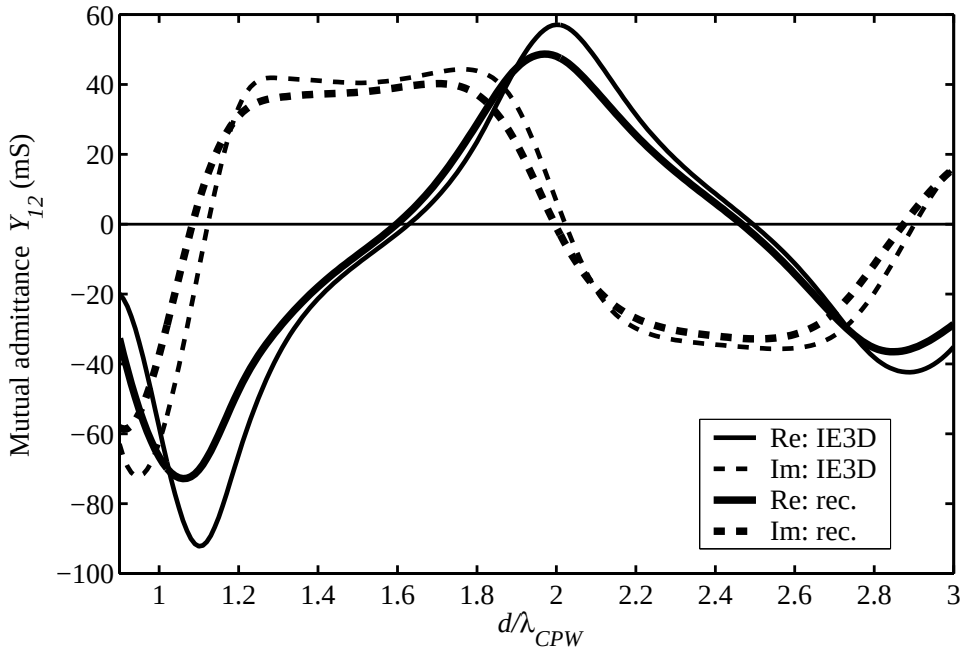

FIGURE 5.63: Mutual admittance Y_{12} against broadside distance d/λ_{CPW} at 10 GHz for CPW-fed twin slots with L_1 = L_2 = L_{res} = 7.77 mm on Substrate II. Reciprocity-expression results were transformed from reference planes $l_f = 0.4\lambda_{CPW}$ to $l_f = 0.5\lambda_{CPW}$ (IE3D results are the same as in Fig. 5.42). W_1 = W_2 = 0.7 mm; h_1 = 1.21 mm; h_2 = 5 mm; ϵ_{r1} = 6.15; ϵ_{r2} = 1.

dielectric layer (RO4003C has $\varepsilon_r = 3.38 \pm 0.05$ and $\tan\delta = 0.0027$ at 10 GHz [91]); polystyrene was used for the bottom (air) layer. The CPW feed lines were each extended for $9\lambda_{CPW,\,10\,GHz}$ beyond the $l_f = 0.5\lambda_{CPW,\,10\,GHz}$ reference planes to allow for proper gating out in the time-domain of transition phenomena associated with the coax-launcher-to-CPW transitions at the edges of the substrate; measured S parameters were subsequently transformed back to the $l_f = 0.5\lambda_{CPW,\,10\,GHz}$ reference planes taking into account dielectric and conductor losses on the CPW extensions that were estimated via a reflection measurement involving a short-circuited section of CPW transmission line. S parameters were converted to Y parameters using standard relations [90, Table 4.2]. Fig. 5.64 shows good agreement between the computed and measured mutual admittance Y_{12} against frequency for the above twin slots.

5.5 CONCLUSIONS

An approach based on a well-known reciprocity-based expression was developed for finding the mutual admittance between two broadside CPW-fed slots on a conductor-backed two-layer substrate. The approach is simpler than a full moment-method analysis, and hence more amenable to repeated evaluation in an array design procedure. It entails a number of simplifying assumptions: these include negligible interaction of radiating slots with CPW feed lines, and of feed lines with themselves; and

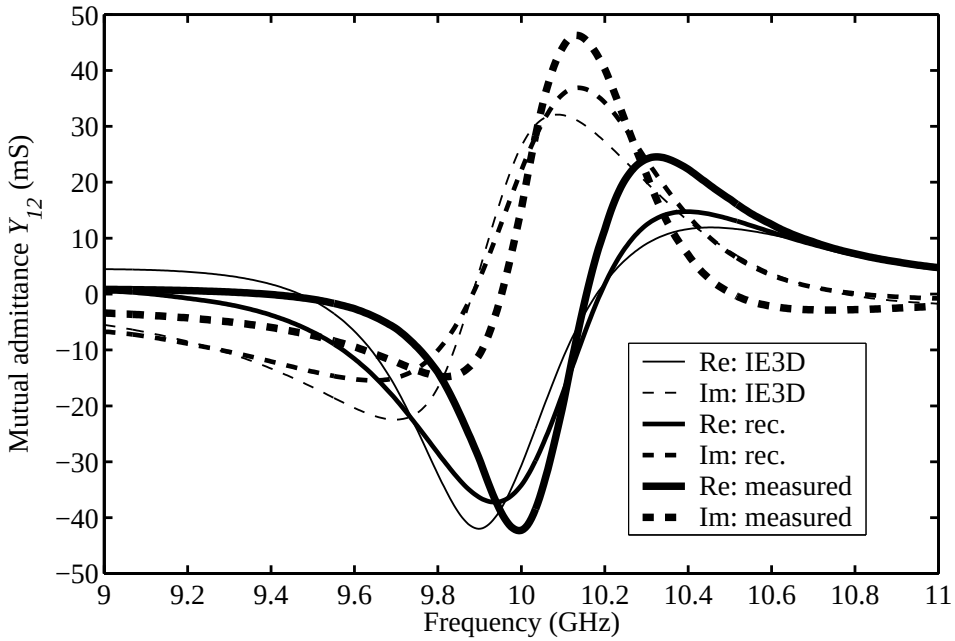

FIGURE 5.64: Mutual admittance Y_{12} against frequency of CPW-fed twin slots on Substrate I. $L_1 = L_2 = L_{res,\,10\,GHz}$ = 10.87 mm; $W_1 = W_2 = 0.4$ mm; $d = \lambda_{CPW,\,10\,GHz}$ = 21.5 mm; h_1 = 0.813 mm; h_2 = 5 mm; ϵ_{r1} = 3.38; ϵ_{r2} = 1.

a radiating slot aperture field that is directed across the width of the slot. In order to compute Y_{12} between two CPW-fed slots against inter-slot spacing d, the reciprocity-expression approach requires the electric field and "terminal" voltage of each slot radiating in isolation (*i.e.*, the voltage at the end of the CPW feed line, which includes the effect of the CPW-to-radiating-slot transition). This implies the necessity of a once-only moment-method analysis of each isolated slot.

The logistic implications for an array design procedure is not excessive, since in traditional design algorithms [19, 35], isolated slot self-admittance data need to be generated anyway (typically by means of the moment method). Afterwards, the reciprocity-expression approach allows for the mutual admittance between slot pairs of arbitrary dimensions and inter-slot spacings to be evaluated using isolated slot terminal voltages in conjunction with isolated slot electric field distributions. Alternatively, only the complex amplitude of the slot field (as opposed to the complete field distribution) can be extracted from the isolated slot analysis, and then used to scale generic functions that approximate the slot field; for example, it is straightforward to relate piecewise sinusoidal functions to slot field magnitudes.

The reciprocity-expression approach evaluates external and internal contributions to the total mutual admittance separately. The internal mutual admittance formulation required derivation of a spatial-domain Green's function for finding the $\hat{x}$-component of the magnetic field inside

the two-layer parallel-plate substrate due to an $\hat{x}$-directed equivalent surface magnetic current density representing a radiating slot in the top conducting plate. From known spectral-domain equivalent circuits for general layered media, equivalent circuits for the TM and TE contributions to the $\hat{x}$-component of the magnetic field of an appropriately-positioned $\hat{x}$-directed HMD in the conductor-backed two-layer substrate were obtained. Using these as a starting point, the spatial-domain Green's function was determined as a sum of singular Sommerfeld-type integrals (to the knowledge of the author, this has not been published before); treatment of the singularities was discussed.

Using the reciprocity-expression approach, mutual admittance Y_{12} against slot separation d was computed for broadside CPW-fed twin slots and some non-identical slot pairs on three different conductor-backed two-layer substrates. The substrates had the same air bottom layer, and top layers of contrasting dielectric thickness. For each substrate, three or four broadside twin slot configurations were considered that had radiating slot half-lengths in the vicinity of the second-resonant half-length of an isolated slot on the substrate. Results from the reciprocity-expression method were compared to results from moment-method-based simulations using IE3D.

Good agreement was observed between the above methods when Y parameter calculations were, as is customary, referred to radiating slot centres by choosing CPW feed lines that were $0.5\lambda_{CPW}$ long. The greatest discrepancy occurred for twin slots that had the same half-length as an isolated second-resonant slot on the substrate. Here, IE3D curves appeared like "irregular" versions of the reciprocity-expression curves, with the deviation the most marked for the substrate with the top layer that had the greatest dielectric thickness. (The effect was considerably less marked for twin slots with half-lengths away from the isolated second-resonant half-length, and virtually unobservable for half-lengths that were 10-15% shorter than the resonant half-length.) Further investigation linked the discrepancy for the resonant-length slots to the manner in which slot self-properties are accounted for in the two models: the reciprocity-expression approach assumes unchanging slot self-admittance values equal to the corresponding isolated slot self-admittances, while IE3D in fact predicted two-port self-admittances that were not constant as a function of inter-slot distance, "oscillating" about the isolated slot self-admittances.

By contrast, completely "regular" IE3D mutual admittance curves, as well as essentially constant two-port self-admittance curves that equalled the isolated slot self-admittance values, were obtained for resonant-length slots when a shift of reference planes was established by reducing feed line lengths, *i.e.*, to $0.4\lambda_{CPW}$ in this particular case. Reciprocity-expression Y_{12} calculations furthermore matched the IE3D results very closely. Starting from this finding, it was established that more

accurate (*i.e.*, "irregular" in the above sense) Y_{12} curves for the resonant-length slots (referred to the centres of radiating slots) can be obtained from the reciprocity-expression approach as follows. First, identify a set of reference planes (and corresponding feed line lengths) for which Y_{11} against d is essentially constant (*e.g.*, $0.4\lambda_{CPW}$ in the above case). Second, since the reciprocity-expression assumption of unchanging self-admittances would be valid, determine Y_{12} with respect to the new reference planes using the reciprocity-expression method; this of course includes a once-off moment-method analysis of the corresponding isolated slots, which for each slot could yield the isolated self-admittance Y_{self} in addition to the terminal voltage and electric field. Finally, construct an approximate Y parameter matrix from Y_{self} and Y_{12} for each value of d, and transform it to the desired $l_f = 0.5\lambda_{CPW}$ reference planes.

Using the reciprocity-expression approach, it was possible to estimate external and internal contributions to the mutual admittance. For the reference substrate, the internal contribution clearly was predominant with a magnitude of more than double that of the external mutual admittance. The relative size of the internal mutual admittance increased as the dielectric thickness of the top layer was increased. The predominance of internal mutual admittance is contrary to the case of longitudinal slots in the broad wall of rectangular waveguide, where in general the external coupling is most pronounced [19, 20].

For the purposes of experimental verification, Y_{12} was computed against frequency for a fixed twin slot configuration on one of the above conductor-backed two-layer substrates using both of the above methods. The antenna was manufactured and its S parameters measured; when converted to Y parameters, the measured Y_{12} agreed well with computations using the reciprocity-expression approach and IE3D.

In conclusion, the present chapter reveals the reciprocity-based approach for mutual admittance calculations between CPW-fed slots on a two-layer parallel-plate substrate to be a viable alternative to a moment-method-based approach. The reciprocity-expression approach would however be significantly simpler to implement in an array design procedure.

CHAPTER 6

CONCLUSIONS AND FUTURE WORK

Main conclusions on the work presented in this thesis are summarized below, and areas for future work are identified.

The thesis had two main objectives.

The first was to alleviate a paucity of work on CPW-fed slot antennas on conductor-backed two-layer substrates by means of a fuller characterization of the behaviour of single CPW-fed slots on such substrates, and by the investigation of a viable minimum antenna configuration, namely a twin slot configuration, that is not disabled by the problem of parallel-plate mode leakage that invariably accompanies single slots.

With respect to single slots it was found that radiation efficiency increased and bandwidth decreased as height h_2 of the bottom substrate layer was increased. Thus it was possible to design a single slot antenna on a substrate with top and bottom dielectric layer heights of about $0.01\lambda_d$ and $0.28\lambda_0$ that had a bandwidth of 13% (VSWR < 1.5) with a radiation efficiency of around 57% in the band, compared to a bandwidth of 18% and a radiation efficiency of around 39% in the band for a slot on a lower-profile substrate (the reference substrate for this investigation) that had top and bottom dielectric layer heights of about $0.01\lambda_d$ and $0.12\lambda_0$. Broadside twin slots on the latter substrate were however shown to yield more than double the radiation efficiency (*i.e.*, about 90%) of the single slot (on the same substrate) when they were spaced close to half a wavelength of the two-layer parallel-plate TM_0 mode apart; the bandwidth of this configuration (13%) was about a third less than that of the single slot. Further investigation showed that radiation efficiency of matched twin slots spaced exactly $\lambda_{TM_0}/2$ apart increased as bottom substrate layer height increased; the improvement was incremental given the already relatively high radiation efficiency (just over 80% at the operating frequency) at the starting $h_2 = 0.08\lambda_0$ value. Bandwidth again decreased with

increasing bottom layer height, albeit less markedly than in the case of a single slot. It was found that radiation efficiency attainable with optimally-spaced twin slots on the reference ($h_2 = 0.12\lambda_0$) conductor-backed two-layer substrate is comparable to the high radiation efficiencies attainable with similarly-spaced twin slots on thick $\lambda_d/4$ substrates (or thin substrates) with a back reflector positioned $\lambda_0/4$ away; at microwave frequencies, the lower profile of the two-layer parallel-plate substrate would likely be an added advantage.

The second main objective of the thesis was to develop an approach for finding the mutual admittance Y_{12} between CPW-fed slots on a conductor-backed two-layer substrate that would be more readily applicable in an iterative array design procedure than a technique based on a full moment-method-based analysis, yet be of comparable accuracy. The approach was to be based on a well-known reciprocity-based expression, and intended to rigorously account for the substrate by use of the appropriate Green's function.

An initial step was an exploratory investigation, using the moment-method-based electromagnetic simulator IE3D, of general aspects of the mutual admittance between identical (twin) CPW-fed slots on a conductor-backed two-layer substrate with an air bottom layer. *First*, curves for mutual admittance Y_{12} between twin CPW-fed slots on such a conductor-backed two-layer substrate as a function of slot separation d along broadside and collinear paths were computed. This was done for slot half-lengths in the vicinities of the first and second resonant half-lengths of the corresponding isolated slots (a characterization of this nature was not yet available in the literature; such data might be used towards a first-order array design). Two-port network parameters were referred to radiating slot centres. Mutual admittance curves for the set of broadside second-resonance twin slots were "irregular" in shape, and shifted with respect to each other, unlike the first-resonance curves that were similar in shape to mutual admittance curves for centre-fed narrow slots in an infinite ground plane; the irregularity was most marked for twin slots with half-length equal to the isolated slot second-resonant half-length. The mutual admittance between broadside second-resonance CPW-fed twin slots referred to the magnitude of the isolated slot self-admittance – a measure of the degree of mutual coupling – was greater than that for first-resonance CPW-fed twin slots, which in turn exceeded that for broadside $0.5\lambda_0$ centre-fed narrow rectangular slots in an infinite ground plane. Compared to the broadside case, mutual coupling between identical collinear slots with half-lengths in the vicinity of the second-resonance half-length was negligible. *Second*, the effect of back plane distance on mutual coupling between CPW-fed twin slots on conductor-backed two-layered substrates was investigated. For the substrate under investigation, a back plane at a distance of $\lambda_0/4$ and $\lambda_0/6$ yielded normalized mutual admittance curves with substantially higher maxima and minima compared to the case where no back plane was present. Normalized mutual admittance in the

$\lambda_0/6$ case was somewhat larger than in the $\lambda_0/4$ case, suggesting that the effect of mutual coupling increases as back plane distance decreases.

The predominant contribution however was the above-mentioned development of an approach based on a standard reciprocity-based expression for finding the mutual admittance between two broadside CPW-fed slots on a conductor-backed two-layer substrate. Simplifying assumptions included negligible interaction of radiating slots with CPW feed lines, and radiating slot aperture fields that are directed across the width of the slot, and are constant across the width of the slot. In order to compute curves of Y_{12} between two CPW-fed slots against slot separation d, the reciprocity-expression approach requires the electric field and "terminal" voltage (*i.e.*, the voltage at the end of the CPW feed line) of each slot radiating in isolation; the terminal voltage includes the effect of the CPW-to-radiating-slot transition. Thus computing Y_{12} against d requires only a once-off moment-method analysis of each slot in isolation, and then calculating external and internal reaction integrals at each value of d; this is computationally more economical than the alternative of a full moment-method analysis of the whole twin-slot structure at every value of d.

In order to evaluate the internal mutual admittance, the relevant component of the spatial-domain Green's function for the conductor-backed two-layer substrate was determined in integral form; this was not available in the open literature.

Using the reciprocity-expression approach, mutual admittance Y_{12} against slot separation d was computed for broadside CPW-fed twin slots – and some non-identical slot pairs – on three different conductor-backed two-layer substrates (the range of d was $0.9\lambda_{CPW} \leq d \leq 3\lambda_{CPW}$). The substrates had top layers of contrasting dielectric thickness, and the same air bottom layer. For each substrate, three or four broadside twin slot configurations were considered that had radiating slot half-lengths in the vicinity of the second-resonant half-length of an isolated slot on the substrate. Results were compared to moment-method-based simulations obtained using IE3D. Y_{12} calculations were referred to radiating slot centres by choosing CPW feed lines that were $0.5\lambda_{CPW}$ long. In general, good agreement was observed between the above methods; the greatest discrepancy occurred for twin slots that had the same half-length as an isolated second-resonant slot on the substrate. Here, IE3D curves appeared like "irregular" versions (in the sense of the above initial explorations) of the reciprocity-expression curves, with the deviation the most marked for the substrate with the top layer that had the greatest electrical height. The discrepancy was related to the manner in which slot self-properties are accounted for in the two models: the reciprocity-expression approach assumes unchanging slot self-admittances equal to isolated slot self-admittances, while IE3D in fact predicted two-port self-admittances that were not constant as a function of slot separation, "oscillating" with a

decaying envelope about the isolated slot self-admittances.

Completely "regular" IE3D mutual admittance curves – as well as two-port self-admittance curves equal to the isolated self-admittance values – were however obtained for the above second-resonant twin slots when a shift of reference planes was established by reducing feed line lengths to $0.4\lambda_{CPW}$; reciprocity-expression Y_{12} calculations furthermore matched the IE3D results very closely. It was subsequently established that more accurate (*i.e.*, "irregular" in the above sense) Y_{12} curves for resonant-length slots referred to the centres of radiating slots can be obtained using the reciprocity-expression approach as follows. First, identify a set of reference planes (and corresponding feed line lengths) for which Y_{11} against d is essentially constant. Second, since the reciprocity-expression assumption of unchanging self-admittances would be valid, determine Y_{12} using the reciprocity-expression method; this implies a once-off moment-method analysis of the corresponding isolated slots, which for each slot could yield the isolated self-admittance Y_{self} in addition to the terminal voltage and electric field. Finally, construct a Y parameter matrix from Y_{self} and Y_{12} for each value of d, and transform it to the desired $l_f = 0.5\lambda_{CPW}$ reference planes.

Using the reciprocity-expression approach, it was established that, for CPW-fed slots on the above conductor-backed two-layer substrates, the internal contribution to the mutual admittance was more than twice that of the external mutual admittance. The relative contribution of the internal mutual admittance was greater for substrates with electrically thicker top layers. The predominance of the internal mutual admittance is contrary to the case of, for example, longitudinal slots in the broad wall of rectangular waveguide, where in general the external coupling is most pronounced.

It was concluded that the reciprocity-based approach for mutual admittance calculations between CPW-fed slots on a two-layer parallel-plate substrate can be a viable alternative to a moment-method-based approach. The reciprocity-expression approach however would have the advantage of being considerably simpler to implement in an array design procedure. Future work could entail the actual incorporation of the method in an array design procedure, as well as investigating methods to optimize the speed of computing the reaction integrals that are part of the method.

REFERENCES

[1] J.-F. Huang and C.-W. Kuo, "CPW-fed slot antenna with CPW tuning stub loading," *Microwave Opt. Technol. Lett.*, vol. 19, no. 4, pp. 257–258, Nov. 1998.

[2] ——, "CPW-fed bow-tie slot antenna," *Microwave Opt. Technol. Lett.*, vol. 19, no. 5, pp. 358–360, Dec. 1998.

[3] E. A. Soliman, S. Brebels, P. Delmotte, G. A. E. Vandenbosch, and E. Beyne, "Bow-tie slot antenna fed by CPW," *Electron. Lett.*, vol. 35, no. 7, pp. 514–515, Apr. 1999.

[4] M. Miao, B. L. Ooi, and P. S. Kooi, "Broadband CPW-fed wide slot antenna," *Microwave Opt. Technol. Lett.*, vol. 25, no. 3, pp. 206–211, May 2000.

[5] R. Chair, A. A. Kishk, and K. F. Lee, "Ultrawide-band coplanar waveguide-fed rectangular slot antenna," *IEEE Antennas Wireless Propagat. Lett.*, vol. 3, no. 1, pp. 227–229, 2004.

[6] E. A. Soliman, S. Brebels, E. Beyne, and G. A. E. Vandenbosch, "CPW-fed cusp antenna," *Microwave Opt. Technol. Lett.*, vol. 22, no. 4, pp. 288–290, Aug. 1999.

[7] W.-S. Chen and K.-L. Wong, "A dual-frequency coplanar waveguide-fed slot antenna," *Microwave Opt. Technol. Lett.*, vol. 25, no. 3, pp. 226–228, May 2000.

[8] T. A. Denidni and M. A. Habib, "Broadband printed CPW-fed circular slot antenna," *Electron. Lett.*, vol. 42, no. 3, pp. 135–136, Feb. 2006.

[9] P. Focardi, A. Neto, and W. R. McGrath, "Coplanar-waveguide-based tetraherts hot-electron-bolometer mixers – improved embedding circuit description," *IEEE Trans. Microwave Theory Tech.*, vol. MTT-50, no. 10, pp. 2374–2383, Oct. 2002.

[10] A. Neto, P. D. Maagt, and S. Maci, "Optimized basis functions for slot antennas excited by coplanar waveguides," *IEEE Trans. Antennas Propagat.*, vol. AP-51, no. 7, pp. 1638–1646, July 2003.

[11] M. Riaziat, R. Majidi-Ahy, and I.-J. Feng, "Propagation modes and dispersion characteristics of coplanar waveguides," *IEEE Trans. Microwave Theory Tech.*, vol. MTT-38, no. 3, pp. 245–251, Mar. 1990.

[12] J.-F. Huang and C.-W. Kuo, "More investigations of leakage and nonleakage conductor-backed coplanar waveguide," *IEEE Trans. Electromagn. Compat.*, vol. EMC-40, no. 3, pp. 257–261, Aug. 1998.

[13] Y. Liu and T. Itoh, "Leakage phenomena in multilayered conductor-backed coplanar waveguides," *IEEE Microwave Guided Wave Lett.*, vol. 3, no. 11, pp. 426–427, Nov. 1993.

[14] H. C. Liu, T. S. Horng, and N. G. Alexopoulos, "Radiation of printed antennas with a coplanar waveguide feed," *IEEE Trans. Antennas Propagat.*, vol. AP-43, no. 10, pp. 1143–1148, Oct. 1995.

[15] C.-Y. Lee, Y. Liu, K. Cha, and T. Itoh, "Analysis and application of nonleaky uniplanar structures with conductor backing," *Int. J. Microwave Millimeter-Wave Computer-Aided Eng.*, vol. 6, no. 5, pp. 319–327, 1996.

[16] X. Ding and A. F. Jacob, "CPW-fed slot antenna with wide radiating apertures," *IEE Proc. Microw. Antennas Propagat.*, vol. 145, no. 1, pp. 104–108, Feb. 1998.

[17] R. S. Elliott and L. A. Kurtz, "The design of small slot arrays," *IEEE Trans. Antennas Propagat.*, vol. AP-26, no. 2, pp. 214–219, Mar. 1978.

[18] R. S. Elliott, *Antenna Theory and Design*. Englewood Cliffs, New Jersey: Prentice-Hall, 1981.

[19] ——, "An improved design procedure for small arrays of shunt slots," *IEEE Trans. Antennas Propagat.*, vol. AP-31, no. 1, pp. 48–53, Jan. 1983.

[20] R. S. Elliott and W. R. O'Loughlin, "The design of slot arrays including internal mutual coupling," *IEEE Trans. Antennas Propagat.*, vol. AP-34, no. 9, pp. 1149–1154, Sep. 1986.

[21] R. Shavit and R. S. Elliott, "Design of transverse slot arrays fed by a boxed stripline," *IEEE Trans. Antennas Propagat.*, vol. AP-31, no. 4, pp. 545–552, Jul. 1983.

[22] P. K. Park and R. S. Elliott, "Design of collinear longitudinal slot arrays fed by boxed stripline," *IEEE Trans. Antennas Propagat.*, vol. AP-29, no. 1, pp. 135–140, Jan. 1981.

[23] N. L. VandenBerg, L. Katehi, J. A. Lick, and G. T. Mooney, "Characterization of strip-fed cavity-backed slots," *IEEE Trans. Antennas Propagat.*, vol. AP-40, no. 4, pp. 405–413, Apr. 1992.

[24] G. D. Massa, "Microstrip slot array design," in *Proc. 2nd Int. Conf. Electromagnetics in Aerospace Appl.*, Sept. 1991, pp. 385–388.

[25] H. G. Akhavan and D. Mirshekar-Syahkal, "Microstrip-fed coupled slots antenna for wide-band applications," in *IEEE AP-S Int. Symp. Dig.*, July 2000, pp. 16–21.

[26] S. H. Kim, J. H. Choi, J. W. Baik, and Y. S. Kim, "CPW-fed log-periodic dumb-bell slot antenna array," *Electron. Lett.*, vol. 42, no. 8, pp. 436–438, Apr. 2006.

[27] H. S. Tsai, M. J. W. Rodwell, and R. A. York, "Planar amplifier array with improved bandwidth using folded-slots," *IEEE Microwave Guided Wave Lett.*, vol. 4, no. 4, pp. 112–114, Apr. 1994.

[28] J. Schoenberg, T. Mader, B. Shaw, and Z. B. Popovic, "Quasi-optical antenna array amplifiers," in *IEEE MTT-S Int. Symp. Dig., vol. 2*, June 1995, pp. 605–608.

[29] A. Grbic and G. Eleftheriades, "Leaky CPW-based slot antenna arrays for millimeter-wave applications," *IEEE Trans. Antennas Propagat.*, vol. AP-50, no. 11, pp. 1494–1504, Nov. 2002.

[30] E. A. Soliman, S. Brebels, E. Beyne, and G. A. E. Vandenbosch, "2x2 and 4x4 arrays of annular slot antennas in MCM-D technology fed by coplanar CPW networks," *IEE Proc. Microw. Antennas Propagat.*, vol. 146, no. 5, pp. 335–338, Oct. 1999.

[31] E. A. Soliman, S. Brebels, G. A. E. Vandenbosch, and E. Beyne, "Antenna arrays in MCM-D technology fed by coplanar CPW networks," *IEEE Trans. Microwave Theory Tech.*, vol. MTT-48, no. 6, pp. 1065–1068, Jun. 2000.

[32] A. Nesic, "Slotted antenna array excited by a coplanar waveguide," *Electron. Lett.*, vol. 18, no. 6, pp. 275–276, Mar. 1982.

[33] H. Kobayashi and Y. Yasuoka, "Slot-array antennas fed by coplanar waveguide for millimeter-wave radiation," *IEEE Trans. Microwave Theory Tech.*, vol. MTT-46, no. 6, pp. 800–805, Jun. 1998.

[34] M. Qiu, M. Simcoe, and G. Eleftheriades, "High-gain meanderless slot arrays on electrically thick substrates at millimeter-wave frequencies," *IEEE Trans. Microwave Theory Tech.*, vol. MTT-50, no. 2, pp. 517–528, Feb. 2002.

[35] T.-F. Huang, S.-W. Lu, and P. Hsu, "Analysis and design of coplanar waveguide-fed slot antenna array," *IEEE Trans. Antennas Propagat.*, vol. AP-47, no. 10, pp. 1560–1565, Oct. 1999.

[36] J. P. Jacobs, J. Joubert, and J. W. Odendaal, "Conductor-backed CPW-fed broadside linear slot antenna array on two-layer dielectric substrate," in *Proc. Int. ITG-Conf. Antennas*, 2003, pp. 61–63.

[37] N. Amitay, V. Galindo, and C. P. Wu, *Theory and Analysis of Phased Array Antennas*. New York: Wiley-Interscience, 1972.

[38] J.-M. Laheurte, L. P. B. Katehi, and G. M. Rebeiz, "CPW-fed slot antennas on multilayer dielectric substrates," *IEEE Trans. Antennas Propagat.*, vol. AP-44, no. 8, pp. 1102–1111, Aug. 1996.

[39] J. P. Jacobs, J. Joubert, and J. W. Odendaal, "Characterization of conductor-backed CPW-fed slot antenna with two-layered dielectric substrate," in *USNC/URSI Dig.*, July 2001, p. 215.

[40] ——, "Radiation efficiency and impedance bandwidth of conductor-backed CPW-fed slot dipole antenna with two-layered dielectric substrate," *Microwave Opt. Technol. Lett.*, vol. 34, no. 2, pp. 138–141, July 2002.

[41] ——, "Use of broadside conductor-backed CPW-fed twin linear-slot antennas for increased radiation efficiency on two-layer dielectric substrates," in *Proc. PIERS*, July 2002, p. 618.

[42] ——, "Radiation efficiency and impedance bandwidth of conductor-backed CPW-fed broadside twin slot antennas on two-layer dielectric substrate," *IEE Proc. Microw. Antennas Propagat.*, vol. 150, pp. 185–190, 2003.

[43] ——, "Effect of back-plane distance on mutual coupling between CPW-fed slots on conductor-backed two-layer substrates," *Microwave Opt. Technol. Lett.*, vol. 47, no. 5, pp. 407–409, Dec. 2005.

[44] ——, "Contributions to the development of a design procedure for non-uniform linear arrays of CPW-fed slots on conductor-backed two-layered substrates," in *USNC/URSI Dig.*, July 2005, p. 786.

[45] ——, "Mutual admittance between CPW-fed slots on two-layer parallel-plate substrates," in *Proc. Mediterranean Microwave Symp.*, Sep. 2006, pp. 495–498.

[46] Zeland Software, *IE3D, Release 8*, 2001.

[47] R. Marg, A. Mallwitz, and A. F. Jacob, "Radiation efficiency of apertures in parallel-plate waveguides," *Microwave Opt. Technol. Lett.*, vol. 21, no. 3, pp. 159–162, May 1999.

[48] G. V. Eleftheriades and M. Simcoe, "Gain and efficiency of linear slot arrays on thick substrates for millimeter-wave wireless applications," in *Proc. IEEE AP-S Int. Symp.*, 1999, pp. 2428–2431.

[49] R. L. Rogers and D. P. Neikirk, "Use of broadside twin element antennas to increase efficiency on electrically thick dielectric substrates," *Int. J. Infrared Millimeter Waves*, vol. 9, no. 11, pp. 949–969, 1988.

[50] D. G. Swanson and W. J. R. Hoefer, *Microwave Circuit Modeling Using Electromagnetic Field Simulation*. Boston: Artech House, 2003.

[51] A. U. Bhobe, C. L. Holloway, M. Piket-May, and R. Hall, "Coplanar waveguide fed wideband slot antenna," *Electron. Lett.*, vol. 36, no. 16, pp. 1340–1342, Aug. 2000.

[52] C. A. Balanis, *Antenna Theory: Analysis and Design*, 2nd ed. New York: Harper and Row, 1997.

[53] R. L. Rogers and D. P. Neikirk, "Radiation properties of slot and dipole elements on layered substrates," *Int. J. Infrared Millimeter Waves*, vol. 10, no. 6, pp. 697–728, 1989.

[54] M. Qiu, M. Simcoe, and G. V. Eleftheriades, "Radiation efficiency of printed slot antennas backed by a ground reflector," in *Proc. IEEE AP-S Int. Symp.*, 2000, pp. 1612–1615.

[55] M. Hickey, M. Qiu, and G. V. Eleftheriades, "A reduced surface-wave twin arc-slot antenna for millimeter-wave applications," *IEEE Microwave Wireless Components Lett.*, vol. 11, no. 11, pp. 459–61, Nov. 2001.

[56] R. F. Harrington, *Time-Harmonic Electromagnetic Fields*. New York: McGraw-Hill, 1961.

[57] G. V. Eleftheriades and G. M. Rebeiz, "Self and mutual admittance of slot antennas on a dielectric half-space," *Int. J. Infrared Millimeter Waves*, vol. 14, no. 10, pp. 1925–1946, 1993.

[58] J. A. G. Malherbe and D. B. Davidson, "Mutual impedance for half-cosinusoid slot voltage distribution: An evaluation," *IEEE Trans. Antennas Propagat.*, vol. AP-32, no. 9, pp. 990–991, Sep. 1984.

[59] C. A. Balanis, *Antenna Theory: Analysis and Design*. New York: Harper and Row, 1982.

[60] Zeland Software, *IE3D, Release 10*, 2004.

[61] M. S. Garino, G. Vecchi, and M. Orefice, "Efficient spectral evaluation of mutual coupling between planar antennas," *Radio Science*, vol. 35, no. 2, pp. 511–523, Mar.–Apr. 2000.

[62] N. G. Alexopoulos and I. E. Rana, "Mutual impedance computation between printed dipoles," *IEEE Trans. Antennas Propagat.*, vol. 29, no. 1, pp. 106–111, Jan. 1981.

[63] D. M. Pozar, "Input impedance and mutual coupling of rectangular microstrip antennas," *IEEE Trans. Antennas Propagat.*, vol. AP-30, pp. 1191–1196, Nov. 1982.

[64] P. B. Katehi, "A generalized method for the evaluation of mutual coupling in microstrip arrays," *IEEE Trans. Antennas Propagat.*, vol. AP-35, no. 2, pp. 125–133, Feb. 1987.

[65] G. V. Eleftheriades and J. R. Mosig, "On the network characterization of planar passive circuits using the method of moments," *IEEE Trans. Microwave Theory Tech.*, vol. MTT-44, no. 3, pp. 438–445, Mar. 1996.

[66] B. K. J. C. Nauwelaers and A. R. Van de Capelle, "Integrals for the mutual coupling between dipoles or between slots: with or without complex conjugate?" *IEEE Trans. Antennas Propagat.*, vol. 36, no. 10, pp. 1375–1381, Oct. 1988.

[67] R. S. Elliott, "On the mutual admittance between clavin elements," *IEEE Trans. Antennas Propagat.*, vol. AP-28, no. 6, pp. 864–870, Nov. 1980.

[68] P. Otero, G. V. Eleftheriades, and J. R. Mosig, "Modeling the coplanar transmission line excitation of planar antennas in the method of moments," *Microwave Opt. Technol. Lett.*, vol. 16, no. 4, pp. 219–225, Nov. 1997.

[69] C. A. Balanis, *Advanced Engineering Electromagnetics*. New York: John Wiley and Sons, 1989.

[70] G. Mazzarella and G. Panariello, "On the evaluation of mutual coupling between slots," *IEEE Trans. Antennas Propagat.*, vol. 35, no. 11, pp. 1289–1293, Nov. 1987.

[71] A. K. Bhattacharyya, *Electromagnetic Fields in Multilayered Structures: Theory and Applications*. Boston: Artech House, 1994.

[72] K. A. Michalski and J. R. Mosig, "Multilayered media Green's functions in integral equation formulations," *IEEE Trans. Antennas Propagat.*, vol. 45, no. 3, pp. 508–519, Mar. 1997.

[73] D. Pasqualini, A. Neto, and R. A. Wyss, "Distributed sources on coplanar waveguides: Application to photomixers for THz local oscillators," *Microwave Opt. Technol. Lett.*, vol. 33, no. 6, pp. 430–435, June 2002.

[74] M. R. Abdul-Gaffoor, H. K. Smith, A. A. Kishk, and A. W. Glisson, "Simple and efficient full-wave modeling of electromagnetic coupling in realistic RF multilayer PCB layouts," *IEEE Trans. Microwave Theory Tech.*, vol. 50, no. 6, pp. 1445–1457, June 2002.

[75] M. S. Sierra-Castañer, M. Vera-Isasa, M. Sierra-Pérez, and J. L. Fernandez-Jambrina, "Double-beam parallel-plate slot antenna," *IEEE Trans. Antennas Propagat.*, vol. AP-53, no. 3, pp. 977–984, Mar. 2005.

[76] M. R. Spiegel, *Mathematical Handbook of Formulas and Tables*. New York: McGraw-Hill, 1968.

[77] L. Tsang, C.-C. Huang, and C. H. Chan, "Surface electric fields and impedance matrix elements of stratified media," *IEEE Trans. Antennas Propagat.*, vol. 48, no. 10, pp. 1533–1543, Oct. 2000.

[78] D. B. Davidson, *Computational Electromagnetics for RF and Microwave Engineering*. Cambridge, UK: Cambridge University Press, 2005.

[79] W. C. Chew, *Waves and Fields in Inhomogeneous Media*. New York: Van Nostrand Reinhold, 1990.

[80] J. R. Mosig, "Integral equation technique," in *Numerical Techniques for Microwave and Millimetre-Wave Passive Structures*, T. Itoh, Ed. New York: Wiley, 1989, pp. 133–213.

[81] D. G. Zill and M. R. Cullen, *Advanced Engineering Mathematics*. Sudbury, MA: Jones and Bartlett, 2002.

[82] K. A. Michalski, "Extrapolation methods for Sommerfeld integral tails," *IEEE Trans. Antennas Propagat.*, vol. 46, no. 10, pp. 1405–1418, Oct. 1998.

[83] L. T. Hildebrand and D. A. McNamara, "A guide to implementational aspects of the spatial-domain integral equation analysis of microstrip antennas," *Appl. Comput. Electromagn. Soc. J.*, vol. 10, no. 1, pp. 40–51, 1995.

[84] H. W. Hansen, *Numerical Solution of Antennas in Layered Media*. Taunton, Somerset, England: Research Studies Press, 1989.

[85] L. Tsang, J.-H. Cha, and J. R. Thomas, "Electric fields of spatial Green's functions of microstrip structures and applications to the calculations of impedance matrix elements," *Microwave Opt. Technol. Lett.*, vol. 20, no. 2, pp. 90–97, Jan. 1999.

[86] L. Tsang, "Near-field radiation from microstrip lines," *Microwave Opt. Technol. Lett.*, vol. 19, no. 3, pp. 176–184, Oct. 1998.

[87] M. Abramowitz and I. A. Stegun (Eds.), *Handbook of Mathematical Functions*. New York: Dover, 1972.

[88] R. Wrede and M. R. Spiegel, *Theory and Problems of Advanced Calculus*, 2nd ed. New York: McGraw-Hill, 2002.

[89] Numerical Algorithms Group, *NAG Foundation Toolbox for MATLAB 6*, Oxford, 2003.

[90] D. M. Pozar, *Microwave Engineering*, 2nd ed. New York: Wiley, 1998.

[91] Rogers Corporation, *RO4000 Series High Frequency Circuit Materials*, [Online document], Available HTTP: http://www.rogerscorporation.com, [cited 30 April 2007].